UNCLASSIFIED
GEMP-334 A

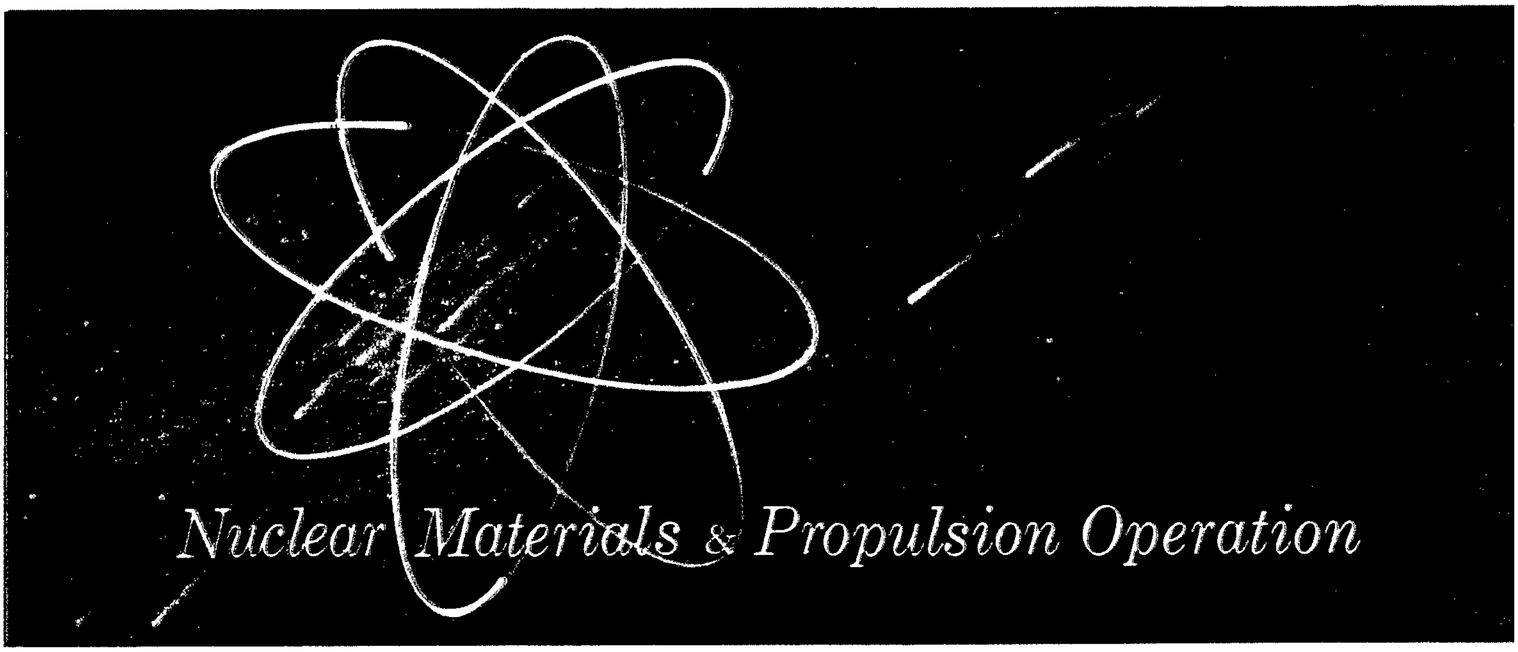

FOURTH ANNUAL REPORT-HIGH-TEMPERATURE MATERIALS AND REACTOR COMPONENT DEVELOPMENT PROGRAMS

Volume I-Materials

February 26, 1965

ADVANCED TECHNOLOGY SERVICES
GENERAL ELECTRIC

UNCLASSIFIED

Printed in USA. Price $6.00. Available from the
Clearinghouse for Federal Scientific and
Technical Information,
National Bureau of Standards,
U. S. Department of Commerce,
Springfield, Virginia

GEMP-334 A

UC-25 Metals, Ceramics,
and Materials
TID-4500 (39th Ed.)

61332

FOURTH ANNUAL REPORT-HIGH-TEMPERATURE MATERIALS AND REACTOR COMPONENT DEVELOPMENT PROGRAMS

Volume I-Materials

[redacted]

DISTRIBUTION STATEMENT A
Approved for Public Release
Distribution Unlimited

February 26, 1965

[redacted]

United States Atomic Energy Commission   Contract No. AT(40-1)-2847

NUCLEAR MATERIALS and PROPULSION OPERATION
ADVANCED TECHNOLOGY SERVICES
GENERAL ELECTRIC
Cincinnati 15, Ohio

DISTRIBUTION

EXTERNAL

AEC Headquarters

G. K. Dicker
I. Hoffman
F. C. Schwenk
J. M. Simmons
W. R. Voigt
G. W. Wensch
M. J. Whitman

AEC, OROO

D. F. Cope (3)
D. S. Zachry, Jr.

AEC, CANEL Project Office

A. J. Alexander

AEC, CAO

C. L. Karl
J. F. Weissenberg

AEC, SAN

Lt. Col. J. B. Radcliffe, Jr.

AEC, MCR Project Office

S. Meyers

General Atomic

D. Ragone

Pratt and Whitney Aircraft (CANEL)

L. M. Raring (3)

Institute for Defense Analyses

R. C. Hamilton

ORNL

R. E. Blanco
W. R. Grimes
W. O. Harms
W. C. Thurber (2)

BMI

R. W. Dayton

Battelle - Northwest

F. W. Albaugh
J. J. Cadwell
R. E. Nightingale

LASL

R. D. Baker

Lawrence Radiation Laboratory

C. Cline
A. J. Rothman

Westinghouse, Astronuclear Lab.

D. C. Goldberg

NASA Headquarters

J. J. Lynch
B. Reznick

NASA, Lewis Research Center

J. W. Creagh
N. Saunders

Atomics International

C. E. Weber
S. C. Carniglia

Argonne National Laboratory

R. Noland

Universal-Cyclops Steel Corp.

L. M. Bianchi

Wah Chang Corporation

S. Worchester

INTERNAL

E. A. Aitken
W. G. Baxter
J. R. Beeler
J. C. Blake
K. M. Bohlander
B. Bonini
H. C. Brassfield
R. W. Brisken
V. P. Calkins
B. A. Chandler
C. L. Chase (3)
C. G. Collins (2)
E. S. Collins
J. F. Collins
P. K. Conn
J. B. Conway
E. B. Delson
H. S. Edwards
E. W. Filer
P. N. Flagella
J. E. Fox
R. E. Fryxell
E. S. Funston
G. F. Hamby
J. O. Hibbits
A. N. Holden, APED (2)
L. D. Jordan
F. Kingsbury
G. Korton
W. C. Kuhlman
W. H. Long
J. E. McConnelee
L. R. McCreight, MSO
J. A. McGurty
C. I. McVey
J. W. Morfitt
J. Moteff
R. E. Motsinger
G. T. Muehlenkamp
C. E. Niemeyer
W. E. Niemuth
G. W. Pomeroy
W. Z. Prickett
R. E. Reid
F. C. Robertshaw
E. J. Schmidt, ATS
L. H. Sjodahl
R. J. Spera
H. R. Stephan
C. L. Storrs
C. O. Tarr
P. P. Turner
F. O. Urban
G. R. VanHouten
H. E. Wagner
J. F. White
V. C. Wilson, RL
O. G. Woike
R. E. Wood
C. S. Wukusick
Library (25)

PREFACE

This report, GEMP-334A, is one of three volumes comprising the fourth annual report on the High-Temperature Materials and Reactor Component Development Programs being conducted by the General Electric Nuclear Materials and Propulsion Operation under Contract No. AT(40-1)-2847 of the Atomic Energy Commission.

Volumes I (GEMP-334A) and II (GEMP-334B) report the progress made from (January 31, 1964 to January 31, 1965) on the unclassified and classified portions, respectively, of the materials program, and Volume III (GEMP-334C) reports the progress on that part of the contract covering instrumentation and controls. Some of these programs were terminated at the end of Fiscal Year 1964, others are continuations of Fiscal Year 1964 programs, and still others were initiated in Fiscal Year 1965. The status of each program is indicated in the more detailed breakdown of each volume given below.

This report also replaces the bimonthly report (GEMP-44) on Ceramics and Chemistry for the period from November 15, 1964 to January 15, 1965, the report (GEMP-45) on Metallurgy covering the period from December 15, 1964 to February 15, 1965, except the 15 days in February, and the report (GEMP-86) on Reactor Instrumentation and Controls for the period from November 1, 1964 to December 31, 1964. The next Ceramics and Chemistry bimonthly report (GEMP-46) will cover the period from February 1, 1965 to March 15, 1965. The next Metallurgy report (GEMP-47) will cover the period from February 1, 1965 to April 15, 1965. The next Instrumentation and Controls report (GEMP-87) will cover the period from January 1, 1965 to February 28, 1965.

GEMP-334A

1. High-Temperature Reactor Materials Research (continuation).
2. Effect of Radiation on High-Temperature Metals and Alloys (continuation).
3. Radiation Effects in BeO (continuation).
4. Fission Gas Diffusion in Unfueled Ceramic Materials (continuation).
5. Fission Product Transport Processes in Refractory-Metal Fuel Systems (continuation).
6. Internal Conversion Ceramic Fuel Element Research (continuation).
7. Oxidation-Resistant Fuel Element Materials Research (continuation).
8. High-Temperature Thermocouple and Electrical Materials Research (Initiated FY-65).

GEMP-334B

1. High-Temperature Studies of Substoichiometric Urania and Urania Solid Solutions (continuation).
2. Refractory-Metal Fuel Element Materials Research (continuation).
3. Burnup Capability of Y_2O_3-Stabilized UO_2 and BeO-Stabilized Fuel Materials (continuation).
4. High-Temperature Carbides and Borides Research (continuation).
5. Moderator (Fueled and Unfueled), Controls, and Shield Materials Research (continuation).
6. High-Flux Reactor Materials Gaseous Fuels Research (continuation).

7. Graphite Fuel Element Materials Research (terminated FY-64).
8. Direct Conversion High-Temperature Materials Research (terminated FY-64).
9. Coated Fuel Particle Development and Evaluation (terminated FY-64).

GEMP-334C

1. Capacitance Temperature Sensor (continuation).
2. Development of Nuclear Sensors (continuation).
3. High-Temperature Extension of Conventional Nuclear Sensors (terminated FY-64).

CONTENTS

FIGURES

Page

Page

Page

TABLES

CONVERSION TABLE

To Convert From	To	Multiply By
Atmospheres	Pounds/inch^2	14.7
Calories (mean)	Btu (mean)	0.00397
Calories/gram-^{o}C	Btu/pound-^{o}F	1.0
Calories/sec-cm-^{o}C	Btu/hr-ft-^{o}F	241.8
Calories/sec-cm^2	Btu/hr-ft^2	1.32×10^4
Calories/sec-cm^2-^{o}C	Btu/hr-ft^2-^{o}F	7370
Centimeters	Feet	0.03281
	Inches	0.3937
Cubic centimeters	Cubic feet	3.531×10^{-5}
	Cubic inches	0.06103
Grams	Pounds	0.002205
Grams/cm^3	Pounds/ft^3	62.43
Grams/cm^2	psi	0.01422
Kilograms	Pounds	2.205
Kilograms/cm^2	Atmospheres	0.9678
	Pounds/ft^2	2048
	Pounds/inch^2	14.22
Kilograms/mm^2	Pounds/inch^2	1422.32
Kilowatts	Btu/sec	0.948
Liters	Cubic feet	0.0353
Meters	Inches	39.37
Millimeters of mercury	Atmospheres	0.001316
Square centimeters	Square feet	0.001076
	Square inches	0.155
Torr	mm of Hg	1.0
	Atmospheres	0.001316
Watts/cm-^{o}C	Btu/hr-ft-^{o}F	57.8
Watt-seconds	Btu	0.000948
Watts/cm^2-^{o}C	Btu/hr-ft^2	3170
Watts/cm^2-^{o}C	Btu/hr-ft^2-^{o}F	1760
Centimeters/sec	Feet/sec	0.03281
Meters/sec	Feet/sec	3.281

INTRODUCTION AND SUMMARY

This report, GEMP-334A, is one of three volumes of the fourth annual progress report on the GE-NMPO high temperature materials and reactor component development programs conducted during Calendar Year 1964 under Contract No. AT(40-1)-2847. This volume covers eight unclassified material development programs: 1. materials for use as fueled and unfueled, high-temperature reactor components; 2. radiation effects on the time-, temperature-, and stress-dependent properties of selected high-temperature alloys and refractory metals; 3. radiation effects in BeO as a function of composition, grain size, density, porosity, and irradiation temperature and dosage; 4. the diffusion of fission gases (Kr, Xe, and I atoms) in ceramic oxides subsequent to their injection via ion bombardment; 5. the fission product transport processes in refractory-metal fuel systems at temperatures exceeding 1700°C; 6. the use and development of a fertile material (thoria) in stabilized-fuel-BeO systems; 7. the development of oxidation- and corrosion-resistant fuel element materials with improved high-temperature properties; 8. high-temperature thermocouples and electrical materials development.

To p. 19

Significant results achieved in these programs are as follows~~:~~

Measurement of creep-rupture properties of refractory metals and alloys to 2800°C in hydrogen and argon was improved by development of an optical extensometer technique for accurately measuring the gage-length strain. This technique was employed in measuring the first-stage creep of tungsten at 2200° to 2600°C. Creep-rupture results showed (1) the Ta - 10W alloy at 1600°C in hydrogen has greater stress-rupture strength and is more creep-resistant than Re or W - 25Re in the stress level of 3 to 6 kg/mm^2; (2) the rupture strength and creep resistance is less for arc-cast tungsten than for wrought powder-metallurgy tungsten in the temperature range of 2200° to 2600°C; however, arc-cast tungsten is more ductile, based on total elongation at rupture; (3) the stress-rupture life and creep resistance of Mo - 50Re is an order of magnitude greater than for molybdenum at 1600°C and 2200°C; (4) all BCC materials evaluated to data have creep-rupture characteristics from 1600° to 2800°C which are linear on a log-log plot, consistent with a power stress law; however, the creep rupture characteristics for rhenium, which is HCP, is concave downward on a similar plot, indicating a change in stress dependency at a certain stress level.

A series of W - 25 to 30Re - 0 to 30Mo (at. %) alloys was identified which melt above 2760°C and, in general, are resistant to loss of room-temperature bend ductility after prolonged heating in the 600° to 2600°C temperature range. Complete resistance to loss of bend ductility after holding at 2600°C was shown by W - 30Re - 30Mo. Some alloys containing 30Re are age-hardenable and, as such, are amenable to the development of alloys with improved strength properties up to 1600°C.

A processing procedure was developed for W - 25Re which results in production of high-purity sheet and extends the high-temperature capability of this alloy. This process is applicable to other tungsten - rhenium-base alloy~~s.~~

Irradiation of tungsten to a fast neutron dose of 8 x 10^{19} nvt increases the time to rupture at 1100°C by factors of greater than 5 with a corresponding decrease in linear creep rate but without changing the ductility. Threshold of observable change in creep-rupture properties at 1100°C (0.37 T_m) is 1 x 10^{19} nvt. Further strengthening results from annealing at a temperature higher than the test temperature of 900°C (0.32 T_m). Isochronal recovery studies of the resistivity properties of irradiated tungsten indicate three resolved recovery peaks at 0.16, 0.22, and 0.31 T_m whereas hardness measurements indicate only one recovery peak at 0.35 T_m. Other BCC metals show recovery peaks at the same fractions of T_m, and the complete recovery of resistivity at 0.31 T_m and hardness at 0.35 T_m is in contrast to the recovery of these properties in the irradiated FCC metals where both occur at 0.5 T_m.

Thermal neutrons cause significant reductions in the time to rupture and in the ductility of Hastelloy X and A-286 alloys over and above that caused by fast neutrons. Calculations indicate that boron atoms segregate to grain boundaries and dislocation lines where, through the thermal neutron B^{10} (n, α) Li^7 reaction, the atom displacements, caused by recoiling lithium atoms and α-particles, and the generated helium atoms all contribute to embrittlement.

Additional data were obtained on the factors influencing the expansion and property changes in irradiated BeO. Equations, indicating that the during-irradiation annealing of both interstitial and vacancy defects follow first order kinetics, describe the expansion reasonably well from 100° to 1200°C; however, the saturation predicted by the equations of this behavior has yet to be confirmed. Both interstitial- and vacancy-type clusters were identified in BeO irradiated at elevated temperatures and in concentrations approximately in agreement with the predicted kinetic relationships. Helium may occupy the vacancy clusters and its diffusion appears to follow the kinetics ascribed to vacancies.

Results from permeation studies at 2400°C indicate that the transport of krypton in or through tantalum is less than 8 x 10^7 atoms/sec. This indicates that (1) krypton cannot be dissolved to any extent in tantalum by thermal energies alone and (2) transport through the grain boundaries is not significant, although the grain size increased by a factor of 10 during the heat treatment. In-pile tests on powder-metallurgy tantalum capsules containing UO_2 were operated at temperatures up to 2200°C. The low values for the fission gas release showed no evidence for volume diffusion of the fission gases, although fission gases were embedded in the cladding by recoil. This indicates that long-range diffusion (greater than 400 microns) does not occur to any significant extent to at least 2200°C.

Well-crystallized solid solutions of $UO_2 : 3ThO_2 : 0.55Y_2O_3$ were developed which, when incorporated at the 7 to 25 volume percent levels in a BeO matrix, exhibit excellent fuel retention properties; e.g., a maximum of 1.7 percent UO_2 is lost in 2000 hours at 1400°C in air, 0.6 percent UO_2 in 4000 hours at 1200°C in air, and no UO_2 loss in 2000 hours at 1200°C in He and in He + 5 volume percent H_2. No significant change in physical or mechanical properties resulted from the above treatments. Sintering the fueled BeO at 1800°C instead of 1675°C resulted in increased fuel retention, possibly because of the elimination of the metastable 4BeO - Y_2O_3 which forms on the surface of fuel elements sintered at 1675°C.

The Fe-Cr-Al-Y system of alloys ~~has~~ continued to show superior oxidation and steam-corrosion resistance at temperatures to 1300°C in comparison to other high-temperature oxidation-resistant alloys. A better understanding of the contribution of each of the alloying elements to the properties of the alloy was obtained. Embrittlement at low temperatures was found to be caused by precipitation of a Cr-rich phase. Reduction of the Cr content was effective in reducing the embrittlement. The interrelationship between oxidation resistance and the Cr and Al contents was established, and alloys with low Cr contents were prepared with good oxidation resistance. Aluminum, which is responsible for the excellent oxidation at elevated temperatures through the formation of an Al_2O_3 surface film, also retards the formation of the Cr-rich phase and thus lowers the embrittling effect of Cr. Yttrium, necessary for good adherence of the Al_2O_3 film, is detrimental to weldability and ductility when present at the 1 percent level. Studies indicated that corrosion resistance can be maintained with lower Y contents (0.1%) to a temperature of 1100°C and thus weldability and ductility are improved.

Fe - 25Cr - 4Al - 1Y-clad Fe-UO_2 and Cr-UO_2 fuel element capsule specimens have shown stability and excellent oxidation resistance for 5000 hours at 950°C and 3000 hours at 1100°C in air.

A theoretical explanation for the ductilizing effect of Re and Ru on Cr-base alloys was developed. The essential feature is removal of the embrittling interstitial elements from the matrix by Re-induced clustering or spinodal decomposition of the Cr-rich phase, thus improving dislocation mobility.

The W / W - 25Re thermocouple showed significant changes in thermoelectric properties in a series of alloys synthesized to represent the transmuted product. Errors of +90°C or more may result after 1 month in a 10^{14} neutron flux.

Gas-tight metal-to-ceramic seals of Nb and Al_2O_3 were developed using high-temperature gas-pressure bonding techniques, which have good tensile bond strength (> 8 kg/cm^2). They demonstrated excellent stability at 1600°C for 466 hours with two returns to room temperature.

This volume covers 8 unclassified materials development programs.

1. HIGH-TEMPERATURE REACTOR-MATERIALS RESEARCH

(57003)

The objective of this program is to develop and evaluate methods of preparing and joining refractory metals and alloys and other high-temperature materials to be used for fueled and non-fueled high-temperature (1000° to 3000°C) reactor structural applications.

Work conducted during Calendar Year 1964 included: (1) measurement of mechanical properties, principally stress-rupture and creep, of refractory metals and alloys from 1600° to 2800°C, (2) continuation of development and evaluation of W-Re alloys and W-Re-Mo alloys, and (3) initiation of a program to study low-cycle fatigue properties of pressure vessel steels at elevated temperatures.

1.1 MECHANICAL PROPERTIES

Mechanical properties measurements of refractory metals and alloys were principally concerned with the determination of stress-rupture and creep properties at temperatures from 1600° to 2800°C. Work was initiated on measurement of tensile properties of tantalum and Ta - 10W* in both hydrogen and helium at temperatures from 600° to 1200°C.

STRESS-RUPTURE AND CREEP EVALUATIONS

Continuing stress-rupture and creep evaluations led to additional data for various refractory metals and refractory metal alloys. Studies were made of Re, W, W - 25Re, Ta - 10W, Mo, Mo - 50Re, and W - 30Re - 30Mo in hydrogen and/or argon in the temperature range of 1600° to 2600°C. At 1600°C a rather extensive comparison was made of the relative strength and creep resistance of W - 25Re, Re, Ta - 10W, and W - 30Re - 30Mo. In addition, developments with the optical extensometer have allowed the high-temperature measurement of gage length elongations. Based on these data, a more accurate interpretation of creep behavior is now possible with the use of the extensometer.

Measurement of Creep

While experimental techniques currently employed in measuring stress-rupture properties at high temperatures are standard practice, the technique for measuring creep characteristics of metals at temperatures above 1600°C is still being developed. The need for this continuing development is brought about by the complexities associated with the higher temperature testing and the fact that numerous requirements for high-temperature strength data were identified only recently.

During the initial phase of stress-rupture testing of refractory metals and alloys at elevated temperatures (1600° to 2800°C), elongation values at varying time intervals were obtained for the total load train movement. Measurements were obtained by sighting a

---

*All compositions in this section are in weight percent unless otherwise specified.

micrometer telescope on the load pan suspended below the furnace. Similar measurements were obtained automatically by using a linear variable differential transformer (LVDT). Without an accurate method for measuring elongation of the test specimen gage section, data were used on a relative basis for comparisons. Later studies showed that these measurements were in error on the order of 10 to 50 percent depending on test conditions.

A technique based on the use of an optical extensometer was developed to yield a more accurate method for the measurement of creep at elevated temperatures. Paired, filar micrometer telescopes, focused on fiducial marks at either end of the specimen gage section, were adjusted manually to follow sample elongation under load. Resulting elongation - time curves gave a more accurate representation of the creep process occurring within the gage section than did the measurement of total train movement formerly used.

After evaluating several different types of fiducial marks, it was found that the most satisfactory consisted of 0.13-mm holes drilled completely through the sheet (0.25- to 1.5-mm-thick) specimen. These holes were small enough to minimize any weakening effect and yet large enough to be easily seen with the 20X magnification afforded by micrometer telescopes. With specimens positioned properly in the furnace, these holes were aligned with separations in the heating element and thermal radiation shields to provide a contrasting background. A clear and distinct image of each hole was then viewed through the telescopes.

Initially the 0.13-mm holes used as fiducial marks were located outside the test specimen gage section (Figure 1.1). This location caused some slight error in gage section elongation and calculated secondary creep rate. To reduce this error, the 0.13-mm holes drilled through the test specimen were placed at each end of the gage section. Although this reduced the cross sectional area by 2 percent, no detrimental effects resulted. Specimens tested to rupture failed near the gage section center with no noticeable area reduction in the vicinity of the holes. The time-to-rupture for specimens tested with holes was identical to that of other specimens tested without holes under the same conditions. This technique for measuring elongations proved satisfactory and was used quite extensively since its development.

A comparison of results obtained with both the LVDT and paired, filar micrometer telescopes during a test of an arc-cast molybdenum sheet (0.05-cm-thick) specimen in hydrogen at 2200°C and a stress of 0.197 kg/mm^2 is shown in Figure 1.2. As expected, total

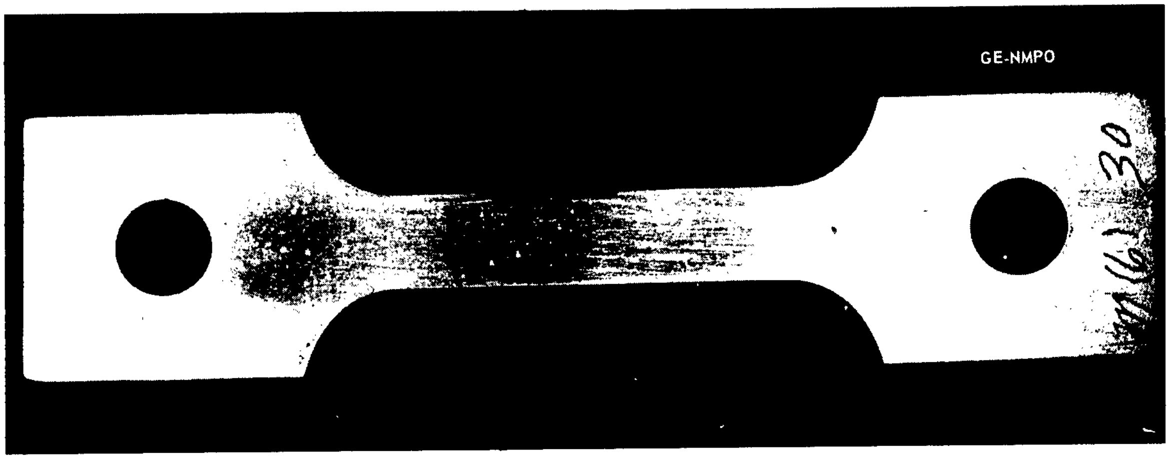

Fig. 1.1 – Typical creep specimen with 0.13-millimeter holes used as fiducial marks for optical extensometer measurements
(Neg. P64-4-3A)

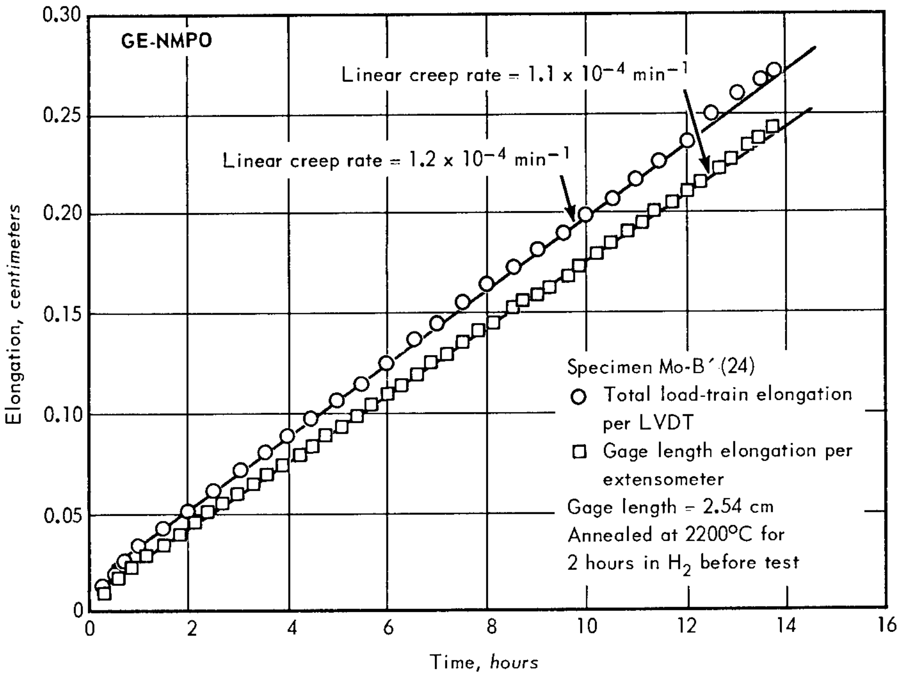

Fig. 1.2 – Comparison of gage length elongation with load-train elongation for arc-cast molybdenum at 2200°C; 0.197 kg/mm^2 stress in hydrogen

train elongations at any instant were always slightly greater than gage section elongations. Also, the secondary stage (linear) creep rate obtained from total load train results was about 10 percent greater than that based on optical extensometer data.

During the course of these creep measurement evaluations, tests were interrupted at various time periods and specimens were brought to room temperature. Measurements of the distance between fiducial marks, with a linear comparator, were found to agree, within 2 percent, of the last measurement obtained with the optical extensometer at test temperature. Since elastic strain and thermal expansion effects were well within the margin of agreement, the accuracy of this optical extensometer measurement using small holes as fiducial marks, appeared to be well confirmed. This same excellence of agreement was obtained after many such test interruptions at strains ranging from 0.13 to 2.50 millimeters.

During the evaluation of several different types of fiducial marks for use in elongation measurements with paired, filar micrometer telescopes, diamond pyramid hardness (DPH) indents placed at each end of the test specimen gage section proved satisfactory for tests at 1600°C. Differences in reflection due to slight depressions associated with DPH marks made these marks easily visible at 1600°C. Although usable for only a limited temperature range, DPH marks do afford an alternate method for accurate elongation measurement of sheet materials difficult to drill or for rod specimens with diameters too large for easy penetration by small diameter holes.

The following creep data are presented on the basis of total load train elongations unless otherwise specified.

Rhenium - Creep-rupture data were obtained for rhenium in the 1600° to 2800°C temperature range using 0.05-cm-thick powder-metallurgy sheet specimens tested in hydrogen. Based on a comparison of stress-rupture data, rhenium was found to be stronger than tungsten at 2200°C and 2600°C but of about equal strength at 1600°C. Tests of rhenium at 2600°C in argon revealed stress-rupture behavior identical to that observed in hydrogen at the same temperature.

Stress-rupture and creep rate data for rhenium are shown in Figures 1.3 and 1.4, respectively. At both 1600°C and 2600°C, and probably also at 2200°C, a deviation from linearity existed in the lower stress range of the stress-rupture plot. This was also noted in creep behavior at 1600°, 2600°, and 2800°C, as shown in Figure 1.4. Such slope changes indicated a change in stress dependency although at this time available data are not sufficient to allow a detailed analysis. Similar creep behavior was observed by Dorn* for an aluminum alloy tested at 531°K. That study showed conclusively that at low stresses a power stress law was applicable, while at higher stresses an exponential creep law was observed. Therefore, a definite change in slope was noted on the type of plot shown in Figure 1.4. Some additional creep data for rhenium are required before the Dorn analysis can be applied to these data. The few additional tests of rhenium specimens now being planned should supply this necessary information.

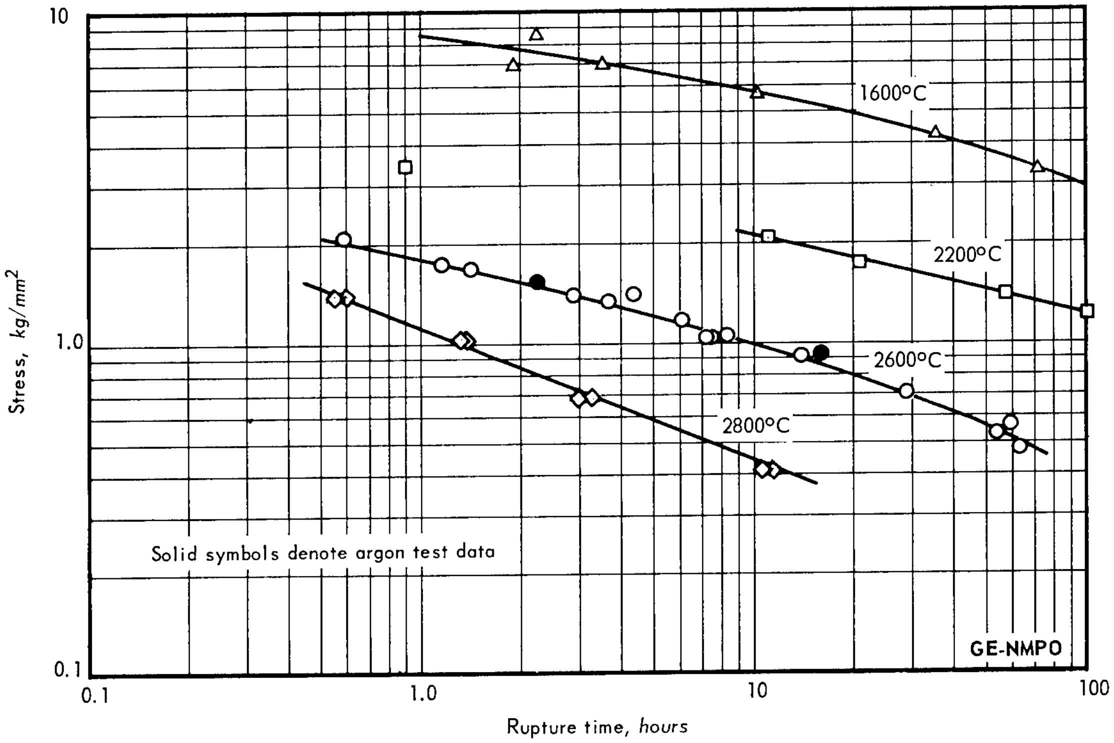

Fig. 1.3 – Stress-rupture data for 0.05-cm-thick powder-metallurgy rhenium in hydrogen

Tungsten - Creep-rupture properties of wrought powder-metallurgy tungsten, designated W(4), obtained from the U. S. Navy Tungsten Sheet Rolling Program, were evaluated. It was received as 0.051-cm-thick warm-worked (73%) sheet; it had been sintered at 2300°C in hydrogen for 9 hours. Chemical analysis of the as-received material showed it to be of high purity with the following gaseous and major solid elements detected: 2 ppm H_2, 10 ppm O_2, 1 ppm N_2, 28 ppm C, 100 ppm Fe, 100 ppm V, and 200 ppm Ni.

---

*J. E. Dorn, "Some Fundamental Experiments on High Temperature Creep," *Journal of the Mechanics and Physics of Solids*, Vol. 3, No. 85, 1955, pp. 85–116.

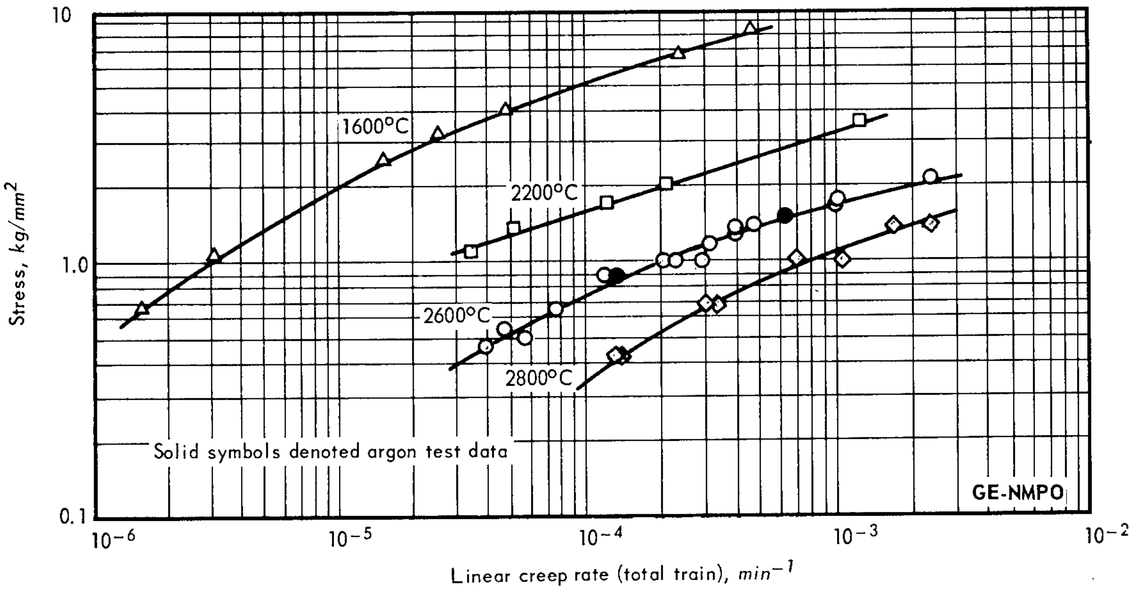

Fig. 1.4 – Creep behavior of 0.05-cm-thick powder-metallurgy rhenium in hydrogen

Stress-rupture and creep results obtained to date are presented in Figures 1.5 and 1.6, respectively. Stress-rupture results obtained in hydrogen at 2200°C were identical to those observed in an argon atmosphere at the same temperature. Creep results were also similar. However, at 2600°C noticeably different results were obtained depending upon whether testing was performed in hydrogen or argon. As shown in Figure 1.5, a higher stress-rupture strength was obtained in hydrogen. While the exact mechanism responsible for this behavior was not identified, it was also noticed in tests of other powder-metallurgy materials, and seemed to be associated with testing at temperatures above those of original sintering. Strengthening observed in hydrogen atmosphere tests was possibly caused by additional sintering. Since this sintering was probably more complete in hydrogen than in argon, a higher strength should result. Another possible mechanism involves more effective impurity removal in hydrogen than in argon. However, until a further study can be made of this mechanism, any interpretations are purely speculative.

A comparison was made of the creep-rupture properties at 2200°C of W(4) tungsten (U.S. Navy Sheet Rolling Program) with data obtained using a commercial powder-metallurgy tungsten. In general, essentially identical behavior was noted; creep rates at the same stresses were identical whether tested in hydrogen or argon. The only difference noted was that the stress-rupture strength of W(4) material was slightly greater. Considerable work remains to be done on W(4) material in obtaining a more extensive comparison with commercial sintered tungsten and also with the arc-cast product now on hand.

W - 25Re - A few measurements of creep-rupture characteristics of commercial wrought powder-metallurgy W - 25Re (at. %), 0.05-cm-thick sheet were completed at 1600°C in hydrogen. Results are plotted in Figure 1.7, together with rhenium data at 1600°C from Figure 1.3. At this temperature W - 25Re alloy was definitely stronger than rhenium in the 10- to 100-hour time period.

A striking similarity exists in linear creep data at 1600°C for W - 25Re (at. %) and rhenium. The W - 25Re data yield essentially the same line as presented in Figure 1.4 for rhenium, particularly in the stress range above 3 kg/mm^2. A creep test of W - 25Re in hydrogen at 1600°C with a stress of 1.05 kg/mm^2 gave a linear creep rate of about

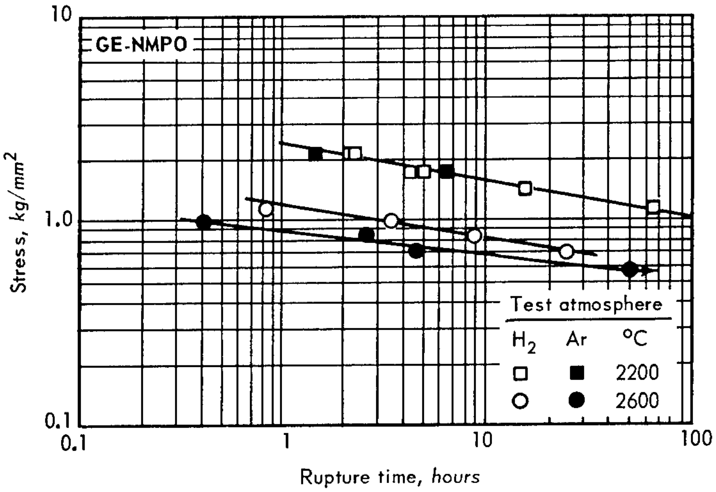

Fig. 1.5 – Stress-rupture data for 0.05-cm-thick powder-metallurgy tungsten sheet material, W(4), from Navy sheet-rolling program

Fig. 1.6 – Creep behavior of 0.05-cm-thick powder-metallurgy tungsten sheet material, W(4), from Navy sheet-rolling program

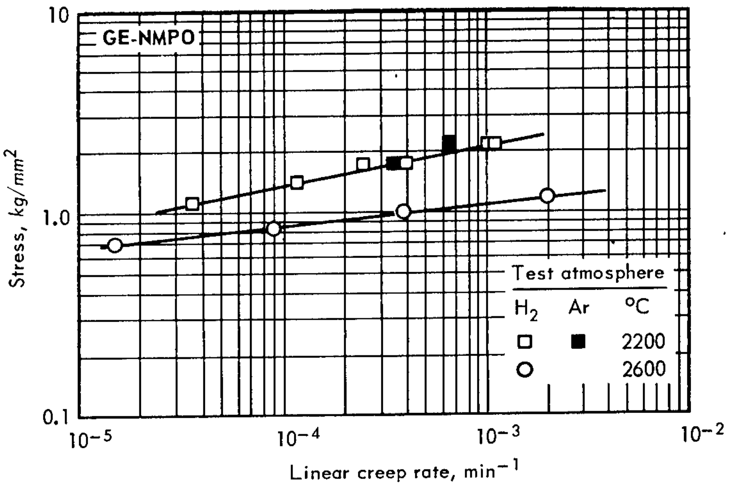

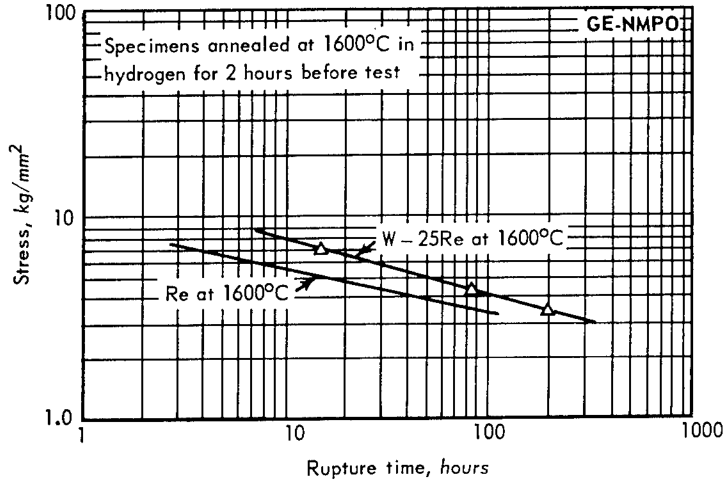

Fig. 1.7 – Stress-rupture data for 0.05-cm-thick powder-metallurgy W – 25Re sheet in hydrogen compared to data for rhenium

1.9×10^{-6} min^{-1}, which was slightly greater than that for rhenium at these same conditions. However, it is significant that this value also results in the same change in slope of the linear creep rate versus stress plot as noted in the rhenium curve at 1600°C. Based on these few data points, stress-rupture results indicated W - 25Re to be stronger than rhenium at 1600°C, whereas creep resistance of the alloy was slightly less than that of pure rhenium.

Ta - 10W - Creep-rupture tests of commercial vacuum arc-melted Ta - 10W were completed at 1600°C in hydrogen using 0.05-cm-thick sheet specimens. In initial tests, specimen contamination was observed despite the usual precautions taken to assure test atmosphere purity. Special furnace shell degassing procedures were employed, and the hydrogen was passed through a palladium diffusion cell prior to use. Despite these precautions, the creep rate for Ta - 10W decreased continually with time. Post-test hardness measurements indicated a several-fold increase compared with pre-test values. Chemical analyses of a specimen after a test at 1600°C for 642 hours revealed nitrogen and oxygen contamination amounting to 13,600 and 700 ppm, respectively.

Considerable success in minimizing specimen contamination was obtained by loosely surrounding the specimen with a 5-mil foil of tantalum that acted as a getter for test atmosphere impurities. Stress-rupture and creep data of Ta - 10W obtained at 1600°C using this protective foil technique are shown in Figures 1.8 and 1.9, respectively. These data reveal that at 1600°C Ta - 10W had a greater stress-rupture strength than either rhenium or W - 25Re (at. %) in the stress range below 6 kg/mm^2. In addition this tantalum alloy was slightly more creep resistant than these other materials in this stress range. In the stress range of 1.0 to 7 kg/mm^2 at 1600°C in hydrogen, data for Ta - 10W, Re, and W - 25Re (at. %) were in agreement within about 20 percent.

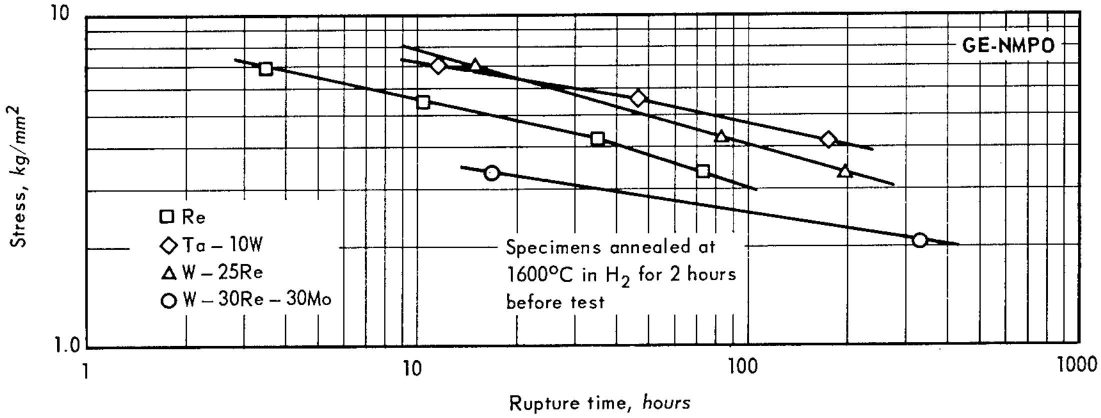

Fig. 1.8 – Stress-rupture data for some refractory metals and alloys at 1600°C in hydrogen

W - 25Re AND Ta - 10W BRAZED JOINTS

In these evaluations brazed lap joints of materials were subjected to stress-rupture tests.* W - 25Re (at. %) specimens were brazed with Cr - 20Ru,† V - 25Nb, and Nb - 40V; Ta - 10W specimens were brazed with pure vanadium and Nb - 40V. All tests were performed in hydrogen at 1600°C under a stress of 7.03 kg/mm^2 in the base metal. Shear

*"High-Temperature Materials Program Progress Report No. 39, Part A," GE-NMPO, GEMP-39A, September 30, 1964, p. 9.

†Braze alloy compositions are in atomic percent.

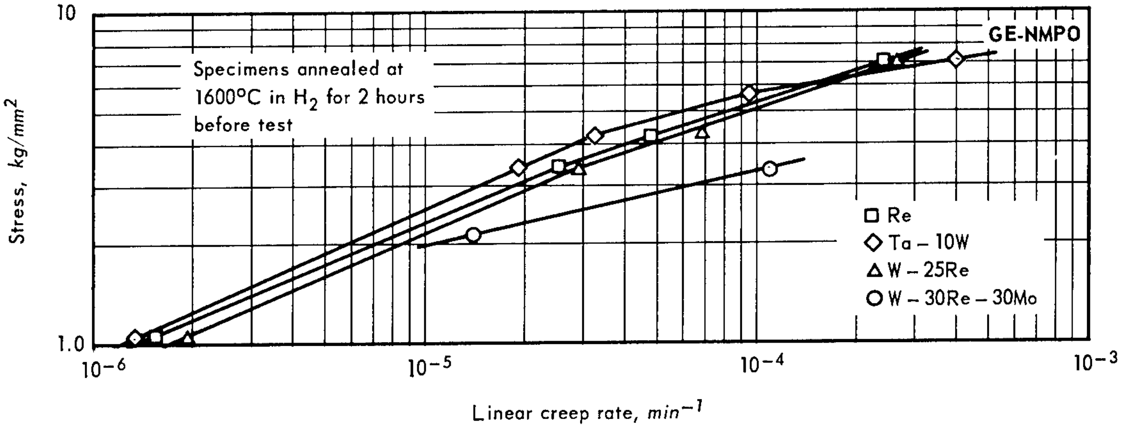

Fig. 1.9 – Comparison of linear creep rates for some refractory metals and alloys at 1600°C in hydrogen

stress in brazed joints was 0.1 kg/mm^2. All specimens prior to test appeared to be successfully brazed. Table 1.1 lists test conditions and results. As noted in the table, W - 25Re (at. %) specimens brazed with Cr - 20Ru failed in shear in the brazed joint in a relatively short time. The W - 25Re specimens brazed with Nb - 40V and V - 25Nb ruptured in the base metal adjacent to the brazed joint fillet at test times equal to that of the W - 25Re control specimen which had no brazed joint. Ta - 10W specimens brazed with either vanadium or Nb - 40V also failed in the base metal adjacent to the brazed joint fillet.

An additional stress-rupture test of a Ta - 10W specimen brazed with Nb - 40V was performed to determine remelt temperature of the brazed alloy. After annealing for 2 hours at 1600°C in hydrogen, the specimen was loaded to a stress of 1.05 kg/mm^2 (base metal)

TABLE 1.1

STRESS-RUPTURE TEST RESULTS OF LAP-SHEAR BRAZE JOINTS AT 1600°C AND A TENSILE STRESS OF 7 kg/mm^2 (SHEAR STRESS OF 0.1 kg/mm^2) IN HYDROGEN[a]

Braze Alloy	Time To Rupture, hours	Type Of Failure
Ta - 10W Base Metal[b]		
None	8.6	Intragranular
V[c]	29.9	Intragranular - adjacent to fillet
V[d]	7.8	Intragranular - adjacent to fillet
Nb - 40V[c]	16.2	Intragranular - adjacent to fillet
Nb - 40V[c]	14.6	Intragranular - adjacent to fillet
W - 25Re (at. %) Base Metal		
None	15.1	Intergranular
Cr - 20Ru	1.09	Shear through braze joint
Cr - 20Ru	0.13	Shear through braze joint
Cr - 20Ru	3.95	Shear through braze joint
Nb - 40V	11.7	Intergranular - adjacent to fillet
Nb - 40V	12.1	Intergranular - adjacent to fillet
V - 25Nb	18.4	Intergranular - adjacent to fillet

[a] All specimens annealed 2 hours at test temperature in hydrogen before testing.
[b] Tested with Ta foil covering to reduce contamination.
[c] No Ta foil covering during brazing.
[d] Ta foil covered during brazing.

and tested at 1600°C for 30 minutes in hydrogen. The temperature was then increased in steps of 50°C and held at each step for 30 minutes. Because rupture did not occur after reaching 2400°C, the test was terminated. This test indicated a considerable increase in remelt temperature for the brazed alloy since the melting point of Nb - 40V is approximately 1850°C.

Mo - 50Re

Commercial wrought powder-metallurgy Mo - 50Re was subjected to stress-rupture and creep evaluations at 1600°C. The as-received material was sintered by the vendor at 2400°C in vacuum for 8 hours and then rolled into 0.05-cm-thick sheet with a reduction of approximately 85 percent. Following this, it was annealed at 1500°C in hydrogen for 30 minutes. A chemical analysis of the material showed it to be of high purity with the following amounts of impurities: 0.3 ppm H_2, 3 ppm N_2, 21 ppm O_2, and 41 ppm Fe; W, Al, Ca, Cu, Mg, Mn, Si, and Sn were less than 1 ppm each.

Prior to load applications, each specimen was annealed for 2 hours at 1600°C in hydrogen. Figure 1.10 presents stress-rupture curves for this alloy and a comparison with other refractory metals previously evaluated at the same temperature. The data show that addition of 50 weight percent rhenium to molybdenum increased rupture life of the alloy by an order of magnitude over unalloyed arc-cast molybdenum. Based on total elongation at rupture, ductility was approximately the same (50%) for the two materials. Figure 1.11 shows Mo - 50Re specimens after testing.

Diamond pyramid hardness (DPH) indents, placed at the ends of a 2.54-cm gage section, were used as fiducial marks for elongation measurements with a twin cathetometer.* Differences in reflection due to slight depressions associated with the DPH marks made these marks easily visible at 1600°C. Figure 1.12 presents stress versus linear (secondary) creep rate curves obtained with the cathetometer measuring gage section elongation and the LVDT measuring total load train movement.

Curve slopes are approximately equal, but creep rates determined from cathetometer measurements are about 50 percent of the LVDT curve. The curve for molybdenum at 1600°C in hydrogen is also shown in Figure 1.12; these data were previously obtained using the LVDT. On the basis of total load train measurements, Mo - 50Re was more creep resistant than molybdenum by about an order of magnitude at stresses of approximately 2 kg/mm^2.

W-Re and W-Re-Mo Alloys

In support of the alloy development program discussed in a later section, stress-rupture and creep characteristics of various W-Re and W-Re-Mo alloys processed at GE-NMPO were evaluated. Tensile specimens were fabricated from 0.04- or 0.05-cm-thick sheet and tested in hydrogen. All specimens were annealed at test temperature in hydrogen for 2 hours before testing. Figure 1.13 presents stress-rupture test results obtained in the temperature range of 1600° to 2000°C. At 1600°C and a stress of 3.37 kg/mm^2, rupture life of W - 30Re exceeded that of any alloy tested to date. As molybdenum content in the alloys was increased and tungsten content was decreased, time-to-rupture decreased for the same temperature and stress. This trend was also observed for W - 30Re and W - 30Re - 30Mo alloys at 2200°C for the stress range from 0.7 to 1.7 kg/mm^2. At both 1600°C and 2000°C the slope of the stress-rupture curve is greater for W - 30Re than for W - 30Re - 30Mo.

---

* "High-Temperature Materials Program Progress Report No. 35, Part A," GE-NMPO, GEMP-35A, May 28, 1964, p. 31.

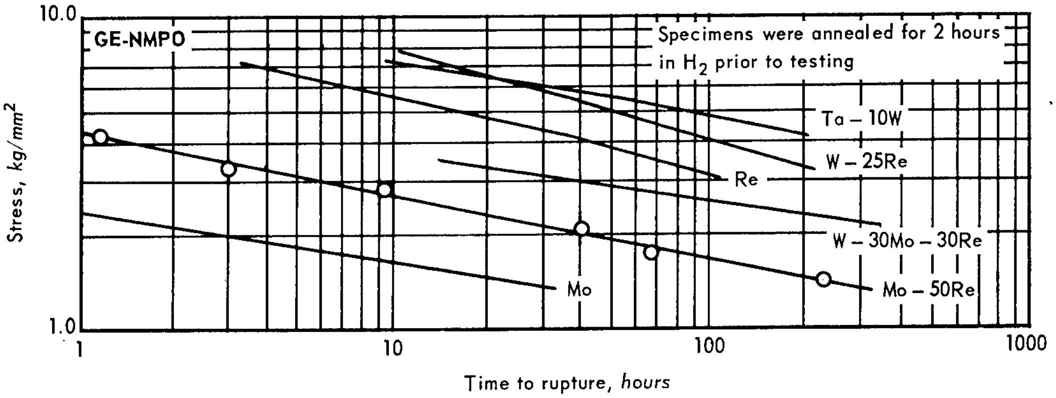

Fig. 1.10 – Stress-rupture life of various refractory metals and refractory-metal alloys at 1600°C in hydrogen

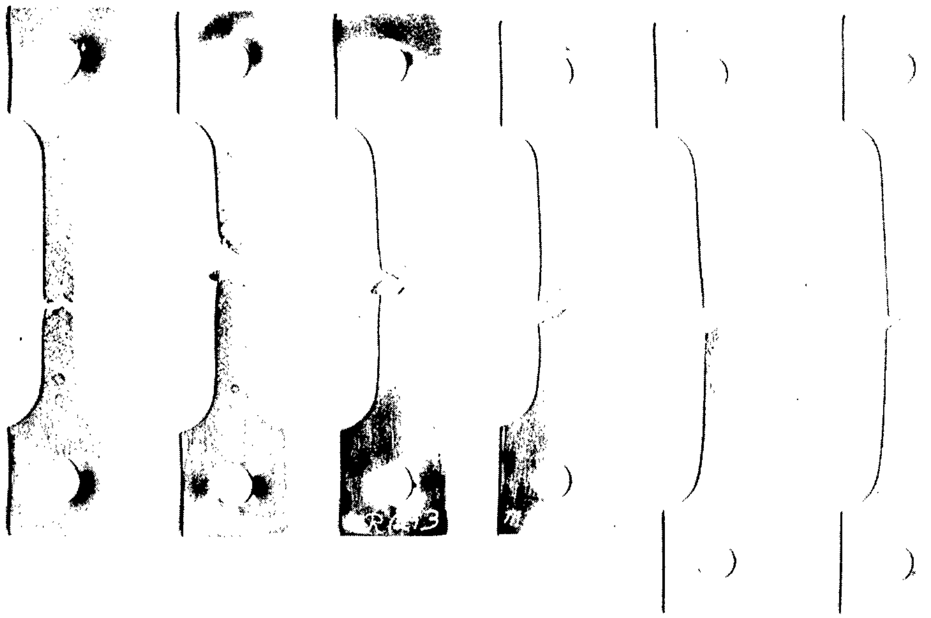

Stress, *kg/mm*^{2}	1.41	1.76	2.11	2.81	3.37	4.22
Time to rupture, *hr*	232.6	66.7	40.3	9.2	3.0	1.1
Rupture elongation, %	56	47	56	48	98	109

Fig. 1.11 – Mo – 50Re stress-rupture specimens (0.05-cm-thick) after testing at 1600°C in hydrogen (specimens were annealed for 2 hours at 1600°C in H_2 before test)

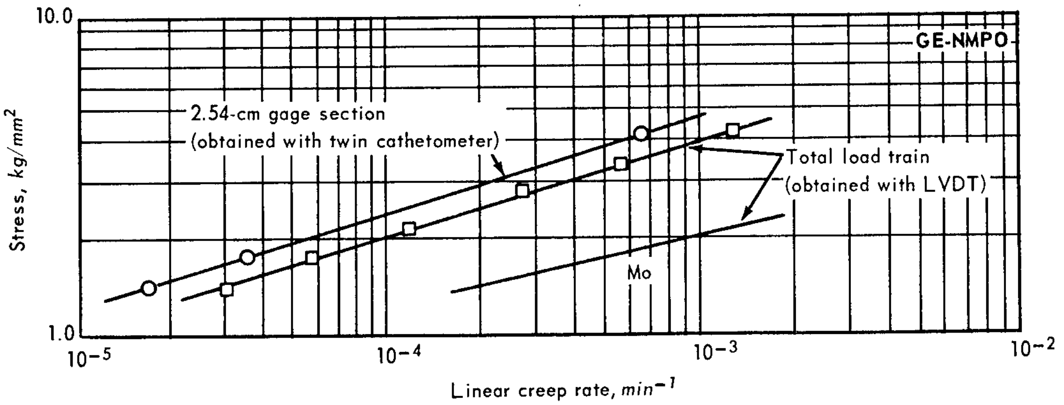

Fig. 1.12 – Linear creep rate of Mo – 50Re at 1600°C in hydrogen (specimens were annealed for 2 hours in H_2 prior to testing)

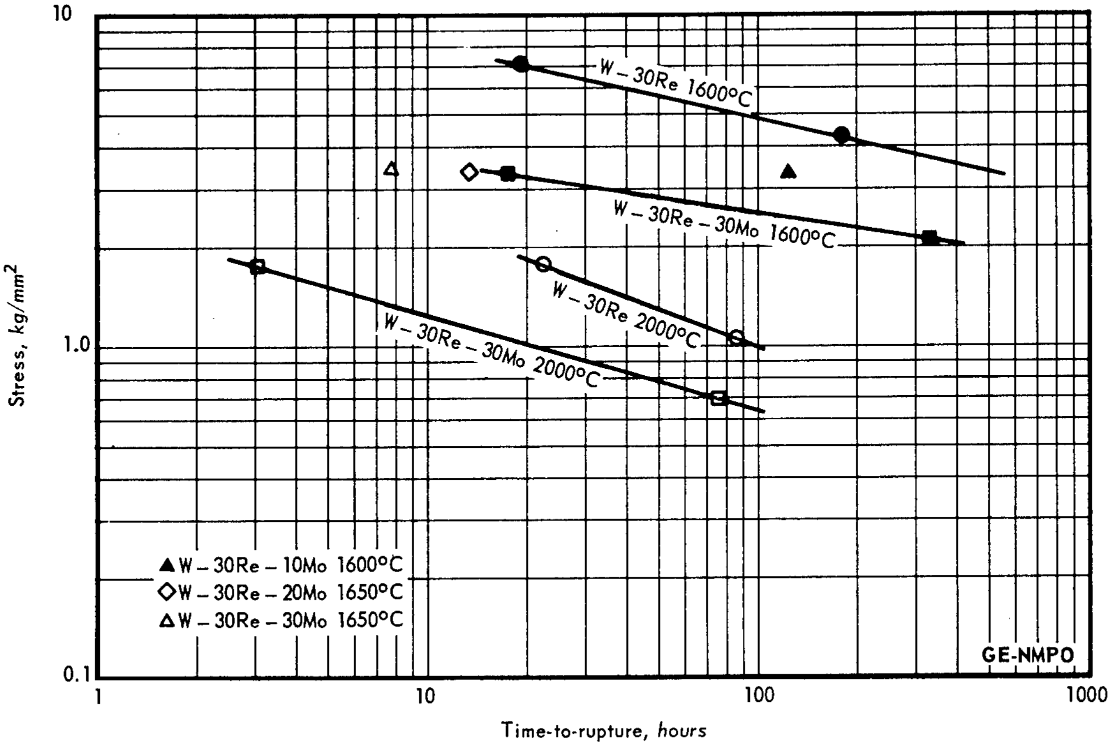

Fig. 1.13 – Stress-rupture data for W – 30Re and W-Re-Mo alloys in hydrogen

A comparison of data for W - 25Re (Figure 1.7) with those for W - 30Re at 1600°C indicates a greater rupture strength for W - 30Re alloy. However, both alloys exhibited approximately the same creep resistance. It is not possible therefore to state categorically that the alloy with the highest tungsten content will necessarily be the strongest. This observation was made in connection with W-Re-Mo alloys but it did not appear to hold for the W-Re alloy system.

Molybdenum

Creep-rupture properties of arc-cast molybdenum sheet, 0.025-, 0.038-, and 0.051-cm-thick, with surface-to-volume ratios (s/v) of 108 to 190, were investigated quite extensively. Arc-cast molybdenum rod specimens, 0.41 cm in diameter with a s/v of 25, were tested at 2200°C in hydrogen to evaluate the effect of s/v on creep-rupture properties. This range of s/v (25 to 190) and test temperature (2200°C) should be sufficient not only to indicate any vaporization effect but also grain-boundary to total-surface-area effect, because large grains (> 0.05 cm in diameter) were developed at 2200°C in arc-cast molybdenum.

Figure 1.14 shows comparative results, which indicate that a s/v from 25 to 190 had no effect on stress-rupture and creep properties of arc-cast molybdenum.

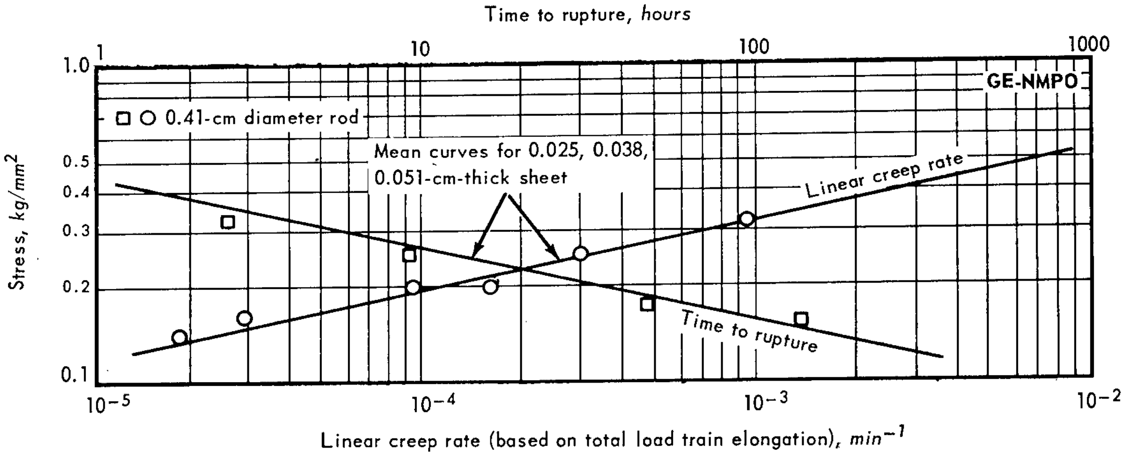

Fig. 1.14 – Stress-rupture life and linear creep rate of arc-cast molybdenum at 2200°C in hydrogen

Comparison of Test Data

Results of all stress-rupture tests of refractory metals and alloys performed to date are summarized in Table 1.2 for 12 different metals and alloys at temperatures from 1600° to 2800°C in various atmospheres, primarily hydrogen and argon. To date 469 tests were completed with durations ranging from 0.2 to 1016 hours.

In most cases stress-rupture data for these refractory metals and alloys, analyzed in terms of Larson-Miller parameter, yielded a linear relationship when these parameter values were plotted against log stress.

Such a functional relationship is described in equation (1.1) as follows:

$$T\ (\log t_R + C) = a + b \log \sigma \qquad (1.1)$$

TABLE 1.2

STRESS-RUPTURE DATA FOR VARIOUS REFRACTORY METALS AND ALLOYS

Reference Numbers For Figures 1.15, 1.16, 1.17	Material	Temperature, °C	Atmosphere	Number Of Tests	Test Range, hours	Stress To Rupture, kg/mm^2		
						1 hour	10 hours	100 hours
1	Molybdenum (Arc-cast - sources B, C, D)	1200	H_2	15	0.4 - 12	8.30	6.47	-
		1600	H_2	3	0.5 - 6	2.46	1.62	-
		1800	H_2	7	0.6 - 10	1.38	0.86	-
		2000	H_2	4	1.4 - 43	0.83	0.51	-
		2200	H_2 and Ar	80	0.2 - 1016	0.44	0.25	0.14
		2400	H_2 and Ar	6	0.3 - 6	0.24	0.14	-
2	Molybdenum (Sintered - source A)	2200	H_2 and Ar	21	0.2 - 80	0.89	0.32	0.12
3	Molybdenum (Sintered - source A')	2200	H_2	8	0.2 - 17	0.68	0.52	-
		2200	Ar	4	0.4 - 4	0.57	0.34	-
4	Molybdenum TZM (Arc-cast)	2000	H_2	2	1.0 - 5.0	1.12	0.70	-
		2200	H_2	3	1.7 - 6.0	0.48	0.28	-
5	Mo - 50Re (Sintered)	1600	H_2	6	1.1 - 232	4.29	2.78	1.69
		2200	H_2 and Ar	16	1.0 - 10	0.77	0.51	-
6	Rhenium (Sintered)	1600	H_2	10	1.9 - 275	-	5.62	2.88
		2200	H_2	5	0.9 - 100	-	2.14	1.23
		2600	H_2 and Ar	21	0.3 - 63	1.83	1.02	0.39
		2800	H_2	8	0.5 - 11	1.12	0.44	-
7	Tantalum (Arc-melted)	2400	H_2 and Ar	8	1.0 - 11	0.22	0.12	-
		2600	H_2 and Ar	12	1.0 - 14	0.14	0.07	-
8	Tantalum (Sintered)	2600	H_2	4	2.5 - 7.0	0.55	0.17	-
		2600	Ar	4	1.0 - 13	0.36	0.15	-
9	Ta - 10W (Arc-melted)	1600	H_2	7	11.6 - 642	-	7.10	4.78
		1650	He	6	0.5 - 20	9.14	6.33	-
		2400	H_2	2	2.6 - 7.3	1.18	0.65	-
		2600	H_2 and Ar	30	1.0 - 11	0.74	0.39	-
		2800	H_2 and Ar	17	1.3 - 9.2	0.42	0.22	-
10	Tungsten (Sintered - source 1)	1600	H_2	14	1.0 - 11	8.79	6.66	-
		2800	H_2 and Ar	5	0.2 - 11	0.87	0.71	-
11	Tungsten (Sintered - source 2)	2200	H_2	7	1.3 - 190	1.90	1.37	0.98
		2200	Ar	3	1.0 - 9.4	1.83	1.24	-
		2400	H_2	8	0.4 - 40	1.44	0.89	0.56
		2400	Ar	6	0.5 - 22	1.20	0.81	-
		2800	H_2 and Ar	11	0.4 - 100	0.76	0.53	0.37
12	Tungsten (Arc-cast - source 3)	2200	H_2	5	5.6 - 237	2.04	1.35	0.88
		2400	H_2	4	9.2 - 146	1.30	0.80	0.51
		2600	H_2 and Ar	2	2.2 - 120	0.84	0.48	0.30
13	Tungsten (Sintered - source 4)	2200	H_2 and Ar	11	1.3 - 61	2.39	1.55	1.02
		2600	H_2	4	0.8 - 25	1.20	0.83	0.56
		2600	Ar	4	0.4 - 4.6	0.89	0.68	-
14	W - 25Re (Sintered - source 1)	1600	H_2	7	3.3 - 297	14.76	7.94	4.29
		2200	H_2 and Ar	11	0.2 - 36	1.76	0.97	0.52
		2400	H_2	5	0.6 - 6.3	1.38	0.52	-
		2400	Ar	5	0.3 - 8.0	0.84	0.30	-
		2600	H_2	18	0.4 - 52	0.86	0.36	0.16
		2600	Ar	11	0.2 - 4.0	0.52	0.23	-
15	W - 25Re (Sintered - source 2)	1600	H_2	2	7.1 - 51	-	6.33	3.16
		2600	H_2 and Ar	6	1.3 - 18	0.97	0.50	-
16	W - 30Re (Sintered)	1600	H_2	2	20.0 - 177	-	8.22	4.78
		2000	H_2	2	22.0 - 85	-	2.39	0.98
17	W - 30Re - 10Mo	1600	H_2	1	124	-	-	-
18	W - 30Re - 20Mo	1650	H_2	1	13.7	-	-	-
19	W - 30Re - 30Mo (Sintered)	1600	H_2	2	17.1 - 333	-	3.65	2.53
		1650	H_2	1	7.8	-	-	-
		2000	H_2	2	3.1 - 73.5	-	1.25	0.64
	Total number of tests			469				

where

T is temperature, degrees absolute
t_R is rupture life, hours
C is the Larson-Miller constant for a given material
σ is the stress, kg/mm^2
a and b are constants.

If rupture life is set at a constant value to yield isochronal data, then this equation specifies that log stress should be linear with respect to temperature. Such isochronal plots for 1-, 10-, and 100-hour data are presented in Figures 1.15, 1.16, and 1.17, respectively, for testing in a hydrogen atmosphere. A definite linearity is exhibited by several materials in these isochronal plots.

Figure 1.15 (1-hour rupture data) shows rhenium was the strongest of the materials evaluated in the range 2600° to 2800°C. As shown in Figures 1.16 and 1.17, the strength of tungsten began to exceed that of rhenium as the rupture time was increased to 10 and 100 hours.

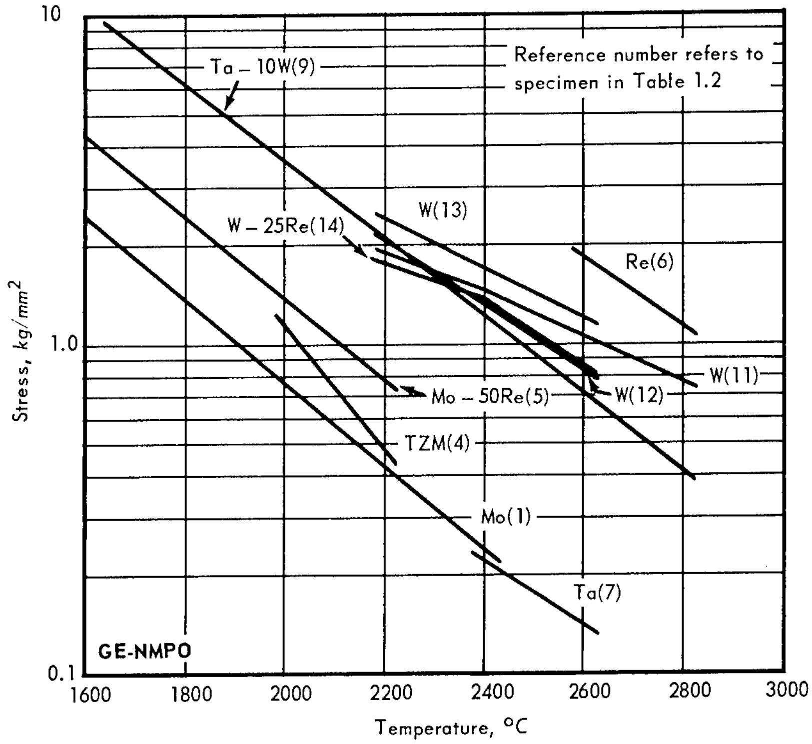

Fig. 1.15 – Isochronal 1-hour stress-rupture data

Three commercial types of powder-metallurgy tungsten and one of arc-cast tungsten were evaluated with results presented in the three figures just mentioned. At any given temperature and rupture time, the powder-metallurgy materials were stronger than arc-cast tungsten for the temperature range of approximately 2200° to 2600°C. This was attributed to factors affecting grain growth. Large-grained arc-cast tungsten was more ductile and less creep resistant. Powder-metallurgy materials had either a relatively fine or a duplex structure. Data for molybdenum at 2200°C, given in Table 1.2, also showed the powder-metallurgy type was stronger than arc-cast for the same rupture time.

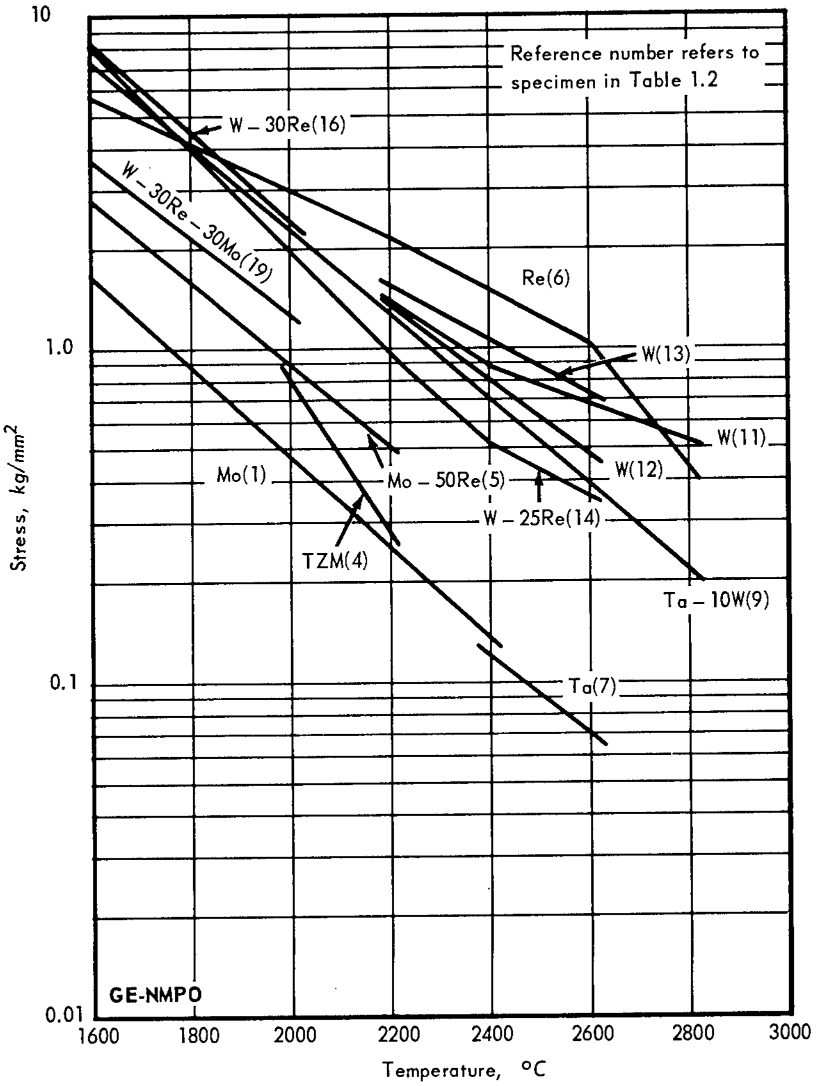

Fig. 1.16 – Isochronal 10-hour stress-rupture data

TENSILE TESTS OF Ta AND Ta - 10W

Ta

Short-time Ta tensile testing of arc-melted Ta and Ta - 10W was initiated in hydrogen and helium atmospheres in the temperature range from 600° to 1200°C to investigate the effect of hydrogen on ductility. Specimens in the form of 0.05-cm-thick sheet were fabricated to the same design as that used for specimens employed in the stress-rupture testing program. To date tests of Ta - 10W were completed in both hydrogen and helium from 600° to 1200°C. In the case of tantalum, tests in only hydrogen at 600°C and 800°C were completed.

Photo

top p. 4

Because of strong gettering action of Ta and Ta - 10W, efforts were made to avoid any specimen contamination by residual impurities which might exist in hydrogen and helium used in these tests. For this reason most test specimens were surrounded with a 0.13-mm-thick tantalum foil to function as a getter. Considerable experience with this protective foil technique showed it to be quite adequate in minimizing specimen contamination. In a few tests protective foil was not employed and, as a result, a completely different behavior was observed.

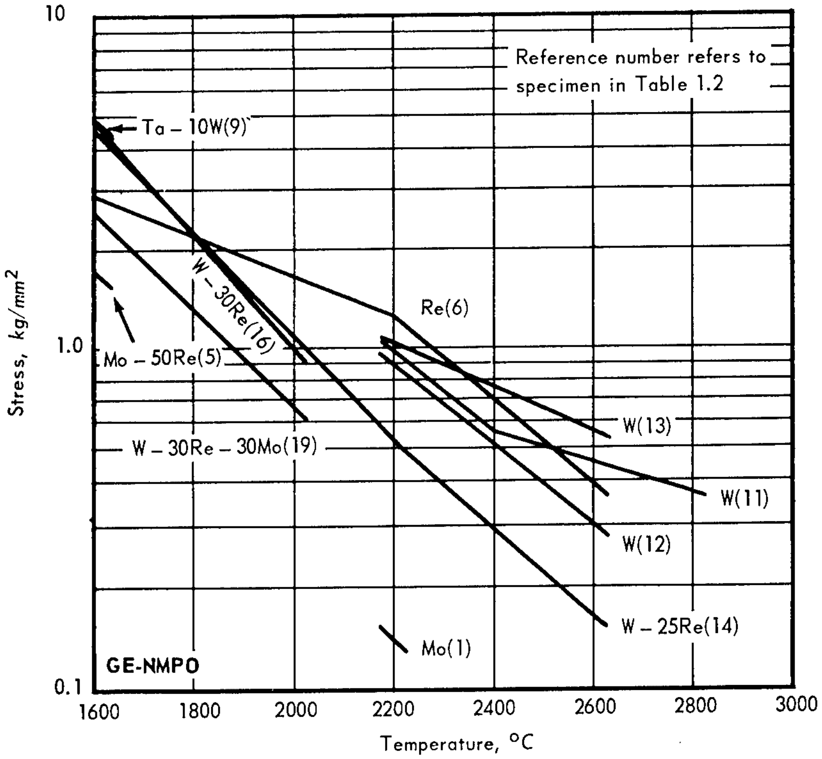

Fig. 1.17 – Isochronal 100-hour stress-rupture data

Short-time tensile tests of Ta - 10W in hydrogen from room temperature to 1200°C showed that ultimate tensile strength and elongation at rupture did not differ greatly from results obtained in helium. Tensile strength values (Table 1.3) decreased from about 49 kg/mm^2 at 600°C to about 20 kg/mm^2 at 1200°C. In this same temperature interval, elongation at rupture varied from 14 to 28 percent. At room temperature, elongation of Ta - 10W was about 25 percent (Figure 1.18) indicating that minimum ductility existed between room temperature and 600°C. Similar results were observed in tensile tests using arc-melted tantalum.

The effectiveness of tantalum foil was demonstrated in two tests of Ta - 10W at a temperature of 800°C in hydrogen. A reduction in elongation at rupture from 17.8 to 2.0 percent was observed when protective tantalum foil was not employed. Vacuum fusion analyses indicated that an increase in oxygen content was the cause for lower ductility. However, because these specimens were also evacuated prior to cooling, the analyses were not necessarily representative of the material as tested.

Results similar to the above were also observed in tests of tantalum with and without protective foil. At 800°C elongation at rupture decreased from 35 to 22 percent when protective foil was not employed. At 600°C loss in ductility was not nearly as pronounced, dropping from 18 to only 13 percent when the protective technique was not employed.

At 600°C elongation at rupture for tantalum tested in hydrogen was 18 percent. In a similar test a tantalum specimen was treated in hydrogen at 600°C for 1 hour and then cooled in hydrogen to room temperature. A tensile test of this specimen at room temperature yielded an elongation at rupture of 1.5 percent, although ultimate tensile strength was relatively unaffected.

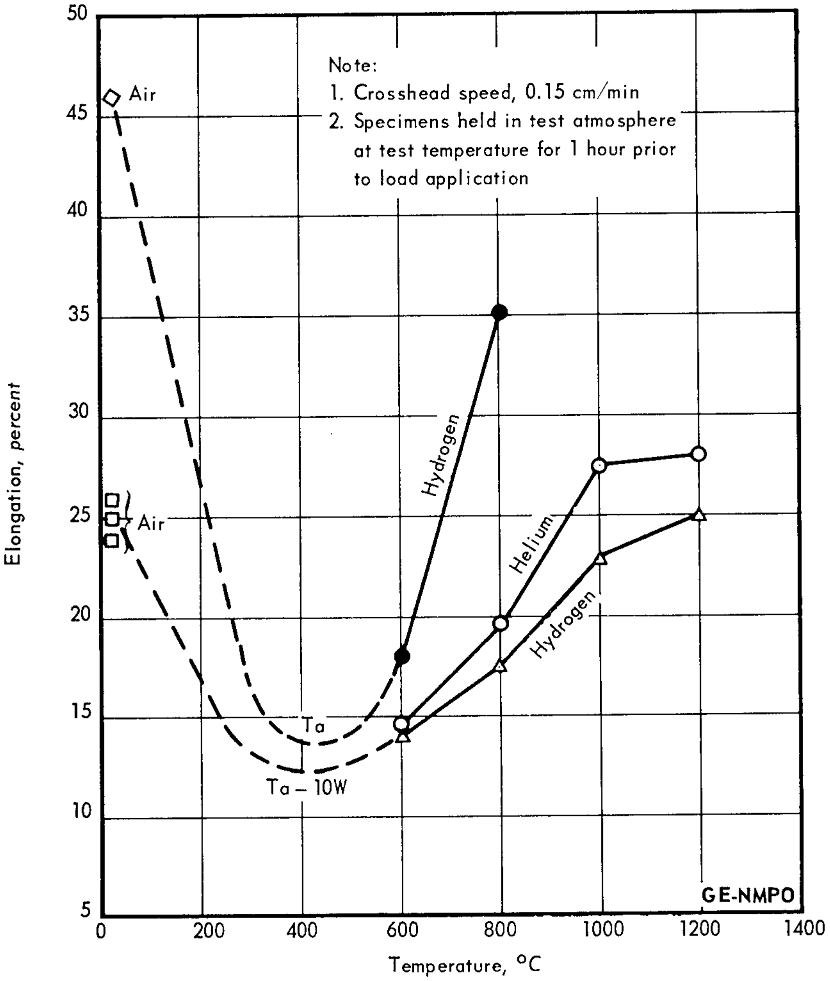

Fig. 1.18 – Tensile test results for arc-melted tantalum and Ta – 10W

1.2 FABRICATION AND ALLOY DEVELOPMENT

The objective of fabrication and alloy development studies is to develop and evaluate refractory metal alloys, including methods of processing and fabricating, for use as fueled and non-fueled high-temperature (1000° to 3000°C) reactor components.

W-Re-Mo ALLOY DEVELOPMENT

A development program* to establish useful W-Re-Mo ternary alloys was continued. New alloys were limited to a composition range shown on the W-Re-Mo ternary diagram in Figure 1.19. Specific alloys within the composition range of interest which were processed to sheet are shown in Figure 1.20. As shown in Table 1.4, each alloy melted above 2760°C.

Initially, W - 25Re† and W - 30Re alloys with 0, 10, 20, and 30 percent Mo content were processed to 0.038-cm-thick sheet. Results of room-temperature bend tests on sheet specimens, after holding for 2, 10, 100, 500, and 1000 hours in the 600° to 2600°C temperature range are given in Table 1.5. Two ductility-loss regions are outlined in Table

---

*"Third Annual Report – High-Temperature Materials and Reactor Component Development Programs, Volume I – Materials," GE-NMPO, GEMP-270A, February 28, 1964, p. 40.

†Compositions are in atomic percent in this subsection unless noted otherwise.

TABLE 1.3

SHORT-TIME TENSILE TEST RESULTS FOR Ta AND Ta - 10W[a]

	Pre-Treatment			Test				
Material[b]	Temperature, °C	Atmosphere	Time, hr	Temperature, °C	Atmosphere	Ultimate Strength, kg/mm²	Post-Test Hardness (DPH)	Elongation, %
Ta - 10W	1600	H_2	2	600	He	49.4	310	14.5
Ta - 10W	1600	H_2	2	800	He	39.5	268	19.5
Ta - 10W	1600	H_2	2	1000	He	25.3	293	27.5
Ta - 10W	1600	H_2	2	1200	He	19.9	285	28.0
Ta - 10W	1600	H_2	2	600	H_2	48.8	319	14.0
Ta - 10W	1600	H_2	2	800	H_2	42.7	270	17.5
Ta - 10W	1600	H_2	2	1000	H_2	29.6	279	23.0
Ta - 10W	1600	H_2	2	1200	H_2	22.0	336	25.0
Ta - 10W	800	H_2	1	800	H_2	43.9	266	17.8
Ta - 10W	800	H_2	1	800	H_2[c]	36.6	443	2.0
Ta - 10W	1600	H_2	2	RT	Air	64.0	235	24.0
Ta - 10W	800	H_2	1	RT	Air	60.1	319	25.0
Ta - 10W	-	-	-	RT	Air	59.5	278	26.0
Ta	-	-	-	RT	Air	33.1	152	45.5
Ta	-	-	-	RT	H_2	31.9	147	42.0
Ta	600	H_2	1	600	H_2	28.6	184	18.0
Ta	600	H_2	2	600	H_2[c]	27.7	243	13.0
Ta	800	H_2	1	800	H_2	20.9	167	35.0
Ta	800	H_2	1	800	H_2[c]	18.8	316	22.0
Ta	600	H_2	1	RT	H_2[d]	30.8	117	1.5

[a] Cross-head speed, 0.15 cm/min; tested with protective foil covering and cooled in vacuum after test.

[b] 0.05-cm-thick sheet; 0.63- by 2.54-cm gage section.

[c] Tested with no protective foil covering.

[d] Cooled in hydrogen.

TABLE 1.4

MELTING CHARACTERISTICS OF W-Re AND W-Re-Mo ALLOYS

	Nominal Composition, at. %			Melting Characteristics[a]			
Alloy No.	W	Re	Mo	2760°C	2800°C	2900°C	3000°C
NMP-250	75	25	-	None	None	None	None
NMP-252	65	25	10	None	None	None	IM[b]
NMP-254	55	25	20	None	None	None	CM[c]
NMP-256	45	25	30	None	None	IM	CM
NMP-300	70	30	-	None	None	None	IM
NMP-302	60	30	10	None	None	None	CM
NMP-304	50	30	20	None	None	IM	CM
NMP-306	40	30	30	None	IM	CM	-

[a] Specimens observed after 2 hours at temperature.

[b] IM - slight or incipient melting.

[c] CM - completely melted.

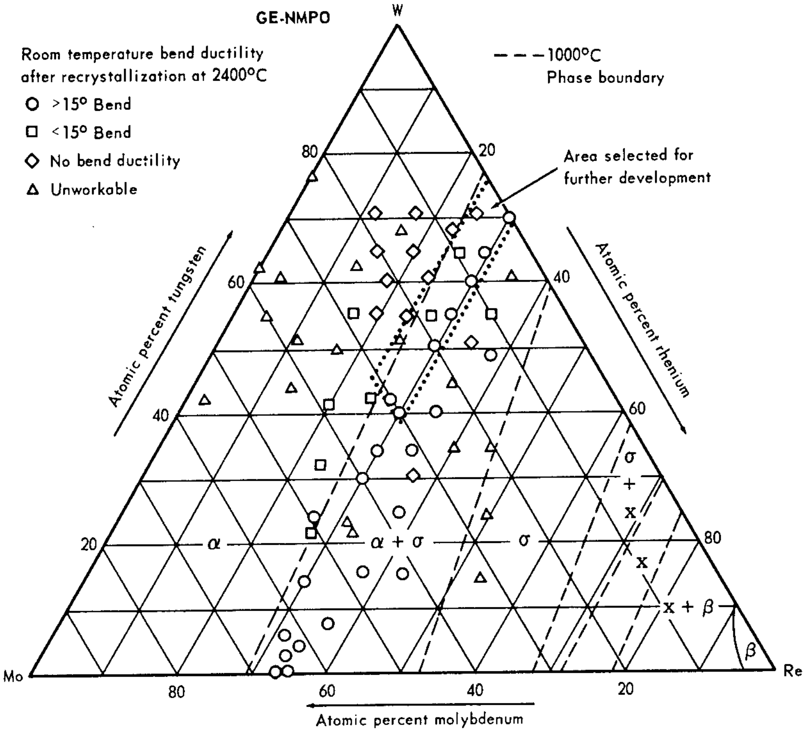

Fig. 1.19 – W-Re-Mo phase diagram with composition range limits shown for alloys evaluated

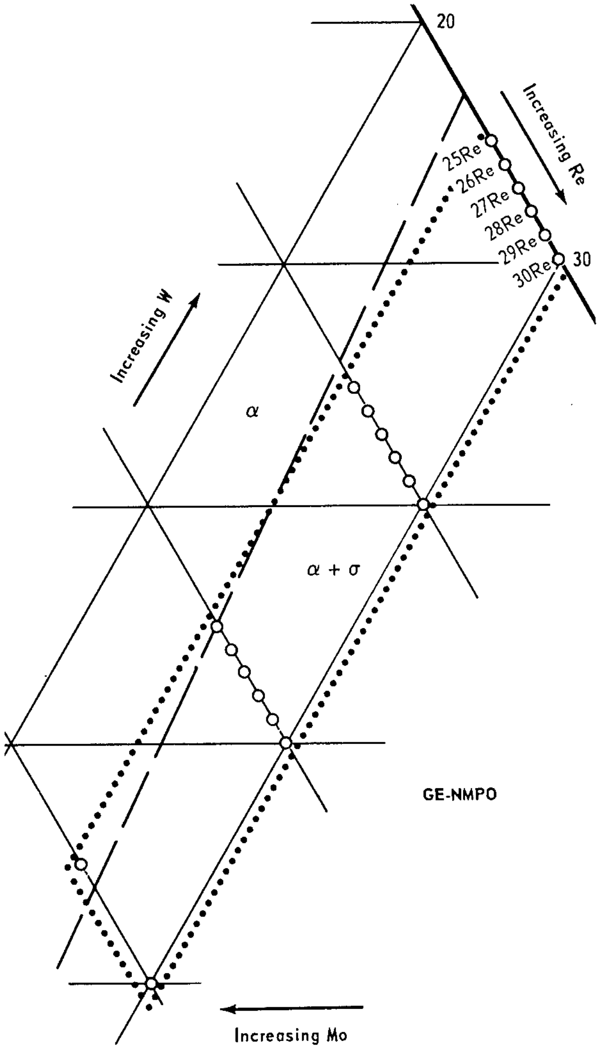

Fig. 1.20 – W-Re-Mo alloys processed to sheet (shown on segment of W-Re-Mo ternary phase diagram)

TABLE 1.5

ROOM-TEMPERATURE 4T BEND TEST RESULTS OF
W-Mo-Re ALLOYS AFTER HOLDING FOR TIMES AND AT TEMPERATURES INDICATED[a]

Holding Temperature, °C	W - 25Re					W - 25Re - 10Mo					W - 25Re - 20Mo					W - 25Re - 30Mo				
	Type NMP 250, Lab No. 403					Type NMP 252, Lab No. 363					Type 254, Lab No. 364					Type 256, Lab No. 365				
	2 hr	10 hr	100 hr	500 hr	1000 hr	2 hr	10 hr	100 hr	500 hr	1000 hr	2 hr	10 hr	100 hr	500 hr	1000 hr	2 hr	10 hr	100 hr	500 hr	1000 hr
600	>90°		>90°					30°	60°	~45°			>90°	>90°	>90°			45°	90°	>90°
800								70°	>90°				>90°	>90°					>90°	
1000	>90°		>90°					90°	>90°				>90°	>90°				>90°	>90°	
1200	>90°		>90°			>90°	>90°	80°	45°	30°	>90°	>90°	>70°	~90°	60°	>90°	>90°	>90°	>90°	>90°
1400	>90°		~60°			>90°	>90°	>90°	30°	45°	>90°	>90°	>90°	45°	30°	>90°	>90°	>90°	45°	30°
1600	60°		80°			>90°		>90°	>90°	>90°	>90°		>90°	>90°	>90°	>90°		>90°	>90°	>90°
1800	60°					>90°					>90°		>90°			>90°	>90°	>90°		
2000	80°					>90°					>90°					>90°				
2200	~60°					>45°	45°				60°	45°				>90°	>90°			
2400	60°					>45°	60°				>90°	60°				>90°	90°			
2600	25°					>45°	90°				>90°	>90°					90°			

Holding Temperature, °C	W - 30Re					W - 30Re - 10Mo					W - 30Re - 20Mo					W - 30Re - 30Mo				
	Type NMP 300, Lab No. 362					Type NMP 302, Lab No. 360					Type NMP 304, Lab No. 386					Type NMP 306, Lab No. 382				
	2 hr	10 hr	100 hr	500 hr	1000 hr	2 hr	10 hr	100 hr	500 hr	1000 hr	2 hr	10 hr	100 hr	500 hr	1000 hr	2 hr	10 hr	100 hr	500 hr	1000 hr
600	>90°	90°	>90°	>90°	>90°	>90°	>90°	>90°	>90°	80°			>90°	>90°	>90°			>90°	>90°	>90°
800	>90°	70°	>90°	>90°					>90°					>90°					>90°	
1000	>90°		>90°	>90°				>90°	>90°				>90°	>90°		>90°	>90°	>90°	>90°	~60°
1200	>90°		70°	30°	~30°	>90°	>90°	>90°	>90°		>90°	>90°	>90°	60°	~30°	>90°	>90°	>90°	90°	20°
1400	>90°		>30°	>20°	>0<5°	>90°	>90°	45°	10°		>90°	>90°	>45°	10°	20°	>90°	>90°	>90°	20°	
1600	>90°		>30°	>20°	>15<30°	>90°	>90°	45°	>30<45°		>90°	>90°	>45°	~45°	~70°	>90°	>90°	>90°	>90°	>90°
1800	>90°		>30°			>90°	>90°	30°	>90°		>90°	>90°	>90°	>90°		>90°	>90°	>90°	>90°	
2000	>90°					>90°	>90°	>90°			>90°	>90°	>90°			>90°	>90°	>90°		
2200	>90°	90°				>90°	>90°	>90°			>90°	>90°	>90°			>90°	>90°	>90°		
2400	>90°	90°				>90°	>90°				>90°	>90°	>90°			>90°	>90°	>90°		
2600	>90°	90°				>90°	>90°				>90°	>90°	>90°			>90°	>90°			

[a] Satisfactory (>90°) bends were also achieved on electron-beam welds in Lab tests No. 360, 386, and 382 after 10 hours at 1800°C, 2000°C, and 2600°C.

1.5. In the 2200°-to-2600°C holding-temperature range, W - 25Re with 0, 10, or 20 percent Mo added showed a moderate loss in room-temperature ductility after holding at temperature, whereas the W - 25Re - 30Mo alloy did not develop a ductility loss. Similarly, W - 30Re alloys with 0, 10, or 20 percent Mo added developed a ductility loss after holding in the 1200° to 1600°C temperature range, whereas W - 30Re - 30Mo alloy did not lose ductility.

The ductility-loss region outlined in Table 1.5 for W - 30Re, W - 30Re - 10Mo, and W - 30Re - 20Mo alloys was attributed to age hardening due to sigma phase precipitation. A high level of creep-rupture strength at 1600°C was obtained in these alloys through the age-hardening reaction. Stress-rupture values for several alloys are given in Table 1.6. The W - 30Re developed a 177-hour rupture life at 4.22 kg/mm^2 at 1600°C in contrast to 90.0 hours for the non-aging W - 25Re alloy. At higher temperatures, the sigma phase was not an effective strengthener, so the strength of the alloys was roughly proportional to tungsten content. Testing of new alloy modifications for 1100° to 1600°C service is continuing.

TABLE 1.6

CREEP-RUPTURE TESTS OF REFRACTORY METAL ALLOYS AT 1600°C AND 1650°C[a]

Laboratory No.[b]	Nominal Composition, at. %			Thickness, cm	Stress		Rupture Time, hr	Elongation 2.54 cm, %	Linear Creep Rate, min^{-1}	Hardness (DPH)	
	W	Mo	Re		psi	kg/mm^2				Before	After
						1600°C Tests					
2-1, 12	75	-	25	0.038	5510	3.9	50.6	23	1.17×10^{-5}	500	418
362-8[a]	70	-	30	0.050	6000	4.2	177.0	38	1.87×10^{-5}	572	623
308-2[b]	40	30	30	0.038	4800	3.37	17.1	24	1.10×10^{-4}	502	391
360-7[a]	60	10	30	0.038	4800	3.37	124.0	46	4.2×10^{-5}	525	575
						1650°C Tests					
382-5[a]	40	30	30	0.038	4800	3.37	7.8	19	2.4×10^{-4}	500	462
386-6[a]	50	20	30	0.038	4800	3.37	13.7	15	1.2×10^{-4}	535	482

[a] "High-Temperature Materials Program Progress Report No. 41, Part A," GE-NMPO, GEMP-41A, November 30, 1964, p.37.

[b] Sheet and creep rupture test number.

As shown in Table 1.5, W - 25Re - 30Mo and W - 30Re - 30Mo alloys appeared uninfluenced by prolonged holding in any portion of the 600° to 2600°C temperature range. Therefore, trial production runs of sheet were completed on both compositions following procedures developed for processing W - 25Re alloy.*

W-Re-BASE ALLOY PROCESSING

Procedures for obtaining sintered W - 25Re of excellent purity were previously developed.† A major advance during the past year was in developing and evaluating processing procedures for producing finished sheet of low impurity content of W - 25Re and W-Re-Mo alloys. An extension of impurity control procedures involved developing methods of eliminating contaminants in the preparation of sheet for welding and in control of carbon contamination resulting from electrodischarge machining operations (Elox machining).

Based on experience to date, preferred processing procedures for W - 25Re or W-Re-Mo sheet are as follows:

---

*"High-Temperature Materials Program Progress Report No. 43, Part A," GE-NMPO, GEMP-43A, January 29, 1965, p. 33.

†"High-Temperature Materials Program Progress Report No. 31, Part A," GE-NMPO, GEMP-31A, January 24, 1964, p. 14.

1. Wet-blend powders, dry, compact (die press), and sinter according to composition:
   a. W-Re binary alloys (W - 25Re to W - 30Re), sinter 2 hours at 3000°C in hydrogen.
   b. W-Re-Mo ternary alloys (W - 25Re - 30Mo, etc.), sinter 3 hours at 2640°C in hydrogen. Sintering at 2640°C prevents melting the molybdenum powder.
2. Heat the sintered compacts in hydrogen at 1400°C and hot-roll in air, reheating the sheet thoroughly between each hot-roll pass (reduction totaling 80 percent is preferred).
3. Heat to 1400° to 2640°C in hydrogen to remove oxygen absorbed by heated metal in hot-rolling.
4. Cold-roll, with 1400°C intermediate stress-relief cycles, to final size. Reductions of greater than 65 percent of the hot-rolled thickness are preferred.

The decontamination step (No. 3 above) was evaluated in eight trial sheet production runs. The effectiveness of this treatment was established by impurity content analysis at each stage in processing. Analytical results are given in Table 1.7.

TABLE 1.7

INFLUENCE OF PROCESSING ON IMPURITY LEVEL OF W-Re AND W-Re-Mo ALLOY SHEET

Sheet No.	Nominal Composition, at. %			Significant Process Step Completed In Processing The Sheet	Impurities, ppm[a]			
	W	Re	Mo		C	H_2	O_2	N_2
8-1	75	25	-	Hot-rolled[b]	ND[c]	0.3	99.0	0.8
403	75	25	-	2 hours at 2640°C in H_2 after hot-rolling[d]	ND[c]	0.3	6.2	0.5
403	75	25	-	16 hours at 1425°C in H_2 after hot-rolling[d]	9.0	0.3	5.1	0.1
365-PR	45	25	30	Hot-rolled[e]	10.0	0.4	106.0	1.0
365-PR	45	25	30	2 hours at 2640°C in H_2 after hot-rolling[d]	9.0	0.4	9.0	0.7

[a] Carbon by conductometric method, and gaseous constituents by vacuum fusion.

[b] Blended powders were sintered at 3000°C after compacting to a bar for hot-rolling. Heated to 1400°C in H_2 for hot-rolling, but rolled in air.

[c] Not determined.

[d] Treatment to remove oxygen absorbed by hot metal in hot-rolling operation.

[e] Similar to footnote "b" except original sintering at 2640°C.

Sheets with low impurity content from trial production runs, as shown in Table 1.7, were evaluated for weld quality by examination of 23 to 38 cm of electron-beam fusion weld for each material. Low impurity content in the sheet yielded a void-free weld structure. A room temperature bend test of radius equal to four sheet thickness was completed on as-welded W - 30Re - 30Mo sheet, as shown in Figure 1.21. The stronger W - 25Re alloy developed a 45- to 70-degree bendability.

Sheet edges are usually ground to size in fabrication of nuclear components due to restrictive dimension tolerances. Welds completed on ground sheet edges showed high porosity due to contamination by the grinding wheel. Leaching with mixed acids (lactic - nitric - HF) and vacuum degassing at 1000°C prior to welding resulted in high-quality electron-beam welds. The electrodischarge method of machining refractory metal alloys was used for structural component preparation. Unfortunately, a workpiece surface

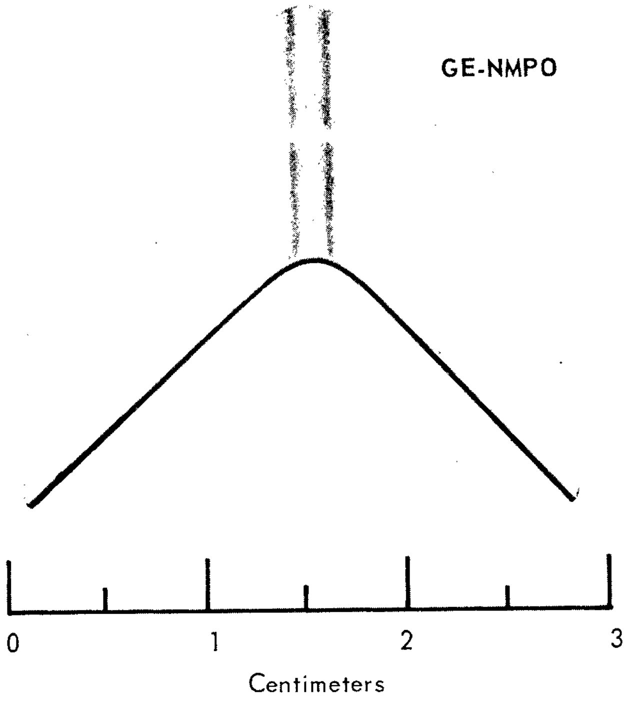

Fig. 1.21 – Room-temperature bend of 4x sheet thickness radius on as-welded sheet of W – 30Re – 30Mo alloy. Twenty-three to 38 linear cm of porosity-free electron-beam weld on trial production run alloys was designated as a quality requirement *(Neg. P64-11-40, 1.3X)*

high in carbon content resulted from discharge machining W-Re-base alloys. Treatment of carbon-contaminated sheet at 1450°C in a hydrogen and water vapor atmosphere effectively reduced undesired carbon, as shown in Table 1.8.

BRAZING

A number of brazing alloys for both tantalum and tungsten joining were developed and evaluated using a T-joint configuration. Results are given in Table 1.9. Brazing temper-

TABLE 1.8

REMOVAL OF CONTAMINANT CARBON FROM ELECTRODISCHARGE MACHINED W - 30Re - 30Mo ALLOY

No.	Treatment Or Processing	C	O_2	H_2	N_2	Remarks
1	Unmachined alloy	13.0	6.0	1.0	0.1	Low impurity content
2	Electrodischarge machined alloy	54.0	12.0	2.0	0.1	Carbon unacceptable
3	Leach machined surface with mixed acids	66.0	-	-	-	Carbon not influenced
4	Treated 17 hours at 1450°C in H_2 + 10 percent H_2O vapor atmosphere	16.0	12.0	2.0	0.1	Carbon contamination reduced
5	Treated 72 hours at 1450°C in H_2 + 10 percent H_2O vapor atmosphere	12.0	-	-	-	Carbon content reduced to original content

TABLE 1.9

SUMMARY OF REFRACTORY-METAL BRAZING SYSTEMS STUDIED

Alloy No.	Composition, wt %	Cold Workability	Brazing Temperature,[a] °C	Fillet Characteristics	Base-Metal Erosion, cm	Fillet Microstructure
Brazing Alloys for Tantalum Base Metal						
CB-11D	Nb - 30Pd	Slight	1950	Medium	None	Slight second phase
CB-11E	Nb - 20Pd	Slight	2150	Large	None	Slight porosity
CB-11F	Nb - 10Pd	Slight	2300	Medium	None	Severe porosity
Brazing Alloys for Tungsten Base Metal						
WB-179B	W - 10Re - 20Ru	None	2550	Medium	0.010	2 or 3 phases
WB-179C	W - 15Re - 25Ru	None	2525	Medium	0.007	2 phase
WB-179D	W - 20Re - 10Ru	None	2825	Large	None	2 phase - slight porosity
WB-179E	W - 40Re - 15Ru	None	2500	Medium	None	Slight cracking
WB-9B	W - 31Ru	None	2300	Small	None	2 phase
WB-10B	W - 28Rh	Slight	2275	Small	None	2 phase eutectic
WB-10C	W - 35Rh	Slight	2200	Small	None	2 phase eutectic
WB-13B	W - 42Ir	Slight	2500	Medium	None	2 phase
WB-8A	100Mo	Slight	2600	Large	None	Large grained
MB-1711B	Mo - 50Re - 15Pd	None		None	-	Excessive vaporization
MB-1711C	Mo - 30Re - 30Pd	None		None	-	Excessive vaporization
MB-22B	Mo - 1B	Moderate	2600	None	-	No melting
MB-4C	Mo - 20V	None	2450	Medium	None	Severe porosity

[a] Dry hydrogen atmosphere.

ature in hydrogen for each braze alloy composition was determined by tests conducted at 50°C intervals.

The braze alloy evaluation work discussed below showed Nb-Pd alloys to be feasible for tantalum brazing, with close braze-operation temperature control. In addition, compositions developing good brazed joints in unalloyed tungsten were noted for W-Re-Ru, W-Rh, and W-Ir braze alloy systems.

Nb-Pd Alloys

Excellent braze joints were obtained in tantalum at 1950°C and 2000°C braze temperatures, as shown in Figure 1.22. Higher brazing temperatures caused porosity to develop in the Nb-Pd alloy.

W-Re-Ru and W-Ru

Tungsten braze alloys with less than a total of 50 percent rhenium and ruthenium showed good potential for joining tungsten. These alloys had low base-metal erosion properties (< 0.010 cm), good flow, and good joint fillet formation. Fillet cracks developed in braze alloys of more than a total of 50 percent rhenium and ruthenium.

W-Rh and W-Ir

Braze alloys of W-Rh and W-Ir developed sound, ductile brazed joints in tungsten without observable base-metal erosion.

Mo

Molybdenum was included in this program as a comparison base for braze alloys of tungsten. Large grains were observed in joint areas. Joining temperatures were above 2600°C for unalloyed molybdenum.

Fig. 1.22 – Photomicrograph showing a tantalum T section brazed with Nb – 30Pd alloy at 2000°C in hydrogen *(Neg. 5065, Unetched, 75X)*

Mo-Re-Pd

Braze alloys of Mo-Re-Pd developed grain boundary attack on the tungsten-base metal. Excessive vaporization and braze area porosity were noted.

Mo-V and Mo-B

Braze alloys of Mo-V and Mo-B were intended to lower the braze temperature of unalloyed Mo, but desired braze temperature reduction was not obtained with either system. In addition, a phase segregation in the Mo-B alloy prevented achieving desired joint quality. SS ES

1.3 LOW-CYCLE FATIGUE PROGRAM

A program to study low-cycle fatigue properties of pressure vessel steels at elevated temperatures was initiated in Calendar Year 1964. A two-phase technical program was formulated, testing equipment ordered, and development and evaluation of auxiliary equipment started. The objective of the program is to gain knowledge of material behavior under cyclic loading conditions at temperatures in the creep range and to generate engineering data for use in design of pressure vessels for nuclear systems. Loading conditions of interest are those that result in fatigue failure after a relatively low number of cycles (<10, 000) in the temperature range from 400° to 800°C.

TECHNICAL PROGRAM

The program was planned as a two-phase effort. The objective of the Phase I effort is to establish a fatigue testing capability and to evaluate test methods. Phase II is to be a continuing program, beginning in Fiscal Year 1966, in which emphasis will be placed on generation of engineering data. The program for Phase I calls for acquisition and characterization of materials to be studied, procurement of fatigue testing equipment, development and evaluation of auxiliary equipment, and instrumentation. A series of tests will be performed to evaluate experimental techniques and identify types of testing required in Phase II. Based on results of these tests several special single-purpose testing assemblies will be designed and fabricated.

MATERIALS

SS ES

Initially, Type ~~316~~ stainless steel and 2.25Cr - 1Mo steel will be used in the low-cycle fatigue program. The former will be procured by Pacific Northwest Laboratories during the present year and the latter will be ordered in Fiscal Year 1966. To permit other laboratories to obtain the same material for related studies, the material was ordered in quantities considerably larger than needed for the GE-NMPO low-cycle fatigue program. The extra material will be stored by the Pacific Northwest Laboratories as part of the inventory of materials presently being used in the various AEC technical programs on material, research, and development. Since Type 316 stainless steel is not available at the present time, the test equipment checkout and preliminary low-cycle fatigue studies will be made on specimens fabricated from Type 304 stainless steel which is being obtained from the AEC materials program inventory.

FATIGUE TEST EQUIPMENT

A servocontrolled hydraulic testing machine was ordered. The machine, MB Electronics Model TM6-20, permits fatigue testing with controlled load, strain, or crosshead motion. Furthermore, testing frequency can be varied, loading sequences of arbitrary shape can be generated, and loading hold periods can be incorporated.

Specimen Heating

Two methods of heating are being pursued. Figure 1.23 shows a resistance-type furnace obtained from the G-E Research Laboratories. An induction-type heater of about the same overall size is being developed. Necessary control and recording equipment for these furnaces is on hand. In preliminary experiments, a satisfactory specimen temperature profile was attained using either heating method.

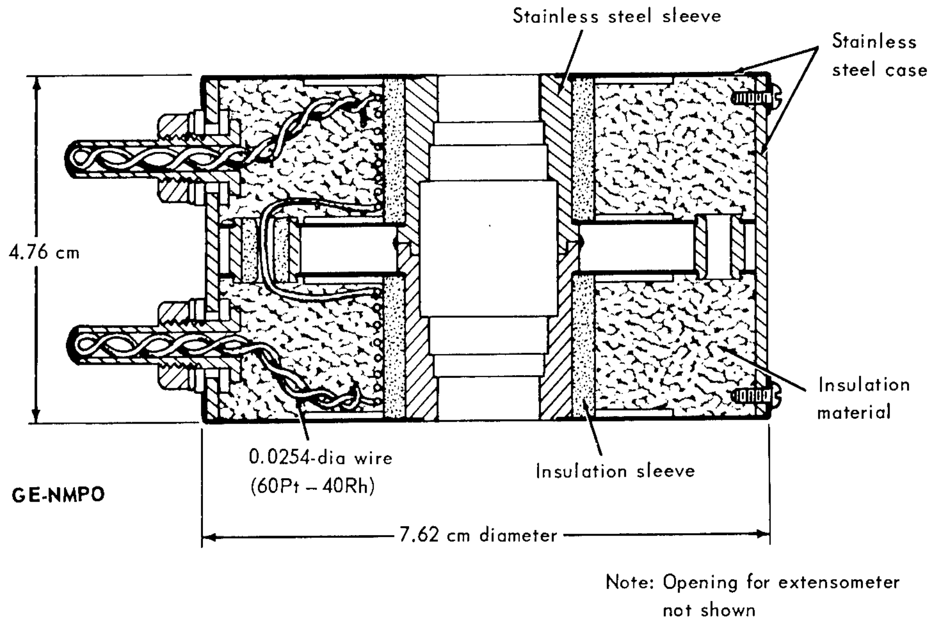

Note: Opening for extensometer not shown

Fig. 1.23 – Resistance heater

Strain Measurement

Present plans call for testing hour-glass specimens in a push - pull mode with controlled diametral strain. Figure 1.24 shows the extensometer being developed for this purpose. The design is characterized by a lightly stressed elastic hinge that permits a built-in mechanical advantage without moving parts. Additional favorable features of the extensometer are a low-contact pressure on the specimen, a geometry that is relatively insensitive to minor temperature fluctuations in the furnace environment, and a large distance separating furnace and sensing element.

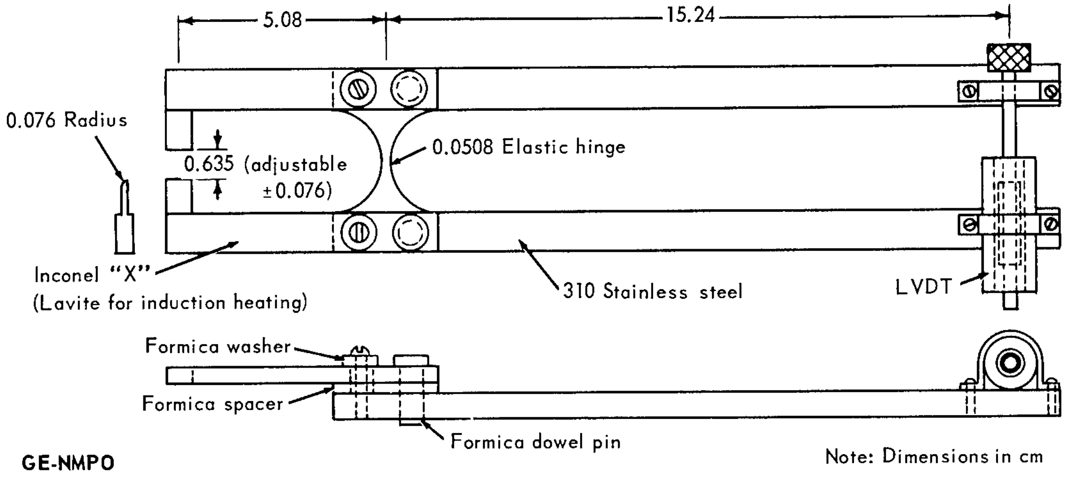

Fig. 1.24 – Extensometer for measuring diametral strain

Specimen Fixture Assembly

Figure 1.25 shows the fixture design selected for specimen mounting and aligning. The design permits the specimen to be completely assembled in the fixture on a work bench. With duplicate sets of fixtures, furnaces, and extensometers, the fatigue machine can be operated at maximum capacity. The fixture provides alignment of the specimen during test through three rods guided in low-friction bushings. It also serves to protect the load cell from any undesirable lateral loads that might result when the specimen fails.

1.4 SUMMARY AND CONCLUSIONS

Stress-rupture and creep evaluations involving several refractory metals and refractory metal alloys were continued in the temperature range of 1600° to 2800°C in hydrogen and argon. A few of the more important observations resulting from these studies are discussed below.

At 1600°C in hydrogen and at stresses ranging from 3 to 6 kg/mm^2, the stress-rupture strength of Ta - 10W was greater than that of Re and W - 25Re (at. %). This alloy was also more creep resistant than either Re or W - 25Re (at. %) under these conditions.

Stress-rupture strength and linear creep rate for powder-metallurgy tungsten tested in hydrogen at 2200° to 2800°C were dependent on the source of material. Powder-metallurgy tungsten was slightly stronger and more creep resistant than arc-cast tungsten in this temperature range. A completely similar pattern was reported previously.*

Stress-rupture and creep data for powder-metallurgy rhenium tested in hydrogen between 1600° and 2800°C indicated a deviation from linearity in plots of log stress versus log rupture life, and log stress versus log linear creep rate.

---

*"Third Annual Report – High-Temperature Materials and Reactor Component Development Programs, Volume I – Materials," GE-NMPO, GEMP-270A, February 28, 1964, p. 41.

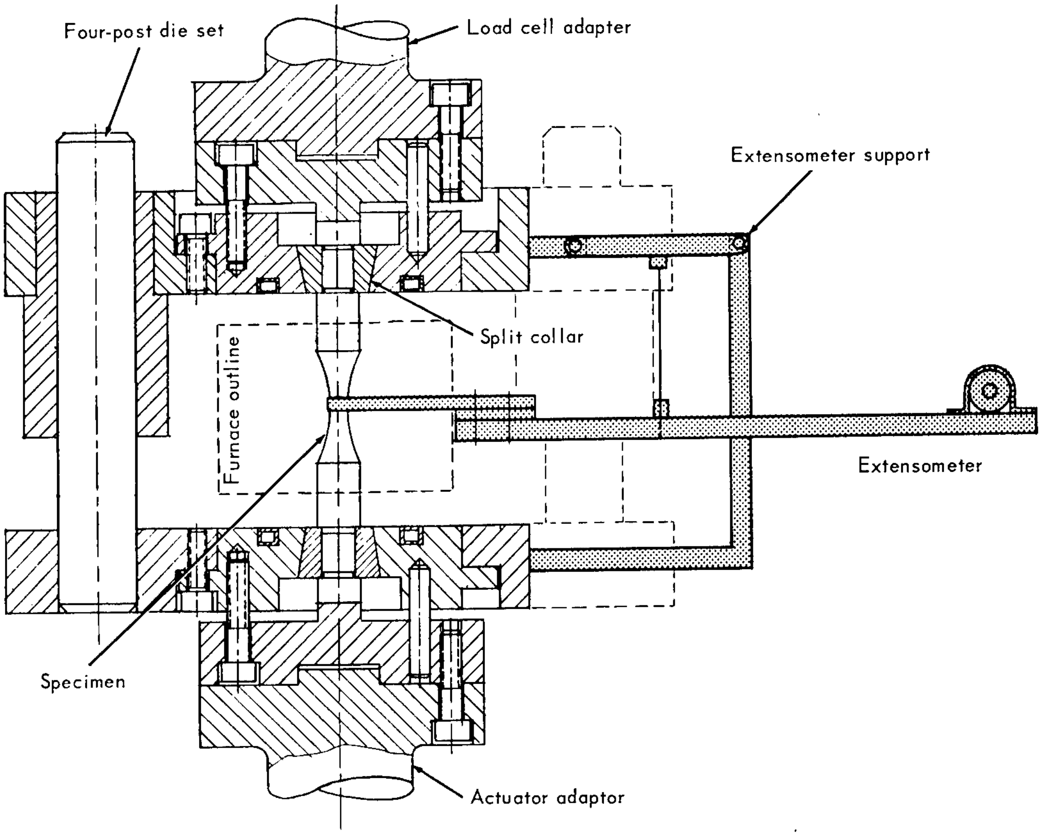

Fig. 1.25 – Fatigue specimen setup

Strain measurements during creep tests at 2200°C in hydrogen were shown to be both reproducible and accurate using an optical extensometer. Evaluations of fiducial marks showed that 0.010-cm holes placed at the ends of the gage section were the most satisfactory and did not affect specimen strength.

Short-time tensile tests of Ta - 10W from room temperature to 1200°C indicated that percent elongation at rupture was essentially the same for tests in both hydrogen and helium atmospheres. However, specimens heated for 1 hour at 600°C in hydrogen and then tested at room temperature were brittle.

A new series of W-Re-Mo alloys with a broad selection of elevated temperature properties was developed. Each alloy of the series melted above 2760°C. A W - 30Re - 30Mo alloy was readily fabricable and exhibited no loss of room-temperature bend ductility after prolonged holding in the 600° to 2600°C temperature range. Alloys of W - 30Re (at. %) and W - 30Re - 10Mo (at. %) were age-hardenable and offer good potential for high creep-rupture strength levels in the 1200° to 1600°C temperature range. Processing procedures were developed for production of high-purity W - 25Re (at. %) sheet and included methods for decontaminating machined material to maintain a high-purity level suitable for welding.

1.5 PLANS AND RECOMMENDATIONS

Stress-rupture and creep studies of refractory metals and alloys will be continued at temperatures from 1600° to 2800°C with the possibility of extending the test temperature to 3000°C where applicable. The following materials will be evaluated in this temperature range: (1) arc-cast and powder-metallurgy tungsten to more definitely establish creep-rupture differences over a wide temperature range, (2) W-Re and W-Re-Mo

51

alloys in support of the alloy development program to identify the more promising compositions, and (3) comparative studies of W - 25Re (at. %) from various vendors will be performed to determine alloy consistency as presently produced commercially.

In addition to determining stress-rupture strength and linear (secondary) creep rates, first-stage creep studies will be performed at temperatures from 1600° to 2200°C using an electro-optical extensometer. More detailed studies of creep mechanism will be made for refractory metals tested at temperatures above one-half their absolute melting points.

Development of W-Re-Mo alloys will be continued with emphasis on meeting alloy requirements of known applications. Both creep-rupture strength and room temperature bend-ductility data will be obtained for alloys in direct support of applications of interest to the AEC.

Research will be conducted on the suitability of rhenium as a base metal for high-strength, elevated-temperature alloys. This program is of interest because these alloys will have a hexagonal close-packed structure whereas other refractory alloys are cubic.

Low-cycle fatigue testing at elevated temperatures will be continued on the Types 304 and 316 stainless steels. Several special single-purpose testing assemblies will be designed and fabricated. Engineering test data will be generated in sufficient quantities to establish the low-cycle fatigue behavior of these two steels at elevated temperatures.

2. EFFECT OF RADIATION ON HIGH-TEMPERATURE METALS AND ALLOYS

(57004)

The objective of this program is to determine the effect of radiation on the time-, temperature-, and stress-dependent properties of selected high-temperature alloys and refractory metals, to identify the causes of any observed changes in these properties, and to develop remedial measures.

2.1 REFRACTORY-METALS PROGRAM

The experimental program*[1] to study the effect of neutron irradiation on the creep-rupture, tensile, hardness, and resistivity properties of refractory metals and alloys is continuing. In addition to studies on the above properties, theoretical calculations on the nature of the neutron-induced defects and direct observations of defects by the use of the transmission electron microscope are also being performed. To date, emphasis has been placed on studying W, W - 25Re, Mo, and Mo-TZM. Other materials, such as Ta, Nb, and alloys of each, are being considered for future studies.

A summary of the experimental program, test conditions, and preliminary results is presented in Table 2.1.

STATUS OF IRRADIATIONS

Approximately 34 capsules have been irradiated in the Oak Ridge Research Reactor and the Engineering Test Reactor, at the National Reactor Test Station in Idaho, during the course of this program. With the exception of two capsules, all irradiations were performed at reactor ambient temperatures. A summary of the irradiation conditions and types of specimens is presented in Table 2.2.

CREEP-RUPTURE TESTS

Post-irradiation creep-rupture testing of W, W - 25Re, and Mo specimens was performed in the temperature range from 0.29 T_m to 0.55 T_m.† In several cases, specimens were annealed at various temperatures prior to the application of stress to determine the influence of temperature on the radiation-induced changes in the creep-rupture properties. As shown in Table 2.2, Mo-TZM, Ta, and Ta - 10W specimens have been irradiated, but have not yet been tested.

Tungsten

Creep-rupture testing at temperatures from 900° to 1700°C was performed on tungsten control specimens and tungsten specimens irradiated at reactor ambient temperature to fast neutron doses ranging up to 1.3×10^{20} nvt. One elevated-temperature irradiation (1000° to 1350°C) was performed at the ETR to a fast neutron dose of about 7×10^{19} nvt.

---

*Superscripts refer to the reference list at the end of this section.

†T_m is the absolute melting temperature of the metal.

TABLE 2.1

SUMMARY OF MAJOR EXPERIMENTS IN THE REFRACTORY METALS AND ALLOYS RADIATION EFFECTS PROGRAM

Exp. No.	Objective	Property	Test Specimen Material[a]	Test Specimen Type	Test Specimen Lot Number[b]	Irradiation Conditions[c] Capsule Number	Irradiation Conditions[c] Temp, °C	nvt, neutrons/cm^2 Thermal	nvt, neutrons/cm^2 ($E_n \geq 1$ Mev)	Post-Irradiation Heat Treatment Temp. °C	Post-Irradiation Heat Treatment Time, hr	Test Conditions	Test Conditions	Percent Change In Property[d]	Percent Change In Property[d]	Percent Change In Property[d]	Comments
		Creep rupture										T, °C	σ(kg/mm^2)	Creep rate	Rupture life	Elongation	
1	To investigate the effects of neutron irradiation on the creep-rupture and tensile properties. To perform supporting studies on the effects of neutron irradiation on the hardness and resistivity properties.		W	Rod	MK137(PM)-X	ORM-4	70	2.2×10^{18}	5.8×10^{17}			1100	19.34	- 10.0	15	- 1	
					MK137(PM)-X	ORM-8	70	9.5×10^{19}	2.5×10^{19}			1100	19.34	- 40.0	74	- 1	
					MK137(PM)-Y	ORM-6	70	2.0×10^{19}	3.7×10^{18}			1100	20.35	-	17	-	
					MK137(PM)-Y	ORM-8	70	9.5×10^{19}	2.5×10^{19}			1100	20.35	- 60	160	- 7	
					MK137(PM)-E	ORM-17	70	7.5×10^{19}	1.6×10^{19}			1100	18.28	- 16	28	-10	
					MK137(PM)-E	ORM-19	70	3.9×10^{20}	8.2×10^{19}			1100	18.28	- 76	490	- 6	
					MK137(PM)-Y	ORM-6	70	2.0×10^{19}	3.7×10^{18}			1400	13.01	-	- 1	10	
					MK137(PM)-Y	ORM-8	70	9.5×10^{19}	2.5×10^{19}			1400	13.01	-	9	14	
					MK137(PM)-J	ORM-19	70	3.9×10^{20}	8.2×10^{19}			1400	10.55	- 6	38	19	
					MK137(PM)-J	ORM-19	70	3.9×10^{20}	8.2×10^{19}			1500	8.44	- 8	10	-29	
					MK137(PM)-J	ORM-19	70	3.9×10^{20}	8.2×10^{19}			1700	5.62	- 13	9	-28	
					MK137(PM)-E	33MT-137	1300	2.2×10^{20}	1.8×10^{20}			900					
					MK137(PM)-J	ORM-17	70	7.5×10^{19}	1.6×10^{19}			900	22.64	- 76	280	-26	
			W	Sheet	PF(PM)	ORM-12	70	9.1×10^{19}	3.2×10^{19}			1100	37.26	- 30	60	8	Warm-worked.
			W - 25Re	Sheet	RWS9(PM)-4	ORM-20	70	3.5×10^{20}	8.0×10^{19}			1100	43.9	- 52	55	-56	
			Mo	Sheet	KDM-515A(AC)-8	ORM-23	70	5.2×10^{19}	1.4×10^{19}			580	21.09	29	- 96	- 4	
					KDM-515A(AC)-2	ORM-13	70	5.5×10^{19}	6.9×10^{18}			980	10.55	- 2	10	14	
					KDM-515A(AC)-1	ORM-16	70	1.4×10^{20}	3.7×10^{19}			580	21.09	210	- 65	-	
					KDM-515A(AC)-1	ORM-16	70	1.4×10^{20}	3.7×10^{19}			600	21.09	57	- 32	-	
			50Mo-50Re	Sheet		ORM-20	70	3.5×10^{20}	8.0×10^{19}								To be tested.
			Ta	Sheet		ORM-23	70	5.2×10^{19}	1.4×10^{19}								To be tested.
			Ta - 10W	Sheet		ORM-23	70	5.2×10^{19}	1.4×10^{19}								To be tested.
		Tensile												Yield Strength	Tensile Strength	Elongation	
			W	Rod	MK142(PM)-G	33MT-138	70	3.6×10^{20}	1.3×10^{20}			371		(Brittle fracture)			Testing continuing at higher temperatures.
					MK142(PM)-B	ORM-9	70	2.8×10^{19}	5.1×10^{18}								To be tested.
					MK142(PM)-C	ORM-10	70	9.3×10^{19}	1.7×10^{19}								To be tested.
		Resistivity													Resistivity		
			W	Rod	MK142(PM)-E	ORM-7	70	2.5×10^{19}	5.3×10^{18}			-196			105		
					MK142(PM)-D	ORM-11	70	1.2×10^{20}	3.3×10^{19}			-196			315		
					MK142(PM)-F	33MT-113	1300	2.2×10^{20}	8.0×10^{19}			-196			39		
			W - 25Re	Rod	RWW5(PM)-A	ORM-14	70	6.2×10^{19}	1.2×10^{19}			-196			10		
					RWW5(PM)-C	33MT-113	1300	2.2×10^{20}	8.0×10^{19}			-196			15		
			Mo	Rod	GEH(PM)-B	ORM-14	70	6.2×10^{19}	1.2×10^{19}			-196			80		Warm-worked.
					GEH(PM)-C	ORM-14	70	6.2×10^{19}	1.2×10^{19}			-196			118		
					GEH(PM)-L	33MT-113	700	2.2×10^{20}	8.0×10^{19}			-196			2		
			Mo-TZM	Rod	ZM6003(AC)-5	ORM-18	70	1.1×10^{20}	3.7×10^{19}			-196			74		
					ZM6003(AC)-5	33MT-113	700	2.2×10^{20}	8.0×10^{19}			-196			7		
		Hardness											Load		DPH Hardness		
			W	Sheet	411-1	ORM-15	70	1.3×10^{20}	3.5×10^{19}			15	500 grams		8		Single crystal.
												650			60		From isochronal
												1300			5		annealing studies.
			Mo	Sheet	KDM-515A(AC)-M(10)	ORM-30	70	9.2×10^{19}	2.6×10^{19}			15	500 grams		18		Polycrystal.
												300			55		From isochronal
												1200			0		annealing studies.

TABLE 2.1 (Cont.)

SUMMARY OF MAJOR EXPERIMENTS IN THE REFRACTORY METALS AND ALLOYS RADIATION EFFECTS PROGRAM

Exp. No.	Objective	Property	Test Specimen			Irradiation Conditions[c]				Post-Irradiation Heat Treatment		Test Conditions		Percent Change In Property[d]			Comments
			Material[a]	Type	Lot Number[b]	Capsule Number	Temp, °C	nvt, neutrons/cm² Thermal	nvt, neutrons/cm² ($E_n \geq 1$ Mev)	Temp, °C	Time, hr						
		Creep rupture										T, °C	σ(kg/mm²)	Creep rate	Rupture life	Elongation	
2	To determine the influence of post-irradiation heat treatment on the creep-rupture and tensile properties. To perform supporting post-irradiation annealing studies on the resistivity and hardness properties and to make direct observations on the sub-structure.		W	Rod	MK137(PM)-Y	ORM-6	70	2.0×10^{19}	3.7×10^{18}	1100	1	1100	20.35	- 27	13	4	
					MK137(PM)-Y	ORM-6	70	2.0×10^{19}	3.7×10^{18}	1400	1	1100	20.35	16	- 15	-	
					MK137(PM)-Y	ORM-8	70	9.5×10^{19}	2.5×10^{19}	1400	1	1100	20.35	- 73	190	-	
					MK137(PM)-E	ORM-19	70	3.9×10^{20}	8.2×10^{19}	1400	1	1100	18.28	- 64	210	- 6	
					MK137(PM)-J	ORM-17	70	7.5×10^{19}	1.6×10^{19}	1050	1	900	22.64	- 74	520	-10	
					MK137(PM)-J	ORM-17	70	7.5×10^{19}	1.6×10^{19}	1200	1	900	22.64	- 91	900	-17	
					MK137(PM)-J	ORM-17	70	7.5×10^{19}	1.6×10^{19}	1300	1	900	22.64	- 61	190	- 7	
					MK137(PM)-J	ORM-17	70	7.5×10^{19}	1.6×10^{19}	1400	1	900	22.64	- 56	160	-	
					MK137(PM)-J	ORM-17	70	7.5×10^{19}	1.6×10^{19}	1700	1	900	22.64	- 46	90	- 7	
					MK137(PM)-M	ORM-19	70	3.9×10^{20}	8.2×10^{19}	1700	43	900		- 80	710	4	
					MK137(PM)-M	ORM-19	70	3.9×10^{20}	8.2×10^{19}	1700	1	900		- 98	-	-	
			W	Sheet	PF(PM)	ORM-12	70	1.5×10^{20}	3.2×10^{19}	1100	3	1100	37.26	- 39	51.9	- 4	Warm-worked.
			Mo	Sheet	KDM-515A(AC)	ORM-23	70	5.2×10^{19}	1.4×10^{19}	757	8	580	21.09	- 27	62.0	-20.8	
						ORM-23	70	5.2×10^{19}	1.4×10^{19}	779	8	580	21.09	- 28	-	-	
		Tensile												Yield Strength	Tensile Strength	Elongation	
			W	Rod	MK142(PM)-B	ORM-9	70	2.5×10^{19}	5.1×10^{18}								To be tested.
					MK142(PM)-C	ORM-10	70	9.3×10^{19}	1.7×10^{19}								To be tested.
		Resistivity													Resistivity		
			W	Rod	MK142(PM)-D	ORM-7	70	2.5×10^{19}	5.3×10^{18}	650	1	-196			6		
					MK142(PM)-D	ORM-14	70	6.2×10^{19}	1.2×10^{19}	650	1	-196			12		
					MK142(PM)-D	ORM-11	70	1.2×10^{20}	3.3×10^{19}	650	1	-196			72		
					MK142(PM)-E	ORM-11	70	1.2×10^{20}	3.3×10^{19}	1900	1	-196			1		
			W - 25Re	Rod	RWW5(PM)-A	ORM-14	70	6.2×10^{19}	1.2×10^{19}	550	1	-196			1		
			Mo	Rod	GEH(PM)-B	ORM-14	70	6.2×10^{19}	1.2×10^{19}	450	1	-196			14		
		Hardness											Load		DPH Hardness		
			W	Sheet	411-1	ORM-15	70	1.3×10^{20}	3.5×10^{19}	650	1	650	500 grams		60		Single crystal.
												1300			5		
			Mo	Sheet	KDM-515A(AC)-M(10)	ORM-30	70	9.2×10^{19}	2.6×10^{19}	300	1	300	500 grams		55		Polycrystal.
										1200	1	1200			0		
3	To investigate the influence of specimen configuration, purity level, structure and substructure on the post-irradiation creep-rupture and tensile properties. To perform supporting studies on the post-irradiation resistivity and hardness properties.	Creep-rupture	W														To be irradiated.
			Mo														To be irradiated.
		Tensile	W														To be irradiated.
			Mo														To be irradiated.
		Resistivity	W														To be irradiated.
			Mo														To be irradiated.
		Hardness	W														To be irradiated.
			Mo														To be irradiated.
4	To determine the in-reactor creep properties of refractory metals and alloys.		W														In planning stage. Test conditions to be established when more data from experiments No. 1 and 2 are evaluated.

---

[a] All materials are in the recrystallized condition unless otherwise noted.

[b] Material lot numbers are followed by parenthetical expressions denoting powder metallurgy (PM) or arc-cast (AC) processing. The last letter or number identifies the sheet or rod stock fabricated from the specified lot. Seven or more test specimens are generally machined from each sheet or rod stock.

[c] The listed irradiation conditions represent approximate values for specimens which were irradiated and represent target values for specimens to be irradiated. A summary of capsule irradiations, designations, and the number and type of specimens is given in Table 2.2.

[d] Property changes represent increases due to the indicated irradiations and test conditions when compared to a corresponding unirradiated test specimen. Negative values represent a decrease in the specified property.

TABLE 2.2

IRRADIATION DATA FOR REFRACTORY-METAL CAPSULES

	Test Specimens			Irradiation Conditions[a]			
					Exposure,	nvt, neutrons/cm^2[c]	
Capsule	Material	Type[b]	Quantity	Facility	hr	Thermal	($E_n \geq 1$ Mev)
ORM-17	W	CR(R)	24	ORR F-2	120.2	7.5×10^{19}	1.6×10^{19}
	W, Mo, Mo-TZM	H-R	3				
ORM-18	W	CR(R)	24	ORR F-2	221	1.4×10^{20}	2.9×10^{19}
	W, Mo, Mo-TZM	H-R	8				
ORM-19	W	CR(R)	24	ORR F-2	617.9	3.9×10^{20}	8.2×10^{19}
ORM-20	Mo	CR(F)	7	ORR F-2	560	3.5×10^{20}	8.0×10^{19}
	50Mo - 50Re	CR(F)	5				
	W - 25Re	CR(F)	7				
	Mo-TZM	CR(F)	12				
ORM-21	Mo	CR(F)	14	ORR F-2	335	7.0×10^{19}	2.0×10^{19}
	Mo-TZM	CR(F)	24				
	W	CR(F)	7				
	W - 25Re	CR(F)	13				
	50Mo - 50Re	CR(F)	5				
ORM-22	W	CR(R)	14	ORR F-2	247	1.1×10^{20}	2.9×10^{19}
	A-286	CR(R)	8				
ORM-23	Mo	CR(F)	7	ORR F-2	123	5.2×10^{19}	1.4×10^{19}
	Mo-TZM	CR(F)	12				
	Ta	CR(F)	5				
	Ta - 10W	CR(F)	5				
ORM-24	Ta	CR(F)	5	ORR F-2	60	2.6×10^{19}	7.1×10^{18}
	Ta - 10W	CR(F)	5				
ORM-26	W	H[d]	1	ORR[e]	119.6	7.2×10^{19}	2.4×10^{19}
		H	1				
		E	12				
ORM-27	W	H[d]	1	ORR[e]	24.0	1.4×10^{19}	4.6×10^{18}
		H	1				
		E	6				
ORM-28	W	H[d]	1	ORR[e]	434	2.2×10^{20}	7.3×10^{19}
		H	1				
		E	5				
ORM-29	W	H	4	ORR[e]	216	1.9×10^{20}	6.0×10^{19}
ORM-30	W	E	6	ORR[e]	210	9.2×10^{19}	2.6×10^{19}
	Mo	H	2				
33MT-113	Mo	H-R	5	ETR-L6[f]		2.2×10^{20}	8.0×10^{19}
	Mo-TZM	H-R	5				
	W - 25Re	H-R	10				
	W	H-R	20				
33MT-138	W	CR(R)	6	ETR-E5	670	3.6×10^{20}	1.1×10^{20}
	W	T	8				
	Mo	H-R	3				
	Mo-TZM	H-R	2				
	W	H-R	3				
33MT-137	W	CR(R)	24	ETR-E5[f]	750	2.2×10^{20}	1.8×10^{20}

[a] Based on N^{58} (n, p) Co^{58} and Co^{59} (n, γ) Co^{60} reactions.

[b] Coded as follows: CR = creep-rupture specimen; (R) = round specimen; (F) = flat type
H-R = hardness and resistivity
T = tensile specimen
E = transmission electron microscopy specimen.

[c] Approximate dosage (within a factor of two). Final dosage values will be summarized in later reports.

[d] Single crystal.

[e] Rabbit facility.

[f] Elevated temperature irradiation; all other irradiations at ambient temperature.

Most of the raw stock material, from which the specimens were made, was annealed at 1750°C for 1 hour in a hydrogen atmosphere. After fabrication, the specimens were stress-relieved at 1600°C for 1 hour in hydrogen.

Initially, it was planned to creep-rupture test irradiated tungsten specimens at temperatures of 1100°C and higher. Based on isochronal recovery of the irradiation-induced hardness, it was determined that a significant change in the flow mechanism must occur at a temperature of about 1050°C (0.36 T_m). Because of the pronounced change observed in the hardness parameters, several irradiated specimens were subsequently creep-rupture tested at 900°C (0.32 T_m) to determine the degree of irradiation-induced change on the creep-rupture properties of tungsten at lower temperatures. Annealing studies at temperatures up to 1700°C were also performed on the irradiated specimens which were creep-rupture tested at 900°C. Finally, the influence of elevated-temperature irradiations was then studied by measuring the creep-rupture properties at both 900°C and 1100°C.

The creep-rupture test results indicate that irradiation affects creep-rupture properties of tungsten by increasing the time to rupture with a corresponding decrease in the linear creep rate; the results also indicate that several independent mechanisms must be operational. In addition, preliminary data show that the lower threshold of the observed radiation-induced strengthening occurs at a fast neutron dose of about 1×10^{19} nvt. It was also found that for a fixed ratio of thermal to fast neutron flux the stress dependency of the strengthening of irradiated tungsten does not seem to change and was the same as that of the control specimens tested in the temperature range of 900° to 1700°C.

The data obtained at all test temperatures for tungsten specimens irradiated at reactor ambient temperatures show that both elongation and reduction in area are not affected as a result of irradiation. However, testing specimens irradiated at elevated temperatures at both 900° and 1100°C resulted in severe embrittlement. The reason for this significant reduction in ductility for elevated-temperature irradiations has not yet been determined.

Post-irradiation heat treatment (annealing) tended to reduce radiation-induced strengthening of tungsten specimens that were tested at 1100°C (0.37 T_m). Testing irradiated specimens at 900°C (0.32 T_m), however, indicated that an initial post-irradiation annealing treatment at temperatures up to 1200°C would further increase the time to rupture over and above that of the as-irradiated specimen by a significant amount. Further annealing at temperatures up to 1700°C reduced the time to rupture compared to that of the as-irradiated specimen, although complete recovery of time to rupture, based on control data, was not achieved. Testing irradiated specimens at 1700°C also showed a residual strengthening. Corresponding changes were also observed in the respective creep rates.

The residual strengthening of irradiated tungsten specimens when tested at higher temperatures (1700°C; 0.54 T_m), where it is believed that most recoverable defects would be completely annealed, may be due in part to the presence of rhenium atoms as a result of transmutations from tungsten atoms by the thermal neutron (n, γ) reaction. Calculations show that a thermal neutron dose of 1×10^{20} nvt should produce about 0.3 atomic percent of rhenium atoms. Quantitative chemical analysis on irradiated tungsten specimens shows good agreement with the theoretical predictions of the rhenium atom production. As a result of these transmutations, a relatively large concentration of foreign atoms is produced which may interact and form complexes with the radiation-induced free interstitial atoms and vacancies, and perhaps nucleate clusters of each.

Creep-rupture data for tungsten control and irradiated specimens are presented in Tables 2.3 through 2.6, and are plotted in Figures 2.1 through 2.8.

TABLE 2.3

SUMMARY OF CREEP-RUPTURE TEST ON TUNGSTEN SPECIMENS, ROD D MATERIAL

		Post-Irradiation Anneal					Rupture	Linear		
Specimen[a]	Condition	Temperature, °C	Time, hr	Atmosphere	Temperature, °C	Stress, kg/mm^2	Life, hr	Creep Rate, sec^{-1}	Elongation, % in 4.54 cm	Reduction In Area, %
1293	Control				1100	16.50	52.90	6.83×10^{-7}	22.2	88.5
1300	Irradiated 33MT-138[b]	-	-	-	1100	17.20	169.49	2.52×10^{-7}	22.0	76.8
1291	Control				1100	17.60	13.54	2.96×10^{-6}	25.0	94.1
1303	Irradiated 33MT-138	-	-	-	1100	17.60	140.26	3.43×10^{-7}	22.8	81.8
1290	Control				1100	18.28	7.07	4.66×10^{-6}	23.4	98.8
1302	Irradiated 33MT-138	-	-	-	1100	18.28	83.86	5.60×10^{-7}	20.4	80.5
1301	Irradiated 33MT-138	-	-	-	1100	19.33	46.85	9.94×10^{-7}	20.6	87.4
1299	Irradiated 33MT-138	1100	166	H_2	1100	19.33	17.85	2.58×10^{-6}	27.6	90.9

[a] Specimens from 0.508-cm-diameter tungsten rod annealed at 1750°C in hydrogen for 1 hour prior to fabrication; stress relieved at 1600°C for 1 hour in hydrogen following grinding.

[b] 33MT-138 irradiated at approximately 1.3×10^{20} nvt ($E_n \geq 1$ Mev) and reactor ambient temperature in ETR-E5 facility.

TABLE 2.4

SUMMARY OF CREEP-RUPTURE TEST ON TUNGSTEN SPECIMENS, ROD E MATERIAL

		Post-Irradiation Anneal					Rupture	Linear		
Specimen[a]	Condition	Temperature, °C	Time, hr	Atmosphere	Temperature, °C	Stress, kg/mm^2	Life, hr	Creep Rate, sec^{-1}	Elongation, % in 4.54 cm	Reduction In Area, %
1203	Irradiated 33MT-137[b]	-	-	-	900	22.64	462.04	4.47×10^{-8}	7.9	25.5
1221	Control				1100	18.28	20.82	1.80×10^{-6}	31.1	94.5
1216	Irradiated ORM-17[c]	-	-	-	1100	18.28	26.63	1.52×10^{-6}	27.9	93.4
1212	Irradiated ORM-19[d]	-	-	-	1100	18.28	122.36	4.43×10^{-7}	29.1	89.2
1215	Irradiated ORM-19	1400	1	H_2	1100	18.28	63.76	6.38×10^{-7}	29.1	90.6
1220	Control				1100	19.33	6.01	6.05×10^{-6}	31.3	94.3
1219	Control				1100	19.33	8.45	4.44×10^{-6}	29.3	95.3
1218	Irradiated ORM-17	-	-	-	1100	19.33	8.96	4.46×10^{-6}	31.0	95.6
1211	Irradiated ORM-19	-	-	-	1100	19.33	37.60	1.45×10^{-6}	25.6	86.1
1217	Irradiated ORM-17	-	-	-	1100	17.60	54.22	6.87×10^{-7}	27.5	91.3
1223	Control				1100	17.60	45.76	8.62×10^{-7}	25.8	93.2
1222	Control				1400	10.55	17.95	2.77×10^{-7}	10.1	35.7

[a] Specimens from 0.508-cm-diameter tungsten rod annealed at 1750°C in hydrogen for 1 hour prior to fabrication; stress-relieved at 1600°C for 1 hour in hydrogen following grinding.

[b] 33MT-137 irradiated at approximately 7×10^{19} nvt ($E_n \geq 1$ Mev) at elevated temperatures, $1000^\circ C < T < 1350^\circ C$, in the ETR.

[c] ORM-17 irradiated at approximately 1.6×10^{19} nvt ($E_n \geq 1$ Mev) and reactor ambient temperature in ORR-F2.

[d] ORM-19 irradiated at approximately 8.2×10^{19} nvt ($E_n \geq 1$ Mev) and reactor ambient temperature in ORR-F2.

TABLE 2.5

SUMMARY OF CREEP-RUPTURE TEST ON TUNGSTEN SPECIMENS, ROD J MATERIAL

Specimen[a]	Condition	Post-Irradiation Anneal Temperature, °C	Post-Irradiation Anneal Time, hr	Post-Irradiation Anneal Atmosphere	Temperature, °C	Stress, kg/mm^2	Rupture Life, hr	Linear Creep Rate, sec^{-1}	Elongation, % in 4.54 cm	Reduction In Area, %
1265	Control				900	22.64	12.45	2.32×10^{-6}	36.2	96.6
1256	Irradiated 33MT-137[b]	-	-		900	22.64	148.00	1.72×10^{-7}	21.7	68.1
1255	Irradiated 33MT-137	-	-		900	22.64	77.30	2.80×10^{-7}	19.5	62.1
1257	Irradiated 33MT-137	-	-		900	22.64	140.00	3.07×10^{-8}	4.5	23.3
1268	Irradiated ORM-17[c]	-	-		900	22.64	47.48	5.46×10^{-7}	26.8	96.5
1263	Irradiated ORM-17	1050	1	H_2	900	22.64	77.04	5.08×10^{-7}	32.5	96.8
1271	Irradiated ORM-17	1200	1	H_2	900	22.64	124.60	1.96×10^{-7}	30.0	96.6
1264	Irradiated ORM-17	1300	1	H_2	900	22.64	36.65	8.97×10^{-7}	33.6	96.2
1266	Irradiated ORM-17	1400	1	H_2	900	22.64	32.20	1.01×10^{-6}	35.3	93.7
1267	Irradiated ORM-17	1700	1	H_2	900	22.64	24.12	1.26×10^{-6}	33.9	94.8
1272	Control				1400	10.55	19.33	2.92×10^{-7}	12.7	35.5
1258	Irradiated ORM-19[d]	-	-		1400	10.55	26.71	2.74×10^{-7}	15.1	26.7
1273	Control				1400	9.84	33.67	1.59×10^{-7}	11.4	33.3
1259	Irradiated ORM-19	-	-		1400	9.84	41.93	1.23×10^{-7}	11.1	17.4
1278	Control				1400	8.44	83.63	3.97×10^{-8}	9.2	23.8
1274	Control				1500	8.44	18.28	2.07×10^{-7}	8.7	21.5
1261	Irradiated ORM-19	-	-		1500	8.44	20.10	1.90×10^{-7}	6.1	16.2
1277	Control				1700	4.22	38.90	1.09×10^{-7}	4.4	11.8
1276	Control				1700	4.92	22.71	1.67×10^{-7}	6.1	15.8
1260	Irradiated ORM-19	-	-		1700	4.92	24.61	1.43×10^{-7}	5.4	13.6
1275	Control				1700	5.62	12.57	2.39×10^{-7}	7.5	8.0
1262	Irradiated ORM-19	-	-		1700	5.62	13.67	2.07×10^{-7}	5.4	10.4

[a] Specimens from 0.508-cm-diameter tungsten rod annealed at 1750°C in hydrogen for 1 hour prior to fabrication; stress-relieved at 1600°C for 1 hour in hydrogen following grinding.

[b] 33MT-137 irradiated at approximately 7×10^{19} nvt ($E_n \geq 1$ Mev) at elevated temperatures, $1000°C < T < 1350°C$, in the ETR.

[c] ORM-17 irradiated at approximately 1.6×10^{19} nvt ($E_n \geq 1$ Mev) and reactor ambient temperature in ORR-F2.

[d] ORM-19 irradiated at approximately 8.2×10^{19} nvt ($E_n \geq 1$ Mev) and reactor ambient temperature in ORR-F2.

TABLE 2.6

SUMMARY OF CREEP-RUPTURE TEST ON TUNGSTEN SPECIMENS, ROD M MATERIAL

		Post-Irradiation Anneal								
Specimen[a]	Condition	Temperature, °C	Time, hr	Atmosphere	Temperature, °C	Stress, kg/mm^2	Rupture Life, hr	Linear Creep Rate, sec^{-1}	Elongation, % in 4.54 cm	Reduction In Area, %
1247	Control				900	22.64	30.8	1.00 x 10^{-6}	31.9	96.1
1240	Irradiated ORM-19[b]	-	-	-	900	22.64	(26)[c]	-	-	-
	Irradiated ORM-19	1050	1	H_2	900	22.64	(46)	-	-	-
	Irradiated ORM-19	1200	1	H_2	900	22.64	(116)	-	-	-
	Irradiated ORM-19	1300	1	H_2	900	22.64	(691)[d]	4.70 x 10^{-8}	-	-
1242	Irradiated ORM-19	1700	1	H_2	900	22.64	(191)	3.60 x 10^{-8}	-	-
					900	23.67	(210)	~2.10 x 10^{-7}	-	-
					900	22.64	(319)	2.40 x 10^{-8}	-	-
					900	23.15	(354)	~8.90 x 10^{-8}	-	-
					900	22.64	(402)	2.40 x 10^{-8}	-	-
					900	24.07	(460)	3.80 x 10^{-7}	35.4	95.4
1241	Irradiated ORM-19	1700	43	H_2	900	22.64	260.0	2.00 x 10^{-7}	33.1	93.9
1228	Irradiated 33MT-137[e]	1700	30	Ar	900	22.64	64.7	4.30 x 10^{-7}	-	-
1238	Irradiated ORM-19	1700	1	H_2	1100	18.28	81.9	4.78 x 10^{-7}	32.7	92.1
1246	Control				1100	18.28	18.1	1.94 x 10^{-6}	30.7	96.5
1235	Irradiated 33MT-137	-	-	-	1100	18.28	150.0	3.57 x 10^{-8}	9.6	45.5
1230	Irradiated 33MT-137	1700	29	Ar	1100	18.28	19.1	2.02 x 10^{-6}	26.4	80.1
1229	Irradiated 33MT-137	1700	30	H_2	1100	18.28	15.7	2.22 x 10^{-6}	32.2	82.5
1233	Irradiated 33MT-137	-	-	-	1400	10.55	13.9	3.61 x 10^{-7}	4.1	8.2

[a] Specimens from 0.508-cm-diameter tungsten rod annealed at 1750°C in hydrogen for 1 hour prior to fabrication; stress-relieved at 1600°C for 1 hour in hydrogen following grinding.

[b] ORM-19 irradiated at approximately 8.2 x 10^{19} nvt ($E_n \geq 1$ Mev) and reactor ambient temperature in ORR-F2.

[c] Hours in parentheses are cumulative time.

[d] Test discontinued.

[e] 33MT-137 irradiated at approximately 7 x 10^{19} nvt ($E_n \geq 1$ Mev) at elevated temperatures, $1000°C < T < 1350°C$, in the ETR.

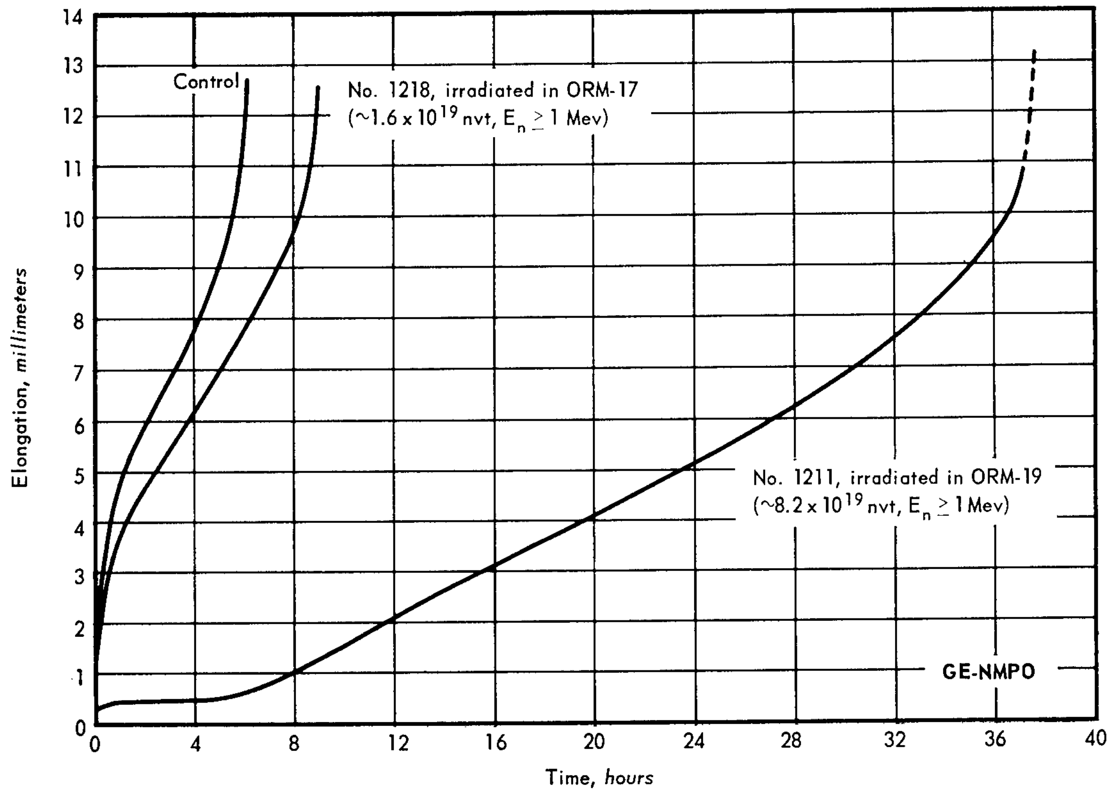

Fig. 2.1 – Elongation versus time for tungsten specimens (Rod E) tested at 19.3 kg/mm^2 and a temperature of 1100°C in hydrogen

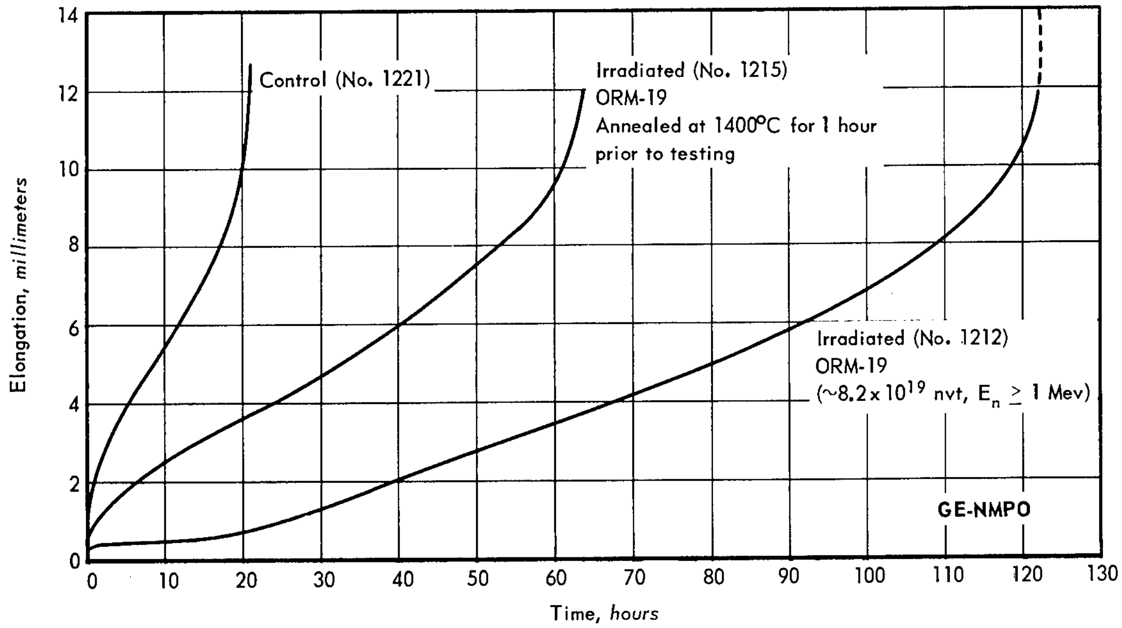

Fig. 2.2 – Elongation versus time for tungsten specimens (Rod E) tested at 18.28 kg/mm^2 and a temperature of 1100°C in hydrogen

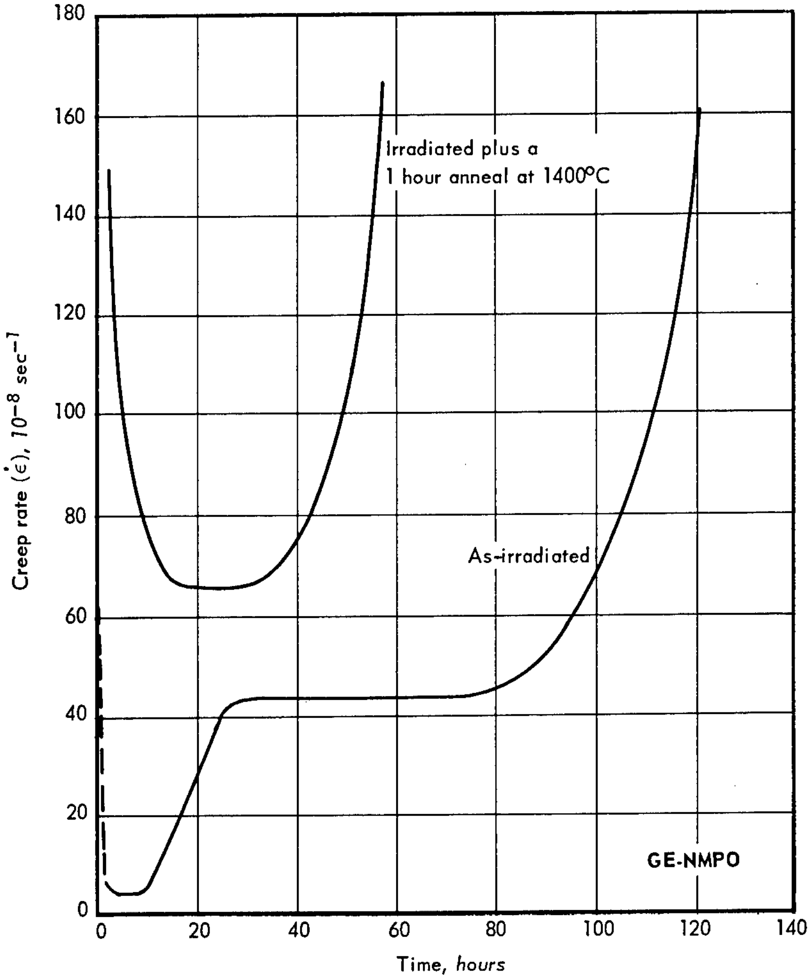

Fig. 2.3 – Creep rate versus time for tungsten specimens (Rod E) tested at 18.28 kg/mm^2 and a temperature of 1100°C in hydrogen. (ORM-19; ~8.2 x 10^{19} nvt, $E_n \geq 1$ Mev)

From the elongation versus time curves, Figures 2.1 and 2.2, it is apparent that irradiation to a relatively low dosage (~1.6 x 10^{19} nvt) does not significantly affect the creep-rupture properties. Irradiation at higher dosage (~8.2 x 10^{19} nvt) shows, as reported previously,[2] that at least two separate flow mechanisms may be affected by the neutron irradiation. The first mechanism is reflected as a period of time (incubation period) in which very little creep occurs and which appears to be stress dependent. For example, the 6-hour incubation period for the specimen tested at a stress of 19.3 kg/mm^2 (Figure 2.1) increased by 300 percent when the stress was reduced 5 percent, to 18.28 kg/mm^2 (Figure 2.2). The second mechanism appears as a significant reduction in the minimum creep rate of the material, as shown in Figures 2.1 and 2.2. It is believed that the two flow mechanisms are independent and are due to the interaction of dislocations with two different types of irradiation-induced defects.

Annealing one of the irradiated specimens at 1400°C for 1 hour appeared to remove the defect causing the anomalous initial creep behavior (incubation period) of the irradiated material. Although the incubation period of the creep curve was removed, the irradiation-induced reduction in the minimum creep rate was not significantly changed from that observed for the specimen tested in the as-irradiated condition (Figure 2.2).

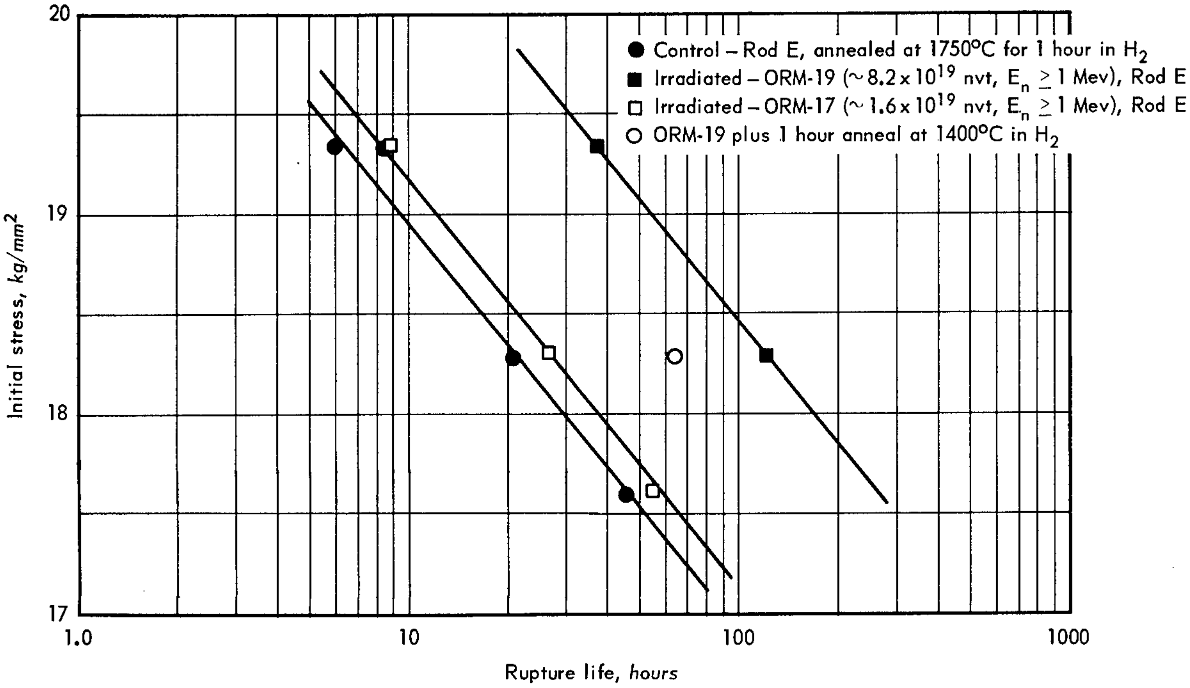

Fig. 2.4 – Stress-rupture strength of tungsten rod specimens tested at 1100°C in hydrogen

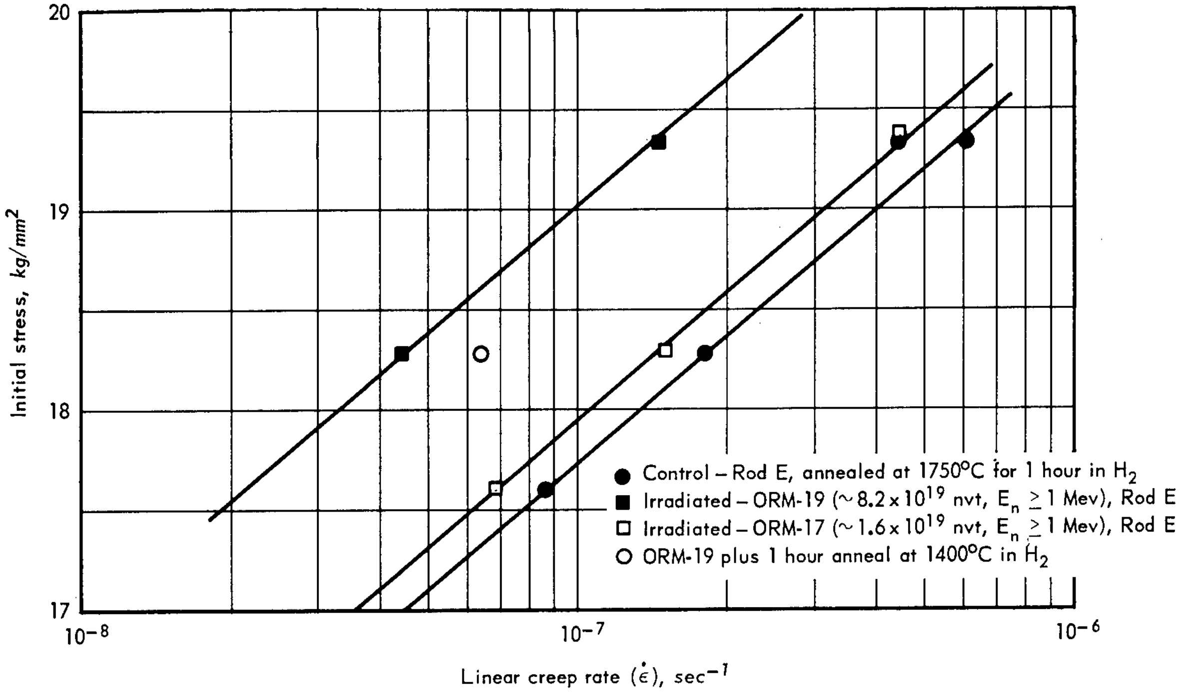

Fig. 2.5 – Stress versus creep rate of tungsten rod specimens at 1100°C in hydrogen

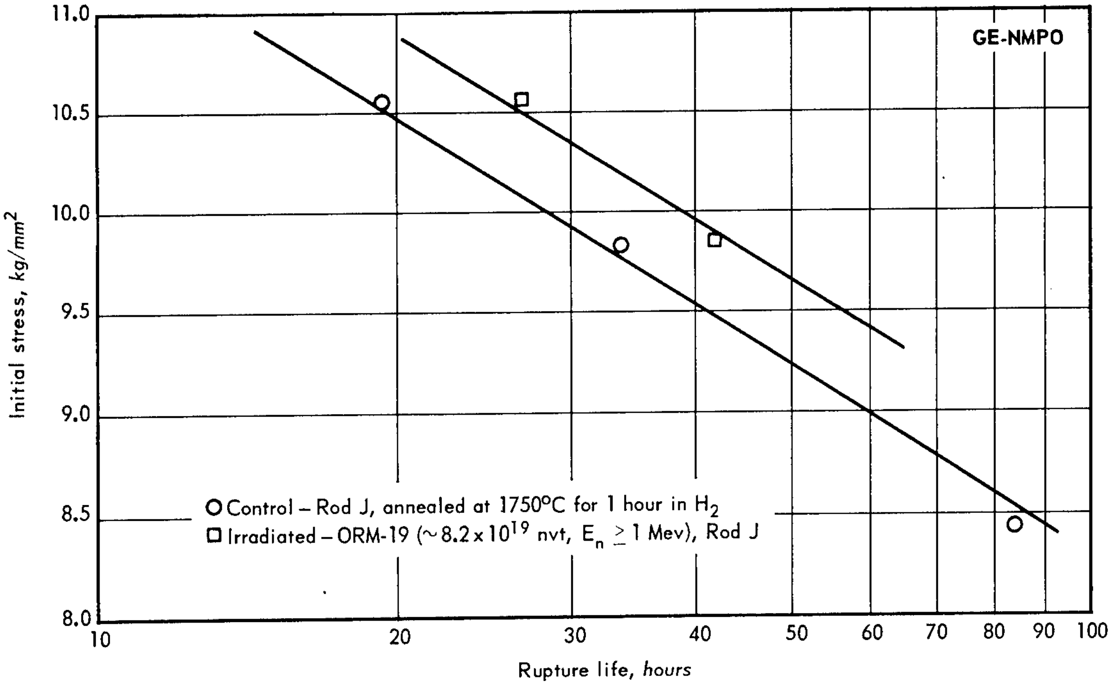

Fig. 2.6 – Stress-rupture strength of tungsten rod specimens tested at 1400°C in hydrogen

The instantaneous creep rate as a function of time for the two irradiated specimens shown in Figure 2. 2 is plotted in Figure 2. 3. The removal of the anomalous initial creep rate is clearly shown in the first 25 hours of test.

The initial stress versus rupture life and linear creep rate for specimens tested at 1100°C are shown in Figures 2. 4 and 2. 5, respectively. The increase in rupture life or corresponding decrease in the minimum creep rate as a result of irradiation appears to be independent of stress over the range considered in these experiments. The data of the irradiated specimen which was annealed for 1 hour at 1400°C are also included in the figures.

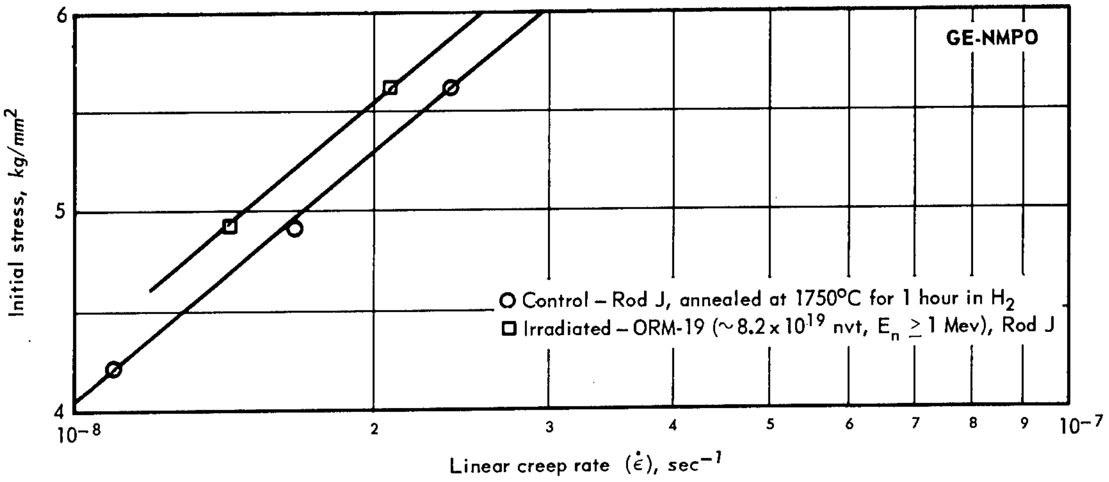

Fig. 2.7 – Stress versus creep rate of tungsten rod specimens tested at 1700°C in hydrogen

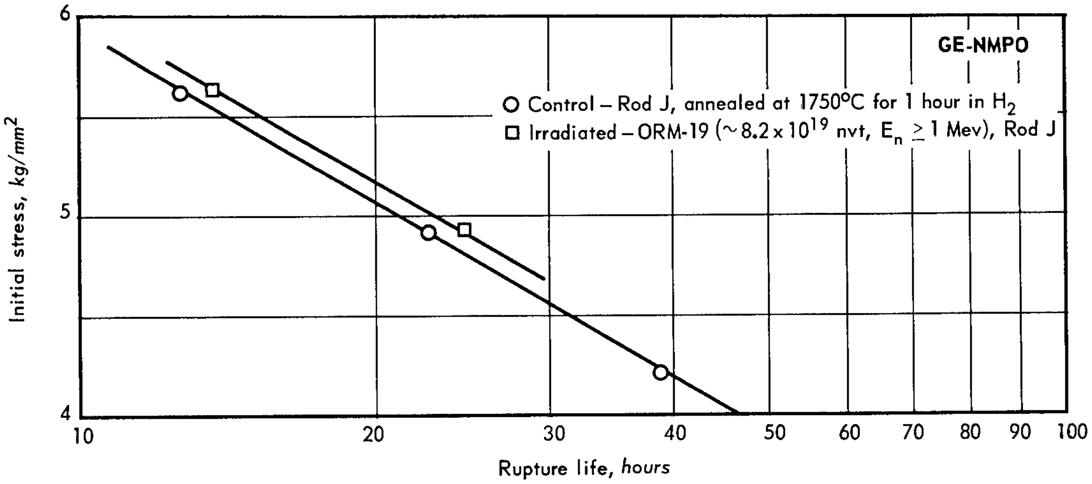

Fig. 2.8 – Stress-rupture strength of tungsten rod specimens tested at 1700°C in hydrogen

The creep-rupture data obtained from specimens tested at higher temperatures (1400°C and 1700°C) are shown in Figures 2.6, 2.7, and 2.8. The 1700°C data presented in Figures 2.7 and 2.8 show slight increase (~9%) in rupture life and corresponding decrease (~13%) in the linear creep rate. It is believed that this residual strengthening is due in part to the presence of rhenium atoms produced by transmutations of tungsten by the thermal neutron (n, γ) reaction. Based on the few data points obtained at these higher temperatures, it appears that the irradiation does not change the stress dependency of the creep-rupture properties.

Photographs of typical fractures occurring in specimens tested in the various temperature ranges are shown in Figure 2.9. As can be seen, the ductility of both the control specimens and the irradiated specimen decreased with increases in temperature. The specimens tested at 900°C (not shown) and at 1100°C showed pronounced necking, at 1400°C the fractures possessed only slight necking, and at 1500°C and 1700°C the specimens failed with brittle shear-type fractures.

Annealing studies were performed on tungsten specimens that were subsequently creep-rupture tested at 900°C and at an initial stress of 22.64 kg/mm^2. The test results for specimens which were irradiated at a fairly low dosage (~1.6 x 10^{19} nvt) are shown in Figures 2.10 through 2.13. These specimens were found to have a rupture life that was greater by a factor of 3.8 than a corresponding control specimen tested at the same temperature and stress. Annealing one irradiated specimen at 1050°C and another at 1200°C resulted in a further strengthening over and above that observed for an as-irradiated specimen. For instance, annealing at 1200°C (0.40 T_m) for 1 hour resulted in an increase in rupture life by a factor of about 10 compared with that of a control specimen. Annealing at still a higher temperature (1300°C; 0.43 T_m) reduced the rupture life and increased the linear creep rate compared to that of an as-irradiated specimen. Even an annealing treatment at 1700°C (0.54 T_m), as shown in Figures 2.10 and 2.11, did not completely remove the irradiation-induced strengthening of this material; there still remained a 90 percent increase in the time to rupture when compared to that of a control specimen.

The further hardening caused by annealing at 1200°C and below ($T \leq 0.40\ T_m$) is believed to be the result of the migration of radiation-induced defects, possibly free vacancies, which form additional clusters. These clusters achieve a critical size and/or spacing

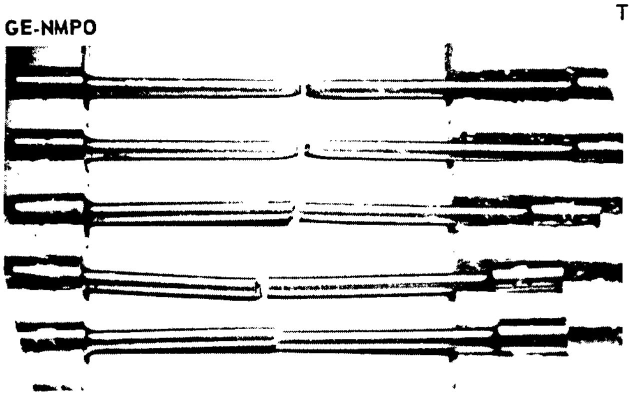

Temperature, °C	Elongation, percent in 4.45 cm gage length	Reduction in Area, %
1100	29.1	89.2
1100	29.1	90.6
1400	15.1	26.7
1700	5.35	13.6
1500	6.11	16.2

Irradiated specimens *(Neg. RML 2280)*

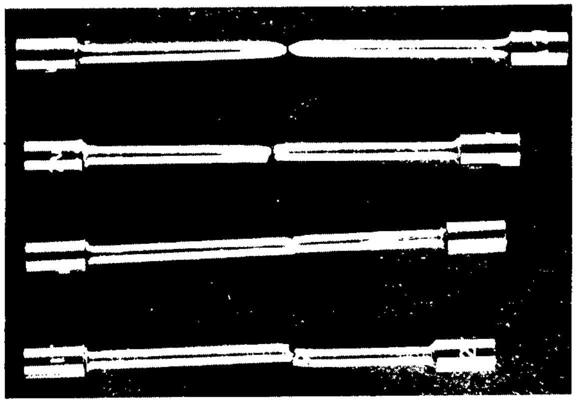

Temperature, °C	Elongation, percent in 4.45 cm gage length	Reduction in Area, %
1100	31.1	94.5
1400	12.7	35.5
1500	8.66	21.5
1700	6.14	15.8

Control specimens *(Neg. 4541)*

Fig. 2.9 – Typical fractures in tungsten specimens

at approximately 1200°C which increases the lattice friction; therefore, the flow stress is a maximum (greater time to rupture for a fixed stress) following an annealing at this temperature. The reduction in the flow stress after annealing at 1300°C and above is attributed to a reduction, by dissociation, in the number of clusters; thus the dispersion becomes progressively less effective in restricting the movement of dislocations. A consistent model explaining the observed property changes will be postulated following completion of the substructure studies. Similar thermal hardening effects were observed by other investigators on the yield strength of irradiated Mo,[3] ferritic steels,[4] and Nb.[5]

Although there were significant effects on the rupture life and the minimum creep rate, these irradiations and subsequent heat treatments did not affect the ductility of the material.

Elongation versus time curves for two annealed specimens, a control specimen, and an as-irradiated specimen are shown in Figures 2.12 and 2.13. As can be seen, the as-irradiated specimen has the lowest initial elongation (or strain) on loading and also appears to have a constant creep rate for the first 3 hours of test. This effect is attributed to the same mechanism which resulted in the anamolous initial creep characteristics observed for as-irradiated specimens when tested at higher temperatures (Figures 2.1 and 2.2). Although the data for all the specimens tested in this series are not shown in these figures, it was observed that they experienced a greater initial elongation on loading with increasing annealing temperatures.

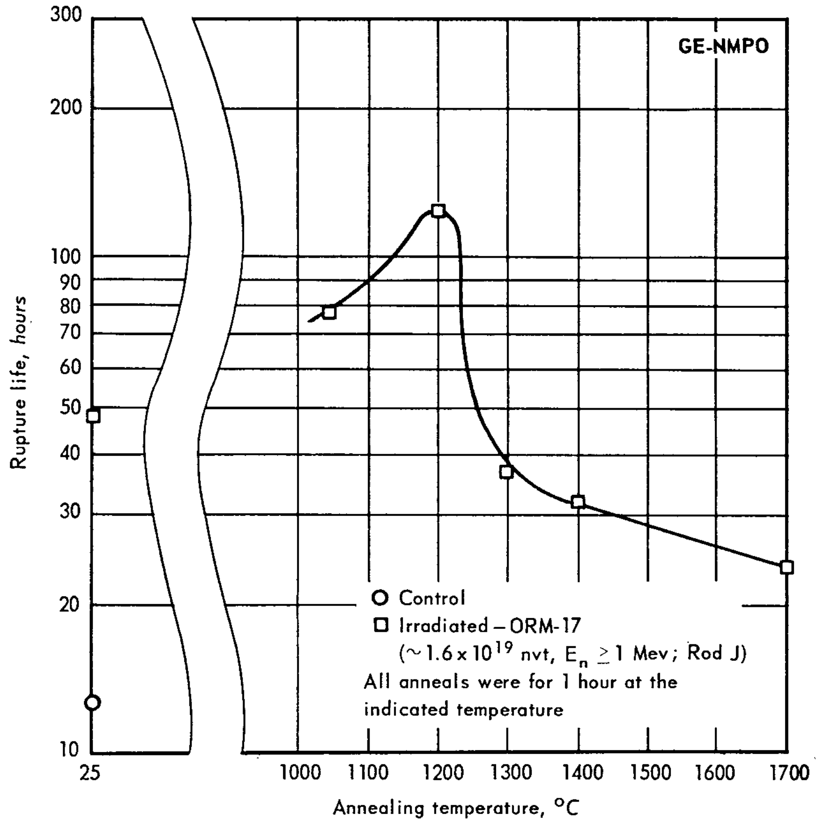

Fig. 2.10 – Rupture life of tungsten specimens tested at 900°C and 22.64 kg/mm^2 as a function of post-irradiation annealing temperature

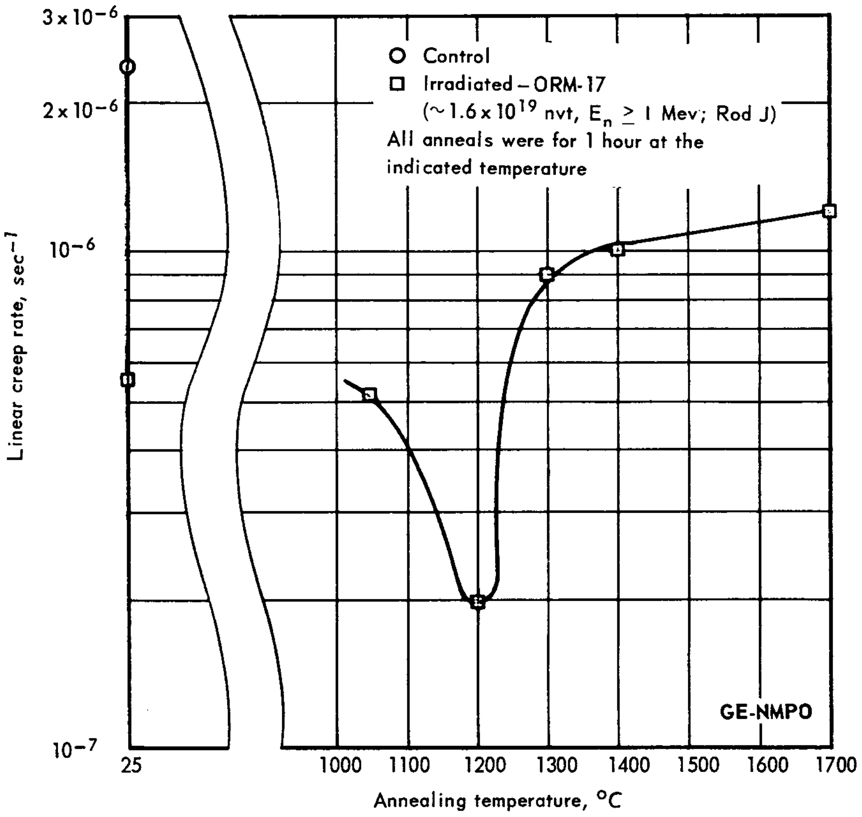

Fig. 2.11 – Creep rate of tungsten specimens tested at 900°C and 22.64 kg/mm^2 as a function of post-irradiation annealing temperature

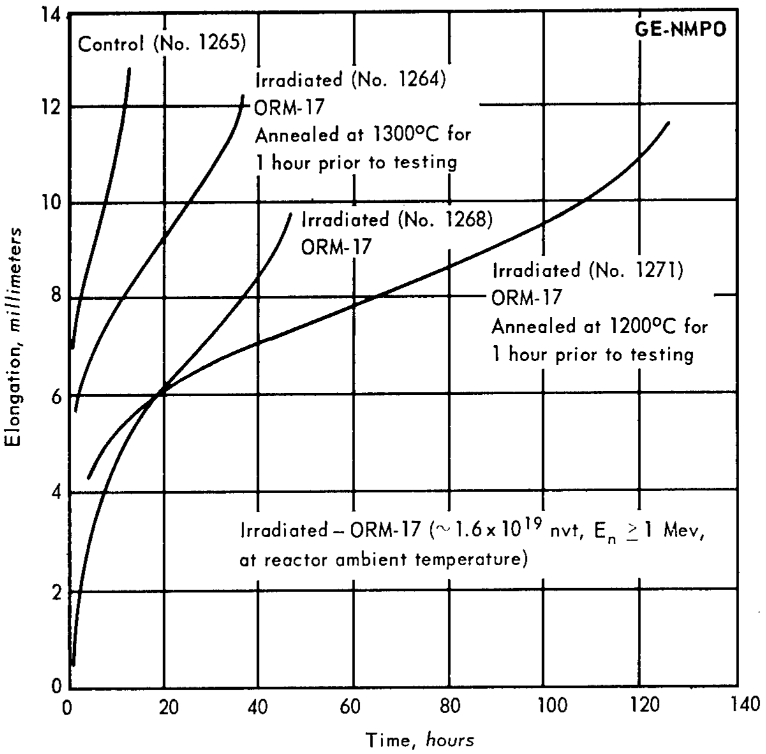

Fig. 2.12 – Elongation versus time for tungsten specimens (Rod J) tested at 900°C and 22.64 kg/mm^2 in hydrogen

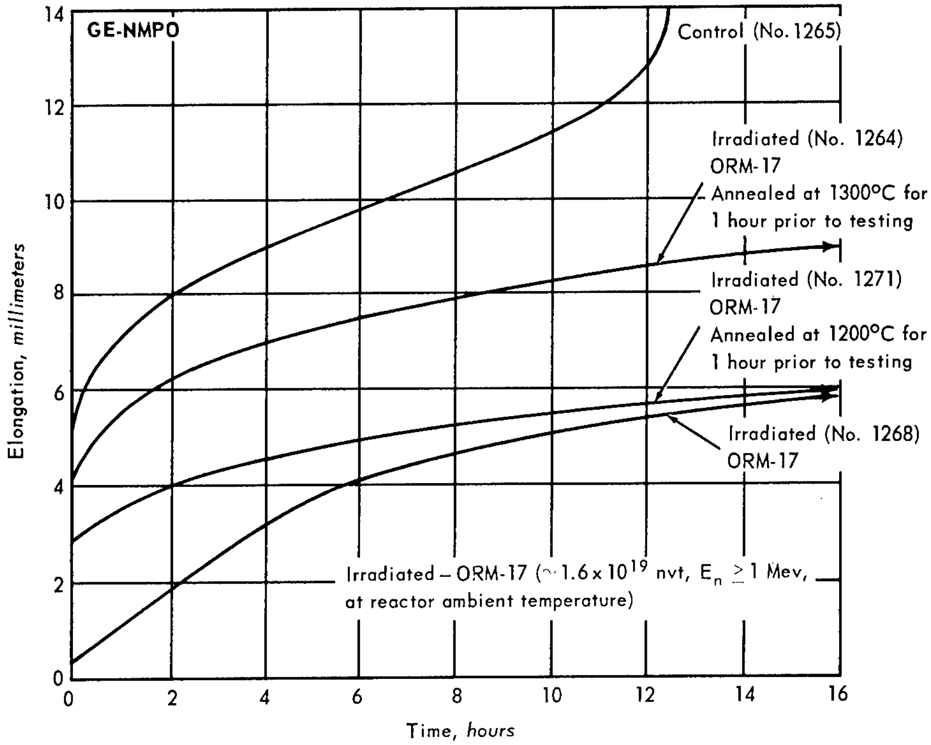

Fig. 2.13 – Elongation versus time for tungsten specimens (Rod J) tested at 900°C and 22.64 kg/mm^2 in hydrogen

Additional annealing studies were conducted on tungsten specimens irradiated at a higher neutron dose (8.2×10^{19} nvt) than those discussed above. The elongation versus time curves for three annealed specimens and a control specimen tested at a temperature of 900°C and a stress of 22.64 kg/mm^2 are shown in Figure 2.14. An irradiated specimen tested at 900°C showed no observable creep during the first 26 hours, nor was any creep noted after 1 hour annealings at 1050°C and 1200°C for an accumulated test time of 166 hours. Annealing the same specimen at 1300°C for 1 hour resulted in a creep rate at 900°C of less than 5×10^{-8} sec^{-1} during the next 425 hours. The creep rate (1×10^{-6} sec^{-1}) of a control specimen tested under similar conditions was more than 20 times greater than that observed for the specimen which was irradiated and annealed at 1300°C.

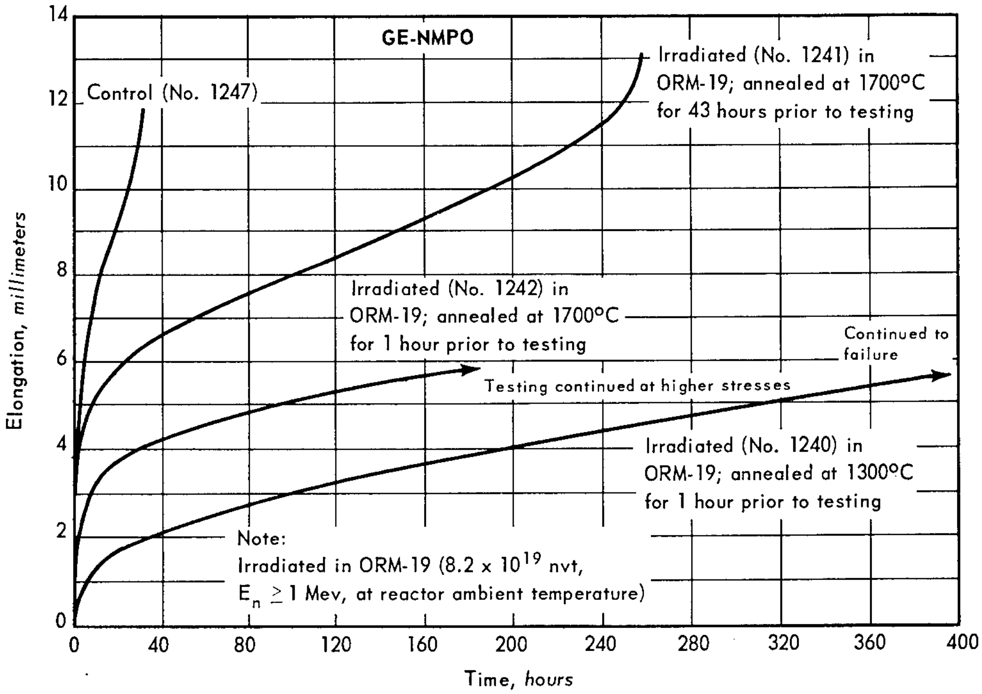

Fig. 2.14 – Elongation versus time for tungsten specimens (Rod M) tested at 900°C and 22.64 kg/mm^2 in hydrogen

Since it was apparent that annealing at 1300°C did not significantly reduce the irradiation-induced hardening, another irradiated specimen was annealed at 1700°C for 1 hour and creep-rupture tested at 900°C. The creep rate did not change significantly from that observed for the specimen that was annealed at 1300°C. A third irradiated specimen annealed at 1700°C for 43 hours and tested at 900°C showed that some recovery did occur in the linear creep rate, resulting in a value of about 2×10^{-7} sec^{-1}, or a ratio of control specimen to irradiated specimen creep rate of 5.0. Although the 1700°C temperature is above one-half the absolute melting temperature of tungsten, where it is believed that self-diffusion is sufficiently prominent so that recovery of irradiation-induced defects may be possible, annealing times longer than 43 hours apparently are required to reach complete recovery, excluding any strengthening due to transmutation effects.

Specimens which were irradiated at elevated temperature to a fast neutron dose of approximately 7×10^{19} nvt experienced a significant loss in ductility when tested at 900°C. Figure 2.15 shows a plot of elongation versus time for one control and two irradiated specimens. One of the irradiated specimens was annealed at 1700°C for 30 hours prior

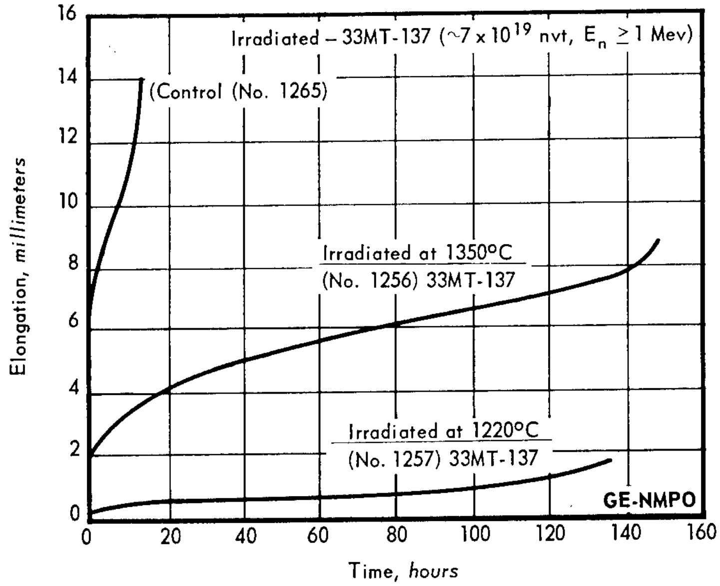

Fig. 2.15 – Elongation versus time for tungsten specimens (Rod J) tested at 900°C and 22.64 kg/mm² in hydrogen

to testing at 900°C. Since the temperature profile was not flat over the complete length of the capsule,[8] the data for these specimens may not be directly compared. For instance, the specimen that was irradiated at 1220°C showed much more embrittlement than the specimen which was irradiated at a slightly higher temperature (1350°C). Both specimens tested in the as-irradiated condition showed significant increases in rupture life and decreases in ductility. A specimen annealed at 1700°C for 30 hours and tested at 900°C showed some recovery of the creep rate; however, the embrittlement was still present. It appears that the specimens experienced a relatively small duration of third-stage creep.

In these elevated-temperature irradiations, the thermal neutron flux is about the same as the fast neutron flux; whereas, in the irradiations at reactor ambient temperatures, the thermal neutron flux is three times greater than the fast neutron flux. The observed embrittlement may be caused by the difference in the ratio of thermal to fast neutron flux since different, and possibly competing, defects are caused by each. This embrittlement may also be due to contamination of the specimens in elevated-temperature irradiations by the possible presence of some impurities in the gas system of the ETR loop.

As-irradiated specimens (elevated temperature) creep-rupture tested at 1100°C showed similar embrittlement, as shown in Figure 2.16. Annealing a specimen at 1700°C for 30 hours in a hydrogen atmosphere and testing at 1100°C resulted in a complete recovery of the time to rupture, creep rate, and ductility when compared to that of a control specimen. Testing another specimen similarly annealed in an argon atmosphere showed the same results. Based on these data, it appears that any strengthening due to the presence of rhenium atoms (transmutations) is possibly counterbalanced by the reduction in dislocation density as a result of annealing the irradiated specimens for longer times than the control specimens. These effects will be evaluated by further annealing studies of both irradiated and control specimens.

W - 25Re

Creep-rupture test data at 1100°C on W - 25Re specimens irradiated at reactor ambient temperatures to a fast neutron dose of 8 x 10^{19} nvt and on W - 25Re control speci-

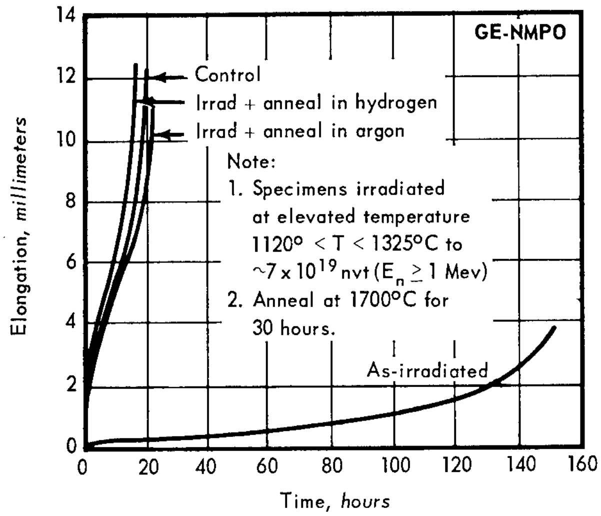

Note:
1. Specimens irradiated at elevated temperature 1120° < T < 1325°C to ~7 x 10^{19} nvt ($E_n \geq 1$ Mev)
2. Anneal at 1700°C for 30 hours.

Fig. 2.16 – Elongation versus time for tungsten specimens (Rod M) tested at 1100°C and 18.28 kg/mm^2 in hydrogen

mens are shown in Figures 2.17 and 2.18. The data are listed in Table 2.7 along with similar data for specimens which were irradiated at a fast neutron dose of 3.7 x 10^{19} nvt.

As can be seen in Table 2.7, one set of specimens was annealed at 1750°C and another set at 1900°C each for 1 hour following specimen fabrication. The raw sheet stock was recrystallized, by the vendor, at 1600°C for 0.5 hour in hydrogen.

Very little change in properties was observed for the specimens which were irradiated at the lower dosage. Even for an irradiation of about 8 x 10^{19} nvt, as shown in Figure 2.17,

TABLE 2.7

SUMMARY OF CREEP-RUPTURE TESTS ON W - 25Re SPECIMENS AT 1100°C

Specimen	Condition	Stress, kg/mm^2	Rupture Life, hr	Linear Creep Rate, sec^{-1}	Elongation, % in 2.54 cm gage length
723[a]	Control	47.5	2.90	2.28 x 10^{-5}	57.10
724[a]	Control	45.7	3.94	1.65 x 10^{-5}	49.80
726[a]	Control	43.9	7.03	9.23 x 10^{-6}	53.30
716[a]	Irradiated ORM-16[b]	47.5	3.13	2.03 x 10^{-5}	45.60
717[a]	Irradiated ORM-16	45.7	3.61	1.73 x 10^{-5}	47.20
718[a]	Irradiated ORM-16	43.9	10.70	6.22 x 10^{-6}	45.10
719[a]	Irradiated ORM-16	42.2	13.05	5.00 x 10^{-6}	54.00
745[c]	Irradiated ORM-20[d]	47.5	5.30	1.37 x 10^{-5}	47.09
748[c]	Control	43.9	6.20	1.18 x 10^{-5}	60.31
742[c]	Irradiated ORM-20	43.9	9.62	5.67 x 10^{-6}	26.70
746[c]	Control	40.0	17.09	4.54 x 10^{-6}	66.06
743[c]	Irradiated ORM-20	40.0	25.07	2.99 x 10^{-6}	37.72
750[c]	Control	34.0	63.41	1.10 x 10^{-6}	63.40

[a] Specimens from 0.051-cm sheet (powder batch RWS-9, ingot No. 2) recrystallized by vendor at 1600°C for 0.5 hour in hydrogen, annealed at 1900°C for 1 hour in hydrogen after fabrication.

[b] ORM-16 irradiated (~3.7 x 10^{19} nvt; $E_n \geq 1$ Mev) at reactor ambient temperature in ORR-F9 facility.

[c] Specimens from 0.051-cm sheet (powder batch RWS-9, ingot No. 4) recrystallized by vendor at 1600°C for 0.5 hour in hydrogen, annealed at 1750°C for 1 hour in hydrogen following specimen fabrication.

[d] ORM-20 irradiated (~8 x 10^{19} nvt; $E_n \geq 1$ Mev) at reactor ambient temperature in ORR-F2 facility.

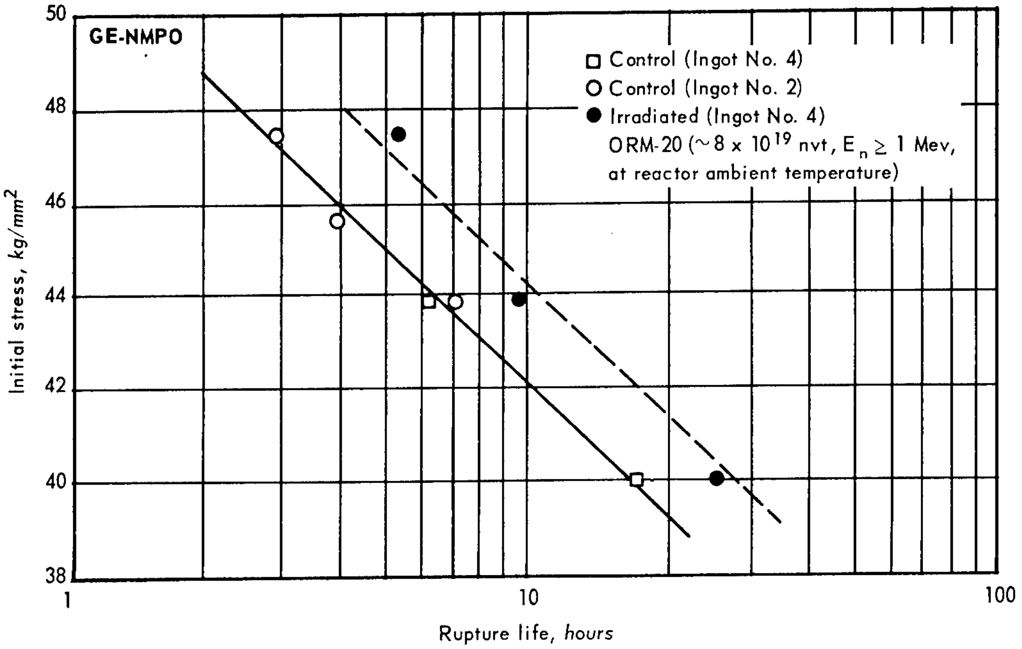

Fig. 2.17 – Stress-rupture strength of W – 25Re specimens tested at 1100°C in hydrogen

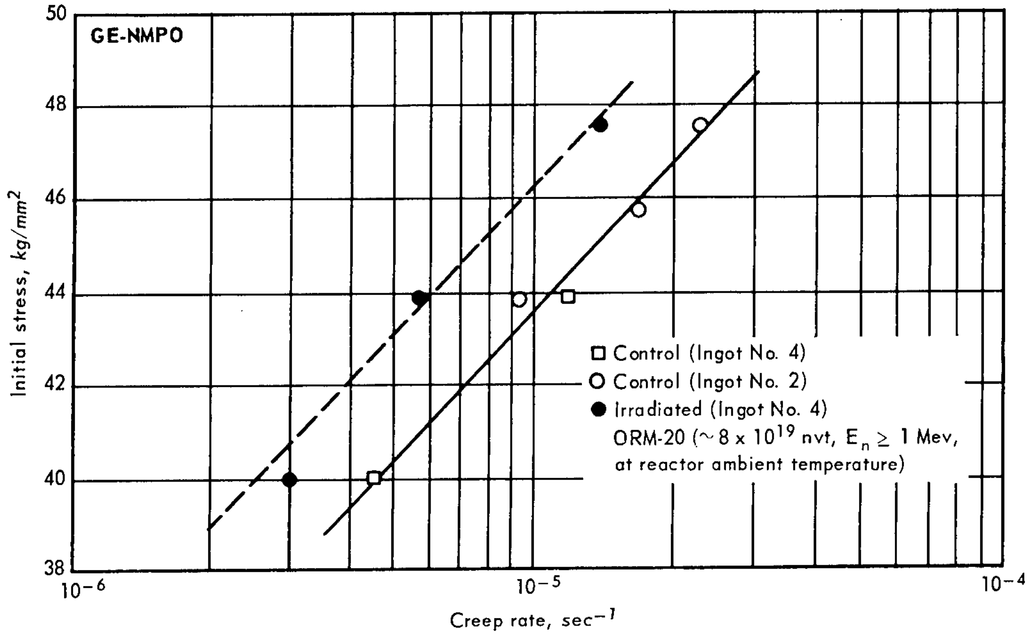

Fig. 2.18 – Linear creep rate of W – 25Re specimens tested at 1100°C in hydrogen

the resulting increase in the rupture life was less than a factor of 1.8. In contrast, tungsten specimens irradiated to the same dosage and tested at the same temperature showed increases in rupture life which were 5 times greater than that of the control specimens. Another notable difference between the effects of neutron irradiation on W - 25Re and tungsten appears to be a reduction in the ductility of the alloy even though the rupture life was not significantly changed. Further testing is continuing on this material at 900°C where it is believed that a change in flow mechanism exists and a pronounced increase in the time to rupture due to the irradiation is anticipated.

Molybdenum

Creep-rupture data of irradiated molybdenum specimens (irradiated to fast neutron doses of 1.0 and 3.7 x 10^{19} nvt) when tested at various temperatures appear to indicate an acceleration of the creep rate, compared to that of a control specimen, in the temperature region of about 580°C (0.30 T_m). Above and below this temperature region the effect is not as significant. Testing is continuing on both control and irradiated molybdenum specimens in the temperature region of 560° to 650°C (0.29 T_m to 0.32 T_m). The data for the present series of studies were performed on specimens listed in Table 2.8 and plotted in Figures 2.19 through 2.22.

TABLE 2.8

SUMMARY OF CREEP-RUPTURE TESTS ON MOLYBDENUM[a] SPECIMENS AT A CONSTANT STRESS OF 21.09 kg/mm^2

Specimen	Sheet No.[b]	Condition	Temperature, °C	Rupture Life, hr	Linear Creep Rate, sec^{-1}	Elongation, % in 2.54-cm gage length
1037	8	Control	580	68.20	5.78 x 10^{-7}	53.4
1042	8	Irradiated ORM-23[c]	580	2.25	~2.16 x 10^{-5}	50.9
1038	8	Irradiated ORM-23	580	3.62	1.47 x 10^{-5}	51.4
1040	8	Irradiated ORM-23; annealed at 757°C[d]	580	110.48	4.22 x 10^{-7}	42.2
1043	8	Irradiated ORM-23; annealed at 779°C[e]	580	75+[f]	4.16 x 10^{-7}	-
1045	8	Control	600	13.50	2.91 x 10^{-6}	60.0
1041	8	Control	620	2.15	1.49 x 10^{-5}	53.8
1039	8	Control	650	0.27	1.19 x 10^{-4}	53.4
850	1	Control	560	487.90	1.01 x 10^{-7}	56.9
692	1	Irradiated ORM-16[g]	560	237.70	2.14 x 10^{-7}	51.9
851	1	Control	580	115.60	3.59 x 10^{-7}	52.3
690	1	Irradiated ORM-16	580	41.30	1.13 x 10^{-6}	53.1
699	1	Control	600	40.30	1.03 x 10^{-6}	49.8
693	1	Irradiated ORM-16	600	27.30	1.62 x 10^{-6}	49.7
698	1	Control	650	5.74	7.70 x 10^{-6}	51.8
853	1	Irradiated ORM-16	650	3.01	1.58 x 10^{-5}	55.8

[a] Arc-cast molybdenum sheet, 0.5-mm-thick, heat KDM-515A; recrystallized by vendor.

[b] Sheet No. 8 annealed in argon for 1 hr at 1200°C after fabrication of specimens.
Sheet No. 1 annealed in hydrogen for 1 hr at 1200°C after fabrication of specimens.

[c] Capsule ORM-23 irradiated at reactor ambient temperature in the ORR-F2 to ~1 x 10^{19} nvt ($E_n \geq 1$ Mev).

[d] Annealed for 1 hr at indicated temperature in unstressed condition.

[e] Annealed for 8 hr at indicated temperature in unstressed condition.

[f] Temperature controller malfunction at 75 hours.

[g] Capsule ORM-16 irradiated at reactor ambient temperature in the ORR-F2 to ~3.7 x 10^{19} nvt ($E_n \geq 1$ Mev).

The two molybdenum sheets used to fabricate the specimens for these studies were rolled under similar conditions from ingots of the same heat (KDM-515A). Control specimens of both sheets had similar creep-rupture properties at the lower temperatures. At higher test temperatures, however, there was more than an order of magnitude difference in the creep-rupture properties with the specimens from sheet No. 1 showing the greater strength. The reason for the significant difference in the creep-rupture properties at the higher temperature is not known at the present time. All the specimens were fabricated at GE-NMPO using the same techniques. The main difference between the two sets of specimens was in the post-fabrication heat treatment. Sheet No. 1 specimens were annealed for 1 hour at 1200°C in a hydrogen atmosphere, and sheet No. 8 specimens were

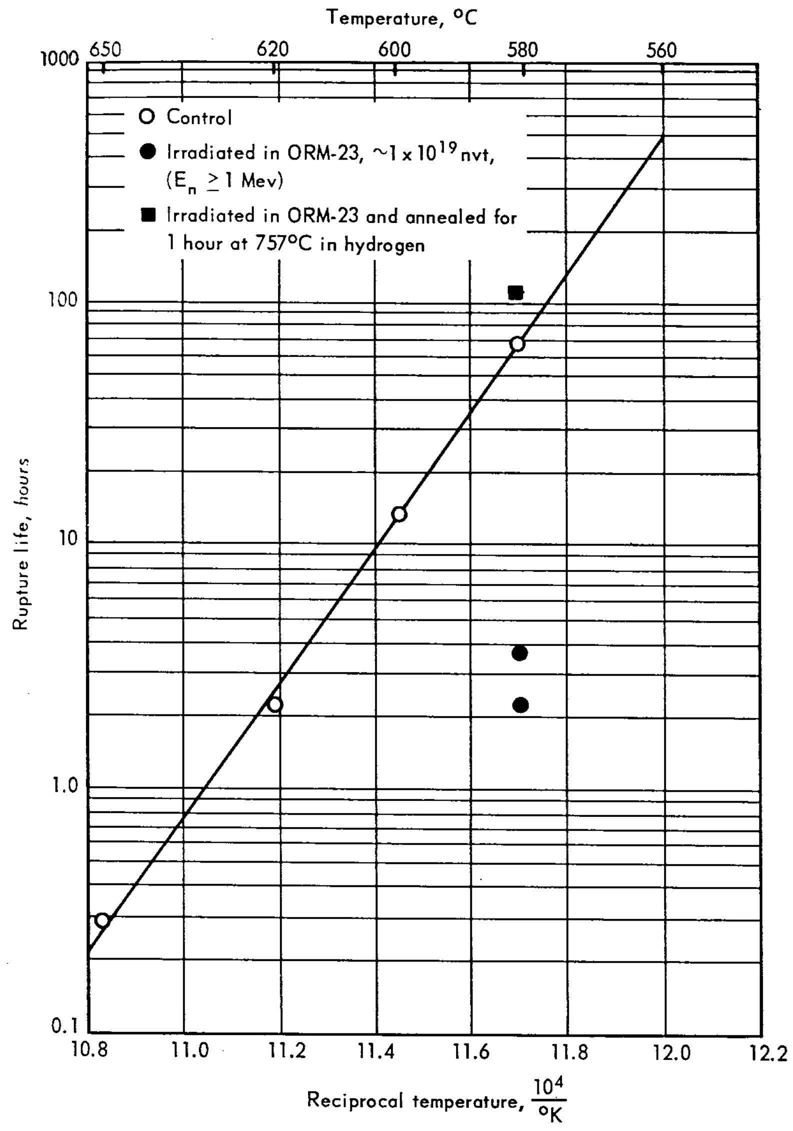

Fig. 2.19 – Rupture life versus reciprocal temperature for molybdenum specimens (Sheet No. 8) tested at 21.09 kg/mm^2 in hydrogen

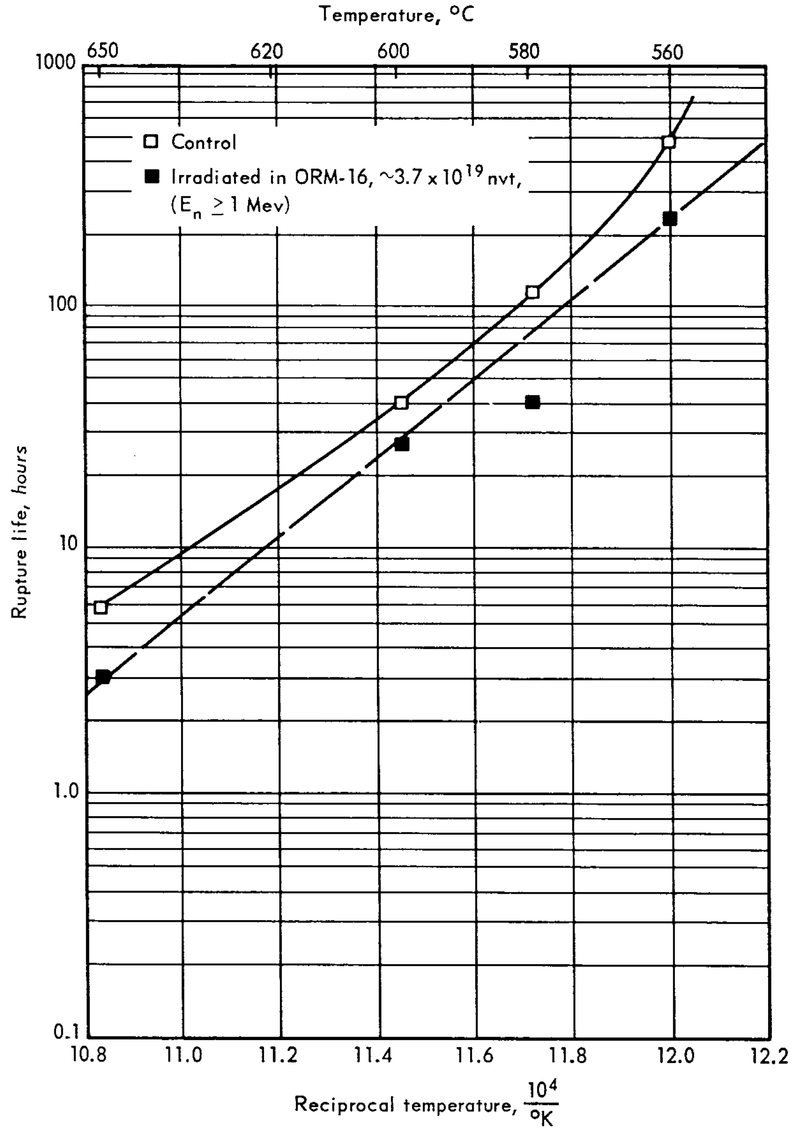

Fig. 2.20 – Rupture life versus reciprocal temperature for molybdenum specimens (Sheet No. 1) tested at 21.09 kg/mm^2 in hydrogen

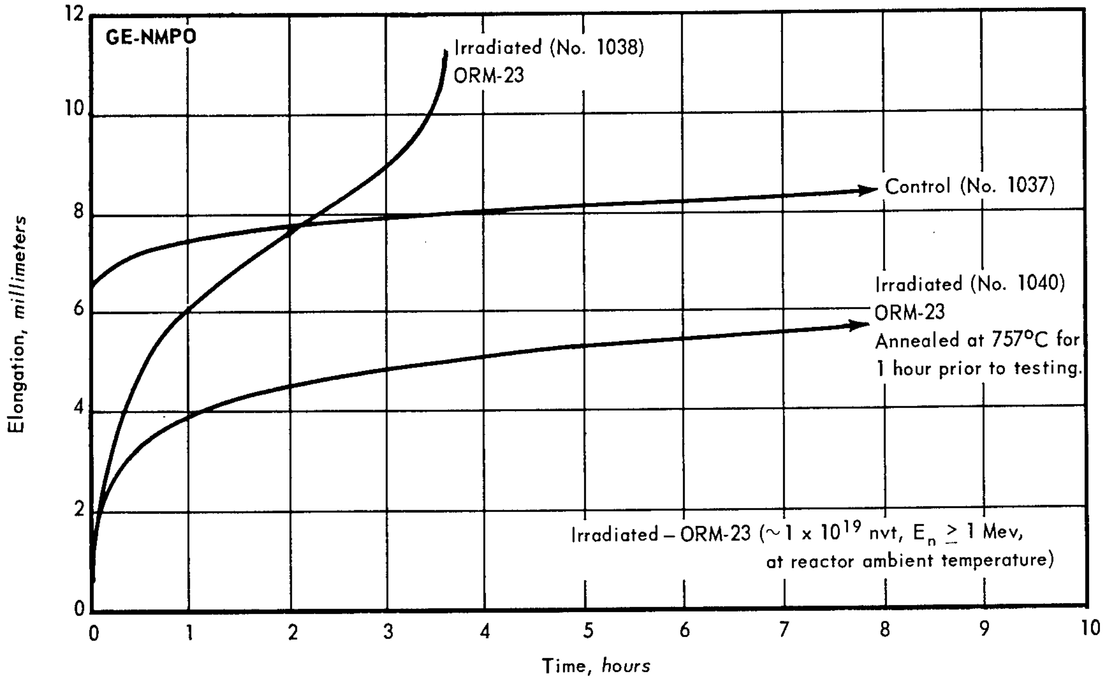

Fig. 2.21 – Elongation versus time for molybdenum specimens tested at 580°C and 21.09 kg/mm² in hydrogen

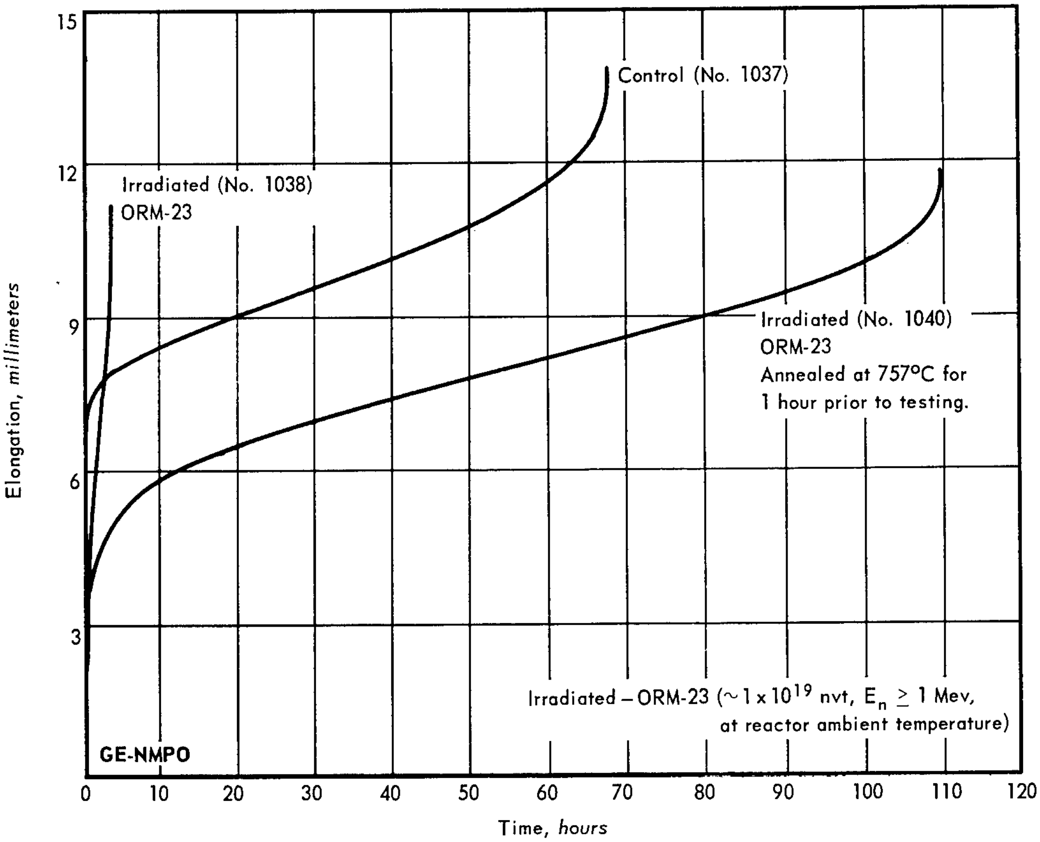

Fig. 2.22 – Elongation versus time for molybdenum specimens tested at 580°C and 21.09 kg/mm² in hydrogen

annealed for 1 hour at 1200°C in an argon atmosphere. Analysis to determine any changes in the interstitial impurity content of control specimens fabricated from both sheets are now being performed.

Rupture life versus the reciprocal absolute temperature of control and irradiated specimens (Figure 2.19) indicate that the creep-rupture properties are significantly changed (factors of 19 to 30) as a result of irradiation to a fast neutron dosage of about 1×10^{19} nvt when creep-rupture tested at 580°C (0.30 T_m). These tests represent the first time in which an accelerated creep rate or a significant reduction in rupture life was observed for irradiated BCC metals; however, all previous tests were performed at temperatures above 0.31 T_m. Irradiated specimens annealed for 1 hour at temperatures slightly above 0.35 T_m and then tested at a temperature of 0.30 T_m showed essentially complete recovery. The inadvertent fracture of four of the sheet No. 8 specimens when capsule ORM-23 was being disassembled precluded studies at other temperatures. Rupture life versus reciprocal absolute temperature for the specimens irradiated to a greater fast neutron dosage (ORM-16; $\sim 3.7 \times 10^{19}$ nvt, Figure 2.20) also showed a slight reduction in rupture life and an increase in the creep rate when compared to the corresponding data for control specimens, with a larger change occurring at 580°C (0.30 T_m).

Elongation versus time curves for specimens irradiated to 1×10^{19} nvt ($E_n \geq 1$ Mev) and tested at 580°C are shown in Figures 2.21 and 2.22. Figure 2.22 is plotted on an expanded time scale to show the three creep stages of the as-irradiated specimen. The as-irradiated specimen exhibited a pronounced decrease (factors greater than 10) in rupture life when compared to a control specimen. When another irradiated specimen from the same capsule was annealed at 757°C (0.36 T_m) for 1 hour and then creep-rupture tested at 580°C, there was about a factor of 1.6 increase in the rupture life when compared to the control specimen.

The accelerated creep rate (for the as-irradiated Mo specimen) is different than that observed from previous tests on irradiated Mo, W, and W - 25Re specimens in which there were decreases in the creep rate resulting in increases in the time to rupture. However, the previous test temperatures, in all cases, were higher than 0.31 T_m of the respective metal. Based on resistivity recovery data of irradiated BCC metals, it was demonstrated[7] that three resolved recovery peaks occur above room temperature; at 0.15 T_m, 0.22 T_m, and 0.31 T_m. It was also proposed that irradiation-induced free vacancies do not migrate at temperatures below the 0.31 T_m peak and that di-vacancies migrate above 0.22 T_m. As a result of annealing heat treatments above 0.31 T_m, migration will occur accompanied by subsequent vacancy clustering. As clusters (10 or more vacancies), the vacancies now become effective dislocation pinning points and may also act as obstacles to dislocation motion, both effects resulting in the observed strengthening of the irradiated and annealed metal.

In the present studies on molybdenum, the test temperatures were below the 0.31 T_m recovery peak. At these temperatures it is assumed that the irradiation-induced defects exist as a super-saturation of immobile vacancies in the unstressed metal. The effective vacancy concentration, therefore, becomes equivalent to that which would be in equilibrium with the metal at some higher temperature. Since the exact deformation mechanisms (i.e., cross-slip, dislocation intersection, dislocation climb, jog motion, etc.) has not been established for BCC metals under these test conditions, the possible influence of the excess vacancies and other defects on the flow stress cannot be postulated at this time.

The creep-rate data (Table 2.8) indicate that the degree of creep acceleration at 580°C decreases with an increase in the exposure dosage. One reason may be that the ratio of the density of the single and di-vacancies ($V_{n=1,2}$) to the density of those vacancy clusters

($V_n \geq 10$) which may effectively impede dislocation motion decreases with an increase in exposure dosage. The mobile vacancies contribute to the accelerated creep at specific temperatures possibly by promoting dislocation climb, whereas the vacancy clusters tend to impede dislocation motion by increasing the lattice friction. These competing mechanisms may account for the changes in the creep-rupture properties which were observed in the present series of experiments.

TENSILE TESTS

The final calibration of the furnace and stress - strain equipment for tensile testing sub-size refractory-metal specimens[8] in argon at temperatures up to 500°C was completed.

Preliminary tensile data on tungsten specimens irradiated at reactor ambient temperature to a fast neutron dose of about 8 x 10^{19} nvt are shown in Table 2.9. For these specimens, the brittle-to-ductile transition temperature apparently occurs at a temperature slightly below 200°C for control specimens and at temperatures above 370°C for the irradiated specimens. Testing of irradiated specimens is continuing at higher temperatures.

TABLE 2.9

TUNGSTEN TENSILE TEST DATA

Specimen[a]	Condition	Temperature, °C	Yield Strength, kg/mm^2	Ultimate Strength, kg/mm^2	Elongation,[b] %	Reduction In Area, %
1307	Control	121	49.4	50.6	0.24	0.25
1316	Control	121	49.6	49.6	0.32	0.25
1317	Control	163	44.2	58.0	3.20	3.20
1313	Control	204	40.9	57.4	24.80	23.98
1305	Irradiated MT-138[c]	163	-	67.5[d]	Nil	Nil
1306	Irradiated MT-138	204	-	71.8[d]	Nil	Nil
1309	Irradiated MT-138	371	-	71.3[d]	Nil	Nil

[a] Specimens from 0.343-cm-diameter rod (Rod G) annealed at 1900°C for 1 hour prior to fabrication; stress-relieved at 1600°C for 1 hour in hydrogen following grinding.

[b] Elongation in 3.18 cm.

[c] 33MT-138 irradiated (~1.3 x 10^{20} nvt, $E_n \geq 1$ Mev) at reactor ambient temperature in ETR-E5 facility.

[d] Fracture strength.

RESISTIVITY TESTS

Isothermal annealing studies on the removal of radiation-induced resistivity increase[9] are continuing on W, W - 25Re, Mo, and Mo-TZM. Irradiation conditions and the number of specimens of each material are listed in Table 2.2.

Specimens were irradiated at reactor ambient and at elevated temperatures to fast neutron doses up to about 8 x 10^{19} nvt. Preliminary measurements of the resistivity changes (Table 2.10) at -196°C indicate that no changes occur in molybdenum when irradiated at approximately 700°C. Ambient temperature irradiation produces a 123-percent increase in the resistivity of recrystallized molybdenum. Irradiation-induced resistivity changes in Mo-TZM were relatively small.

Irradiating tungsten at approximately 1300°C to a fast neutron dose of about 8 x 10^{19} nvt resulted in about a 39-percent increase in the resistivity at -196°C. Ambient irradiations at a lower neutron dosage (~3.3 x 10^{19} nvt) resulted in a 300-percent increase in resistivity. Changes in W - 25Re were relatively small. The residual resistivity increment observed in the tungsten specimens, even after annealing at temperatures where most simple irradiation-induced defects should be removed[10] is probably caused by transmutations of tungsten atoms to rhenium atoms. Several of the tungsten isotopes have

TABLE 2.10

RESISTIVITY CHANGES OF IRRADIATED BCC METALS

Material[a]	Irradiation Conditions Temperature, °C	Irradiation Conditions Dosage, nvt ($E_n \geq 1$ Mev)	Resistivity Increase, %[b]
W	70	3.3×10^{19}	300
W	1300	8.0×10^{19}	39
W	1300	8.0×10^{19}	25[c]
W - 25Re	70	1.3×10^{19}	11
W - 25Re	1300	8.0×10^{19}	16[c]
Mo	70	1.3×10^{19}	123[d]
Mo	70	1.3×10^{19}	80[e]
Mo	700	8.0×10^{19}	0[f]
Mo-TZM	70	2.9×10^{19}	74[f]
Mo-TZM	700	8.0×10^{19}	9[f]

[a] All material in irradiated as-received (vendor recrystallized) condition unless noted.

[b] Resistivity measured at -196°C.

[c] Pre-irradiation annealed at 1900°C for 1 hour in H_2.

[d] Pre-irradiation annealed at 1175°C for 1.2 hours in H_2.

[e] Material in warm worked condition.

[f] Pre-irradiation annealed at 1500°C for 1 hour in H_2.

fairly high cross sections which lead to the formation of rhenium atoms. On the other hand, molybdenum isotopes collectively have a much lower thermal neutron cross section than the tungsten isotopes, and many of the molybdenum neutron absorption reactions lead to stable molybdenum isotopes which would not change the resistivity of molybdenum in the manner that rhenium isotopes change that of tungsten. Figure 2.23 shows the experimetally determined effect of rhenium atoms on the resistivity of tungsten when measured at a temperature of -196°C.

Isochronal recovery studies[11,12] of irradiated tungsten and molybdenum specimens show that three resolved recovery peaks occur at homologous temperatures of about $0.15\ T_m$, $0.22\ T_m$, and $0.31\ T_m$. Typical recovery spectra for tungsten are shown in Figure 2.24. At these temperature regions there apparently are significant changes in the sub-structure of BCC metals which affect their mechanical properties. The nature and the kinetic behavior of the defects which are responsible for the above peaks and their interaction with dislocations are presently being investigated.

Isothermal recovery studies[12] in the region of the $0.15\ T_m$ temperature peak indicate that second-order annealing kinetics are followed. Comparison of the natural logarithm of the fractional resistivity remaining (f_1) and also the reciprocal of this fraction minus unity (f_2), both as a function of time, are plotted in Figure 2.25.

When second-order annealing kinetics are assumed, an expression relating resistivity and annealing time is obtained as given in equation (2.1):

$$\frac{d\Delta\rho}{dt} = -B(\Delta\rho)^2 \qquad (2.1)$$

where $\Delta\rho = \rho - \rho_\infty$ and ρ_∞ is the asymptote of the isothermal annealing curve, B is a constant and t is the time variable. If there are several remaining recoverable defects contributing to the resistivity following the removal of the defect being studied, then $\rho_\infty = \rho_d + \rho_c$ where ρ_d is the resistivity due to the remaining defects and ρ_c is the resistivity due to the

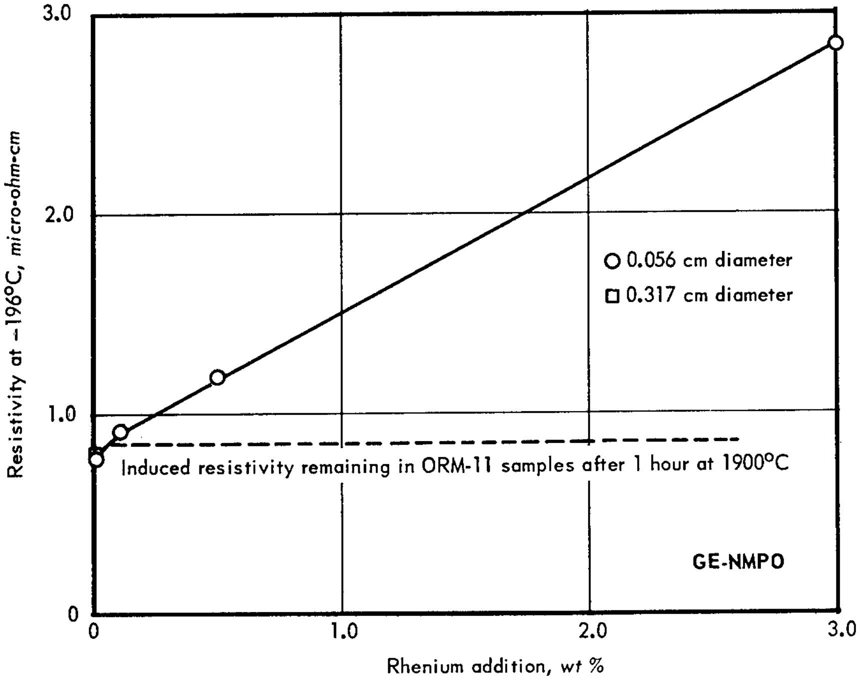

Fig. 2.23 – Effect of rhenium addition to resistivity of recrystallized tungsten wire

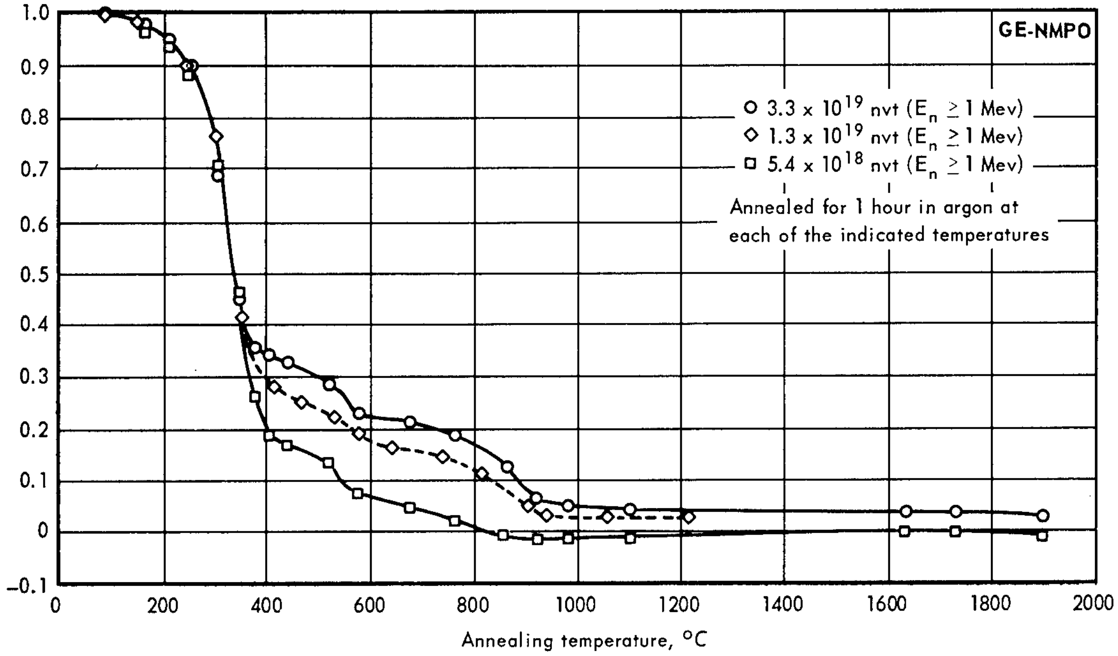

Fig. 2.24 – Normalized isochronal recovery of recrystallized tungsten irradiated at approximately 70°C

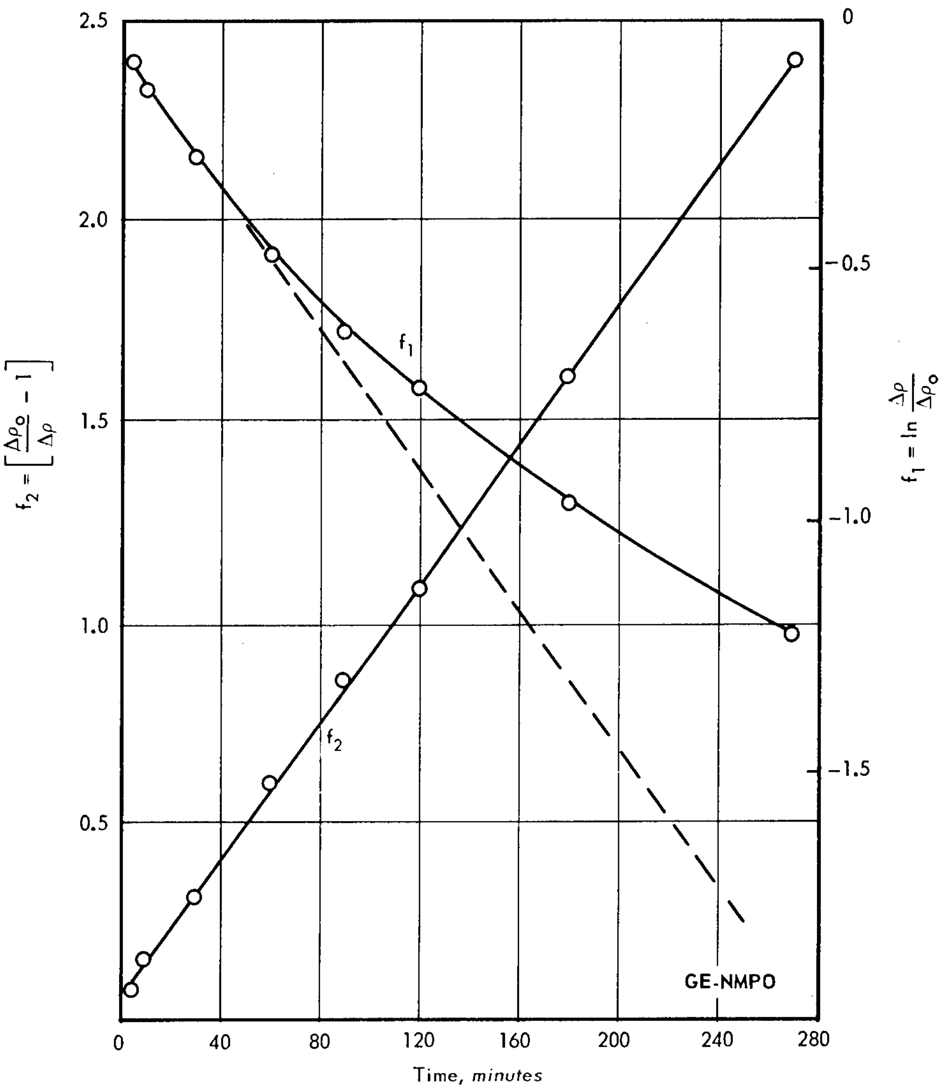

Fig. 2.25 – Isothermal recovery at 333°C for tungsten irradiated to a fast neutron dose of 1.3×10^{19} nvt($E_n \geq 1$ Mev) at approximately 70°C

characteristic unirradiated material, including impurities. The solution of this differential equation is given in equation (2.2):

$$(\rho - \rho_\infty)^{-1} - (\rho_o - \rho_\infty)^{-1} = Bt \qquad (2.2)$$

where ρ_o is the value of ρ at t = o or that value of the as-irradiated resistivity in the present studies. Equation (2.2) may be written as equation (2.3).

$$\frac{1}{\Delta\rho} - \frac{1}{\Delta\rho_o} = Bt$$

$$\frac{\Delta\rho_o}{\Delta\rho} - 1 = (B\Delta\rho_o)\,t = f_2 \qquad (2.3)$$

If the recovery processes obey second-order kinetics the plot of f_2 versus t will yield a straight line.

The data presented in Figure 2.25 for an irradiated tungsten specimen indicate a second-order recovery process occurring at the 333°C (0.16 T_m) isotherm. The value of ρ_∞ which was used in equation (2. 2) was obtained from isochronal plots at 400°C.[13] The value at this temperature represents a minimum in the recovery spectrum following the 0. 16 T_m peak. The same value for ρ_∞ also yielded straight lines for similar plots of the other isotherms in this temperature region.

A similar attempt to learn whether the same data could be represented by first-order kinetics gave negative results. First-order processes would yield a linear curve of f_1 versus t, where f_1 is given in equation (2. 4):

$$f_1 = \ln \frac{\Delta\rho}{\Delta\rho_0} = - Ct \tag{2. 4}$$

where C is a constant.

Equations (2. 3) and (2. 4) were evaluated by using upper and lower limits of ρ_∞ and, in no case, did the ln $(\Delta\rho/\rho_0)$ plots yield straight lines, and the f_2 plots did not deviate seriously from linearity.

Activation energy determinations for the recovery of irradiation-induced resistivity increments are now in progress in the 0. 31 T_m temperature region.

HARDNESS TESTS

Tungsten single crystals which were irradiated to a fast neutron dose of about 3.5×10^{19} nvt were hot-hardness tested in the temperature range of 15° to 1300°C. Figure 2. 26 shows a plot of the diamond pyramid hardness versus temperature on a semi-logarithmic scale. Data for the control specimen indicate changes in slope at about 280°, 800°, and 1000°C. The change in slope of the irradiated specimen occurs at about the same lower temperature as the control specimen. Another change occurs at slightly above 900°C after which the hardness values approach a slope parallel to that of the control data at temperatures above 1100°C. A large part of the residual hardness increment remaining after annealing at 1300°C is probably caused by the presence of rhenium atoms as a result of tungsten transmutations. The specimens were removed from the hot-hardness tester and annealed for 1 hour at 1900°C. The resulting hardness data at 500°C, when compared with that obtained after the 1300°C anneal, indicated very little change in the 500°C hardness.

The data from the irradiated specimen indicate very little hardness increase at room temperature (~7%), whereas a significant increase (~60%) was observed above 280°C. It appears that neutron irradiation does not affect the strongly temperature-dependent component of the hardness. If a comparison of the flow mechanism for hardness data may be made with those of tensile tests, then the rate-controlling mechanism for the deformation of this metal at the lower temperatures is overcoming the Peierls-Nabarro stress.[14]

A plot of the microhardness increment fraction, ΔH_f, defined by equation (2. 5), is presented in Figure 2. 27 as a function of temperature:

$$\Delta H_i = \frac{H_i - H_c}{H_c} \tag{2. 5}$$

where H_i is the microhardness of the irradiated specimen at some temperature and H_c is the microhardness of the unirradiated specimen at the same temperature. As shown in Figure 2. 27, the radiation-induced hardening is more significant at temperatures above 200°C where the temperature-sensitive component becomes less important. This hardening persists at temperatures up to about 700°C where it begins to anneal with a further increase in temperature. The spectra indicate that a recovery peak occurs at a temperature near 0. 35 T_m. This recovery peak of the mechanical properties is in marked contrast to the recovery peak of 0. 31 T_m which was observed in the resistivity annealing studies.

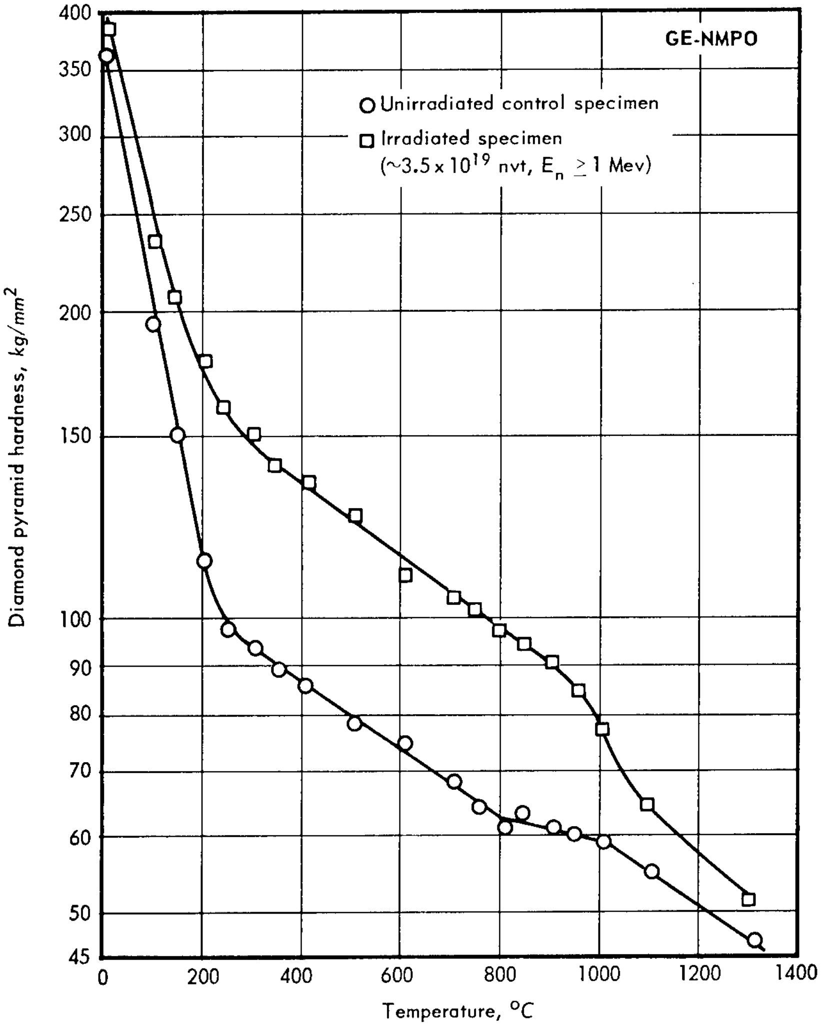

Fig. 2.26 – Hardness of irradiated and unirradiated tungsten single crystal as a function of temperature

A detailed study of the slip deformation around hardness indentations was also initiated. Previous observations[15] indicated that extensive slip occurred around the room-temperature indentations in irradiated polycrystalline tungsten. Current work, in connection with the hot-hardness study on tungsten single crystals, showed extensive slip around all indentations made in irradiated tungsten from 50° to 1000°C. Slip lines are not evident in unirradiated tungsten at temperatures below 200°C. A comparison of room-temperature indentations in irradiated and unirradiated single crystals made on a (411) face is shown in Figure 2.28. Complete absence of slip lines is evident in the unirradiated material. From X-ray diffraction data it appears that the slip system operative in the bottom of the photomicrograph (Figure 2.28) may be the (110) system in BCC metals; however, sectioning of the sample should confirm this observation. The general appearance of the deformation around the indentations in the irradiated material does not change markedly even at temperatures up to 800°C (Figure 2.29). At 900°C the slip lines of both the control and irradiated specimens are similar to those of the irradiated specimens at 800°C. At 1000°C the slip patterns about the indentations of the irradiated specimen (Figure 2.30) show a pronounced change compared to those observed at the lower temperatures and are essentially the same as those of the indentation of the control specimens. This apparent

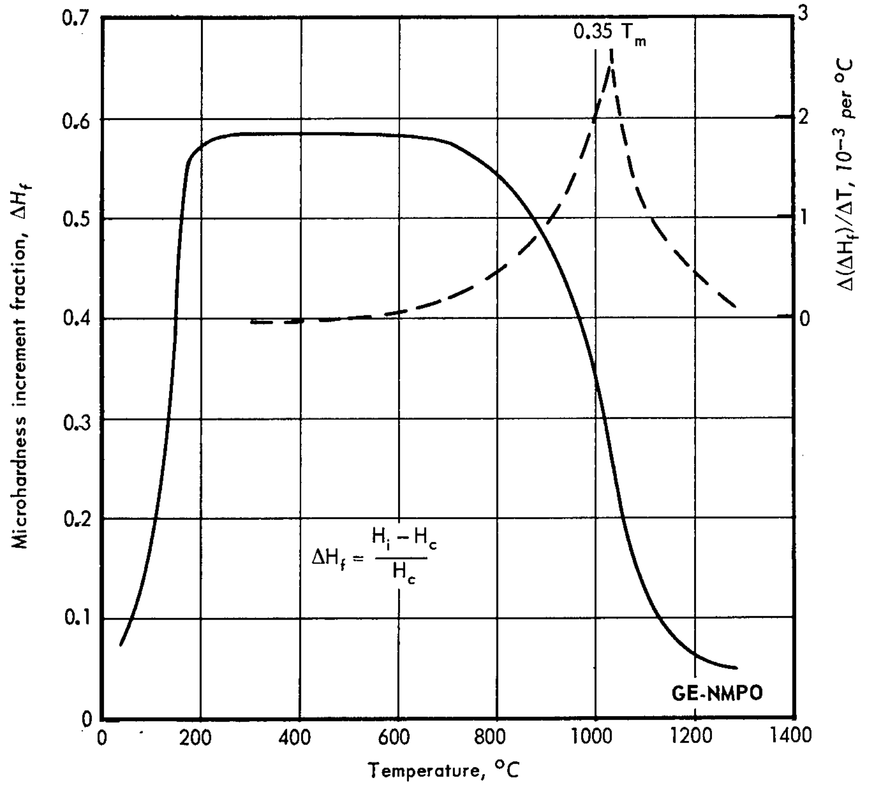

Fig. 2.27 – Microhardness increment fraction and recovery spectrum of irradiated tungsten single crystal as a function of temperature

GE-NMPO

Unirradiated *(Neg. R805)* Irradiated 3.5 x 10^{19} nvt *(Neg. R816)*

Fig. 2.28 – Tungsten single crystal {411} hardness indentations at 15°C
(Original magnification – 500X)

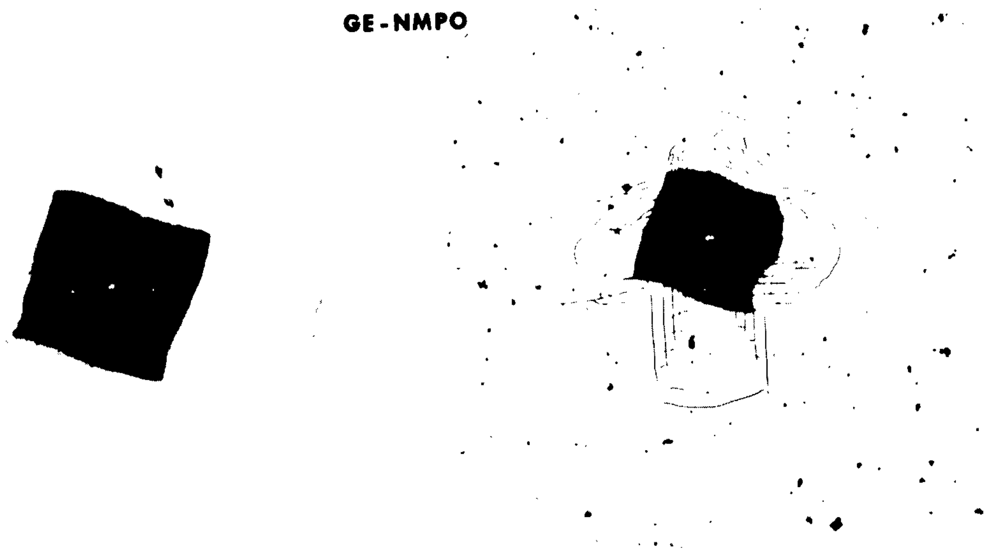

Unirradiated *(Neg. R813)* Irradiated 3.5 x 10^{19} nvt *(Neg. R824)*

Fig. 2.29 – Tungsten single crystal {411} hardness indentations at 800°C
(Original magnification – 250X)

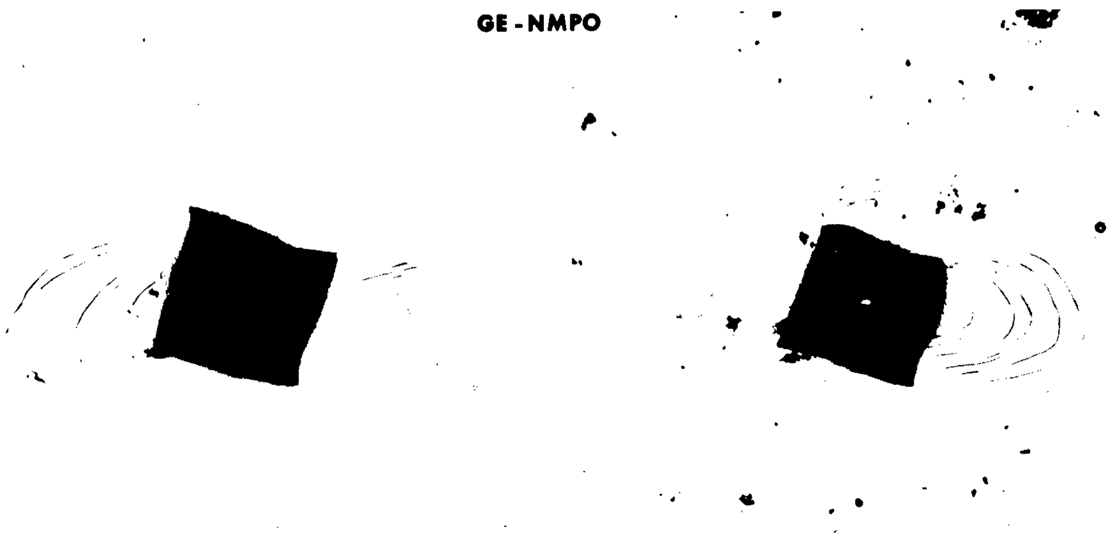

Unirradiated *(Neg. R815)* Irradiated 3.5 x 10^{19} nvt *(Neg. R826)*

Fig. 2.30 – Tungsten single crystal {411} hardness indentations at 1000°C
(Original magnification – 250X)

smoothing and blending of the slip lines in both specimens is attributed to dislocation climb[16] becoming a significant mode of deformation.

SUBSTRUCTURE STUDIES

Substructure studies using the transmission electron microscope were initiated to supplement the mechanical and physical property measurements being performed on tungsten and other refractory metals and alloys. The objective of these studies is to expand the means of measuring and understanding the mechanisms which affect the properties of these materials when they are irradiated in a reactor environment.

Neutron Irradiated Tungsten Single Crystals

First attempts to study neutron irradiation damage in tungsten were conducted on single crystal specimens obtained from worked tungsten sheet stock recrystallized above 2200°C for various lengths of time. These treatments produced very large grains which were confirmed as being single crystals initially by macroetching and subsequently by X-ray diffraction. Selected single crystals were then chemically thinned and photochemically machined as previously described[17] to provide approximately 25 specimens, 0.3 cm in diameter by 0.015 cm thick, similar to the one labeled "B" in Figure 2.31.

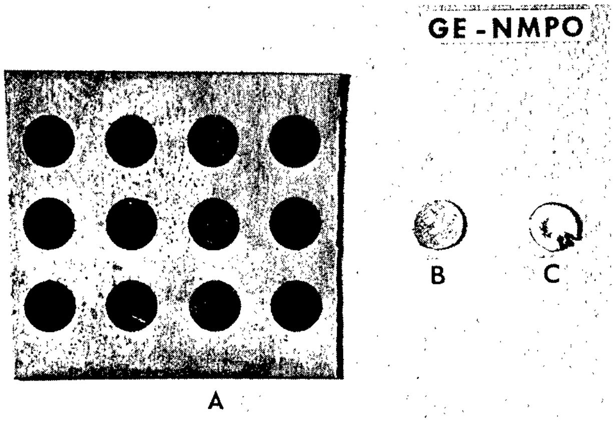

Fig. 2.31 – Sequence of sample preparation from (A) sheet stock, (B) after photochemical machining, and (C) electropolishing *(Neg. 4582, 2X)*

The specimens were separated into several groups and loaded into capsules designated as ORM-26, ORM-27, ORM-28, and ORM-30 (Table 2.2). These capsules were aluminum half-cylinders with machined recessed compartments to accommodate the tungsten specimens. The assembled half-cylinders containing the specimens were then loaded into an aluminum can, evacuated, and back-filled with helium prior to irradiation. Irradiations were conducted at reactor ambient temperatures in the ORR Rabbit Facility for nominal durations of 1, 5, 9, and 18 days. The resulting fast neutron dosages are estimated to range up to approximately 8×10^{19} nvt.

This range of dosages was considered sufficient to allow for a preliminary irradiation damage investigation. Single crystal specimens were studied in the as-grown, as-irradiated, and irradiated plus annealed conditions to follow as nearly as possible the introduction, development, and removal of irradiation-induced defects.

Previously, nearly all of the electron microscopy studies on irradiation damage in metals has been on the FCC materials. However, Eyre[18] and Bryner[19] reported their observations on neutron irradiated α-iron and Ferrovac-E iron, respectively. Studies on neutron irradiated molybdenum have been reported by Downey and Eyre,[20] and by Meakin and Greenfield.[21] The observations of these and other investigators have been a source of direction and corroboration in this study on neutron irradiated tungsten.

The first results of this study are shown in Figures 2. 32, 2. 33, and 2. 34. These observations were made using an electron microscope operating at 100 kv. Figure 2. 32 shows the control specimen of tungsten to be nearly completely free of any defects. There were a few isolated dislocations randomly dispersed throughout the crystal but the micrograph shown is typical of the bulk material. Specimen foils from capsule ORM-28 which received an estimated fast neutron dosage of 8 x 10^{19} nvt are shown in Figures 2. 33 and 2. 34.

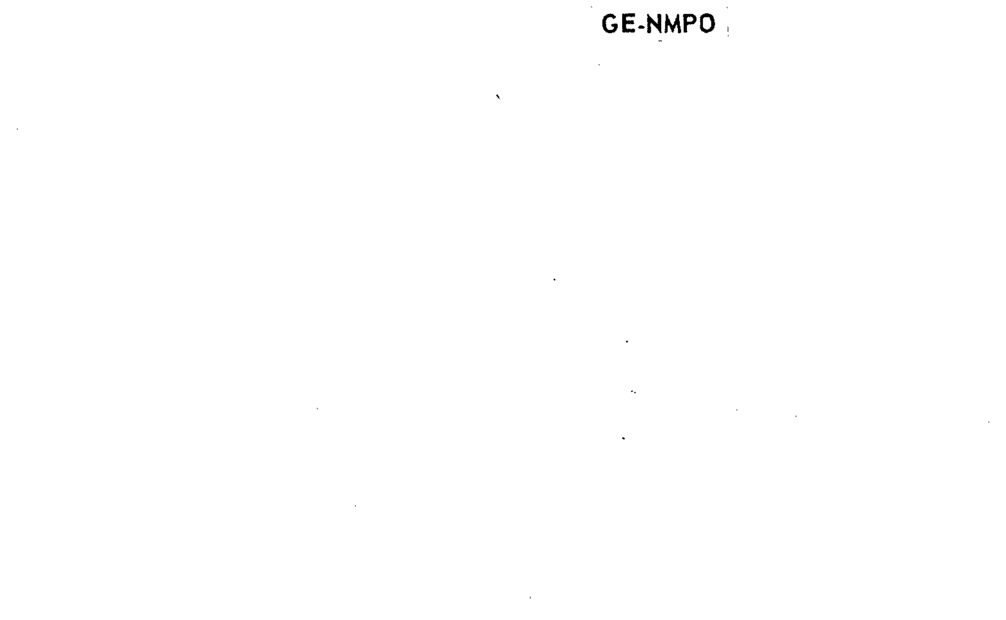

Fig. 2.32 – Unirradiated tungsten single crystal *(60,000X)*

The extensive uniform damage shown in the as-irradiated condition (Figure 2. 33) was found to exist throughout the specimen. This structure is similar to that found by Eyre in α-iron after a neutron dose of 1 x 10^{19} nvt ($\geq$1 Mev). Eyre reported "black spots" about 50 to 75 Å in diameter but in a quantity considerably less than observed here. Downey and Eyre reported a condition in molybdenum which had received the integrated thermal and fission neutron doses of 8. 24 x 10^{20} and 2. 5 x 10^{20} nvt, respectively, that was very similar to that observed in tungsten. They concluded that the "black spots" were clusters of interstitial point defects.

The substructure of the irradiated tungsten after it was annealed for 1 hour at 1090°C (0. 37 T_m) in argon is shown in Figure 2. 34. Bryner reported that after annealing for 4 hours at 400°C (0. 37 T_m), 100 Å diameter loops were developed in Ferrovac-E iron which was irradiated to 2 x 10^{20} nvt. Further, Downey and Eyre reported that there was little change in the as-irradiated observable clusters on annealing molybdenum up to 800°C (0. 37 T_m), although there were measured physical property recovery peaks at lower temperatures. The substructure shown in Figure 2. 34 is somewhat similar to both that of the irradiated iron and molybdenum after the comparable annealings. It can be noted that much of the damage has been removed and what remains appears to be small, well-

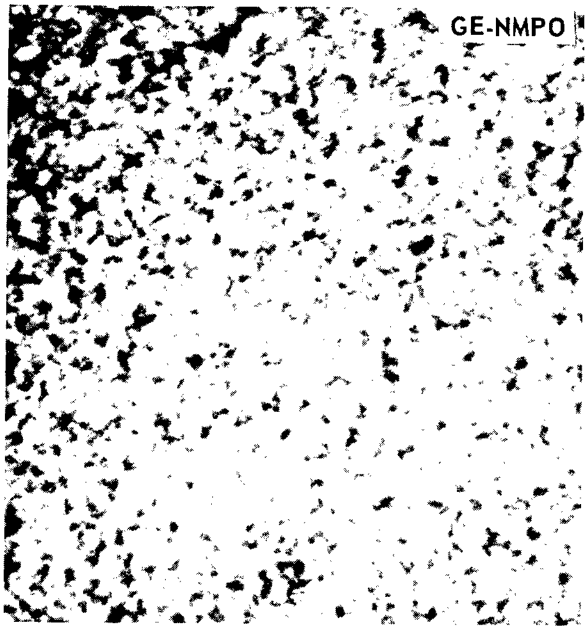

Fig. 2.33 – As-irradiated (~8×10^{19} nvt, $E_n \geq 1$ Mev) tungsten single crystal *(60,000X)*

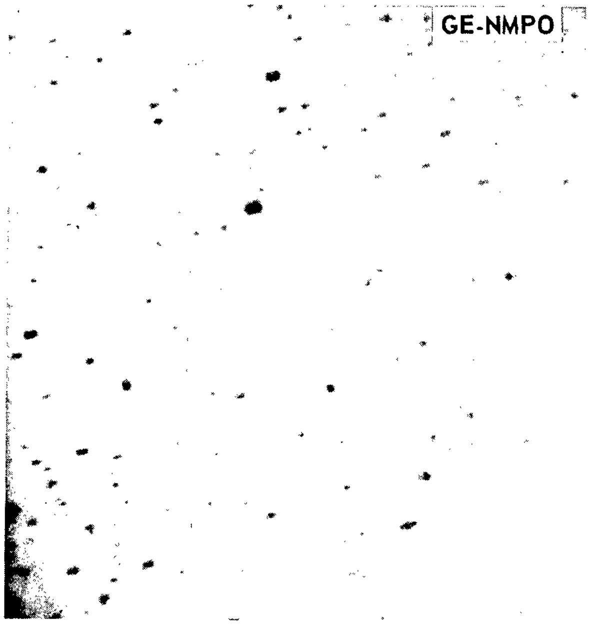

Fig. 2.34 – Irradiated (~8×10^{19}nvt, $E_n \geq 1$ Mev) tungsten single crystal following a 1 hour anneal at 1090°C (0.37 T_m) in argon *(60,000X)*

defined clusters of the point defects even to the extent of the presence of some loops. The loops appear to have nominal diameters of 100 to 300 Å.

Thus far, only these preliminary results have been obtained; however, studies will be continued. Initially, specimens will be further annealed to follow the development and growth of the dislocation loops and any possible resulting formation of networks. Sufficient annealing should completely remove the loops to yield a substructure comparable to that observed in the starting single crystals. Additionally, the larger defects will offer an opportunity to define the nature of the defects; i.e., vacancy or interstitial. Both Downey and Eyre, and Meakin and Greenfield identified their point defect clusters and prismatic loops, respectively, to be interstitial defects. The density of point defects and of defect clusters will also be determined as a function of fast neutron dose.

Although the above information will be of considerable interest, the primary objective of these substructure studies will be to obtain a better understanding of the effect of neutron damage on the mechanical properties of refractory metals and alloys. It has been demonstrated[12] that neutron damage recovery peaks in the BCC metals occur at homologous temperatures of 0.15, 0.22, 0.31, and 0.35 T_m. If these recovery peaks are accompanied by observable substructure changes, especially in the region of the 0.35 T_m recovery peak, then this would be of metallurgical interest. However, others have reported very little variation in defect concentration at temperatures below 0.37 T_m for both α-iron and molybdenum, and therefore the changes in physical and mechanical properties may be due to changes in sub-microscopic defects. The effects of such parameters as total dose, dose rate, irradiation temperature, and impurity content will also be investigated in future substructure studies.

2.2 HIGH-TEMPERATURE ALLOYS PROGRAM

Creep-rupture testing is continuing on three high-temperature alloys. These alloys include three heats of A-286[22] which contain various concentrations of natural boron and A-286 specimens which were irradiated in the shielded - unshielded capsule[23] (33MT-104A and 33MT-104B). Hastelloy X specimens were also irradiated in shielded - unshielded capsules. Creep-rupture testing was recently initiated on control specimens of Hastelloy N (INORD-8 alloy) which were obtained from the Molten Salt Reactor Experiment Project of ORNL. Hastelloy N specimens were irradiated in Capsule GEFP2-128 at reactor ambient temperatures in the ETR[24] and are presently being irradiated at a temperature of 650°C in Capsule GEFP2-139 to a fast neutron dose of approximately 1.2×10^{20} nvt.

A fourth material, A350-LF3,* which is used in pressure vessels is currently being investigated. Resistivity and hardness specimens have been fabricated from this material and will be irradiated at different depths in a mockup of a slab of similar material containing extensive dosimetry. The change in hardness and also resistivity as a function of depth will then be correlated with theoretical predictions of the number of irradiation-induced defects in the material. This correlation will also be compared with existing impact specimen data on brittle-to-ductile transition temperature changes caused by irradiation. In addition to the magnitude of the change, annealing studies will also be performed on resistivity and hardness specimens to study the kinetics of any recovery processes.

CREEP-RUPTURE PROPERTIES

Hastelloy X

Creep-rupture tests at 650°C and 732°C in constant load rupture stands were conducted on shielded (with 0.5 mm Cd) and unshielded Hastelloy X specimens from capsules

---

*Army PM-2A material.

33MT-104A and 33MT-104B. These data are presented in Table 2.11, and strain versus time curves are plotted in Figure 2.35 for a temperature of 732°C and a fixed stress of 19.69 kg/mm^2. One unshielded specimen was annealed at 732°C for 119 hours prior to the application of the load. As shown in Figure 2.35, this annealing treatment resulted in almost complete recovery of the time to rupture and also ductility of this material. The as-irradiated unshielded specimen showed factors of approximately 8 and 2.6 reduction in the elongation and time to rupture, respectively, when compared to the corresponding data of a control specimen. In comparison, the as-irradiated shielded specimen showed factors of about 2.0 and 1.4 reduction in elongation and time to rupture, respectively. Unlike the results of the irradiated precipitation hardening alloys (A-286 and Rene' 41), the annealing treatment tends to restore the ductility and rupture life of Hastelloy X.

TABLE 2.11

STRESS-RUPTURE TEST RESULTS
OF SHIELDED - UNSHIELDED HASTELLOY X SPECIMENS[a]

Specimen	Test Temperature, °C	Stress, kg/mm^2	Rupture Time, hr	Elongation, % in 3.8-cm gage length	Reduction In Area, %
Control					
34 HCS	650	31.6	99.8	26.5	20.8
35 HCS	650	24.6	509.1	23.3	47.8
134 HS	732	19.7	42.1	40.8	59.1
Unshielded[b]					
25 HCS	650	28.1	136.8	17.1	28.9
123 HS	650	24.6	215.4	9.0	28.2
125 HS	650	31.6	44.2	8.2	27.8
130 HS	732	15.5	123.8	10.6	36.2
135 HS	732	19.7	15.7	5.3	20.1
136 HS[c]	732	19.7	38.4	29.9	34.6
Shielded[d]					
39 HCS	650	28.1	88.9	14.7	25.9
40 HCS	650	31.6	65.1	19.5	28.0
41 HCS	650	24.6	329.9	20.5	26.8
122 HS	732	24.6	5.2	11.0	16.8
128 HS	732	19.7	30.3	19.9	30.2
137 HS	732	15.5	85.6	5.3	18.4

[a] Smooth bar specimens from heat E-9500 which were heat-treated at 1175°C for 1 hour and then rapidly cooled in air.

[b] Irradiated in capsule 33MT-104A; 3.6 x 10^{19} nvt ($E_n \geq 1$ Mev), 11.0 x 10^{19} nvt, thermal.

[c] Post-irradiation annealed at 732°C in air for 119 hours.

[d] Irradiated in capsule 33MT-104B shielded with 0.5-mm cadmium-coated steel jacket; 3.5 x 10^{19} nvt ($E_n \geq 1$ Mev), 2.3 x 10^{19} nvt, thermal.

A-286

Preliminary creep-rupture results for A-286 specimens containing various concentrations of natural boron were reported previously.[25,26] Testing has now been resumed on these specimens.

Creep-rupture test results of A-286 specimens irradiated in the same shielded - unshielded capsules as the Hastelloy X specimens are listed in Table 2.12, and stress versus time-to-rupture curves are plotted in Figures 2.36 and 2.37. There was a factor of about 5.8 reduction in the rupture life (Figure 2.36) of the unshielded specimen compared to the shielded specimens when tested at a temperature of 650°C and a stress of

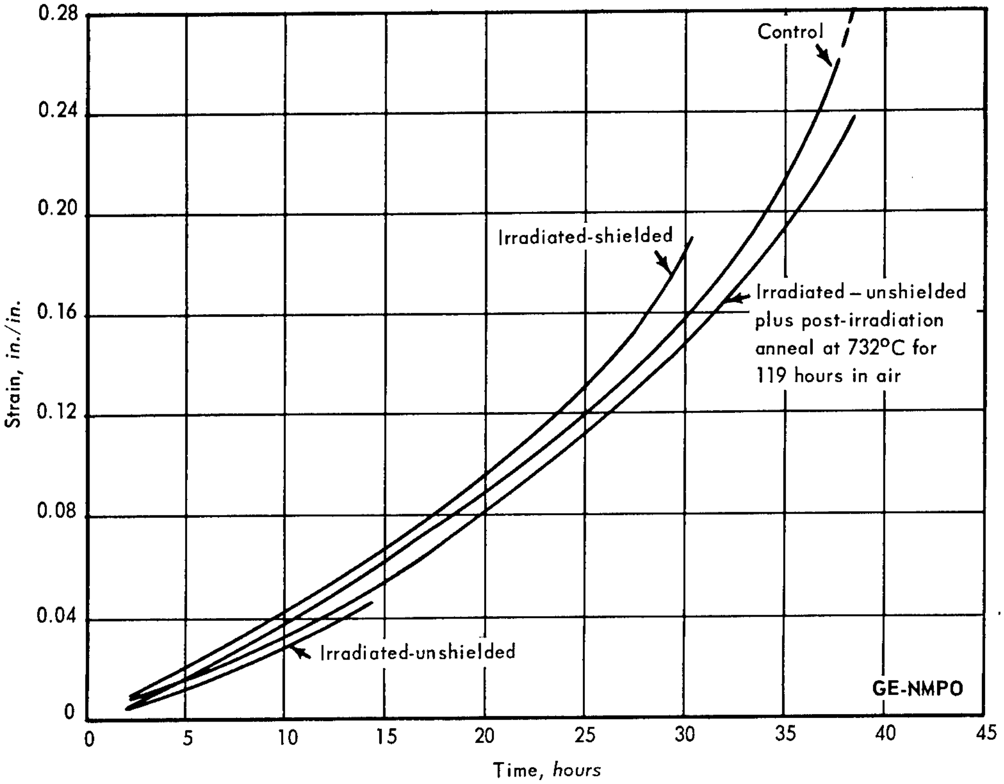

Fig. 2.35 – Strain versus time for Hastelloy X specimens tested at 19.69 kg/mm^2 and 732°C

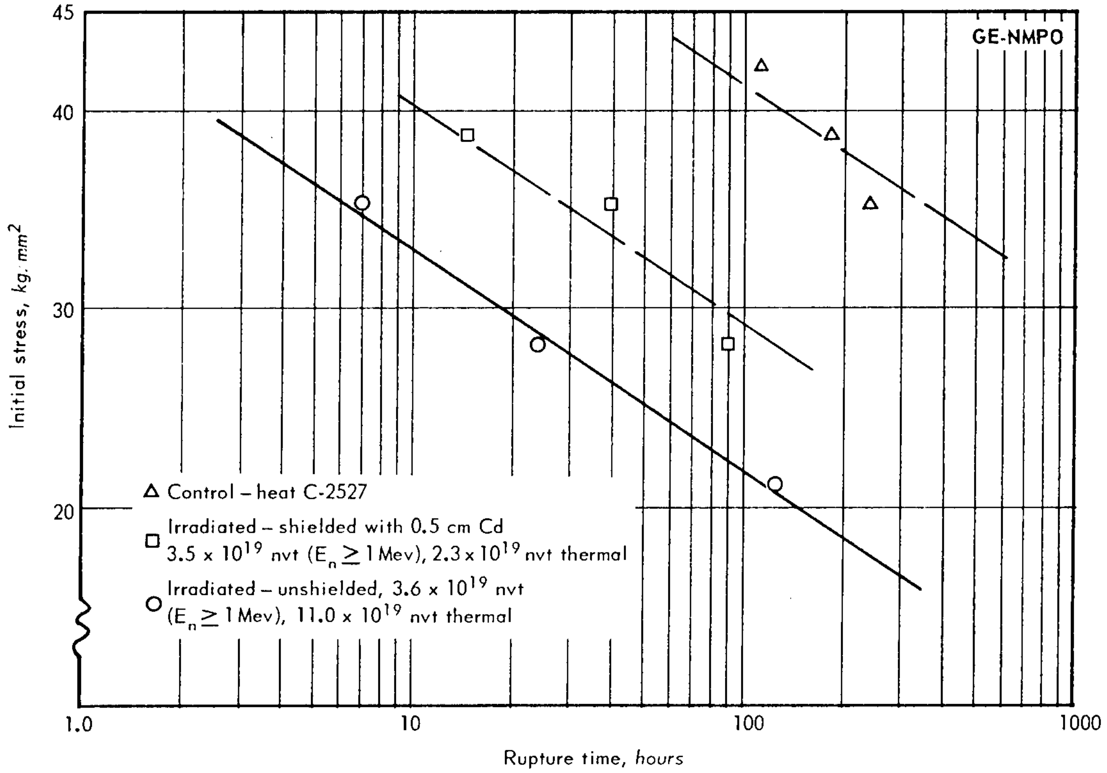

Fig. 2.36 – Stress-rupture strength of A-286 specimens at 650°C (shielded – unshielded experiment)

TABLE 2.12

STRESS-RUPTURE TEST RESULTS
OF SHIELDED - UNSHIELDED A-286 SPECIMENS[a]

Specimen	Test Temperature, °C	Stress, kg/mm^2	Rupture Time, hr	Elongation % in 3.8-cm gage length	Reduction In Area, %
Control					
36 ACS	650	38.7	181.2	13.5	20.1
185 ACS	650	35.2	237.5	13.6	17.1
191 AS	650	42.2	111.7	11.9	14.2
192 AS	732	24.6	36.3	33.0	60.8
194 AS	732	17.7	211.3	37.5	44.4
Unshielded[b]					
186 AS	650	35.2	6.8	1.1	6.44
187 AS	650	28.1	23.8	2.8	11.6
188 AS	650	21.1	125.6	1.4	11.2
189 AS	732	12.7	38.5	2.3	4.49
190 AS	732	18.3	4.0	0.4	5.41
193 AS[c]	732	18.3	4.7	6.3	29.7
Shielded[d]					
28 ANS	650	35.2	39.5	1.2	5.20
29 ACS	650	38.7	14.5	1.2	3.99
33 ACS	650	28.1	89.8	3.2	2.79
34 ACS	732	21.1	3.1	-	12.2
183 AS	732	18.3	6.8	0.7	-
184 AS	732	12.7	50.7	1.3	11.6

[a] Smooth bar specimens from heat C-2527 heat-treated as follows:
900°C - 2 hours - water cooled
720°C - 16 hours - air cooled
650°C - 16 hours - air cooled

[b] Irradiated in capsule 33MT-104A; 3.6 x 10^{19} nvt ($E_n \geq 1$ Mev), 11.0 x 10^{19} nvt, thermal.

[c] Post-irradiation annealed in air at 732°C for 9.1 hours.

[d] Irradiated in capsule 33MT-104B shielded with a 0.5-mm cadmium-coated steel jacket; 3.5 x 10^{19} nvt ($E_n \geq 1$ Mev), 2.3 x 10^{19} nvt, thermal.

35.2 kg/mm^2. The rupture life of the unshielded specimen is a factor of 35 less than the control specimen at the same test conditions.

The ductility, as noted from elongation and reduction in area in Table 2.12, of the irradiated specimens was considerably lower than that of the control specimens. The percent elongation at 650°C has changed from a range of 13.6 to 11.9 percent for the control specimens to a range of 3.2 to 1.1 percent for irradiated specimens. Reduction in area likewise has changed from a range of 20.1 to 14.2 percent for control specimens to a range of 11.6 to 2.8 percent for irradiated specimens. There appears to be no significant difference between the ductility of shielded and unshielded specimens when tested at 650°C.

The reduction in rupture life for unshielded specimens tested at 732°C (Figure 2.37) was not much different from the unshielded specimens tested at 650°C. There was a factor of about 34 reduction in rupture life of the unshielded specimen compared to the control specimen; from shielded to unshielded specimen, the reduction was a factor of about 1.4. The change in ductility due to irradiation was more pronounced in specimens tested at 732°C.

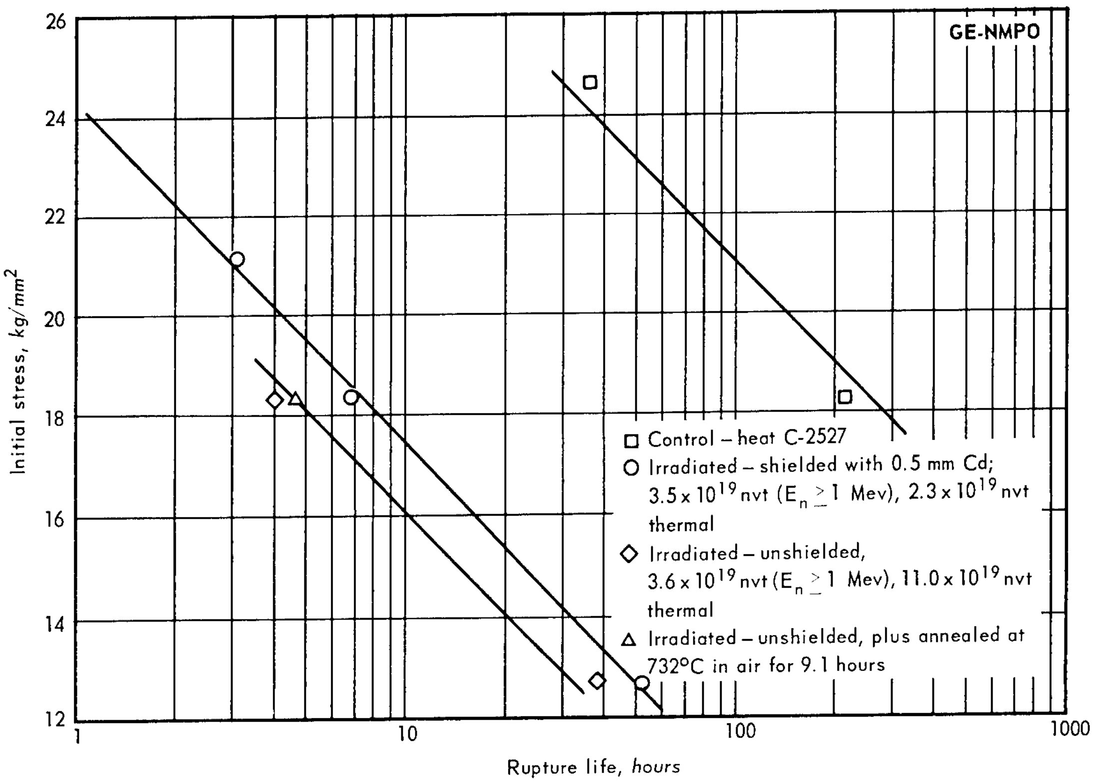

Fig. 2.37 – Stress-rupture strength of A-286 shielded and unshielded specimens tested at 732°C

One of the unshielded specimens tested at a stress of 18.3 kg/mm^2 was annealed for 9 hours in air at 732°C before applying the load and testing at 732°C. The rupture life changed from 4.0 hours on the unannealed specimen to 4.7 hours on the annealed specimen, which is not considered to be significant. There was, however, some return of the ductility indices: reduction of area increased from 5.4 to 29.7 percent, and elongation increased from 0.4 to 6.3 percent.

BORON SEGREGATION TO GRAIN BOUNDARIES

Based on the results obtained from (1) the shielded - unshielded experiments, (2) the boron experiments, and (3) the threshold of radiation-induced changes in the creep-rupture properties of high-temperature alloys, it is apparent that a concentration of some high neutron cross section element in a critical location within the alloy[27] is responsible for the reduction in the elevated-temperature ductility. Boron was found to influence the ductility of many high-temperature precipitation hardening alloys as a result of segregation within the grain boundaries relative to that within the grains, and coupled to the high thermal neutron cross section for the (n, α) reaction, may be responsible for the elevated-temperature embrittlement and loss in rupture strength when these alloys are irradiated.

Calculations by Myers[28] showed that boron (n, α) reactions contribute about 4.5 percent of the displaced atoms caused by fast neutron collisions in an iron-base alloy containing 0.003 weight percent natural boron, assuming the thermal neutron flux (ϕ_{th}) is equivalent to the fast neutron flux (ϕ_f).

The approximate fraction (D_B) of the total displaced atoms due to the boron (n, α) reaction in an iron (or equivalent) matrix containing 0.003 weight percent natural boron is given by equation (2.6):

$$D_B \approx 4.5 \times 10^{-2}\ \phi_{th}/\phi_f \qquad (2.6)$$

In considering a similar calculation of boron segregation at the grain boundaries, the following reasoning is used. A 0.003 weight percent natural boron concentration in an iron-base alloy results in an atomic percent of about 0.016 if the concentration is assumed to be uniformly distributed throughout the grains, and also is not involved in various precipitates. In view of the strong indirect evidence for equilibrium segregation of boron (and carbon) to the region of the grain boundaries, it is possible that the concentration in these regions may be 2 or 3 orders of magnitude higher than that within the grains. Based on these grain-boundary concentrations, the number of atom displacements in the region of the grain boundaries, due to the $B^{10}(n, \alpha)Li^7$ reaction, could also be 2 to 3 orders of magnitude higher than those calculated by Myers for equivalent fast and thermal neutron dosages.

To estimate the fraction of atoms (D_{BGB}) which is displaced in the region of grain boundaries, due to the boron (n, α) reaction, relative to those which are displaced as a result of the fast neutron collisions, equation (2.6) may be modified as the relationship of equation (2.7):

$$D_{BGB} \approx 4.5 \times 10^{-2}\ (\phi_{th}/\phi_f)\ F_{GB}F_B \qquad (2.7)$$

where F_{GB} is the grain boundary boron concentration and F_B is a correction factor which is unity when the reported boron concentration in the alloys is 0.003 weight percent. The correction factor (F_B) is equal to $N_B/0.003$ or $N_B/0.016$ with N_B being the concentration (weight percent and atom percent, respectively) of boron generally listed in the chemical analysis of the respective alloy.

Theoretical calculations[29] of the concentration of boron in the grain boundaries of an iron-base alloy may be obtained by using equation (2.8):[30]

$$n_2^b = \frac{n_2 \exp (Q/RT)}{(1 - n_2) + n_2 \exp (Q/RT)} \qquad (2.8)$$

where n_2 is the atom fraction of boron in the material and n_2^b is the atom fraction of boron in the grain boundary. Values of n_2^b are plotted as a function of n_2 for various temperatures in Figure 2.38. With an activation energy of Q = 13.2 kcal/mole and a temperature of 650°C, equation (2.8) yields a value of $n_2^b = 0.16$. The boundary, therefore, contains 16 atomic percent boron or a factor of about 1400 greater than that in the grain. At this temperature (650°C), however, the mobility of boron may not be high enough to cause significant segregation. If the temperature at which the material is heat treated (900°C) is used, equation (2.8) gives a value of $n_2^b = 0.042$ or 4.2 atomic percent. At this temperature, the grain-boundary concentration would be about a factor of 360 greater than that within the grains. For the case of the exposures used in the shielded - unshielded experiments, the number of displaced atoms in the region of the grain boundaries is about 65 times higher for the unshielded specimens as a result of the boron (n, α) reaction than that due to collisions of fast neutrons with iron or equivalent mass elements.

HYDROGEN AND HELIUM ATOM PRODUCTION THROUGH (n, p) AND (n, α) REACTIONS

Since the neutron flux of most of the reactor test facilities used for irradiation damage studies has a predominant thermal neutron component, the application of test data obtained in these environments to reactor component designs for reactor systems in which the neutron spectrum consists primarily of fast neutrons must be considered with extreme caution. For instance, the presence of hydrogen[31] (proton) or helium[32] (α-particle)

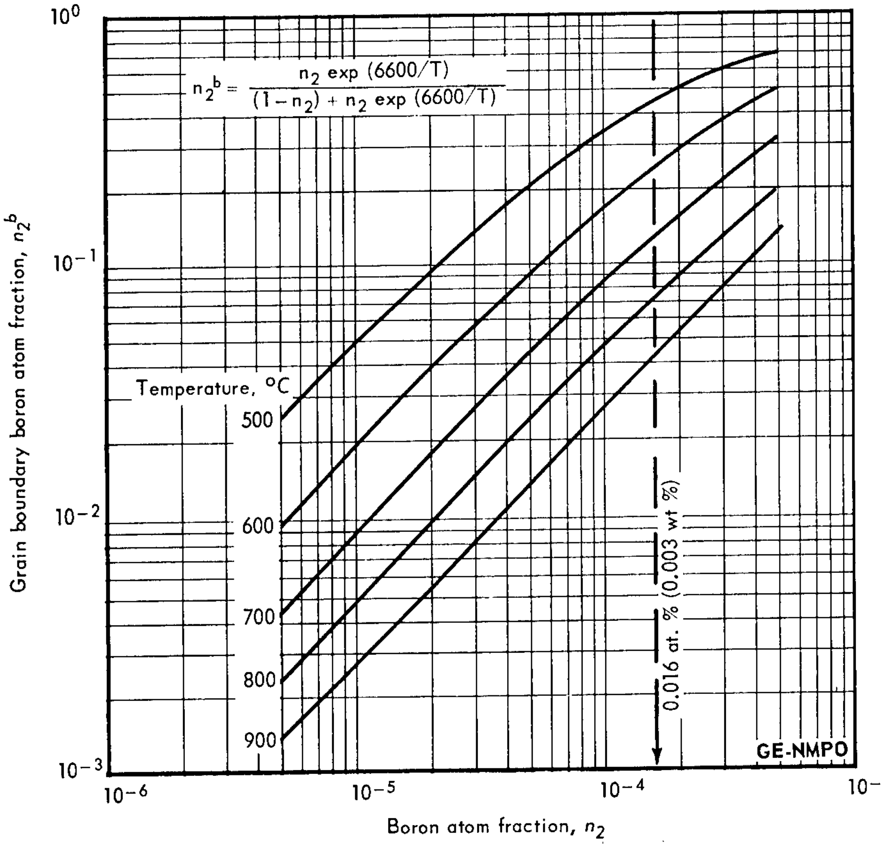

Fig. 2.38 – Grain boundary boron atom fraction as a function of matrix boron atom fraction for various temperatures

atoms can affect the mechanical properties of metals significantly and their rates of formation are greatly dependent on the neutron spectrum and the flux level in addition to the presence of elements with large neutron cross sections for the (n, p) or (n, α) reactions.

About 50 percent of the total neutrons in a typical ETR core spectrum lie at an energy below 25 kev; however, about 81 percent of the $B^{10}(n, \alpha)Li^7$ reactions will be the result of captures for those neutrons (13%) which lie below 0.4 ev, generally assumed to be the thermal neutron or sub-cadmium component of the spectrum. The number of helium atoms produced as a result of the $B^{10}(n, \alpha)Li^7$ reaction for those neutron energies above 1 Mev are within a factor of 2 for the case of a water-moderated core spectrum (ETR, MTR, ORR) and the watt fission spectrum and represent a small fraction (2×10^{-4}) of the total helium atoms produced over the entire neutron energy range of the water-moderated spectrum.

Unlike the thermal neutron capture cross sections which show an $E^{-1/2}$ energy dependence (reciprocal velocity), such as those for $B^{10}(n, \alpha)Li^7$ and $Li^6(n, \alpha)H^3$, and possibly $N^{14}(n, p)C^{14}$, there is another family of cross sections in which some threshold neutron energy is required before the (n, p) or (n, α) reaction may take place. Most of these reactions occur when the neutron energy exceeds about 1 Mev. It is possible, therefore, that hydrogen and helium atoms may be produced as a result of fast neutron interactions with Fe, Ni, Ti, Cr, Al, N_2, Si, or essentially all the elements found in structural material. For instance, the $Ni^{58}(n, p)Co^{58}$ cross section yielding hydrogen atoms when averaged over a fission spectrum is relatively high compared to many of the other elements and will be the key contributor of hydrogen in the nickel-base alloys. The

$Fe^{56}(n, p)Mn^{56}$ and $Fe^{56}(n, \alpha)Cr^{53}$ reactions will contribute significantly to the hydrogen and the helium production, respectively, in the iron-base alloys.

Nitrogen appears to have a fairly large (n, α) fast neutron cross section. Calculations indicate that approximately 0.06 atomic percent present in Hastelloy X will contribute more helium atoms (~15%) than any other constituent in this alloy with the exception of the nickel (~56%) in a fast-spectrum reactor. The chromium and iron present in about 40 weight percent of this alloy each account for less than 13 percent of the helium atoms produced. Five ppm natural boron accounts for about 2 percent of the helium atoms which are produced for the case of a fast neutron spectrum. With the exception of the boron (n, α) reaction, the helium and the hydrogen production rates will generally be within a factor of 2 for most reactor spectra when normalized to unit flux for those neutrons above 1 Mev.

The resulting helium and hydrogen production in an iron-base (A-286) and a nickel-base (Hastelloy X) alloy as a function of fast neutron dose ($E_n \geq 1$ Mev) is presented in Figure 2.39. Reactions due to low-energy neutrons should be included in the total helium production especially if boron concentrations in the alloy are high. A large fraction of the hydrogen atoms are produced through the $Ni^{58}(n, p)Co^{58}$ reaction in both alloys. The base metals contributed more helium atoms from their respective (n, α) reactions than any other constituent. For instance, nickel in Hastelloy X yielded about 56 percent and iron in the A-286 alloy yielded about 35 percent of the total helium concentration. Since many of the threshold reaction cross sections are not yet well known and the high-energy neutron spectrum and the chemical composition of these alloys may vary by factors of 2 to 3, the data presented in Figure 2.39 should, therefore, be considered only as values which are valid to within a factor of 5.

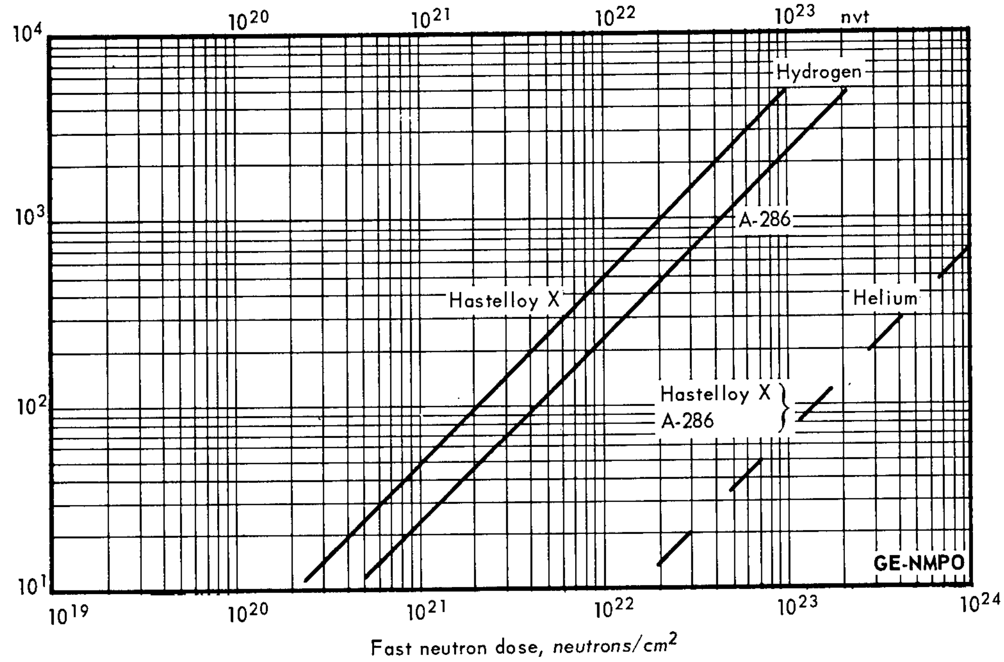

Fig. 2.39 – Production of hydrogen and helium atoms in Hastelloy X and A-286 alloys as a function of fast neutron dose

Figure 2.40 shows the production of helium atoms in the two alloys as a function of thermal neutron dose. These calculations are based on the $B^{10}(n, \alpha)Li^7$ reaction and reflect the higher concentration of natural boron in the A-286 alloy (250 ppm) compared to that in the Hastelloy X alloy (25 ppm). The data shown in Figures 2.39 and 2.40 indicate that the helium atom production as a result of fast neutron threshold reactions will

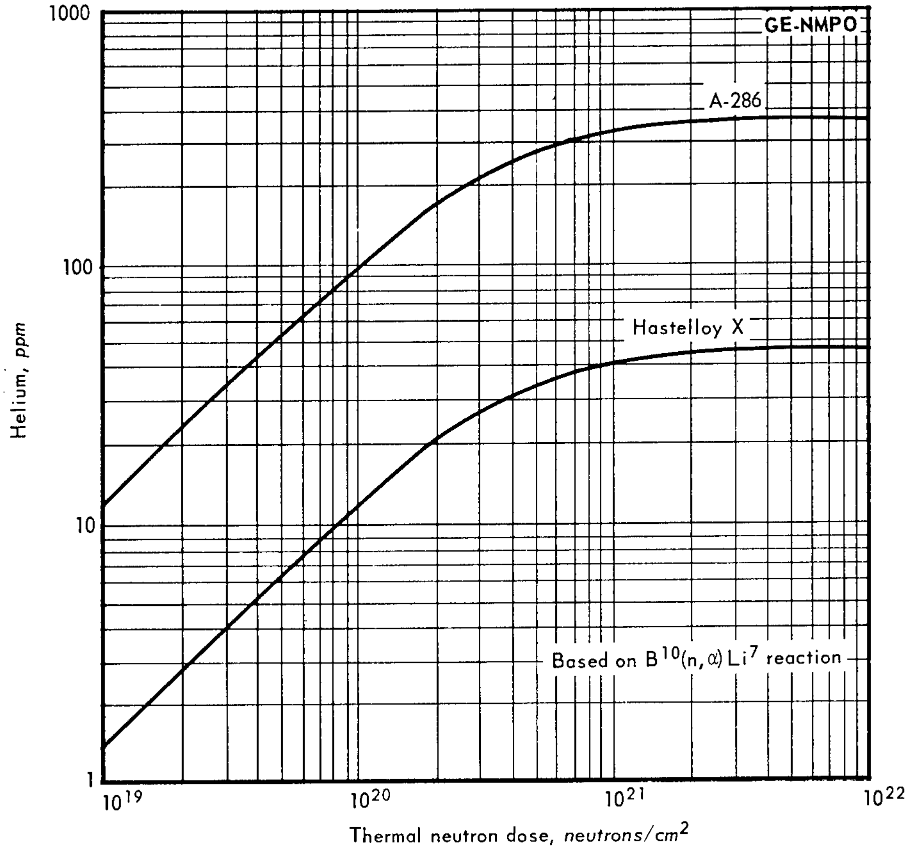

Fig. 2.40 – Production of helium atoms in Hastelloy X and A-286 alloys as a function of thermal neutron dose

be greater than that due to the $B^{10}(n, \alpha)Li^7$ reaction when the ratio of fast to thermal flux is greater than 200.

As a result of the possible influence of neutron spectrum in the production of helium (and hydrogen) and the resulting effects on the mechanical properties, such as the elevated-temperature embrittlement observed in many metals, a direct application of irradiation effects data obtained in water-moderated neutron spectra should not be made without proper corrections to the design considerations of components to be used in a predominantly fast neutron spectrum environment.

2.3 FUNDAMENTAL STUDIES

Interactions among three imperfection distributions largely determine the mechanical property irradiation effects observed in neutron-irradiated metals and alloys. These fundamental distributions are (1) the dislocation arrangement, (2) the spatial distribution of impurity atoms, and (3) the primary damage state. As is well-known, any crystalline solid specimen contains dislocations and impurity atoms; even a perfectly pure specimen contains transmutation-produced impurity atoms after neutron irradiation. The primary damage state is the spatial distribution of vacancy and interstitial defects produced directly during irradiation at absolute zero temperature where any defect re-arrangement is caused purely by strain energy relaxation, not by diffusion.

The dislocation arrangement and impurity distribution are, in general, changed by irradiation. Also, the damage state existing after irradiation is, in general, different from the primary damage state. These changes are the consequence of interactions among the three fundamental distributions during irradiation. The extent of these changes, for a given specimen composition, depends primarily upon the irradiation temperature, the neutron energy spectrum, the dose rate, and the total integrated dose. In principle, these changes should occur even for irradiation at absolute zero temperature as a result of interactions among the strain fields of dislocations, impurity atoms, vacancies, and interstitials. In any event, the fundamental defect distribution for estimating the contribution of vacancies and interstitials to irradiation effects at either absolute zero or a finite temperature is the primary damage state. This follows from the observation[12] that an isothermal annealing curve obtained by starting at a temperature T_2 runs smoothly into one started at any lower temperature $T_1 < T_2$.

The primary damage state and the distribution of transmutation-produced impurities appear to describe the fundamental changes produced in a crystalline solid by neutron irradiation. A detailed knowledge of these two distributions is an essential part of the foundation for a theory of irradiation effects. The computational work described here is concerned with a theoretical description of the primary damage state, and prediction of the damage state for irradiation at a finite temperature from the primary damage state and impurity atom distribution. This work was performed for pure α-iron using the high-speed computer experiment technique. By definition, this technique consists of simulating physical processes on a computer.[33] In the present study the processes simulated were neutron collision chains and atomic collision cascades.

An account is given of computer experiment work on (1) the need for absolute damage calculations, (2) defect deployment in a displacement spike, (3) displacement and defect cluster production functions, (4) defect cluster production per unit neutron exposure, (5) pressure shell embrittlement, (6) the saturated damage state, and (7) the annealing of irradiation-produced interstitials in α-iron.

NEED AND METHOD FOR ABSOLUTE DAMAGE CALCULATIONS

Experimental evidence strongly suggests that the effect of irradiation on mechanical properties is determined primarily by the distribution and structure of imperfections at the level of atomic dimensions. This circumstance requires that damage computations must give an absolute description of the defect spatial distribution at this dimensional level if they are to be of service in the interpretation of experimental data. In this regard, Eyre[34] has obtained transmission electron microscope photomicrographs which show localized dislocation bending at invisible imperfection structures in iron. These obstructions are directly tied to irradiation because their density increases with neutron exposure. The localized dislocation bending indicates that the obstructions are not randomly distributed point defects. If this were the case, the bends would be both more frequent and more gentle. The fact that the obstructions are invisible shows that they are not defect aggregates formed via point defect diffusion because such aggregates (about 100 Å in diameter) are easily resolved in the electron microscope. Harries et al.[35] find that neutron irradiation-induced changes in both the lower yield point and ductile - brittle transition temperature of ferritic steels correlate better with the displacement spike density than with the total number of displacements. Finally, GE-NMPO data* indicate that neutron irradiation increases the creep resistance of tungsten but does not change its ductility. These observations cannot be explained on the basis of a simple, total displacement theory of radiation effects which ignores the influence of the way imperfections are deployed within the irradiated specimen. An effort was made, therefore, to compute an absolute description of the damage distribution in body-centered cubic (BCC) metals, in the face of strong evidence that this type of theoretical description is required to explain the complex behaviors observed. The only practicable computational technique available for accomplishing this end is the computer experiment.[33]

*See Figures 2.1 through 2.14.

In the case of metals, neutron irradiation damage production can be separated into two independent stages,[36, 37] provided the neutron exposure is sufficiently low that the damage state remains unsaturated as schematically illustrated in Figure 2.41. Stage I consists of primary knock-on atom (PKA) displacements by neutrons. Stage II consists of displacement spike production by PKA. A schematic magnified view of the branching sequence of successive knock-on atom collisions in a PKA-initiated collision cascade appears in Figure 2.41 for PKA No. 2. The collection of isolated vacancies, isolated interstitials, vacancy clusters, and interstitial clusters produced directly during the evolution of a collision cascade is a displacement spike[36] in α-iron. The relative displacement spike size in Figure 2.41 is greatly exaggerated. In reality, the mean distance between neutron collisions which produce PKA is at least six orders of magnitude greater than the diameter of a displacement spike. A collision cascade in α-iron, as given by computer experiments, is shown in Figure 2.42. The irregular exterior shape of a displacement spike is illustrated by Figure 2.43.

A Monte Carlo calculation[38] was used to simulate PKA production in Stage I. The factors appearing in Table 2.13 were considered in this simulation. This calculation gives the PKA yield density per unit exposure, y, and the PKA differential energy spectrum, f(E), as a function of position in an irradiated specimen. The PKA yield density is the number of PKA produced per cm^3 given one incident neutron per cm^2 of specimen surface, and f(E)dE is the fraction of all PKA produced with energies in the interval dE at E. Stage II calculations were performed by simulating the evolution of about 100 complete collision cascades at each of a set of PKA energies ranging from 0.5 to 20 kev. All PKA were started from normal lattice sites and all knock-on atom collision trajectories were traced out in the BCC atomic array of α-iron. This was done using the CASCADE program.[39] The factors which should be considered in a collision cascade simulation are listed in Table 2.14. Unfortunately, there is no well-developed theory for treating individual inelastic atomic collisions in solids. Hence, CASCADE was not used to describe collision cascades initiated by PKA with energies above 20 kev, the important range for inelastic atomic collisions in iron. The Erginsoy-Vineyard[40] interatomic potential for α-iron was used in all CASCADE calculations discussed here.

DEFECT DEPLOYMENT IN A DISPLACEMENT SPIKE

The displacement spike shapes given by the CASCADE calculations were highly irregular. Although it is not possible to give an example of a typical shape, the general impression given by the drawing of a 15-kev spike in Figure 2.43 corresponds to that for the most frequently encountered shape. Each sheet in the figure represents the extent of the region containing vacancies and interstitials in four successive (002) atom planes as it appears when projected onto a (001) plane. Above 5 kev, the average displacement density inside a spike was 2.3 atomic percent. This density, therefore, constitutes the upper limit on the displacement density for an unsaturated damage state produced at 0°K. The internal structure of a spike was like that of Swiss cheese, with the hole structure in the cheese corresponding to undamaged material. It is within this multi-ply connected damaged volume that the displacement concentration was 2.3 atomic percent. If the entire volume inside the smallest simple surface which would enclose the spike were considered, the average displacement density would be about half that in the multiple-connected volume. Hence, the defect density pertinent to a consideration of the peripheral overlap of spikes is 1.2 atomic percent and that pertinent to estimating the upper bound on the concentration in the saturated state is 2.3 atomic percent.

Defect deployment in the center sheet (four successive atom planes) from a 5-kev spike appears in Figure 2.44. This particular spike was chosen because its damage pattern illustrates the principal defect distribution idiosyncrasies connected with irradiation hardening, at the level of atomic dimensions. The open squares represent vacancies and the

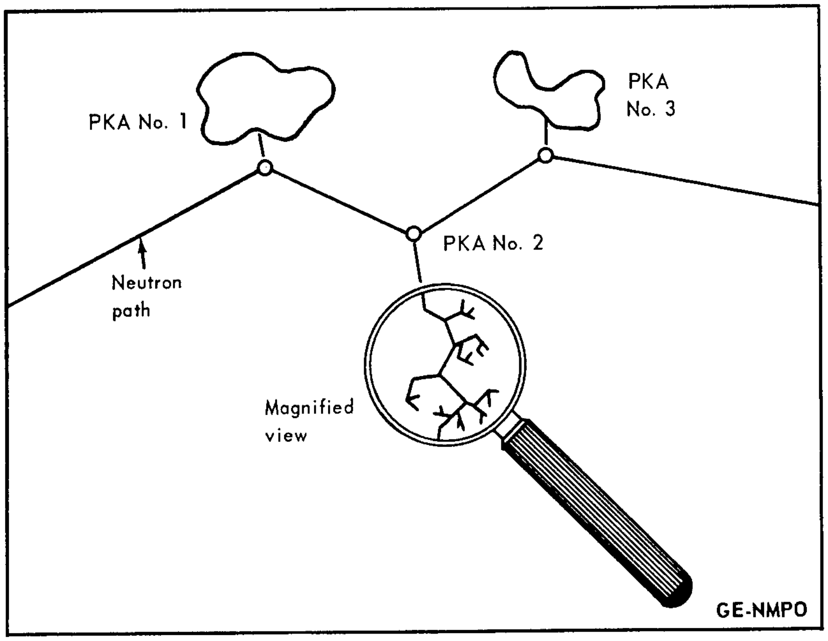

Fig. 2.41 – Neutron irradiation damage production in a metal. Stage I: Incident neutron (solid line) displaces several primary knock-on (PKA) atoms. Stage II: Each PKA independently produces a displacement spike. Magnified view of PKA No. 2 schematically represents collision cascade trajectories leading to displacement spike.

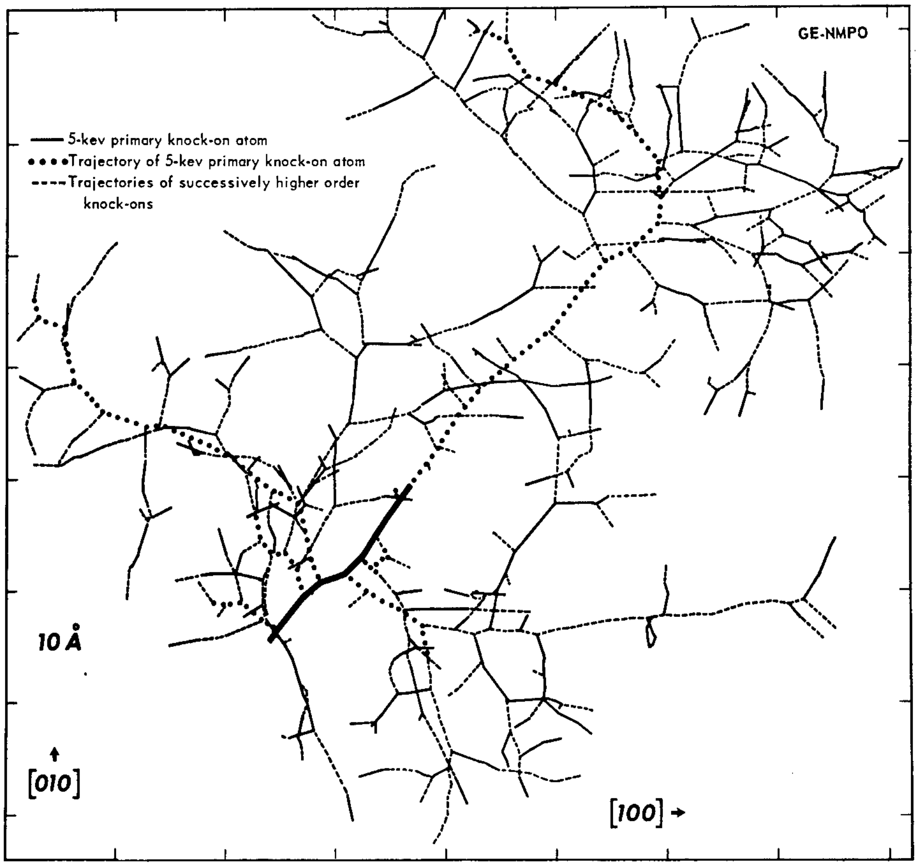

Fig. 2.42 – Projection of all knock-on atom trajectories in a collision cascade initiated by a 5-kev atom

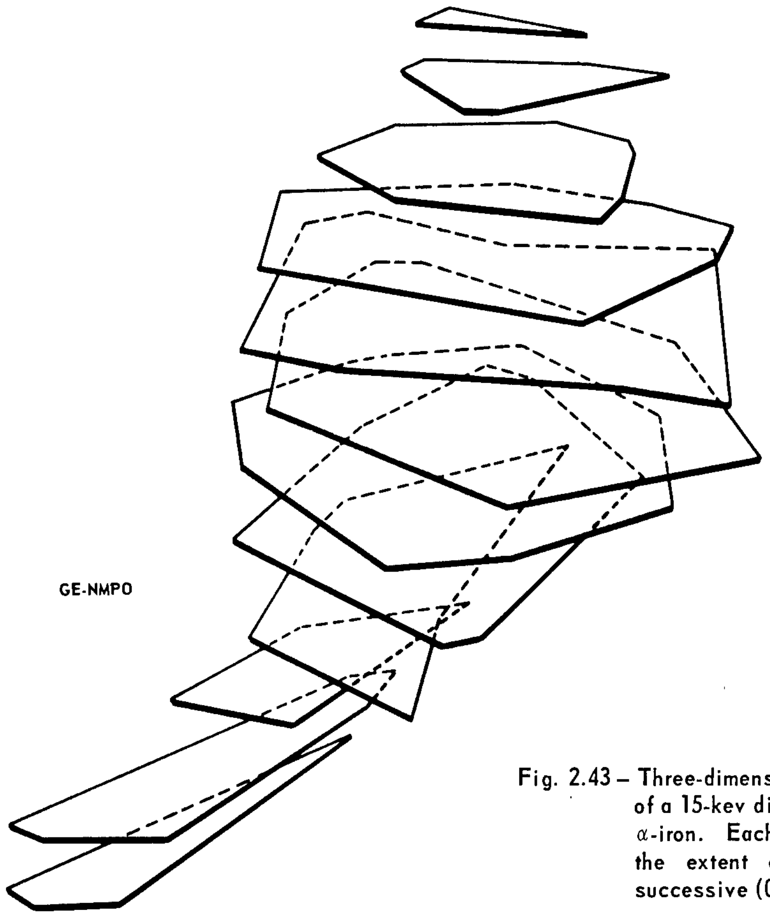

Fig. 2.43 – Three-dimensional representation of a 15-kev displacement spike in α-iron. Each sheet represents the extent of damage in four successive (002) planes.

TABLE 2.13

FACTORS CONSIDERED IN COMPUTING PKA PRODUCTION IN α-IRON USING THE MONTE CARLO PROGRAM

1. Incident neutron energy spectrum.
2. Incident neutron angular distribution.
3. Neutron elastic scattering anisotropy as a function of neutron energy.
4. Neutron inelastic scattering as a function of neutron energy.
5. Effect of finite specimen size on the length of the neutron collision chain and the energy spectrum of colliding neutrons.

TABLE 2.14

FACTORS CONSIDERED IN ATOMIC COLLISION CASCADE SIMULATION IN α-IRON USING THE CASCADE PROGRAM

1. Crystal structure and damage state dependent displacement criterion.
2. Erginsoy - Vineyard instability region for vacancy - interstitial pairs.
3. Channeling.
4. Focused collision chains along close-packed directions.
5. Radiation annealing.

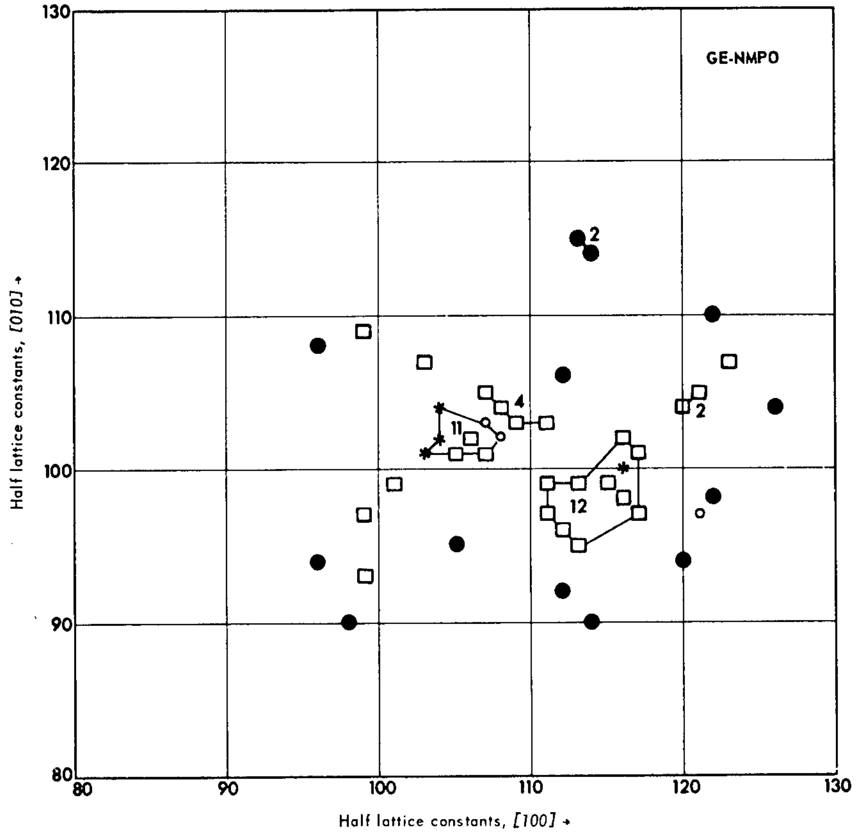

Fig. 2.44 – A sheet from the center of a 5-kev spike in α-iron which contained large clusters

filled circles represent interstitials. The numbers beside a cluster denote number of defects it contains. An asterisk denotes a defect contained in a cluster but lying in a plane below the four concerned in the figure. Similarly, a small open circle denotes a defect lying in a plane above those concerned in the figure.

Perhaps the most salient feature of this damage pattern is the non-uniform character of the defect deployment. This indicates that an annealing calculation should not be based on a uniform defect distribution in the case of neutron irradiation. As shown later, the true annealing rate is much faster than that predicted by an initially uniform defect-distribution annealing calculation. In particular, a high degree of vacancy - interstitial segregation exists. Note that vacancies tend to be positioned in the interior and interstitials at the periphery of the damaged region. In this particular instance, 26 vacancies, but only 13 interstitials, appear in the damage pattern. This disparity in the populations of the two defect types is a general characteristic of displacement spikes in iron. Sheets from the center of a spike usually contained from 1.5 to 2.5 times as many vacancies as interstitials. This imbalance in the populations of the two defect types goes in the opposite direction at the ends of a spike. The segregation of vacancies and interstitials, both in directions parallel and normal to the spike axis, and the corresponding local imbalance in the two defect populations suggest that at least two large interstitial clusters centered about a single large vacancy cluster might be formed per spike at temperatures sufficiently high for vacancy migration but not high enough to induce cluster dissociation.

A sheet from the center of a 5-kev spike which contained only small vacancy clusters is shown in Figure 2.45. This figure illustrates that the number of vacancies exceeds the

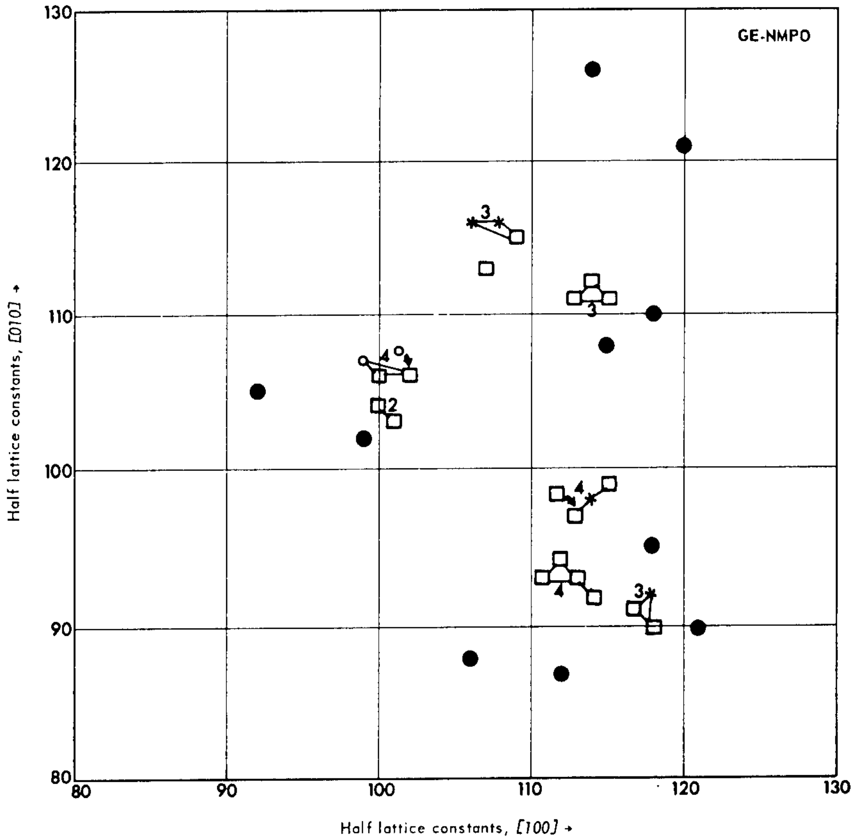

Fig. 2.45 – A sheet from the center of a 5-kev spike in α-iron which contained no large clusters

number of interstitials at the center of a spike even when large clusters (10 or more vacancies) are absent. Interstitial clusters were rare. The largest interstitial cluster observed contained only three defects.

DISPLACEMENT AND DEFECT CLUSTER PRODUCTION FUNCTIONS

As illustrated by Figures 2.44 and 2.45, a significant fraction of the vacancies produced in the primary damage state simulations were contained in defect clusters of various sizes. One source of radiation hardening is thought to be connected with the size, structure, and scale of dispersion of these defect clusters. Current opinion is that they induce hardening by impeding dislocation generation and/or movement.[41] In this regard the association of the vacancies and self interstitials, produced by irradiation, with impurity atoms to form defect - impurity complexes also appears to be important.[42] The impurities concerned may be either those initially present before irradiation or those produced by transmutation reactions during irradiation.[26,43,*]

An elastic collision displacement function and defect cluster production functions were evaluated for α-iron from the cascade simulation results. Each of these functions implicitly describes the known effects of crystal structure on the displacement of atoms in an elastic collision cascade. Until recently, radiation damage production calculations were performed by first computing the number of displacements which would be produced at 0°K in a random (structureless) solid if all atomic collisions were elastic.[44] This result would then be amended to approximate the required corrections given in Figure 2.46.

---

[*] See Figures 2.39 and 2.40.

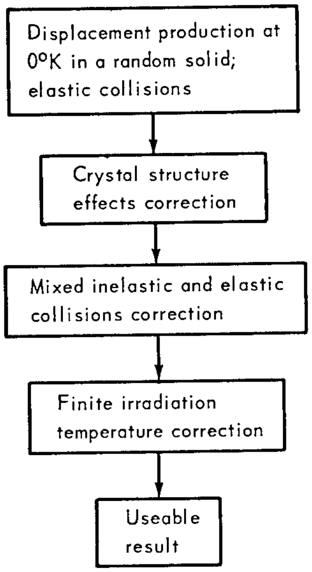

Fig. 2.46 – Corrections required to obtain a useable result from the random solid-elastic collision model for displacement production by PKA

Because the defect distribution at 0^oK is not given by this method, the effect of temperature upon the damage state cannot be estimated within the scope of this approach. Progress has been made recently at the AERE (Harwell) and GE-NMPO toward the establishment of a computational model which simultaneously accounts for the effects cited in Figure 2.46. Thompson and Wright,[45] at the AERE, have treated the effect of mixed elastic and inelastic collisions in a structureless solid. Their work pertained to graphite. The GE-NMPO calculations described here treat crystal structure effects in elastic collision cascades.

In this discussion, the number of displacements produced in a collision cascade initiated by a PKA with energy E will be denoted by $\nu(E)$. The number of displacements associated with the production of a PKA, by a neutron collision, with energy E will be denoted by g(E). The quantities $\nu(E)$ and g(E) are related as given in equation (2.9).

$$g(E) = 1 + \nu(E) \tag{2.9}$$

The unit summand in equation (2.9) represents the displacement of the PKA by the primary radiation. In turn, $\nu(E)$ is given by equation (2.10).

$$\nu(E) = K(E)E \tag{2.10}$$

The term, K(E), is called the displacement efficiency because it gives the average number of displacements per unit initial PKA energy. Perhaps the most often used displacement function of the random solid, elastic collision type is that of Kinchin and Pease.[46] In the energy range concerned here (above 0.1 kev), the Kinchin-Pease displacement efficiency, K_{kp}, is expressed in equation (2.11).

$$K_{kp} = \frac{1}{2E_d} \tag{2.11}$$

where E_d is the threshold energy for an atomic displacement. The energy, E_d, is taken to be about 25 ev for iron. Inelastic collision effects are roughly approximated in this model by assuming that all collisions are elastic below an energy E^* and that only elastic collisions produce displacements. In the case of iron, E^* is about 56 kev.[47]

The displacement efficiency for α-iron given by elastic collision cascade simulations is given by equation (2.12) and plotted in Figure 2.47.

$$K(E) = 12.33\ (1 - 0.04109 \log_e E) \qquad 0.5 \leq E \leq 20 \text{ kev} \qquad (2.12)$$

Note that K(E) decreases with PKA energy. The constant value of K_{kp}, for $E_d = 25$ ev, is 20 displacements per kev. At least two crystal structure effects cause K(E) for a collision cascade in a BCC array of atoms to be different from K_{kp} for a random solid. One of these effects is channeling.[48] A channeled atom follows a trajectory confined within the open tunnel-like cores which run parallel to the principal crystallographic directions in any crystal. The other, and apparently most important, structure effect is the ease of vacancy - interstitial recombination along <111> lines of atoms. This type of effect was first defined by Gibson, et al.,[49] for <110> lines in copper and then by Erginsoy, et al.,[40] for α-iron using Vineyard's GRAPE program. Sizmann[50] has indicated its importance in electron irradiation, for copper, as a mechanism for the segregation of vacancies and interstitials. Erginsoy, et al., found that each vacancy in α-iron was centered within a 30-site instability region with respect to recombination with an interstitial. Of these 30 sites, 24 lie on the <111> lines passing through the vacancy. Some of the displacements allowed by the Kinchin-Pease, single displacement energy criterion are not allowed when the effect of this instability region is invoked, as it was in the present collision cascade simulations.

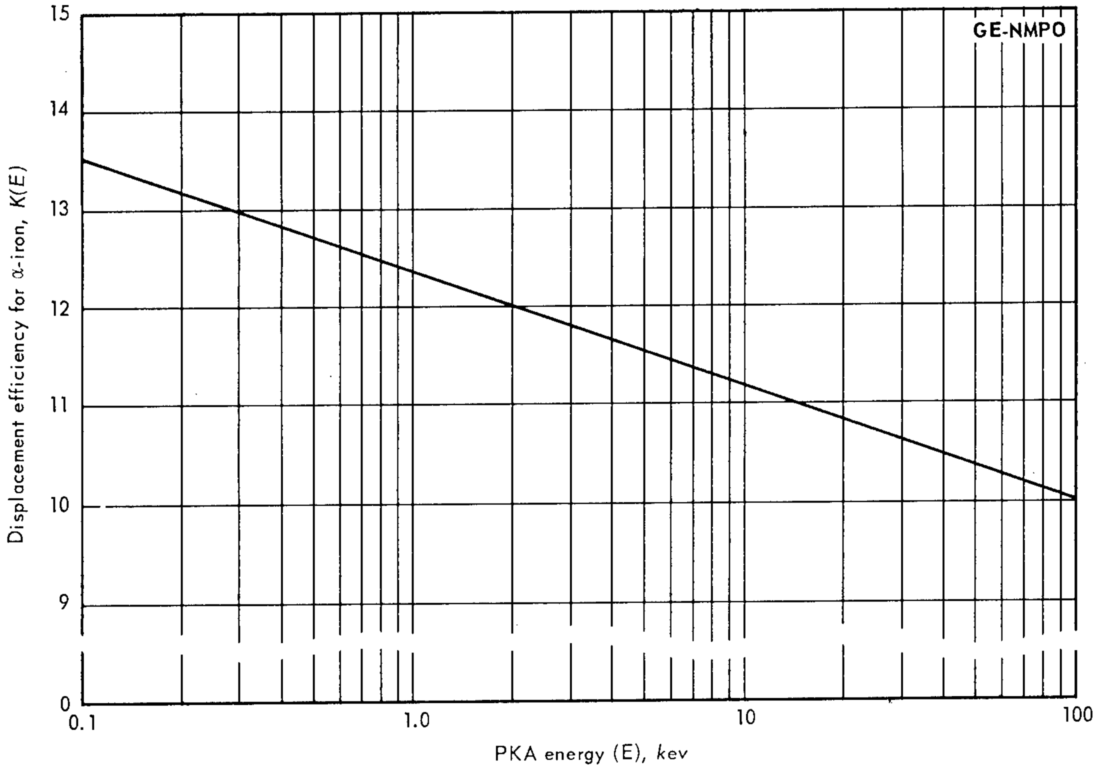

Fig. 2.47 – Displacement efficiency K(E) for α-iron

The existence of the instability region for vacancy - interstitial recombination has an important consequence with regard to the meaning of E_d. In practice, E_d values are usually determined by electron irradiation experiments.[47] However, the defect deployment in electron irradiated specimens is known to be different than that left by an atomic collision cascade. The cascade simulations clearly indicate that the effective displacement energy increases with the spatial extent of a cascade. Hence, E_d as determined from an electron irradiation experiment need not apply directly to damage production in a collision cascade. Further evidence that E_d, as used in the Kinchin-Pease model, must depend upon the damage state will be given in the discussion of saturation effects.

The displacement production function, $\nu(E)$, for PKA is plotted in Figure 2.48 as given by the present work and as given by Kinchin and Pease. Their assumption that all collisions are inelastic for energies above 56 kev was followed in preparing Figure 2.48. The ratio of K_{kp} to K_{mix} for mixed elastic and inelastic collisions, was taken as a function of E/E^* from the work of Thompson and Wright and applied to the structure-dependent K(E) given by the cascade simulations. The displacement production given by this approximation for the combined effects of crystal structure and mixed collision types is given by the dashed curve in Figure 2.48. This indicates that the major correction to the random solid-elastic collision model, below E^*, is the crystal structure correction and that above E^* is the correction for mixed inelastic and elastic collisions.

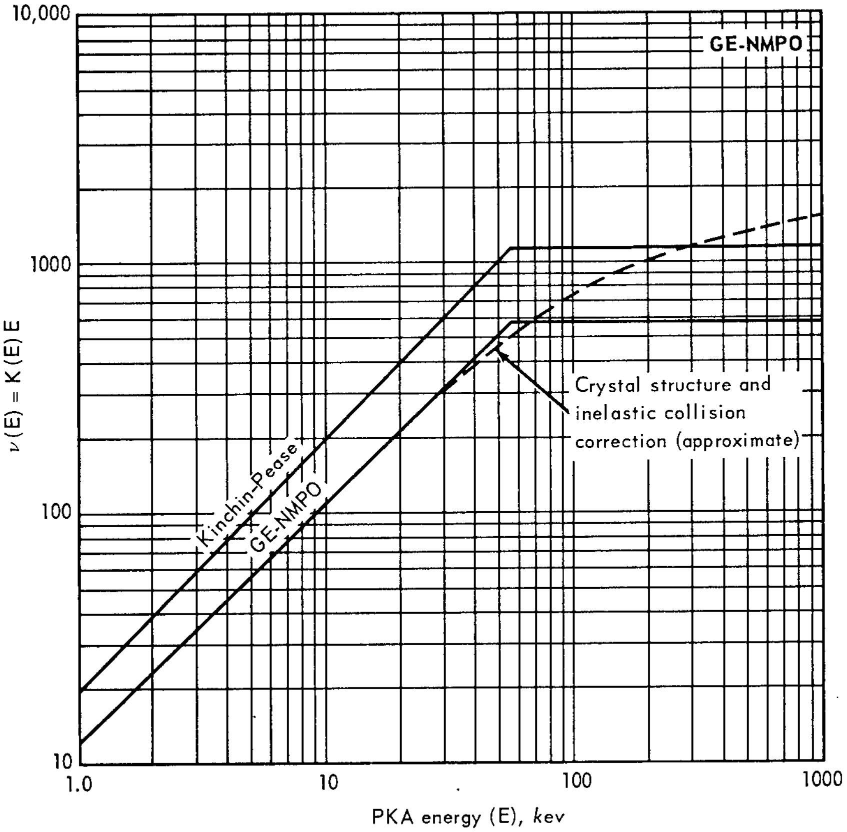

Fig. 2.48 – The relationship $\nu(E) = K(E)E$ for α-iron

Tables 2.15 and 2.16 describe the distribution of vacancy clusters in a displacement spike as a function of the initiating PKA energy. An n-vacancy cluster is denoted by V_n. Table 2.15 gives the absolute numbers of clusters containing 10 or less vacancies and the combined number of those containing 10 or more vacancies. The demarcation at the size n = 10 was made in view of the indications cited by Thomas and Washburn[41] that vacancy clusters of size 10 or larger are those most important to irradiation hardening. Vineyard discusses evidence for the possible importance of smaller clusters. The fractions of vacancies contained in v_1, v_2, v_3, and v_4 clusters, listed in Table 2.16, appear to be independent of the PKA energy. However, the fractions contained in each of the larger

TABLE 2.15

AVERAGE NUMBER OF n-DEFECT VACANCY CLUSTERS (v_n) PER DISPLACEMENT SPIKE IN THE α-IRON PRIMARY DAMAGE STATE[a]

	Number Of Defects (n)										
E	1	2	3	4	5	6	7	8	9	10	≥10
0.5	2.2	0.66	0.27	0.14	0.12	0.07	0.05	0	0	0	0
1	4.1	1.2	0.52	0.33	0.18	0.14	0.07	0.06	0.04	0	0
2.5	9.8	3.2	1.2	0.69	0.38	0.20	0.19	0.12	0.04	0.07	0.14
5	19.3	5.5	2.8	1.6	0.69	0.43	0.23	0.14	0.06	0.04	0.24
10	39.2	11.3	5.1	2.6	1.4	0.87	0.45	0.30	0.27	0.10	0.36
15	57.8	15.7	7.0	3.6	2.2	1.1	0.74	0.62	0.30	0.19	0.62
20	77.1	22.3	9.6	5.0	3.1	1.6	1.0	0.66	0.33	0.19	0.78

[a] Erginsoy-Vineyard potential.

TABLE 2.16

FRACTION OF ALL VACANCIES IN THE α-IRON PRIMARY DAMAGE STATE WHICH ARE CONTAINED IN v_n[a]

	Number Of Defects (n)										
E	1	2	3	4	5	6	7	8	9	10	≥10
0.5	0.35	0.21	0.13	0.09	0.10	0.07	0.06	0	0	0	0
1	0.33	0.19	0.12	0.11	0.07	0.06	0.04	0.04	0.03	0	0
2.5	0.33	0.21	0.12	0.09	0.06	0.04	0.04	0.03	0.01	0.02	0.05
5	0.34	0.19	0.14	0.11	0.06	0.04	0.03	0.02	0.01	0.01	0.05
10	0.35	0.20	0.14	0.10	0.06	0.05	0.03	0.02	0.02	0.01	0.04
15	0.36	0.19	0.13	0.09	0.07	0.04	0.03	0.03	0.02	0.01	0.05
20	0.35	0.20	0.13	0.09	0.07	0.04	0.03	0.02	0.01	0.01	0.04

[a] Erginsoy-Vineyard potential.

cluster sizes change as a function of energy up to about 5 kev. This occurs because the maximum cluster size for a given energy increased up to this energy and then remained fixed. This maximum size was $n_{max} = 21$. The average number of large clusters per spike and the probability that a given spike will contain at least one large cluster are plotted in Figure 2.49.

The cluster production function, $g(E; v_n)$, is the average number of n-vacancy clusters produced in an E-kev displacement spike. By definition, the displacement function g(E) and the cluster production functions are related as given in equation (2.13).

$$g(E) = 1 + \sum_{n=1}^{n_{max}} n\, g(E; v_n)\, E \qquad (2.13)$$

Table 2.17 lists the $g(E; v_n)$ for α-iron given by cascade simulations. Tables 2.18 and 2.19 describe interstitial cluster production in a displacement spike. No interstitial cluster containing more than three defects was observed.

DEFECT CLUSTER PRODUCTION PER UNIT NEUTRON EXPOSURE

The defect cluster production functions $g(E; v_n)$ and $g(E; i_n)$ for vacancy and interstitial clusters, respectively, were used to evaluate the density of defect clusters produced in a typical research irradiation specimen as a function of neutron energy. Although these densities do not completely define the primary damage state they do furnish a basis for

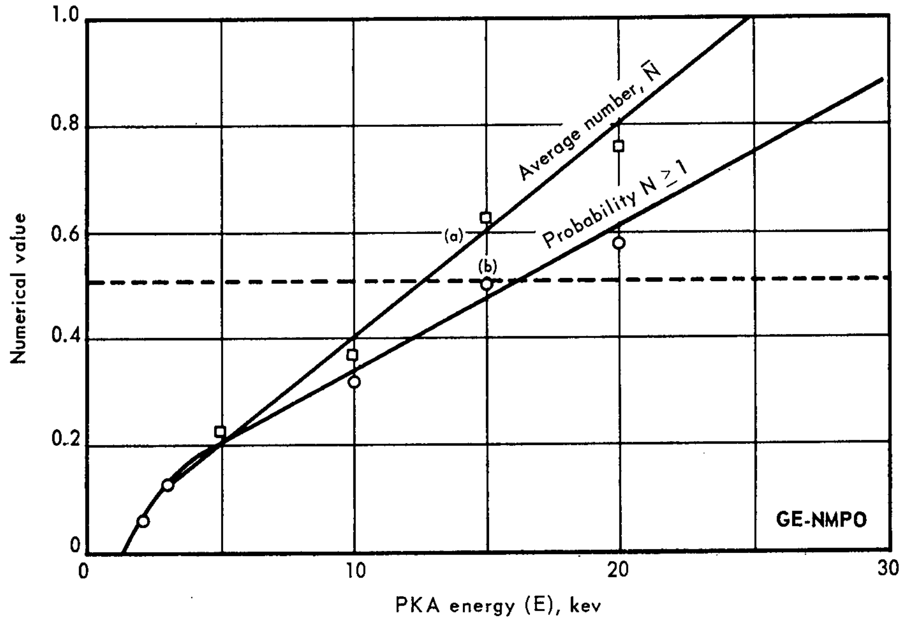

Fig. 2.49 – Average number, $\bar{N}$, of large clusters per displacement spike and the probability that a given spike will contain at least one large cluster for various PKA energies.

TABLE 2.17

DAMAGE FUNCTIONS $g(E; v_n)$ FOR VACANCY CLUSTERS ($n \geq 1$) IN TERMS OF THE RATIO $[g(E; v_n)]/E$[a]

n	$[g(E; v_n)]/E$	Condition on E, kev
1	3.88	All $E \leq 56$
2	1.08	All $E \leq 56$
3	0.490	All $E \leq 56$
4-6	0.477	All $E \leq 56$
7-9	0.103	$0.5 < E \leq 56$
≤ 10	0.0394	$1.0 < E \leq 56$

[a] Erginsoy-Vineyard potential.

TABLE 2.18

AVERAGE NUMBER OF n-DEFECT INTERSTITIAL CLUSTERS (i_n) PER DISPLACEMENT SPIKE IN THE α-IRON PRIMARY DAMAGE STATE[a]

n	Energy, kev						
	0.5	1	2.5	5	10	15	20
1	6.1	12.0	28.5	54.6	106	152	206
2	0.1	0.2	0.64	1.3	3.1	4.7	6.4
3	0	0	0.02	0.02	0.09	0.15	0.20

[a] Erginsoy-Vineyard potential.

TABLE 2.19

FRACTION OF ALL INTERSTITIALS IN THE α-IRON PRIMARY DAMAGE STATE WHICH ARE CONTAINED IN i_n[a]

	Energy, kev						
n	0.5	1	2.5	5	10	15	20
1	0.98	0.97	0.96	0.95	0.94	0.94	0.94
2	0.02	0.03	0.04	0.05	0.06	0.06	0.06
3	0	0	0.001	0.001	0.003	0.003	0.003

[a] Erginsoy-Vineyard potential.

establishing a more refined interpretation of experimental data than is afforded by g(E) alone. The vacancy density per unit exposure is given by equation (2.14)

$$d = y \int g(E)f(E)dE \qquad (2.14)$$

and the density of vacancy clusters v_n by equation (2.15)

$$d(v_n) = y \int g(E; v_n)f(E)dE \qquad n \geq 1 \qquad (2.15)$$

Given an arbitrary neutron exposure $\epsilon(E_N)$ at neutron energy E_N, the total displacement density would be $\epsilon(E_N)d$ and the v_n cluster density would be $\epsilon(E_N)d(v_n)$. These densities are valid for the unsaturated damage state in either α-iron or ferritic steel rods with diameters between 0.1 and 0.5 cm and length h > 5 cm. Figures 2.50 through 2.52 summarize the results. Most reactor neutron spectra are dominated by neutrons with energies below 3 Mev. The shape of the various cluster densities therefore indicates that decade 0.3 to 3.0 Mev is perhaps the most important neutron energy region so far as vacancy and interstitial defect production is concerned.

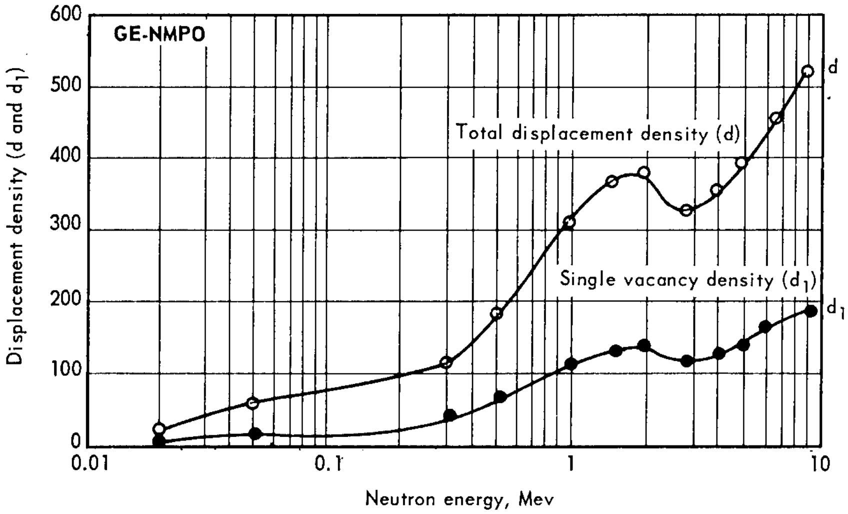

Fig. 2.50 – Total displacement density, d, per unit exposure in an iron rod, approximately 0.3 cm in diameter, as a function of neutron energy for an isotropically incident neutron flux and single vacancy density, d_1, for the same sample and irradiation conditions.

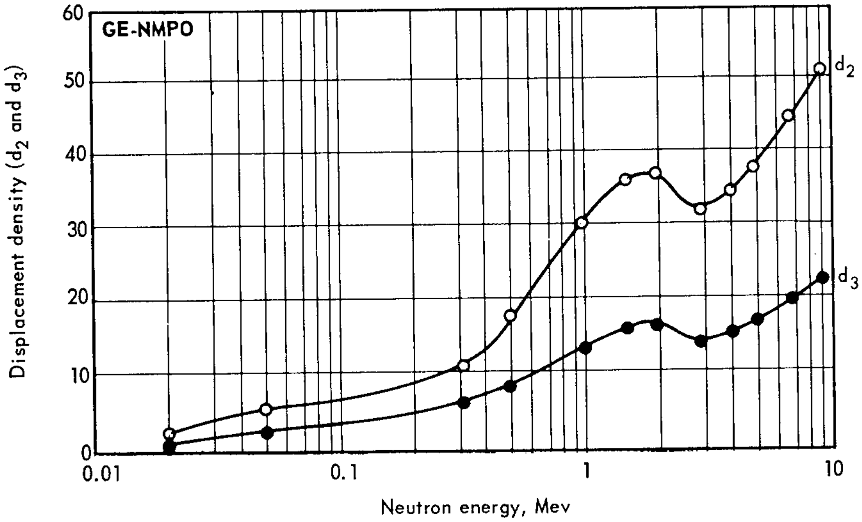

Fig. 2.51 – Displacement densities for divacancies, d_2, and trivacancies, d_3, for an iron rod, approximately 0.3 cm in diameter, as a function of neutron energy for an isotropically incident neutron flux

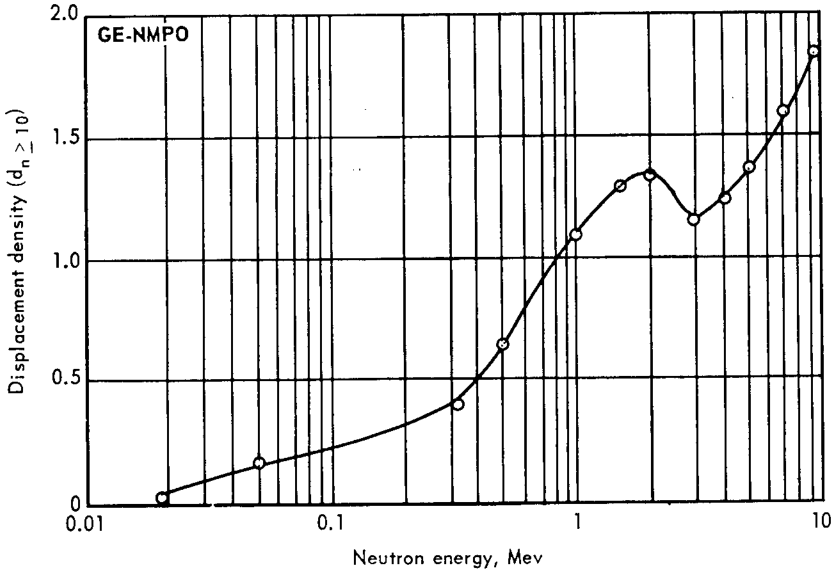

Fig. 2.52 – Large cluster ($\bar{n} \geq 10$) displacement density for an iron rod, approximately 0.3 cm in diameter, as a function of neutron energy for an isotropically incident neutron flux

PRESSURE SHELL EMBRITTLEMENT

The position of the interface between saturated and unsaturated damage regions in an iron slab, irradiated on one surface, was computed as a function of neutron energy and exposure. In small samples, damage saturation occurs after a unique saturation exposure, ϵ_s, because the damage density is then nearly uniform.[51,52] In a pressure shell subjected to isotropically incident neutrons, however, saturation occurs first at the exposed surface and then proceeds into the shell at a rate determined by the neutron energy and the shell thickness. Assuming that saturation begins when the damaged regions produced by individual PKA are sufficiently numerous to experience peripheral contact, the saturation exposure is inversely proportional to the density of irradiation-produced vacancies.

Figure 2.53 shows the vacancy density variation in a 6.75-cm-thick shell (2.65 inch) as a function of depth, z, relative to the exposed surface. This thickness corresponds to that of the PM-2A pressure shell. These vacancy density curves do not follow the neutron-collision-density curves. This figure also gives the exposure, ϵ_s, required to advance the saturated - unsaturated damage interface to position z in units of the exposure, $\epsilon_0(z)$, for saturation at a z of 0.01 cm.[53] The exposure required to saturate a 0.25-cm-thick layer at the exposed surface was practically the same as that required to produce saturation in a

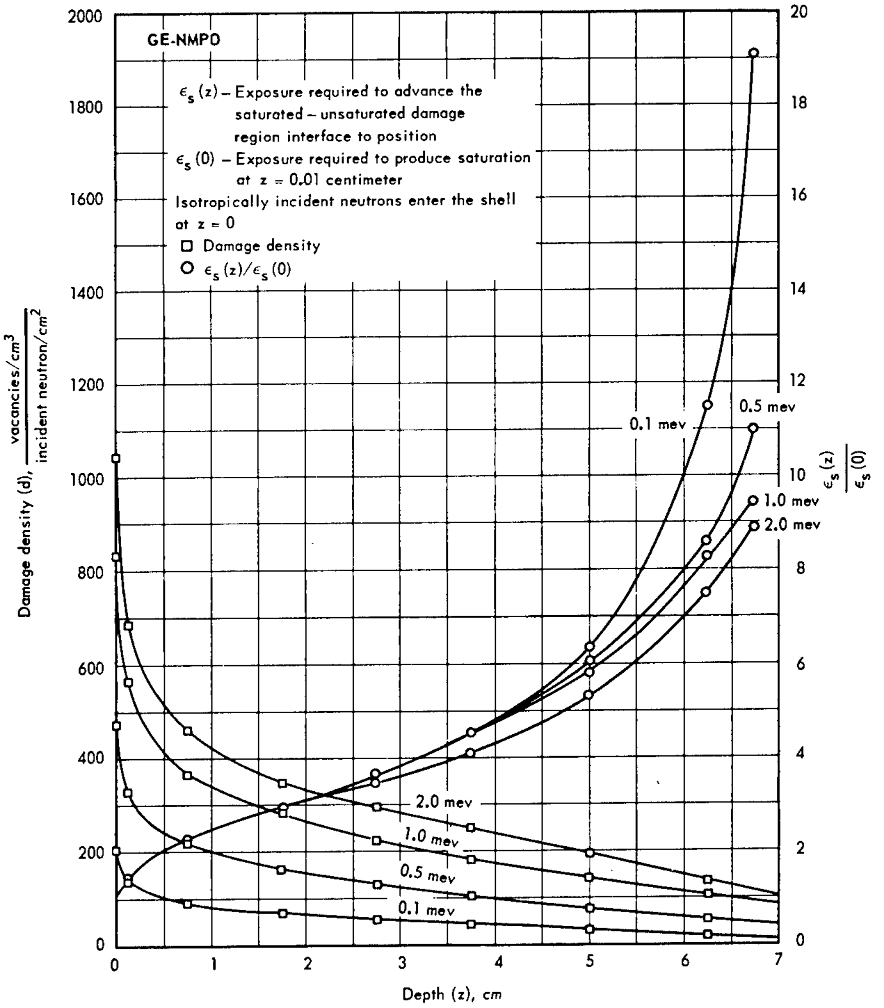

Fig. 2.53 – Damage density, (d), and normalized exposure ratio, $\epsilon_s(z)/\epsilon_s(0)$, as a function of penetration distance

0.25-cm-diameter iron rod. This supports the use of surveillance samples (of this size) to monitor the damage state in this layer. The damage density in the shell interior can be determined given the density in the surveillance sample.

For a 0.25-cm iron rod, irradiated in a graphite reactor at 60° to 90°C, Chow, et al.,[54] show that ϵ_s exceeds 10^{19} nvt ($E_n \geq 1$ Mev), and the present calculations predict ϵ_s is greater than 2.6×10^{19} nvt ($E_n \geq 1$ Mev). They also show that an exposure of at least 2×10^{18} nvt ($E_n \geq 1$ Mev) is required to change the brittle - ductile fracture transition temperature in this rod. The penetration rate of the irradiation embrittled region is, therefore, at least 13 times greater than that of the saturated damage region.

Figure 2.53 shows that saturation and embrittlement penetration is limited to a depth, d_{max}. For a 0.1-Mev neutron irradiation, d_{max} is approximately equal to 7 cm. Up to 2.5 cm, the saturation and embrittlement penetration rate is independent of neutron energy ($0.1 \leq E \leq 2$ Mev). These results are clearly of interest in the consideration of brittle - fracture,[55] crack-arrest,[55] and fatigue properties[56] if the current theory of irradiation hardening is accepted; i. e., defect obstruction to dislocation generation and motion.[41,57,58,59] In addition, the energy and spatial dependence shown are directly pertinent to the selection of test samples and data interpretation in an experimental investigation of mechanical property variation in an irradiated shell as a function of depth.

SATURATED DAMAGE STATE

Diehl,[60] for example, has pointed out that the essential condition for a saturation of defect production in neutron-irradiated metals is that the current defect distribution be capable of influencing the production of new defects. At 0°K there are at least two mechanisms for the mutual annihilation of old and new defects: (1) extant interstitials could be knocked into vacancy positions directly by atomic collisions; and (2) new defects could be produced within the instability regions of extant defects. At finite temperatures, thermally activated migration and defect cluster dissociation provide additional modes for the mutual annihilation of old and new defects.

The saturation process at 0°K is currently being studied by shooting a series of PKA into the same crystal region using the CASCADE program. The first PKA is shot into an undamaged crystal from a normal lattice site and its defect production noted. A second PKA with the same energy and initial direction is then shot from another normal lattice site, separated from that for the first PKA by no more than the diameter of the first pass displacement spike, and its defect production is noted. The second PKA is shot into a crystal containing the damage stage produced by the first. Since the energies and initial directions of the two PKA are identical, any difference between their displacement efficiencies must be due purely to the saturation effect.

Each successive PKA always produced fewer defects than it predecessor. This decrease in displacement efficiency is not a simple function of the distance between the starting points of the PKA concerned. In the course of the study thus far, the decrease in displacement efficiency has ranged from 13 to 40 percent. This variation is principally caused by the Swiss cheese structure of displacement spikes. The damage state after as many as three passes always contained some defects produced in each individual pass, but these defects were seldom in their original cluster group. The defect distribution in a multiple-pass spike (saturated damage state) was not the same as that for a single-pass spike (unsaturated damage state). It appears that the saturated damage state contains predominantly the extreme cluster sizes, i.e., monodefects and large clusters. The largest cluster size observed in a multiple-pass spike is several times larger than that for a single-pass spike. It appears that the intermediate cluster size population tends to be destroyed.

A semi-indirect process by which struck interstitials were induced to recombine with existing vacancies should be of significance. This is recombination along a <111> line of atoms even though the momentum transfer was for a different direction. Erginsoy, et al., found that an interstitial would recombine with a vacancy on a common <111> line at $0^{o}K$ in α-iron provided the initial separation distance between it and the vacancy was no greater than $3d_1$, where d_1 is the first neighbor separation distance. Vineyard's GRAPE program is being used at GE-NMPO to investigate induced interstitial - vacancy recombination along a <111> line over distances greater than $3d_1$. This induced recombination is of interest in the theory of damage saturation and that of radiation annealing. It has been found, for example, that an interstitial will recombine with a vacancy at least as far away as $4d_1$ on a <111> line when excited with an energy of 0.33 ev and with its initial momentum along <110>. This excitation energy is the interstitial migration energy given by Johnson's calculation for α-iron.[61] Recombination occurred within 5×10^{-13} seconds and was an entirely unidirectional process. This suggests that interstitials receiving energies as small as their migration energy for diffusion in an otherwise perfect crystal can directly recombine with vacancies over a distance which would prevent recombination at $0^{o}K$. This result also strongly suggests that the extent of the Frenkel pair instability region should increase significantly with temperature.

ANNEALING OF IRRADIATION-PRODUCED INTERSTITIALS

Stage III Annealing in α-Iron

The damage state produced by neutron irradiation at a finite temperature can now be approximated. In particular the damage state produced in α-iron at a temperature T less than $500^{o}C$ can be approximated by first simulating the formation of the primary damage state and then using this damage state as the initial defect distribution from which a Monte Carlo simulation of the annealing process is run for temperature T. The Monte Carlo program, ANNEAL, was written for this purpose. Given the primary damage state computed by CASCADE, ANNEAL generates simultaneous random walks for all mobile defect configurations in the current defect distribution.[62] The thermal dissociation of di-vacancies and di-interstitials is simulated, but all larger clusters are assumed to be stable against thermal dissociation. Program ANNEAL computes the defect distribution, at the level of atomic dimensions, as a function of time and temperature.

Calculations on interstitial annealing in 1-kev and 2.5-kev displacement spikes have been performed. These calculations were limited to the time interval for the first 100 jumps per mobile defect. According to Nihoul,[63] the migration of interstitials corresponds to Stage III recovery in BCC systems. Impurity atom effects were not considered. Any interstitial entering the instability region of Erginsoy, et al., was immediately recombined with the associated vacancy. The number of mobile interstitials was reduced by a factor of three within the annealing time considered. About two-thirds of the reduction was caused by interstitial - vacancy recombination; the remainder, by interstitial clustering. There was a clear tendency for the interstitial and vacancy populations to be principally contained in immobile clusters after annealing. This leads to the conclusion that mobile vacancy configurations in a pure material would begin their migration in a field of immobile clusters.

A visual impression of the interstitial annealing process is given by Figures 2.54 to 2.59. Figures 2.54, 2.56, and 2.58 describe the primary damage state in a 2.5-kev displacement spike. Figures 2.55, 2.57, and 2.59 describe the defect distribution which evolves from the primary damage state during 37τ* seconds, with Figure 2.55 pertaining to the same crystal region as Figure 2.54; Figure 2.57 to the same region as Figure 2.56; and Figure 2.59 to the same region as Figure 2.58. Each figure is the projection of the defect distribution in four successive atom planes onto a (001) plane; i.e., an x-y plane. Because of this, 14 symbols do not appear in the description of the 14-vacancy cluster,

---

*τ = interstitial jump time.

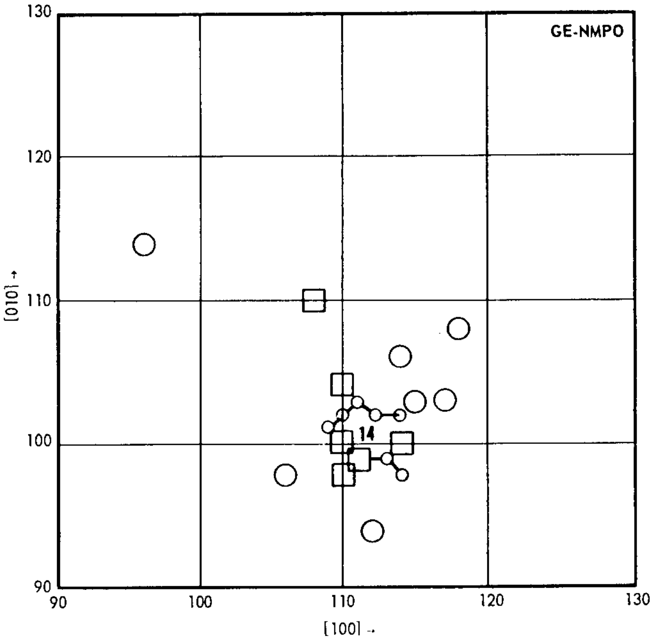

Fig. 2.54 – Projection of defect positions in the primary damage state of planes z = 96 through z = 99 onto a (001) plane contained in a 2.5-kev displacement spike

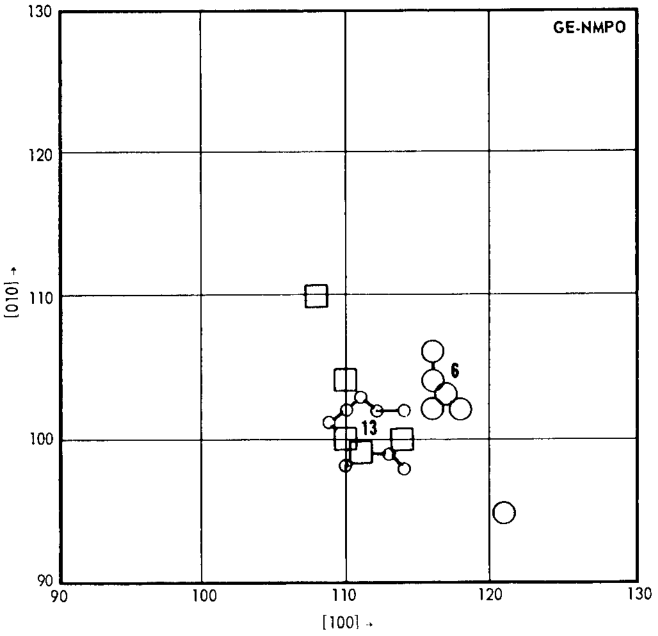

Fig. 2.55 – Projection of defect positions in the annealed damage state after 37τ seconds, evolving from the primary damage state shown in Figure 2.54

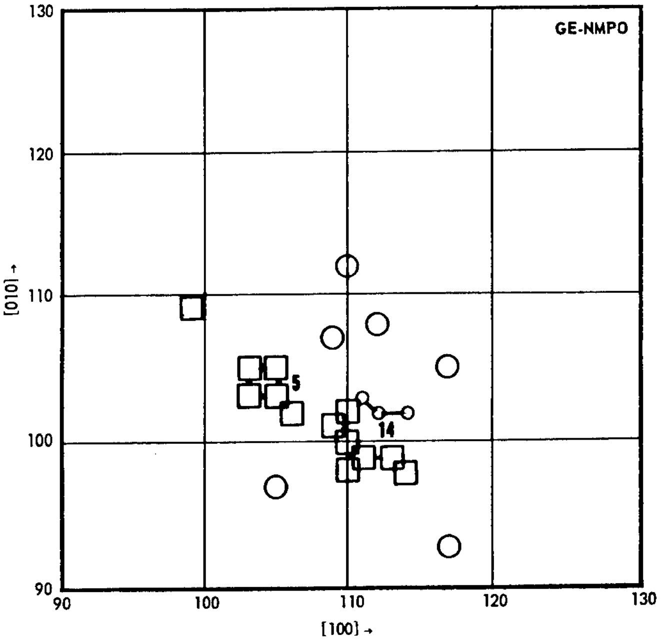

Fig. 2.56 – Primary damage state projection onto a (001) plane for planes z = 100 through z = 103 of the same spike concerned in Figure 2.54

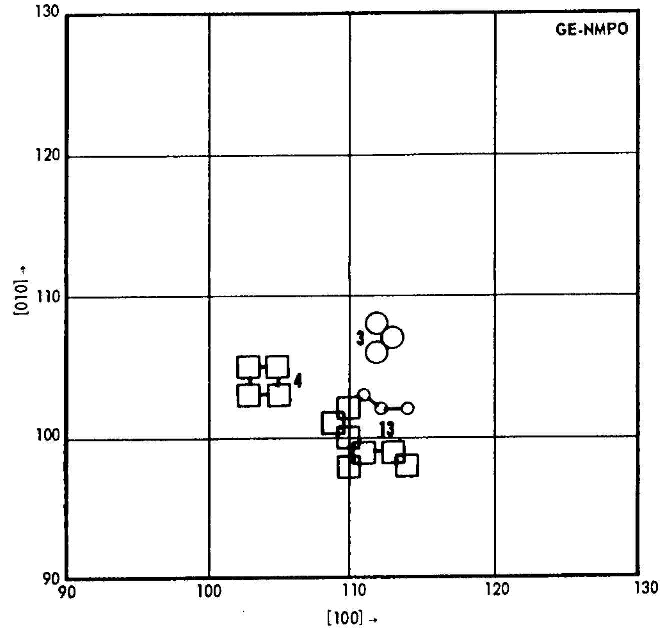

Fig. 2.57 – Projection of annealed state, after 37·τ seconds, evolving from the damage state of Figure 2.56

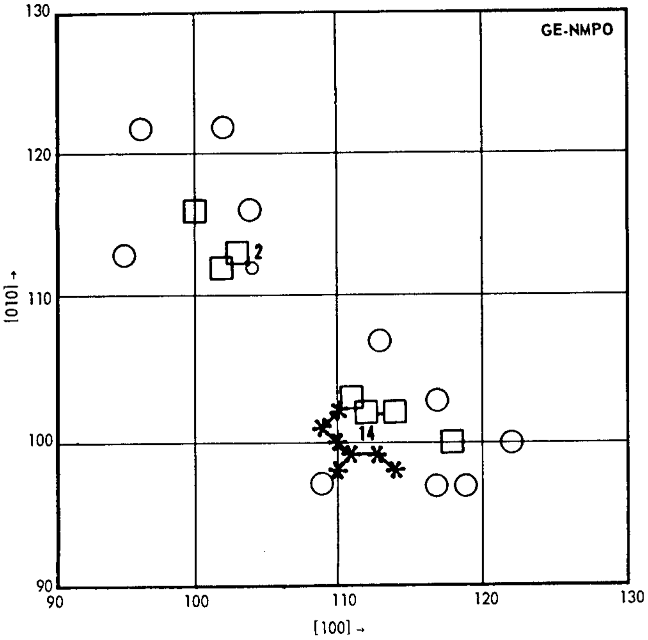

Fig. 2.58 – Primary damage state projection onto a (001) plane for planes z = 104 through z = 107 of the same spike concerned in Figure 2.54

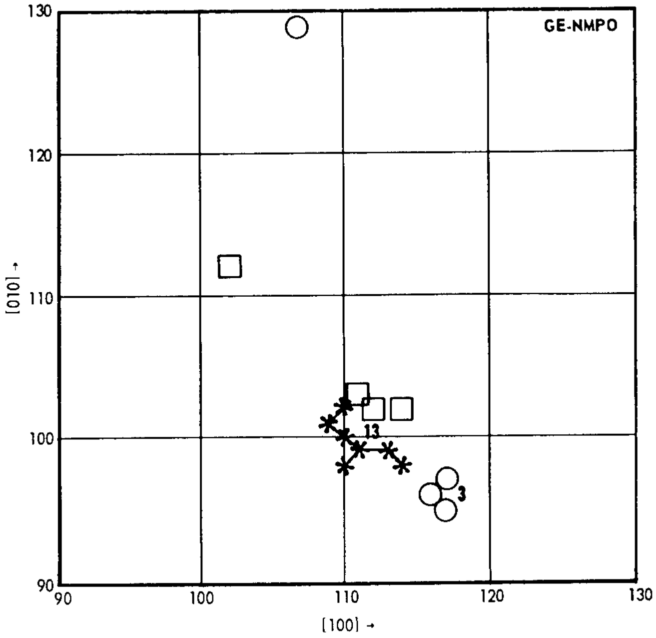

Fig. 2.59 – Projection of annealed state, after 37τ seconds, evolving from the damage state of Figure 2.58

for example, since some vacancies obscure others in the "top view" projection. As before, a full-sized square and circle signify a vacancy and an interstitial, respectively, in one of the four planes concerned in each figure. A small circle indicates the balance of a cluster lying in planes above the four concerned in the figure and an asterisk the balance lying in planes below the four planes concerned. These drawings give one a clear impression of the three-dimensional "cleaning up" which takes place during an annealing process. The initial annealing rate is at least an order of magnitude larger than that predicted by diffusion theory on the basis of a uniform initial defect distribution.[62]

2.4 SUMMARY AND CONCLUSIONS

Isochronal annealing studies of neutron-induced defects in recrystallized BCC metals show that the resistivity properties recover with three resolved peaks occurring at 15, 22, and 31 percent of the absolute melting temperature for the respective metals. Isothermal annealing studies on irradiated tungsten indicate that the reaction kinetics for the defect migration at the 0.15 T_m recovery peak obey second order processes. A possible mechanism which could account for the recovery at the 0.15 T_m peak is the migration of either free interstitial atoms or of those interstitial atoms which are released from impurity traps and migrate to the immobile free vacancies where the interstitial - vacancy defect is annihilated. The mechanisms of the resistivity recovery which occur at the two higher temperatures are believed to be caused by the migration of di-vacancies and mono-vacancies agglomerating into vacancy clusters, or to the release of vacancies from impurity atom traps where they quickly migrate to annihilation points or to combinations of both.

Studies on the recovery of neutron-induced hardening of tungsten single crystals show that only one recovery peak occurs at 0.35 T_m. It was further determined that the irradiation affects the athermal component of the hardness which appears above 0.15 T_m, and not the strong temperature- dependent component which becomes prominent below this temperature. Based on the slip patterns observed about the indentations above and below the 0.35 T_m temperature region, it is concluded that a significant change in the flow mechanism must also occur at this temperature.

Creep-rupture testing of irradiated tungsten specimens at temperatures at or above 1100°C (0.35 T_m) indicates that the irradiation tends to strengthen the material without affecting the ductility for the case in which the thermal neutron flux is about a factor of 3 greater than the fast neutron flux. The strength increase appears to occur at a fast neutron dose of about 1×10^{19} nvt and varies linearly with dose up to about 8×10^{19} nvt. Testing specimens at temperatures up to 1700°C (0.54 T_m) indicates that some radiation-induced strengthening is still present at temperatures where it is believed that recoverable defects should be completely removed.

The slight increase in creep-rupture strength at high temperatures (1700°C) and the residual irradiation-induced hardness and resistivity values observed in tungsten specimens following annealing at temperatures up to 1900°C is caused by the presence of rhenium atoms from transmutations of tungsten by the thermal neutron (n, γ) reaction. Theoretical calculations of the number of transmutations agree with radiochemical quantitative analysis. It was further determined that an appreciable amount of Os^{188} atoms are produced as a result of the W^{187} (n, γ) W^{188} reaction which decays to Re^{188} with a 65-day half-life and then to Os^{188} with a 17-hour half-life.

Creep-rupture testing of irradiated tungsten specimens at temperatures below the 0.35 T_m temperature region shows that the irradiation-induced strengthening is much more pronounced than that observed for specimens tested above this temperature. Specimens tested at 900°C (0.35 T_m) show further irradiation-induced strengthening over and above that observed in the as-irradiated condition following the annealing treatments at temperatures between 900° and 1200°C.

Irradiated W - 25Re specimens when tested at 1100°C do not show the significant changes in the creep-rupture properties which were observed for the case of tungsten specimens irradiated under similar conditions. In addition, there appears to be a relative shortening of the duration of third stage creep and a slight lowering of the ductility of irradiated W - 25Re when compared to the unirradiated material.

Irradiated molybdenum specimens appear to show an accelerated creep rate when tested in the temperature region of about 0.30 T_m. Above and below this temperature region, the effect is not as pronounced. The tendency for accelerated creep rate, therefore, seems to be critically dependent on the test temperature and the irradiation dose. It is believed that, for a temperature below 0.31 T_m, a supersaturation of vacancies will exist in the material as a result of the irradiation. If the vacancies become mobile at a temperature in the region of 0.31 T_m, they may promote dislocation climb and thereby surmounting obstacles which would normally impede dislocation motion at that temperature. As in the case of the irradiated tungsten specimens, the ductility of the irradiated molybdenum specimens is not appreciably different than that of the controls.

Ni, B SS

The high-temperature alloys (Hastelloy X and A-286) continue to show significant reductions in both the time to rupture and in the ductility as a result of neutron irradiation. It was further determined that thermal neutrons play an important role in the irradiation effects on the creep-rupture properties of these alloys.

to p. 121

A model is proposed in which boron atoms segregate to grain boundaries, near incoherent precipitates, and along dislocations where, by the $B^{10}(n, \alpha) Li^7$ reaction, they cause significant atom displacements in the critical regions of the grain resulting in the subsequent nucleation of precipitates, generation of dislocation networks, and in the formation of small helium gas bubbles. These irradiation-induced defects and their distribution within the critical regions of the grain will tend to impede dislocation movement and thereby limit slip to within the grain. Grain boundary sliding and sub-grain rotation will also be reduced which will result in the severe embrittlement observed in these alloys.

It has also been determined that hydrogen and helium atoms may be produced through the (n, p) and (n, α) fast neutron reactions with essentially all the elements found in structural alloys. The (n, α) reaction with the trace quantities of nitrogen in Hastelloy X, for instance, contributes a relatively large quantity of helium atoms when compared with that produced by the iron (n, α) reaction, even though the nitrogen concentration is much lower than the iron. The nickel (n, p) reaction results in a large production of hydrogen atoms for the case of nickel-base alloys.

The helium atoms produced by the fast neutrons, with the exception of the nitrogen reaction, will generally be distributed homogeneously throughout the grains for conditions below helium migration temperatures, while those helium atoms produced by the thermal neutrons (with the B^{10} isotope) will be predominantly produced in the regions of the grain boundaries and near dislocations. As a result, any influence of helium atoms on the flow and fracture properties of irradiated metals will be quite sensitive to reactor neutron spectrum. Therefore, the application of experimental test data which are obtained in water moderated test reactors to the design considerations of fast spectrum reactor systems should be carefully evaluated before major design decisions based on irradiation effects are made.

Recent experiments strongly suggest that damage computations must give an absolute description of the defect spatial distribution, at the level of atomic dimensions, if they are to be of service in the interpretation of radiation effects data. This very fine scale description is necessary because mechanical property radiation effects are determined by interactions among dislocations, impurity atoms, and radiation-produced structural defects (vacancies and interstitials). All of these interactions depend strongly on the structure and deployment of the imperfections concerned, and are importantly influenced by impurity atoms produced by transmutation reactions during irradiation. An absolute method for computing neutron-irradiation-damage production and annealing in cubic metals was, therefore, developed for use in the GE-NMPO radiation effects program and the PM-2A pressure shell analysis program. This method is based upon a computer experiment technique in which neutron collision chains and atomic collision cascades are simulated on a computer. The effects of the current damage state and of crystal structure upon either damage production or annealing are automatically included in these simulations. Because it considers the influence of the current damage state on new damage production, the method can be used to compute the damage state produced at a finite temperature and a saturated damage state.

An extensive study was made for α-iron. The production of primary knock-on atoms (PKA) by neutrons was studied as a function of specimen size, the incident neutron energy spectrum and the incident neutron angular distribution. Displacement spike production by PKA with energies in the range of 0.5 to 20 kev was simulated. Crystal structure effects decreased displacement production at $0^{o}K$ by a factor of 1.8 relative to that predicted for a structureless solid of the same density. Up to about a 60-kev PKA energy, only the crystal structure correction to the structureless solid model is important. Above this energy both crystal structure and inelastic atomic scattering corrections must be made. The number of displacements produced at $0^{o}K$ is at least a factor of 3 larger than that produced at a temperature sufficiently high that interstitials can migrate, but not high enough to allow vacancy migration; i.e., up to $250^{o}C$. The primary damage state (that produced at $0^{o}K$) contained vacancy clusters of up to 21 defects but no interstitial clusters containing more than 3 defects. In contrast, the damage state produced at temperatures up to $250^{o}C$ contained interstitial clusters as well as vacancy clusters. The displacement concentration in a displacement spike produced at $0^{o}K$ was 2.3 atomic percent; that in a spike produced at temperatures up to $250^{o}C$ was less than 1 atomic percent. Vacancy clusters produced at $0^{o}K$ tended to exhibit stringy structures rather than being compact "voids." As such they would be invisible in transmission electron microscopy even though they were up to 40 Å in extent.

2.5 PLANS AND RECOMMENDATIONS

The post-irradiation creep-rupture testing of W, W - 25Re, Mo, and Mo-TZM specimens will continue with major emphasis being put on the alloys. Studies on the new materials, tantalum, niobium, and alloys of each, will be initiated on a limited basis. Preliminary capsule designs and the test conditions to be considered for an in-reactor creep-rupture experiment of tungsten will be evaluated, and a test program implemented.

The effects of neutron irradiation on other properties such as tensile, hardness, and resistivity will be continued for the BCC metals. Of special importance will be the studies on the defect recovery kinetics which will be performed by combinations of isochronal and isothermal annealing.

Creep-rupture studies will continue on the high-temperature alloys. The primary effort will be placed on Hastelloy-N and on a special split heat of a precipitation-hardening iron-base alloy. The main objective of these tests will be to determine the basic cause of the elevated temperature irradiation-induced embrittlement observed in these types of alloys.

Pressure vessel embrittlement studies will be continued with major emphasis on the A350-LF5 alloy. These studies will include the measurements of the irradiation-induced change in the hardness and resistivity properties of this material as a function of thickness in a 6.73-cm slab. Detailed dosimetry and computer calculations of irradiation-induced defects and of their annealing characteristics will be compared with the experimental data.

Theoretical studies on the neutron-induced defects in the base metals, particularly tungsten and also some of the alloys, will be evaluated by comparing: (1) measured activation energies for defect migration; (2) substructure as observed by transmission electron microscopy; and (3) mechanical property changes obtained in the testing program.

2.6 REFERENCES

1. "High-Temperature Materials Program Progress Report No. 19, Part A," GE-NMPO, GEMP-19A, January 25, 1963, pp. 21-25.
2. "Third Annual Report - High-Temperature Materials and Reactor Component Development Programs, Volume I - Materials," GE-NMPO, GEMP-270A, February 28, 1964, Figures 2.1 and 2.2, pp. 50-51.
3. Wronski, A. S., and Johnson, A. A., "A Hardening Effect Associated with Stage III Recovery in Neutron Irradiated Molybdenum," Philosophical Magazine, Vol. 8, 1963, pp. 1067-1070.
4. Nichols, R. W., and Harries, D. R., "Brittle Fracture and Irradiation Effects in Ferritic Pressure Vessel Steels," ASTM Special Technical Publication No. 341, 1963, pp. 162-198.
5. Makin, M. J., and Minter, F. J., "The Mechanical Properties of Niobium," Acta Metallurgica, Vol. 7, 1959, pp. 361-366.
6. "High-Temperature Materials Program Progress Report No. 37, Part A," GE-NMPO, GEMP-37A, July 31, 1964, Figure 3.1, p. 31.
7. Moteff, J., and Smith, J. P., "Recovery of Defects in Neutron Irradiated Tungsten," ASTM Symposium on Flow and Fracture Behavior of Metals and Alloys in Nuclear Environments, June 22-24, 1964. (To be published in ASTM Proceedings of the meeting.)
8. "Second Annual Report - High-Temperature Materials and Reactor Component Development Programs, Volume I - Materials," GE-NMPO, GEMP-177A, February 28, 1963, Figure 2.1-33, p. 98.
9. "Third Annual Report - High-Temperature Materials and Reactor Component Development Programs, Volume I - Materials," GE-NMPO, GEMP-270A, February 28, 1964, pp. 65-71.
10. "High-Temperature Materials Program Progress Report No. 29, Part A," GE-NMPO, GEMP-29A, November 30, 1963, Figure 3.13, p. 44.
11. "Third Annual Report - High-Temperature Materials and Reactor Component Development Programs, Volume I - Materials," GE-NMPO, GEMP-270A, February 28, 1964, Figures 2.20 and 2.23, pp. 68 and 71.
12. Moteff, J., and Smith, J. P., "Recovery of Defects in Neutron Irradiated Tungsten," ASTM Symposium on Flow and Fracture Behavior of Metals and Alloys in Nuclear Environments," June 22-24, 1964. (To be published in ASTM Proceedings of the meeting.)
13. "High-Temperature Materials Program Progress Report No. 29, Part A," GE-NMPO, GEMP-29A, November 30, 1963, Figure 3.12, p. 43.
14. Conrad, H., and Hayes, W., "Correlation of the Thermal Component of the Yield Stress of the bcc Metals," Transactions of the ASTM, Vol. 56, 1963, pp. 125-134.
15. "Third Annual Report - High-Temperature Materials and Reactor Component Development Programs, Volume I - Materials," GE-NMPO, GEMP-270A, February 28, 1964, Figure 2.24, p. 72.

16. Petty, E. R., "The Hardness Anisotropy of Aluminum Single Crystals," Journal of Institute of Metals, Vol. 91, 1962-1963, pp. 54-62.
17. "High-Temperature Materials Program Progress Report No. 37, Part A," GE-NMPO, GEMP-37A, July 31, 1964, pp. 46-51.
18. Eyre, B. L., "Direct Observations of Neutron Irradiation Damage in α-Iron," Philosophical Magazine, Vol. 7, 1962, pp. 2107-2113.
19. Bryner, J. S., "Electron Microscopic Study of the Effects of Neutron Irradiation on Iron," Quarterly Progress Report: Irradiation Effects on Reactor Structural Materials, GE-HAPO, HW-80794, February 14, 1964.
20. Downey, M. E., and Eyre, B. L., "Neutron Irradiation Damage in Molybdenum," AERE-R-4632, May 1964.
21. Meakin, J. D., and Greenfield, I. G., "Interstitial Loops in Neutron Irradiated Molybdenum," to be published in Philosophical Magazine.
22. "Third Annual Report - High-Temperature Materials and Reactor Component Development Programs, Volume I - Materials," GE-NMPO, GEMP-270A, February 28, 1964, Table 2.13, p. 81.
23. "Third Annual Report - High-Temperature Materials and Reactor Component Development Programs, Volume I - Materials," GE-NMPO, GEMP-270A, February 28, 1964, Figure 2.28, p. 79, and Table 2.11, p. 77.
24. "High-Temperature Materials Program Progress Report No. 43, Part A," GE-NMPO, GEMP-43A, January 29, 1965, p. 55.
25. "Third Annual Report - High-Temperature Materials and Reactor Component Development Programs, Volume I - Materials," GE-NMPO, GEMP-270A, February 28, 1964, Tables 2.12 and 2.13, Figures 2.29, 2.30, 2.31, and 2.32, pp. 80-84.
26. Moteff, J., Kingsbury, F. D., and Lovell, A. J., "The Dual Role of Boron in the Elevated Temperature Embrittlement of Irradiated Complex Heat Resistant Alloys," Nature, Vol. 202, 1964, p. 997.
27. Moteff, J., Robertshaw, F. C., and Kingsbury, F. D., "Effects of Neutron Irradiation on the Stress-Rupture Properties of High Temperature Precipitation Hardening Alloys," to be published in the Journal of Nuclear Materials.
28. Myers, H. P., "Neutron Damage in Steels Containing Small Amounts of Boron," AE-53, 1961.
29. Private communications with Dr. M. Hoch, University of Cincinnati.
30. Swalin, R. A., Thermodynamics of Solids, Wiley, New York, 1961, (Equation 14.19).
31. McCoy, H. E., Jr., "Effects of Hydrogen on the High Temperature Flow and Fracture Characteristics of Metals," Oak Ridge National Laboratories, ORNL-3600, June 1964.
32. Barnes, R. S., "A Theory of Swelling and Gas Release for Reactor Materials," Journal of Nuclear Materials, Vol. II, 1964, p. 135.
33. Beeler, J. R., Jr., "High-Speed Computer Techniques," Physics of Many Particle Systems, E. Meeron, Editor, Gordon and Breach Science Publishers, New York and London, 1965.
34. Eyre, B. L., "A Study of Neutron Irradiation in α-Iron and a 1Cr - 0.5Mo Pressure Vessel Steel," ASTM Special Technical Publication No. 341, 1963, p. 294.
35. Harries, D. R., Barton, P. J., and Wright, S. B., "Effects of Neutron Spectrum and Dose Rate on Radiation Hardening and Embrittlement in Steels," Journal of the British Nuclear Energy Society, October 1963, p. 398.
36. Brinkman, J. A., "Production of Atomic Displacements by High-Energy Particles," American Journal of Physics, Vol. 24, 1956, p. 246.
37. Seitz, F., "The Effects of Irradiation on Metals," Review of Modern Physics, Vol. 34, 1962, pp. 656-666.

38. Beeler, J. R., Jr., and McGurn, J. L., "A Method for Computing Primary Knock-On Spectra and Populations in Polyatomic Material Irradiated by Neutrons," GE-NMPO, GEMP-101, October 1961.
39. Besco, D. G., and Beeler, J. R., Jr., "Computer Programs Describing Collision Cascades in Binary Materials. III. Body-Centered Cubic and Face-Centered Cubic Structures," GE-NMPO, GEMP-243, August 1963.
40. Erginsoy, C., Vineyard, G. H., and Englert, A., "Dynamics of Radiation in a Body-Centered Cubic Lattice," The Physical Review, Vol. 133, 1964, p. A595.
41. Thomas, G., and Washburn, J., "Precipitation of Vacancies in Metals," Review of Modern Physics, Vol. 35, 1963, pp. 992-1011.
42. Eyre, B. L., and Bartlett, A. F., "An Electron Study of Neutron Irradiation Damage in α-Iron," AERE-R4752, November 1964.
43. Roberts, A. C., and Harries, D. R., Nature, Vol. 200, 1963, p. 772.
44. Seitz, F., and Koehler, J. S., "Displacement of Atoms During Irradiation," Solid State Physics, Vol. 2, 1956, p. 305.
45. Thompson, M. W., and Wright, S. B., "A New Damage Function for Graphite," AERE-R4701, August 1964.
46. Kinchin, G. H., and Pease, R. S., "The Displacement of Atoms in Solids by Radiation," Reports on Progress in Physics, Vol. 18, 1955, p. 1.
47. Dienes, G. J., and Vineyard, G. H., Radiation Effects in Solids, Interscience Publishers, 1957.
48. Beeler, J. R., Jr., and Besco, D. G., "Effects of Channeling on Damage Production in Iron," The Physical Review, Vol. 134, 1964, p. A530.
49. Gibson, J. B., Goland, A. N., Milgram, M., and Vineyard, G. H., "Dynamics of Radiation Damage," The Physical Review, Vol. 120, 1960, p. 1229.
50. Sizmann, R., private communication.
51. Beeler, J. R., Jr., "Effect of Sample Size on Neutron Damage in Iron," Transactions of American Nuclear Society, Vol. 6, No. 1, 1963, p. 44.
52. Beeler, J. R., Jr., "Primary Damage State in Neutron-Irradiated Iron," Journal of Applied Physics, Vol. 35, 1964, p. 2226.
53. Cotterill, R. M. J., and Segall, R. L., "The Effect of Quenching History, Quenching Temperature and Trace Impurities on Vacancy Clusters in Aluminum and Gold," Philosophical Magazine, Vol. 8, No. 91, July 1963, pp. 1105-1125.
54. Chow, J. G. Y., McRickard, S. B., and Gurinsky, D. H., "Effect of Fast Neutron Irradiation on the Mechanical Properties of Pure Iron," Radiation Damage in Solids, Vol. I, International Atomic Energy Agency, Vienna, 1962, pp. 299-308.
55. Pellini, W. S., Steele, L. E., and Hawthorne, J. R., "Analysis of Engineering and Basic Research Aspects of Neutron Embrittlement of Steels," Radiation Damage in Solids, Vol. II, International Atomic Energy Agency, Vienna, 1962, pp. 113-151.
56. Segall, R. L., "Lattice Defects in Fatigued Metals," Electron Microscopy and Strength of Crystals, G. Thomas and J. Washburn, Editors, Interscience Publishers, New York, 1963, pp. 515-534.
57. Koppenaal, T. J., and Kuhlman-Wilsdorf, D., "The Effect of Prestressing on the Strength of Neutron-Irradiated Copper Single Crystals," Applied Physics Letters, 1964, p. 59.
58. Kuhlman-Wilsdorf, D., "A New Theory of Work Hardening," Transactions of Metallurgical Society, AIME, Vol. 224, 1962, p. 1047.
59. Seeger, A., "The Nature of Radiation Damage in Metals," Radiation Damage in Solids, Vol. I, International Atomic Energy Agency, Vienna, 1962, pp. 101-127.
60. Diehl, J., "The Influence of Neutron Irradiation on the Mechanical Properties of Face-Centered Cubic Metal Crystals," Radiation Damage in Solids, Vol. I, International Atomic Energy Agency, Vienna, 1962, pp. 129-154.

61. Johnson, R. A., "Interstitials and Vacancies in α-Iron," The Physical Review, Vol. 134, June 1964, p. A1329.

62. Beeler, J. R., Jr., "Distribution Functions for the Number of Distinct Sites Visited in a Random Walk on Cubic Lattices: Relation to Defect Annealing," The Physical Review, Vol. 134, p. A1396.

63. Nihoul, J., Note on the paper of D. Peacock and A. Johnson, entitled, "Stage III Recovery in Neutron Irradiated Molybdenum and Niobium," Philosophical Magazine, Vol. 9, 1964, pp. 167-170.

3. RADIATION EFFECTS IN BeO

(57063)

The purpose of this program is to define the irradiation behavior of BeO in terms of the composition and microstructure variables that contribute to extended radiation stability.

[illegible] 167

During CY-64, the experimental program included continued irradiation testing and post-irradiation examination of specimens of a range of grain sizes and densities. Similar work was in progress on specimens containing different glass-phase additives in concentrations of 1 to 2 percent. Post-irradiation measurements were predominantly of dimensional and lattice changes, but also included strength, elastic constants, helium analyses, and microstructural examinations. Construction of equipment for transient thermal resistivity measurements was completed and calibration runs were in progress at the end of the year.

Further information was obtained on factors influencing expansion and on property changes in irradiated BeO. Equations were postulated indicating that the annealing of both interstitial and vacancy defects follows first-order kinetics during irradiation. These equations describe the expansion reasonably well over the temperature range 100° to 1200°C; however, the predicted saturation is yet to be observed and remains questionable. Defect clusters formed at elevated temperatures consisted of both interstitial and vacancy types in concentrations which were in approximate agreement with kinetic relationships. Data on helium content in irradiated samples indicate that more helium escapes at low than at elevated irradiation temperatures as a result of microcracking. The possibility of expansion due to growth of helium bubbles in the grain boundaries was demonstrated in annealing experiments. Further data were obtained on the elastic constants of unirradiated and irradiated BeO. There was no change in the enthalpy of specimens irradiated at 1000°C at temperatures up to 900°C. Elevated-temperature strength, similar to room-temperature strength, appeared essentially unchanged in the absence of microcracking.

Sections outlining the experimental program and summarizing measurements on specimen materials in an unirradiated condition precede a discussion of irradiation results.

3.1 PROGRAM DESCRIPTION

The principal series of irradiations was concerned with the effects of grain size and density. Specimens used in this series were made primarily from AOX- and UOX-grades of BeO, but some made from Minox AAA-grade were included. Grain sizes ranged from about 3 to 110 microns at nominal densities of 2.6, 2.75, and 2.9 g/cm^3. The basic irradiation program outlined in Figure 3.1 was followed. However, variations in the reactor cycle length and the flux-profile in various irradiation facilities resulted in dosages near the indicated values. In the highest dosage tests, specimens consisted exclusively of the small grain sizes (5, 10, 20 microns), since early results* indicated that these materials

---

*"Third Annual Report – High-Temperature Materials and Reactor Component Development Programs, Volume I – Materials," GE-NMPO, GEMP-270A, February 28, 1964, pp. 107–136.

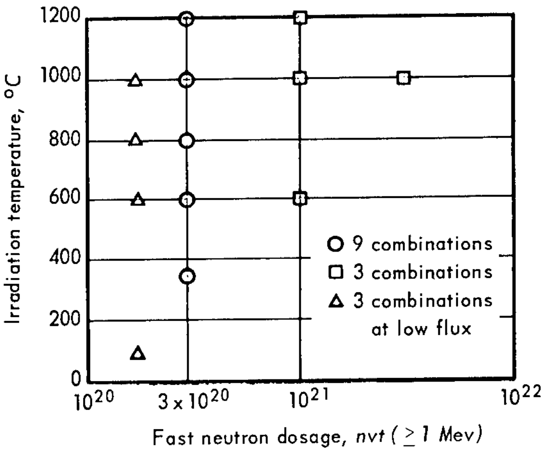

Compositions

1. AOX-grade BeO
2. UOX-grade BeO plus 0.5 wt % MgO
3. HPA-grade BeO

Grain size and density combinations

Density, g/cm^3	Grain size, microns
2.95 – 3.00	5, 20
2.90 – 2.95	5, 10, 20, 50, 80, 100
2.75 – 2.80	5, 10, 20, 50, 80
2.60 – 2.65	10, 20, 50, 80

(Not all of the listed combinations are used in all three compositions.)

GE-NMPO

Fig. 3.1 – Irradiation and measurement conditions of grain size – density series

possessed superior radiation stability in terms of expansion and strength changes. All originally planned irradiations of this series were completed, as summarized in Table 3.1. Post-irradiation measurements of dimensional changes were completed for most of these tests. Current work consists of more detailed measurements, such as helium analyses, lattice and microscopic expansion, and property measurements.

A second test series in progress is concerned with the influence on irradiation behavior of additives which either are, or form, glass-phases in BeO. In addition to promoting sinterability, it was considered possible that the glass phase might increase dimensional stability of the BeO at lower irradiation temperatures by relieving the grain boundary stresses that result in microcracking. The principal composition in this series is UOX-grade BeO containing 1.0 weight percent bentonite, a montmorillonite clay. This is the composition selected by General Atomics for use in the Experimental Beryllium Oxide Reactor (EBOR). Four other compositions are also being examined to some extent in this series; these include UOX-grade BeO plus 2 weight percent bentonite, and UOX plus 1 weight percent of high-, medium-, and low-silica glasses of compositions listed in Table 3.2. Grain sizes of the EBOR specimens obtained from EBOR production blocks range from 22 to 28 microns, and the densities from 2.85 to 2.88 g/cm^3. The grain size and density of BeO plus 2 weight percent bentonite are comparable to EBOR material, while the three silica glass compositions are of both 5 and 20 micron grain sizes with densities of 2.85 to 2.9 g/cm^3. Irradiation conditions for this series of tests are outlined in Figure 3.2. With the exception of the 100°C test, these irradiations were combined with those of specimens and tests of the grain size - density series summarized in Table 3.1. While all irradiations were completed, dimensional measurements of 100°C specimens and most detailed measurements and property changes of all specimens are yet to be completed.

Further irradiations planned or currently in preparation are summarized in Table 3.3. These include a test at 100°C to evaluate BeO compositions containing 1 to 2 percent Be additions and Thermalox 995, a Brush Beryllium Company commercial- and nuclear-grade BeO containing about 0.4 weight percent Al_2O_3 and about 0.1 weight percent SiO_2 in UOX-grade BeO.* A combined size effect and in-pile thermal conductivity test (relative) utilizing specimens 2.5 cm in diameter by 2.5 cm long is also planned. The last two tests indicated in Table 3.3 were re-insertions of samples previously irradiated to high dosages

---

*The composition of Thermalox 995 was stated incorrectly in "High-Temperature Materials Program Progress Report No. 42, Part A," GE-NMPO, GEMP-42A, December 18, 1964.

TABLE 3.1

IRRADIATION TEST SCHEDULE AND STATUS FOR BeO SPECIMENS OF GRAIN SIZE - DENSITY SERIES

Test No.	No. Of Specimens	Temperature, °C	Dosage,[a] 10^{20} nvt (≥1 Mev)	Irradiation ETR Cycle Dates		Facility	No. Of Cartridges	Status
				Start	End			
Tests at a flux of 1.5 to 4 x 10^{14} nv (≥1 Mev)								
33MT61	54	600	10.7 to 17.6	3-19-62	8-6-62	I-13	3	Completed
66MT50	366	1000	7.6 to 12.2	7-8-62	10-15-62	66	1	Completed
33MT76	81[b]	100	1.0 to 6.9	7-8-62	8-6-62	I-13	1	Completed
33MT73	36	100	3.2 to 5.0	7-8-62	8-6-62	L-6	1	Completed
33MT75	108[c]	100	0.8 to 2.6	7-8-62	8-6-62	E-5	3	Completed
33MT72	36	600	100	-	-	-	2	Cancelled
33MT82	24	300, 400, 500, 600	3.3 to 3.8	8-6-62	9-17-62	I-13	1	Completed
33MT68	54	1000	5.9 to 11.5	8-6-62	11-26-62	I-13	3	Completed
33MT59	18	1200	3.7 to 4.3	9-17-62	10-15-62	I-13	1	Completed
33MT89	108	100	0.5 to 1.2	9-17-62	10-15-62	E-5	3	Completed
66MT49	183	600	5.1 to 9.3	10-15-62	2-18-63	66	1	Completed
66MT49	183	800	9.3 to 12.2	10-15-62	2-18-63	66	1	Completed
33MT91	18	1200	3.1 to 3.6	10-15-62	11-26-62	I-13	1	Completed
33MT92	18	1200	(9 to 12)	11-26-62	2-18-63	I-13	1	Completed
66MT62	197[e]	300	(2 to 3)	1-7-63	4-1-63	66	1	Cancelled
33MT64	54	1200	9.0 to 19.5	11-26-62	4-1-63	I-13	3	Completed
33MT95[e]	36	1000	(30 to 50)	11-26-62	9-13-63	L-6	1	Completed
33MT95-2B[f]	18	1000	(30 to 50)	8-5-63	5-4-64	L-6	1	Completed
33MT111	36	1000	(30 to 50)	10-28-63	9-15-64	I-13	1	Completed
33MT105[f]	72	1000	(7.5 to 15)	10-28-63	1-19-64	I-13	2	Completed
Tests at a flux of ~6 x 10^{13} nv (≥1 Mev)								
33MT97	36	100	(1.9 to 2.4)	2-18-63	5-13-63	N-14	1	Completed
33MT83[f]	18	700	1.8 to 2.8	3-16-63	6-24-63	E-5	1	Completed
33MT90[f]	18	500	2.2 to 3.1	3-16-63	6-24-63	N-14	1	Completed
33MT98	36	300	(1.6 to 2.4)	6-24-63	9-13-63	E-5	1	Completed
33MT101	36	400	(2.0 to 2.8)	6-24-63	9-13-63	N-14	1	Completed
33MT127	36	>900	(~2)	-	-	E-5	1	Cancelled
Tests at a flux of ~9 x 10^{13} nv (≥1 Mev)								
33MT96	36	1000	(1.5 to 2.3)	4-3-63	5-31-63	E-14	1	Failed
33MT106[f]	36	600	(2.0 to 3.2)	8-5-63	10-28-63	E-14	1	Completed
33MT140[f, g]	126	100	(1.5 to 2)	1-20-64	3-1-64	E-14, F-15	3	Completed
33MT108[f]	36	200-350	(2.0 to 2.8)	10-28-63	1-19-64	N-14	1	Completed
Tests at a flux of 2 to 4 x 10^{13} nv (≥1 Mev)								
33MT110	36	300-400	-	-	-	F-15	-	Cancelled

[a] Dosages enclosed in parentheses are estimated.

[b] Consists of 18 full-length and sixty-three 2.54-cm specimens. The objective is to define the dosage required to initiate grain-boundary separation in irradiations at 100°C.

[c] 36 specimens to replace low dosage irradiation of composition series.

[d] This includes 14 specimens 8.9 cm long by 2.517 cm in diameter for thermal conductivity measurements.

[e] Replacement for 33MT72.

[f] These tests include specimens containing glass-phase additives; see Figure 2.1 for program outline.

[g] Formerly designated 33MT107.

in the 33MT95 and 33MT111 tests. These tests were specifically directed toward verification of the kinetic relationships derived for the radiation-induced expansion. The last planned test (GEFP2-135) is tentative pending developments in computations or experimental results in the near future.

3.2 SPECIMEN DESCRIPTION AND PROPERTIES

SPECIMEN DESCRIPTION

Size

Specimens used in most of the earlier tests listed in Table 3.1 were solid, right cylinders 0.605 cm in diameter by 8.9 cm long. In later tests, particularly the high-dosage tests and those involving glass-phase additives, specimen length was reduced to either 4.44 or 3.63 centimeters.

TABLE 3.2

COMPOSITION OF GLASSES TO BE USED AS ADDITIVES IN BeO[a]

	Silica Glass Composition, wt %		
Compound	High	Medium	Low
SiO_2	82	53	30
Al_2O_3	4	22	20
CaO	-	10	20
MgO	-	7	10
BeO	-	8	10
Na_2O	10	-	-
ZrO_2	4	-	10

[a] Additives used in 1 weight percent concentration in UOX-grade BeO. Specimen density 92 to 95 percent of theoretical density.

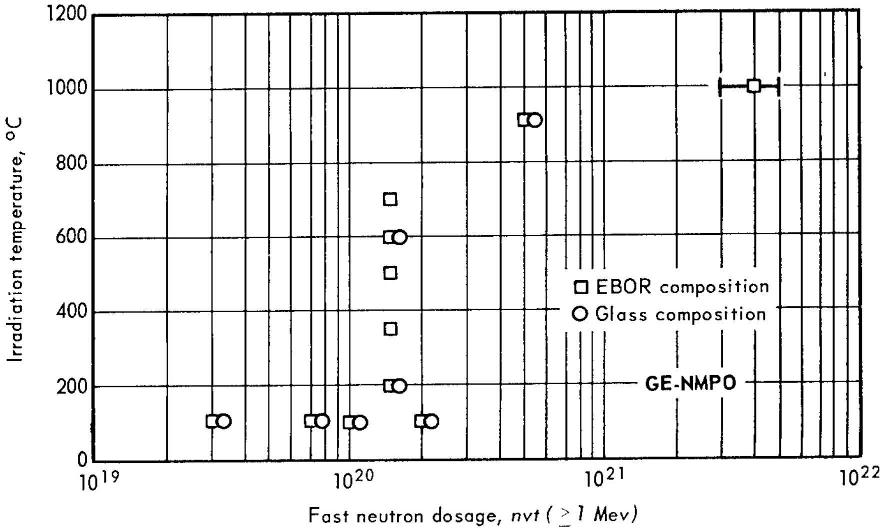

Fig. 3.2 – Nominal irradiation conditions for BeO containing glass-phase additives

Preparation

Specimens of the grain size - density series were prepared principally by extrusion and isostatic pressing. Formed bodies were sintered in hydrogen and centerless ground to size. Those of the glass-phase series, with the exception of the EBOR composition, were prepared in a similar manner. Specimens of the EBOR material were obtained from core drillings of EBOR production blocks prepared by cold-pressing and sintering in air. All specimens were made from AOX-, UOX-, and HPA-grades of BeO. Each of these powders is briefly described below:

1. AOX-grade BeO, supplied by Brush Beryllium Company, is a relatively low-purity material, averaging about 1500 to 2000 ppm total impurities. Principal impurity elements, present in concentrations of 100 ppm or higher, are Fe, Na, Si, C, and Mg. Size of crystallites determined by X-ray analysis is about 400 Å.

TABLE 3.3

PLANNED IRRADIATION TESTS OF BeO

Test Number	Irradiation Conditions		Purpose	Approximate Irradiation Dates	
	Temperature, °C	Dosage, 10^{20} nvt ($\geq$1 Mev)		Start	End
GEFP2-216	100	1 to 2	Evaluation of BeO + Be and Thermalox 995 compositions	1/1/65	3/31/65
GEFP2-217	100	2 to 5			
GEFP2-134	1000	10 to 20	Size effect and relative thermal conductivity	3/29/65	2/66
GEFP2-132	1000	20 to 40[a]	Determine if saturation of expansion occurs	6/15/65	1/15/66
GEFP2-135	1200	2 to 4[a]	Determine in-pile annealing of previously induced defects	6/15/65	3/31/65

[a] Figures shown are dosages to be added in this irradiation. These specimens have accumulated dosages of 2 to 6 x 10^{21} nvt ($\geq$1 Mev) at about 1000°C in previous irradiations.

2. UOX-grade BeO is also supplied by Brush Beryllium Company. Although the production process was not described by the manufacturer, UOX-grade BeO is generally considered to be derived from the sulfate. Principal impurity elements are S (400 to 1000 ppm), Ca (~100 ppm), and C (~100 ppm); total impurity concentrations range from 800 to 1500 ppm. Crystallite sizes range from 600 to 1000 Å, with small concentrations of rod-like crystallites ranging up to 150 microns in length. This is the most readily sinterable of the three grades of powder.
3. HPA-grade BeO is a GE-NMPO designation for high-purity BeO derived from the basic acetate process. The material used in this program is obtained from Mineral Concentrates and Chemical Company as beryllium hydroxide. After being calcined to BeO at 950°C, the material contains a total of 100 to 150 ppm of impurities and is comprised of crystallites about 1000 Å in diameter.

A more detailed description of these powders and of the production and inspection processes were presented in the first GE-NMPO annual report.*

Purity

There is comparatively little difference in impurity concentrations of various compositions in the as-sintered condition. Total impurities, exclusive of additives, nominally range from 400 to about 800 ppm, with HPA materials falling at the low end of this range. Impurities present in concentrations of the order of 100 ppm include Fe, C, Si, Mg, and Ca. In terms of induced radioactivity, AOX materials are the most impure. Scandium is the principal impurity observed (2 to 3 months after irradiation), its level in AOX being about four times that in UOX.

Microstructure

With the exception of UOX-ZrO_2, all compositions studied, including those containing glass-phase additives, appeared to be single-phase materials in electron micrographs. Evidence from electron microprobe studies, microhardness measurements, and thermal etching techniques indicated that MgO and glass additives were concentrated to some extent in grain boundaries. Photomicrographs typical of structures of various grain sizes† and densities were presented in a previous report.‡

---

* "First Annual Report – High-Temperature Materials and Reactor Component Development Programs, Volume I – Materials," GE-NMPO, GEMP-106A, February 28, 1962, pp. 76–88.

† Grain sizes reported are calculated from lineal analysis of polished sections, as described in ASTM Method E112.

‡ "Second Annual Report – High-Temperature Materials and Reactor Component Development Programs, Volume I – Materials," GE-NMPO, GEMP-177A, February 28, 1963, pp. 118–120.

Porosity

Pore size and type vary with both grain size and density. In materials of 3 to 7 micron grain size, porosity is almost entirely of the intergranular type. The amount of open or surface-connected porosity appears to increase linearly with the increase in total porosity. In some low-density specimens of this type, essentially all porosity was open; for example, many specimens of bulk density of about 2.6 g/cm^3 (~85% of theoretical density) had an apparent density within 0.2 to 0.3 percent of the theoretical density of 3.01 g/cm^3.* In specimens with grain sizes 20 microns and larger and bulk densities 96 to 98 percent of theoretical, about 90 percent of the porosity is intragranular. Individual pores in 20-micron materials were more or less uniformly 1 to 2 microns in size and spherical to ellipsoidal in shape. In materials with grain sizes of 60 to 100 microns, the pores in a given grain varied in size up to 20 microns but were predominantly 3 to 5 microns. Generally, in specimens with grain sizes of 20 microns or larger, increases in total porosity appeared to occur mainly by added intergranular pores. This was particularly true in the specimens having the lowest density (~15% total porosity) since it was necessary to add resin particles to attain low density and control of grain size. Voids left after burn-out of these resins resulted in predominantly intergranular pores.

Orientation

Orientation measurements of crystallographic axes in finished specimens established that AOX- and HPA-grade BeO specimens were essentially randomly oriented irrespective of the processing method. UOX-grade BeO specimens were also essentially randomly oriented when fabricated by isostatic pressing; when fabricated by extrusion, however, they contained a considerable amount of c-axis orientation along the longitudinal axis of the specimen. This preferential orientation, which was of simple <001> fiber texture, increased in amount with increasing specimen grain size. It increased linearly from about 5 percent in specimens of 3- to 5-micron grain size to about 55 percent in specimens of 20-micron grain size, and ranged from 75 to 80 percent in specimens larger than 45 microns.† Although the amount of orientation varied in specimens prepared from different lots of UOX powder, it was not significantly influenced within a given lot by variation of specimen density.‡ Planar orientation, i.e., c-axis orientation in the transverse plane of the specimen, has also been observed in cold-pressed materials; it occurs in small amounts (~15%) in some EBOR materials. Details of measurement techniques, distribution, magnitude, and causes of this preferential orientation were presented previously.§

PHYSICAL AND MECHANICAL PROPERTIES

A summary of physical and mechanical property measurements completed on specimens used in irradiation tests, together with other pertinent BeO data, are presented in Table 3.4. Details of these data were summarized previously.⊕

Measurements obtained on unirradiated material included modulus-of-rupture data on the EBOR composition, a few enthalpy determinations (cited later) made for comparison

---

* Bulk densities were determined essentially by ASTM Method C20-46, using diethylphthalate instead of water and vacuum impregnation instead of boiling. Apparent densities were determined by hydrostatic weighing in toluene following vacuum impregnation.

† Percent orientation is defined here as average projection of the crystallographic c-axis of grains on the longitudinal axis of specimens, with random orientation considered as zero percent orientation.

‡ "High-Temperature Materials Program Progress Report No. 28, Part A," GE-NMPO, GEMP-28A, November 11, 1963, p. 8.

§ "Second Annual Report – High-Temperature Materials and Reactor Component Development Programs, Volume I – Materials," GE-NMPO, GEMP-177A, February 28, 1963, pp. 117–126.

⊕ Ibid., pp. 126–151.

TABLE 3.4

PHYSICAL AND MECHANICAL PROPERTIES OF UNIRRADIATED BeO

References

DYNAMIC ELASTIC CONSTANTS ($20^{o}C$, 10^{12} dynes/cm^2, porosity range 0.02-0.16) GEMP-177[a]

AOX (Extruded)

This table

Young's Modulus $E = E_o \left[1 + \frac{AP}{1 - (A + 1)P}\right]$ (Hasselman Equation)

D. P. H. Hasselman, Journal American Ceramic Society, 45, 9, 452-53, 1962.

Grain Size, microns	E_o				A
	10^{12} dynes/cm^2	σ	10^6 psi	σ	
5	3.974	0.078	57.64	1.14	-2.75
10	3.964	0.006	57.50	0.09	-2.60
20	3.902	0.008	56.59	0.12	-2.03
50	3.906	0.004	56.65	0.06	-2.01
80	3.861	0.052	56.00	0.75	-2.01
Combined	3.919	0.052	56.84	0.75	-2.10

Shear Modulus (Torsion) $G = G_o \left[1 + \frac{AP}{1-(A+1)P}\right]$ (Hasselman Equation)

D. P. H. Hasselman, Journal American Ceramic Society, 45, 9, 452-53, 1962.

This table

Grain Size, microns	G_o				A
	10^{12} dynes/cm^2	σ	10^6 psi	σ	
5	1.640	0.026	23.79	0.38	-2.84
10	1.648	0.014	23.91	0.20	-2.73
20	1.640	0.005	23.79	0.07	-2.42
50	1.627	0.004	23.60	0.06	-2.26
80	1.606	0.015	23.30	0.22	-2.26
Combined	1.633	0.019	23.69	0.27	-2.52

Young's And Shear Moduli Versus Temperature, ^{o}C
Extruded AOX, 20^{o}-$1400^{o}C$, 5-50 micron grain size, 0.02-0.09 porosity

This table

$$\% \Delta E \text{ from } 20^{o}C = 7.77 \times 10^{-3} (T-20) + 4.76 \times 10^{-7} (T-20)^2 + 1.23 \times 10^{-9} (T-20)^3$$

Symbols: E = Young's modulus, 10^{12} dynes/cm^2; E_o = Young's modulus, 10^{12} dynes/cm^2 at theoretical density of 3.01 g/cm^3; G = shear modulus, 10^{12} dynes/cm^2; G_o = shear modulus, 10^{12} dynes/cm^2 at theoretical density of 3.01 g/cm^3; P = fractional porosity; A = porosity coefficient; T = temperature, ^{o}C; σ = standard deviation of observed E or G values compared to the values calculated from the equation using the listed equation constants.

MODULUS OF RUPTURE
(4 point, 7.6 cm span, third point loading, 0.15 cm/min head travel)

$$S = kG^{-a} e^{-bP}$$

(10-100 micron grain size, 0.02-0.16 fractional porosity)

F. P. Knudsen, Journal American Ceramic Society, 42, 376-387, 1959.

This table

Temp., ^{o}C	AOX (extruded)			UOX-MgO (extruded)		
	k	a	b	k	a	b
20	9.98(142)*	0.50	2.51	6.17(87.7)*	0.35	2.19
300	9.98(142)	0.49	2.95	6.05(86.0)	0.31	3.79
500	7.94(113)	0.44	1.54	6.17(87.8)	0.31	3.57
800	5.32(75.7)	0.28	2.32	5.37(76.4)	0.23	2.85
1000	2.93(41.7)	0.15	1.52	4.50(64.0)	0.19	2.97
1200	1.68(23.9)	0.03	1.44	3.47(49.4)	0.11	4.25

Symbols: S = M/R, 10^3 kg/cm^2; G = grain size, microns; P= fractional porosity.

*Values in parentheses refer to English system where S = M/R, 10^3 psi.

THERMAL EXPANSION

Linear Coefficient, μ cm/cm-^{o}C, AOX (extruded) 25^{o}-$1200^{o}C$

This table

$$\alpha = 5.866 + 3.870 \times 10^{-3} (T-25) - 7.034 \times 10^{-7} (T-25)^2$$

Percent Linear Expansion, AOX (extruded) 25^{o}-$1200^{o}C$

GEMP-177A[a]

$$\% \text{ Exp.} = 5.866 \times 10^{-4} (T-25) + 3.870 \times 10^{-7} (T-25)^2 - 7.034 \times 10^{-11} (T-25)^3$$

COMPRESSIVE CREEP AT $1200^{o}C$

(0-422 kg/cm^2, 5-100 micron grain size)

Creep Rate, μ cm/cm-hr	Diffusion Coefficient, cm^2/sec*	GEMP-22A *GEMP-177A[a]
AOX (extruded) $\dot{\epsilon} = 102.7 \times 10^{-7} \sigma/\mu^2$ ($\dot{\epsilon} = 7.22 \times 10^{-7} \sigma/\mu^2$)†	$D = 1 \times 10^{-14} cm^2/sec$	
UOX-MgO (extruded) $\dot{\epsilon} = 58.7 \times 10^{-7} \sigma/\mu^2$ ($\dot{\epsilon} = 4.13 \times 10^{-7} \sigma/\mu^2$)†	$D = 6 \times 10^{-15} cm^2/sec$	

Symbols: $\dot{\epsilon}$ = creep rate, μ cm/cm-hr; σ = compressive stress, kg/cm^2; μ= grain size, microns

†English system where $\dot{\epsilon}$ = creep rate, μ in./in.-hr; σ = compressive stress, psi.

TABLE 3.4

PHYSICAL AND MECHANICAL PROPERTIES OF UNIRRADIATED BeO

References

DYNAMIC ELASTIC CONSTANTS ($20^{o}C$, 10^{12} dynes/cm^2, porosity range 0.02-0.16) GEMP-177[a]

Grain Size, microns	AOX (Extruded)				
	E_o				A
	10^{12} dynes/cm^2	σ	10^6 psi	σ	

This table

Young's Modulus $E = E_o \left[1 + \frac{AP}{1 - (A+1)P}\right]$ (Hasselman Equation)

D. P. H. Hasselman, Journal American Ceramic Society, 45, 9, 452-53, 1962.

Grain Size, microns	E_o 10^{12} dynes/cm^2	σ	10^6 psi	σ	A
5	3.974	0.078	57.64	1.14	-2.75
10	3.964	0.006	57.50	0.09	-2.60
20	3.902	0.008	56.59	0.12	-2.03
50	3.906	0.004	56.65	0.06	-2.01
80	3.861	0.052	56.00	0.75	-2.01
Combined	3.919	0.052	56.84	0.75	-2.10

Shear Modulus (Torsion) $G = G_o \left[1 + \frac{AP}{1-(A+1)P}\right]$ (Hasselman Equation)

D. P. H. Hasselman, Journal American Ceramic Society, 45, 9, 452-53, 1962.

This table

Grain Size, microns	G_o 10^{12} dynes/cm^2	σ	10^6 psi	σ	A
5	1.640	0.026	23.79	0.38	-2.84
10	1.648	0.014	23.91	0.20	-2.73
20	1.640	0.005	23.79	0.07	-2.42
50	1.627	0.004	23.60	0.06	-2.26
80	1.606	0.015	23.30	0.22	-2.26
Combined	1.633	0.019	23.69	0.27	-2.52

Young's And Shear Moduli Versus Temperature, ^{o}C

Extruded AOX, 20^{o}-$1400^{o}C$, 5-50 micron grain size, 0.02-0.09 porosity

This table

$$\% \Delta E \text{ from } 20^{o}C = 7.77 \times 10^{-3}(T-20) + 4.76 \times 10^{-7}(T-20)^2 + 1.23 \times 10^{-9}(T-20)^3$$

Symbols: E = Young's modulus, 10^{12} dynes/cm^2; E_o = Young's modulus, 10^{12} dynes/cm^2 at theoretical density of 3.01 g/cm^3; G = shear modulus, 10^{12} dynes/cm^2; G_o = shear modulus, 10^{12} dynes/cm^2 at theoretical density of 3.01 g/cm^3; P = fractional porosity; A = porosity coefficient; T = temperature, ^{o}C; σ = standard deviation of observed E or G values compared to the values calculated from the equation using the listed equation constants.

MODULUS OF RUPTURE

(4 point, 7.6 cm span, third point loading, 0.15 cm/min head travel)

$$S = kG^{-a} e^{-bP}$$

(10-100 micron grain size, 0.02-0.16 fractional porosity)

F. P. Knudsen, Journal American Ceramic Society, 42, 376-387, 1959.

This table

Temp., ^{o}C	AOX (extruded) k	AOX (extruded) a	AOX (extruded) b	UOX-MgO (extruded) k	UOX-MgO (extruded) a	UOX-MgO (extruded) b
20	9.98(142)*	0.50	2.51	6.17(87.7)*	0.35	2.19
300	9.98(142)	0.49	2.95	6.05(86.0)	0.31	3.79
500	7.94(113)	0.44	1.54	6.17(87.8)	0.31	3.57
800	5.32(75.7)	0.28	2.32	5.37(76.4)	0.23	2.85
1000	2.93(41.7)	0.15	1.52	4.50(64.0)	0.19	2.97
1200	1.68(23.9)	0.03	1.44	3.47(49.4)	0.11	4.25

Symbols: S = M/R, 10^3 kg/cm^2; G = grain size, microns; P = fractional porosity.

*Values in parentheses refer to English system where S = M/R, 10^3 psi.

THERMAL EXPANSION

Linear Coefficient, μcm/cm-^{o}C, AOX (extruded) 25^{o}-$1200^{o}C$

$$\alpha = 5.866 + 3.870 \times 10^{-3}(T-25) - 7.034 \times 10^{-7}(T-25)^2$$

This table

Percent Linear Expansion, AOX (extruded) 25^{o}-$1200^{o}C$

$$\% \text{ Exp.} = 5.866 \times 10^{-4}(T-25) + 3.870 \times 10^{-7}(T-25)^2 - 7.034 \times 10^{-11}(T-25)^3$$

GEMP-177A[a]

COMPRESSIVE CREEP AT $1200^{o}C$

(0-422 kg/cm^2, 5-100 micron grain size)

	Creep Rate, μ cm/cm-hr	Diffusion Coefficient, cm^2/sec*
AOX (extruded)	$\dot{\epsilon} = 102.7 \times 10^{-7}\ \sigma/\mu^2$ ($\dot{\epsilon} = 7.22 \times 10^{-7}\ \sigma/\mu^2$)†	$D = 1 \times 10^{-14}$ cm^2/sec
UOX-MgO (extruded)	$\dot{\epsilon} = 58.7 \times 10^{-7}\ \sigma/\mu^2$ ($\dot{\epsilon} = 4.13 \times 10^{-7}\ \sigma/\mu^2$)†	$D = 6 \times 10^{-15}$ cm^2/sec

GEMP-22A
*GEMP-177A[a]

Symbols: $\dot{\epsilon}$ = creep rate, μcm/cm-hr; σ = compressive stress, kg/cm^2; μ = grain size, microns

†English system where $\dot{\epsilon}$ = creep rate, μin./in.-hr; σ = compressive stress, psi.

with those for irradiated material, and additional elastic constant data. Strength measurements on the EBOR material yielded average room-temperature modulus-of-rupture values ranging from 1.87 to 2.52 x 10^3 kg/cm^2 for specimens obtained from five production blocks.* Elastic constant data are summarized in the following paragraphs.

Elastic Constants

Equipment was assembled for measuring resonant vibration frequencies of specimens over a much larger range than was possible with usual equipment. The extended frequency capability aided in identification of resonant vibration modes through observation of both the fundamental frequencies and their harmonics. It also extended the capability of measuring elastic constants in irradiated material as well as in relatively small specimens (2.5 to 3.7 cm long by 0.6 cm in diameter) such as those used in EBOR material studies. A schematic diagram of the instrument assembly is shown in Figure 3.3. With this equipment and lead zirconate - lead titanate transducer crystals,† resonant frequencies were followed up to 880 kilocycles.

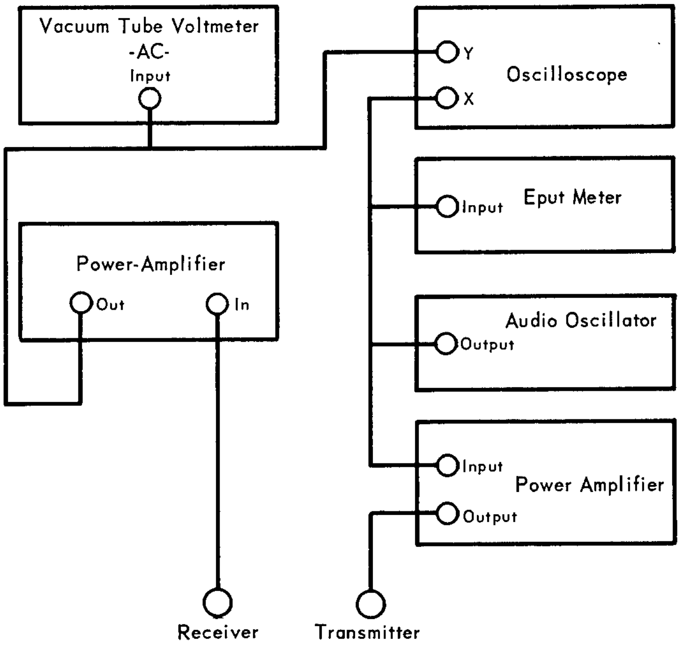

Fig. 3.3 – Instruments and circuit utilized in resonant frequency measurements for determining elastic constants up to approximately 1 megacycle. The transducer crystals employed are lead zirconate-lead titanate.

Representative measurements on three BeO compositions of different specimen sizes are summarized in Table 3.5. These data list all apparent resonant frequencies.

Elastic constants for several BeO compositions determined with the high-frequency equipment are summarized in Table 3.6. Listed values include shear modulus, based on the average of torsional frequencies; Young's moduli, based on flexural and longitudinal frequencies and on the average of the two frequencies. Young's moduli determined from flexural and longitudinal vibration modes agreed, in general, within 1.0 per-

---

* "High-Temperature Materials Program Progress Report No. 40, Part A," GE-NMPO, GEMP-40A, October 15, 1964, p. 15.

† Crystals obtained from Gulton Industries, Inc., Metuchen, New Jersey, were ground to a size (about 3 mm thick by 2.5 cm in diameter) to resonate at about 600 kilocycles.

TABLE 3.5

RESONANT FREQUENCIES OBSERVED IN ELASTIC CONSTANT MEASUREMENTS

AOX-grade BeO 17-micron grain size; 2.90 g/cm^3 density; 0.6 cm diameter by 8.89 cm long			UOX + MgO-grade BeO 17-micron grain size; 2.90 g/cm^3 density; 0.6 cm diameter by 8.89 cm long			AOX-grade BeO 10-micron grain size; 2.90 g/cm^3 density; 0.6 cm diameter by 4.37 cm long			EBOR 25-micron grain size; 2.83 g/cm^3 density; 0.6 cm diameter by 3.66 cm long		
Identified Vibration Mode[a]	Observed Resonant Frequencies, kc/sec	Summary Of Resonant Frequencies	Identified Vibration Mode	Observed Resonant Frequencies, kc/sec	Summary Of Resonant Frequencies	Identified Vibration Mode	Observed Resonant Frequencies, kc/sec	Summary Of Resonant Frequencies	Identified Vibration Mode	Observed Resonant Frequencies, kc/sec	Summary Of Resonant Frequencies
F_1	7.520	$T_{4/4}$ = 40.348	F_1	7.682	T_1 = 39.692		27.558			25.345	
F_2	20.251	$T_{5/5}$ = 40.356	F_2	20.726	$T_{4/4}$ = 39.731	F_1	29.613			34.768	
	27.581	$T_{7/7}$ = 40.349		27.523	$T_{5/5}$ = 39.738	F_2	76.178		F_1	40.676	T_1 = 95.011
	27.955	$T_{8/8}$ = 40.351		28.666	$T_{7/7}$ = 39.734		79.166	T_1 = 81.302		53.197	$T_{2/2}$ = 95.416
	35.385	$T_{10/10}$ = 40.351	F_3	39.453	$T_{10/10}$ = 39.733	T_1	81.302	$T_{2/2}$ = 81.284		69.068	$T_{3/3}$ = 95.360
F_3	38.614	$T_{11/11}$ = 40.352	T_1	39.692			84.556	$T_{4/4}$ = 81.294		73.027	
	51.228	$T_{14/14}$ = 40.349		50.802			86.634	$T_{5/5}$ = 81.299		78.501	$\overline{T}$ = 95.262
	53.141			52.712			99.556			79.735	
F_4	61.561	$\overline{T}$ = 40.351	F_4	63.009	$\overline{T}$ = 39.734	L_1	126.532	$\overline{T}$ = 81.295		86.183	
	61.811		L_1	64.117		F_3	137.106			90.655	
L_1	62.724			77.399		T_2	162.567		T_1	95.011	
	76.805	L_1 = 62.724	F_5	90.320	L_1 = 64.117	F_4	206.757			101.840	L_1 = 147.533
	79.286	$L_{2/2}$ = 62.654	F_6	120.733	$L_{2/2}$ = 64.090		223.734	L_1 = 126.532	F_2	102.394	$L_{2/2}$ = 147.529
	84.773	$L_{3/3}$ = 62.640	L_2	128.179	$L_{3/3}$ = 64.071	L_2	252.473	$L_{2/2}$ = 126.236		105.989	$L_{3/3}$ = 146.873
	86.663	$L_{4/4}$ = 62.571	T_4	158.923	$L_{4/4}$ = 64.011		262.193		L_1	147.533	
F_5	88.064	$L_{5/5}$ = 62.506	L_3	192.212	$L_{5/5}$ = 63.941		281.442		F_3	180.027	
	93.182	$L_{7/7}$ = 62.297	T_5	198.692	$L_{7/7}$ = 63.757	T_4	325.176		T_2	190.833	
	100.094			224.246	$L_{8/8}$ = 63.608	F_6	359.133			220.122	F_2/F_1 = 2.52
F_6	118.816		L_4	256.044		T_5	406.493	F_2/F_1 = 2.57		223.240	F_3/F_1 = 4.42
L_2	125.307			261.460			437.800	F_3/F_1 = 4.63	F_4	266.280	F_4/F_1 = 6.55
	126.997	F_2/F_1 = 2.69	T_7	278.141	F_2/F_1 = 2.70		516.336	F_4/F_1 = 6.98	T_3	286.081	
F_7	151.348	F_3/F_1 = 5.13		299.347	F_3/F_1 = 5.14				L_2	295.058	
T_4	161.392	F_4/F_1 = 8.19	L_5	319.705	F_4/F_1 = 8.20			F_6/F_1 = 12.13	L_3	440.618	
L_3	187.919	F_5/F_1 = 11.71		337.813	F_5/F_1 = 11.76					448.644	$\nu_{est.}$ = 0.199
T_5	201.780	F_6/F_1 = 15.80		376.728	F_6/F_1 = 15.72			$\nu_{est.}$ = 0.211			
	220.679	F_7/F_1 = 20.12	T_{10}	397.332							
L_4	250.283			415.897							
	259.040		L_7	446.300							
T_7	282.443		L_8	508.864	$\nu_{est.}$ = 0.302						
	297.110	$\nu_{est.}$ = 0.208[b]									
L_5	312.528										
T_8	322.814										
	335.786										
T_{10}	403.513										
	414.417										
L_7	436.077										
T_{11}	443.877										
	533.476										
T_{14}	564.885										

---

[a] The letters F, T, and L designate respectively the resonant frequencies of the flexural (transverse), torsional, and longitudinal vibration modes. The subscripts refer to the harmonics of the particular vibration mode with 1 designating the fundamental. The unmarked frequencies include additional harmonics of the flexural mode of vibration as well as various resonant frequencies of the "system" which includes the specimen, its support, the driving and receiving wires, and the driving and receiving crystals.

[b] The estimated value of Poisson's ratio, $\nu_{est.}$, is calculated from the equation, $\nu = \frac{1}{2}\left(\frac{L_1}{T}\right)^2 - 1$. This value is approximate only because a small correction factor must be applied to the longitudinal frequency.

TABLE 3.6

DYNAMIC ELASTIC CONSTANTS OF SEVERAL BeO COMPOSITIONS

Composition	Specimen Description: Grain Size, microns	Specimen Description: Density, g/cm^3	Specimen Description: Nominal Length, cm	Shear Modulus, (torsional vibration)		Young's Modulus, (flexural vibration)		Young's Modulus, (longitudinal vibration)		Young's Modulus, (average of flexural and longitudinal)		Poisson's Ratio (average)[a]
				10^6 psi	10^{12} dynes/cm^2	10^6 psi	10^{12} dynes/cm^2	10^6 psi	10^{12} dynes/cm^2	10^6 psi	10^{12} dynes/cm^2	
AOX	20	2.90	8.89	21.4	1.48	51.8	3.57	51.7	3.56	51.7	3.56	0.21
	17	2.90	8.89	21.6	1.49	52.0	3.58	52.1	3.59	52.0	3.58	0.21
	17	2.90	8.89	21.4	1.48	51.7	3.56	51.6	3.56	51.7	3.56	0.21
	12	2.58	4.37	16.6	1.14	41.4	2.85	41.6	2.87	41.5	2.86	0.25
	10	2.86	4.37	20.9	1.44	50.3	3.47	50.7	3.50	50.5	3.48	0.21
UOX-MgO	17	2.91	8.89	21.0	1.45	55.0	3.79	55.6	3.83	55.3	3.81	0.31
	17	2.91	8.89	21.1	1.45	54.7	3.77	55.2	3.80	54.9	3.78	0.30
	17	2.91	8.89	21.0	1.45	55.0	3.79	54.8	3.78	54.9	3.78	0.31
	18	2.90	4.37	20.8	1.43	53.8	3.71	54.9	3.78	54.4	3.75	0.31
	18	2.90	4.37	21.0	1.45	55.0	3.79	56.0	3.86	55.5	3.83	0.32
	22	2.78	4.37	19.2	1.32	51.2	3.53	52.3	3.60	51.7	3.56	0.34
UOX-Glass (2% high-silica glass)[b]	18	2.88	8.89	20.3	1.40	52.4	3.61	52.8	3.64	52.6	3.63	0.30
	18	2.88	4.37	20.2	1.39	52.8	3.64	53.5	3.69	53.1	3.66	0.31
	18	2.88	4.37	20.3	1.40	52.6	3.63	53.1	3.66	52.8	3.64	0.30
	20	2.88	4.37	20.3	1.40	52.5	3.62	53.1	3.66	52.8	3.64	0.30
	20	2.88	4.37	20.3	1.40	52.4	3.61	53.0	3.65	52.8	3.64	0.30
	24	2.87	4.37	20.1	1.38	52.3	3.60	52.9	3.65	52.5	3.62	0.31
	24	2.87	4.37	20.0	1.38	51.9	3.58	52.5	3.62	52.1	3.59	0.30
UOX-2% Bentonite	18	2.86	4.37	20.1	1.38	51.0	3.52	51.4	3.54	51.2	3.53	0.27
	18	2.86	4.37	20.2	1.39	51.7	3.56	52.1	3.59	51.8	3.57	0.28
	22	2.86	8.89	20.2	1.39	51.5	3.55	51.4	3.54	51.4	3.54	0.28
	22	2.86	4.37	20.3	1.40	51.7	3.56	51.8	3.57	51.7	3.56	0.27
	22	2.86	4.37	20.2	1.39	51.5	3.55	51.9	3.58	51.6	3.56	0.28

[a] Poisson's ratio values listed were computed from the shear modulus and the average Young's modulus as listed in the penultimate column.

[b] Composition of the glass additive is $82SiO_2 - 4Al_2O_3 - 10Na_2O - 4ZrO_2$ (wt %).

TABLE 3.6 (Cont.)

DYNAMIC ELASTIC CONSTANTS OF SEVERAL BeO COMPOSITIONS

Composition	Specimen Description			Shear Modulus (torsional vibration)		Young's Modulus, (fluxural vibration)		Young's Modulus, (longitudinal vibration)		Young's Modulus, (average of flexural and longitudinal)		Poisson's Ratio (average)[a]
	Grain Size, microns	Density, g/cm^3	Nominal Length, cm	10^6 psi	10^{12} dynes/cm^2	10^6 psi	10^{12} dynes/cm^2	10^6 psi	10^{12} dynes/cm^2	10^6 psi	10^{12} dynes/cm^2	
EBOR[c]												
Block B75-93	17	2.81	3.66	19.8	1.36	47.4	3.27	47.6	3.28	47.5	3.27	0.20
B75-93	17	2.80	3.66	19.7	1.36	47.2	3.25	47.3	3.26	47.2	3.25	0.20
B79-100	24	2.79	3.66	19.9	1.37	47.4	3.27	47.8	3.30	47.5	3.27	0.20
B79-100	24	2.82	3.66	19.5	1.34	46.9	3.23	47.1	3.25	47.0	3.24	0.20
B86-47	29	2.82	3.66	20.1	1.38	48.0	3.31	48.4	3.34	48.2	3.32	0.20
B86-47	29	2.82	3.66	20.0	1.38	48.0	3.31	48.1	3.32	48.0	3.31	0.20
B78-33	29	2.79	3.66	19.4	1.34	46.4	3.20	46.5	3.21	46.4	3.20	0.20
B78-33	29	2.83	3.66	19.9	1.37	48.1	3.32	47.8	3.30	48.0	3.31	0.20
EBOR[d]												
Block B106-45	22	2.82	3.66	19.6	1.35	46.9	3.23	47.1	3.25	47.0	3.24	0.20
Samples cut parallel	22	2.82	3.66	19.2	1.32	46.0	3.17	46.4	3.20	46.2	3.18	0.20
to pressing direction	22	2.82	3.66	19.1	1.32	45.8	3.16	46.0	3.17	45.9	3.16	0.20
	22	2.82	3.66	19.2	1.32	45.9	3.16	46.1	3.18	46.0	3.17	0.20
Block B106-45	22	2.82	3.66	19.6	1.35	46.9	3.23	47.2	3.25	47.0	3.24	0.20
Samples cut normal	22	2.82	3.66	19.9	1.37	47.1	3.25	47.1	3.25	47.1	3.25	0.18
to pressing direction	22	2.82	3.66	19.9	1.37	47.6	3.28	47.2	3.25	47.4	3.27	0.19
	22	2.82	3.66	19.4	1.34	46.2	3.18	46.6	3.21	46.4	3.20	0.20
Plug B147-8[e]	25	2.83	3.66	19.7	1.37	47.3	3.26	47.6	3.28	47.4	3.27	0.20
Samples cut parallel	25	2.83	3.66	20.1	1.38	48.3	3.33	48.7	3.36	48.5	3.34	0.20
to cylinder axis	25	2.83	3.66	19.8	1.36	47.6	3.28	47.9	3.30	47.8	3.30	0.20
Samples cut normal	25	2.83	3.66	19.8	1.36	47.5	3.27	47.8	3.30	47.6	3.28	0.20
to cylinder axis	25	2.83	3.66	20.0	1.38	47.9	3.30	48.3	3.33	48.0	3.31	0.20

[c] Samples were cut from EBOR production blocks supplied by General Atomic; the EBOR composition is UOX plus 1 wt % bentonite. Samples were obtained from core drillings taken parallel to the pressing direction; all samples were centerless ground to a final diameter of 0.6 ± 0.00254 cm.

[d] We are indebted to the Brush Beryllium Company for supplying these special samples from EBOR production materials.

[e] The plug is an isostatically pressed right cylinder approximately 4.76 cm diameter by 15.24 cm long.

cent, particularly for randomly oriented material (AOX-grade BeO). There was no apparent pattern of differences because of specimen size.

In UOX compositions, the difference ranged up to 2 percent, with the greatest disagreement occurring in shorter specimen lengths. The poorer agreement in the UOX compositions is related to the relatively high degree of preferred orientation (~50%*) in these extruded bodies. The Young's modulus and Poisson's ratio values cited for these materials are the apparent values obtained with equations that are strictly applicable only to isotropic bodies; correct mathematical treatment of the resonant frequency data, to be discussed in a future report, brings the Poisson's ratio values into approximate agreement with the 0.2 value obtained for randomly oriented material and results in a small change in the Young's moduli.

Elastic constant data for the EBOR BeO composition (UOX + 1 wt % bentonite) were about the same for different production blocks but varied to some extent with small amounts of preferred orientation within the blocks. These data are given in Table 3.6. The first group listed includes samples cut from production blocks used in irradiation tests completed or in progress. These samples were all cut parallel to the pressing direction.† The second group of samples listed, supplied by Brush Beryllium Company from production lots, included samples cut both parallel and normal to the pressing direction. Small amounts of planar orientation, ranging up to about 15 percent, probably account for variations in these samples.

Data shown in Table 3.7 for specimens of various grain sizes and densities were examined in terms of the Hasselman equations‡ which relate elastic constants to specimen porosity. These equations are:

$$E = E_0 \left[1 + \frac{AP}{1 - (A + 1)P}\right]$$

$$G = G_0 \left[1 + \frac{AP}{1 - (A + 1)P}\right]$$

where:

E is Young's modulus of a specimen of fractional porosity P

E_0 is extrapolated value of Young's modulus of BeO of theoretical density

G and G_0 are corresponding terms for shear modulus

A is an empirically determined constant.

Fractional porosity was determined from $P = 1 -$ (measured density/theoretical density). Constants determined by least-squares analysis and the standard deviation, σ, of measured values about the equation are recorded in Table 3.7. This analysis was limited to specimens with total porosity ranging up to 10 percent since the data for specimens of higher porosity deviated in the same direction from the equations and consequently appeared to be part of a separate population.

The variation of the equation constants for the different grain sizes corresponds roughly to differences in the type of porosity; however, no direct cause and effect relationship has been established. The Hasselman equations were derived for spherical pores; hence, some variation of the equation constants is to be expected from the irregular pore shapes occurring at grain boundaries. Hashin's analysis indicates that the constant A should have a value of -2.0 in a material with a Poisson's ratio of 0.2.§ The best fit of the experi-

---

*This percentage figure is based on average projection of the c-axis of grains on the longitudinal axis of the specimen as compared to randomly oriented material.

†The blocks were cold-pressed and sintered.

‡D. P. H. Hasselman, "On the Porosity Dependence of the Elastic Moduli of Polycrystalline Refractory Materials," *Journal of American Ceramic Society*, Vol. 45, 1962, p. 452.

§Z. Hashin, "The Elastic Moduli of Heterogeneous Materials," Paper No. 61-WA-39, presented at the annual meeting of the ASME, New York, November 1961.

TABLE 3.7

ELASTIC CONSTANT DATA FOR UNIRRADIATED AOX-GRADE BeO

Specimen Description		Young's Modulus[a]		Shear Modulus[b]			Equation Constants[c]										
Grain Size, microns	Bulk Density, gm/cm^3	10^6 psi	10^{12} dynes/cm^2	10^6 psi	10^{12} dynes/cm^2	Poisson's Ratio	E_o, 10^6 psi	σ, 10^6 psi	E_o, 10^{12} dynes/cm^2	σ, 10^{12} dynes/cm^2	A	G_o, 10^6 psi	σ, 10^6 psi	G_o, 10^{12} dynes/cm^2	σ, 10^{12} dynes/cm^2	A	ν_0
2	2.73	43.7	3.01	18.0	1.24	0.21	57.64	1.14	3.974	0.078	-2.75	23.79	0.38	1.640	0.026	-2.84	0.21
3	2.63	41.3	2.85	17.0	1.17	0.22											
6	2.80	48.9	3.37	20.0	1.38	0.22											
4	2.79	48.6	3.35	19.9	1.37	0.22											
5	2.90	51.9	3.58	21.3	1.47	0.22											
5	2.90	51.7	3.56	21.4	1.48	0.21											
12	2.58	41.5	2.86	16.6	1.14	0.25	57.50	0.09	3.964	0.006	-2.60	23.91	0.20	1.648	0.014	-2.73	0.20
12	2.59	41.5	2.86	16.5	1.14	0.26											
12	2.59	41.5	2.86	16.5	1.14	0.26											
9	2.76	46.6	3.21	19.2	1.32	0.21											
9	2.77	46.9	3.23	19.3	1.33	0.22											
10	2.86	50.5	3.48	20.9	1.44	0.21											
10	2.88	51.7	3.56	21.4	1.48	0.21											
10	2.90	52.2	3.60	21.6	1.49	0.21											
19	2.54	40.2	2.77	16.2	1.12	0.24	56.59	0.12	3.902	0.008	-2.03	23.79	0.07	1.640	0.005	-2.42	0.19
16	2.67	45.0	3.10	17.9	1.23	0.26											
17	2.76	47.7	3.29	19.4	1.34	0.23											
16	2.76	47.6	3.28	19.5	1.34	0.22											
17	2.89	52.3	3.60	21.7	1.50	0.21											
20	2.90	51.7	3.56	21.4	1.48	0.21											
17	2.90	52.0	3.58	21.6	1.49	0.21											
17	2.90	51.7	3.56	21.4	1.48	0.21											
42	2.66	43.6	3.01	17.8	1.23	0.22	56.65	0.06	3.906	0.004	-2.01	23.60	0.06	1.627	0.004	-2.26	0.20
41	2.69	44.7	3.08	18.4	1.27	0.22											
48	2.76	48.1	3.32	19.6	1.35	0.22											
48	2.77	48.2	3.32	19.8	1.36	0.22											
43	2.92	53.3	3.67	22.0	1.52	0.21											
43	2.92	53.3	3.67	22.0	1.52	0.21											
62	2.76	46.4	3.20	19.2	1.32	0.21	56.00	0.75	3.861	0.052	-2.10	23.30	0.22	1.606	0.015	-2.26	0.20
64	2.80	49.0	3.38	20.1	1.38	0.22											
74	2.86	51.2	3.53	21.1	1.45	0.21											
72	2.96	53.3	3.67	22.2	1.53	0.20											
(All grain sizes combined)							56.84	0.75	3.919	0.052	-2.30	23.69	0.27	1.633	0.019	-2.52	0.20

[a] Young's modulus values are the average of values calculated from the fundamental and the first two overtones of the resonant frequencies of both the flexural and the longitudinal modes of vibration.

[b] The shear modulus values are calculated from an average fundamental resonant frequency of the torsional mode of vibration. As many harmonics as can be detected are utilized. Methods of calculation are described in "High-Temperature Materials Program Progress Report No. 40, Part A," GEMP-40A, Oct. 15, 1964, pp. 9-15.

[c] Constants are for the Hasselman Equation,

$$E = E_o \left[1 + \frac{AP}{1-(A+1)P}\right]$$

in which P equals fractional porosity, $1 - \frac{\text{density}}{\text{theoretical density}}$.

[d] σ = Standard deviation of the observed E or G values compared to the values calculated from the equation using the listed equation constants.

mental data, and the closest approach to an A value of -2.0, occurs in the specimens of 15- to 50-micron grain size in which the pores are predominantly intragranular and spherical in shape. In contrast, the progressively larger A values for the specimens of 8- to 12-micron and 3- to 7-micron grain sizes is in the direction of increasing intergranular porosity. This latter trend was further indicated by the deviation between the observed and calculated values; in general, the observed E and G values of low-porosity specimens were smaller than the calculated values while the reverse was true for specimens of average porosity.

3.3 RADIATION EFFECTS

Previously reported studies* established that the most important aspect of the irradiation behavior was dimensional expansion and that the most important part of the expansion was the occurrence of grain boundary separation, or microcracking. The strength, elastic constants, and other properties of the irradiated material were found to be simply related to the microcracking which occurred even at elevated temperatures. Kinetic relationships indicated that microcracking might be avoided by the proper selection of temperature and irradiation flux. Accordingly, in CY-64, studies were made of the kinetics and of the factors that contribute to the expansion and microcracking. Results obtained in these areas are summarized in this section; in most instances a brief review of previous findings is given. An up-to-date summary of the irradiation behavior of BeO is presented in Table 3.8; further details of items noted in the table that are not covered in this report will be found in the previous annual report.*

KINETICS OF THE RADIATION-INDUCED EXPANSION

Continued efforts to define the kinetics of the expansion resulted in the derivation of separate equations for vacancy and interstitial defect concentrations in terms of flux, time, and irradiation temperature. The combined equations accurately predict the expansion, exclusive of microcracking, throughout the temperature range of 100° to $1200^{\circ}C$, at least for the time periods of the irradiations examined to date. Since expansion in this temperature range can be computed, it is possible to examine quantitatively the effects on expansion of the temperature cycling which accompanies the power variations during shutdown and startup of the reactor.

As noted in previous reports, analysis of the expansion data was made in terms of first-order kinetics, based in part on the indications of post-irradiation annealing studies. For the first-order case, the defect concentration, c, as a function of time is given by equation (3.1):

$$\frac{dc}{dt} = K - Ac \qquad (3.1)$$

where K is the defect production rate, A is an annealing rate constant proportional to the diffusion rate of the defects, and t is the time of irradiation. Integration results in equation (3.2):

$$c = \frac{K}{A} 1 - \exp(-At) \qquad (3.2)$$

which is applicable to either interstitial or vacancy defects with the appropriate definition of A. In considering the expansion data, the defect concentration was assumed to be proportional either to the volume or to the lattice expansion, as noted subsequently, and the pertinent value substituted for c. The defect production rate was based on 3.3 percent

---

*"Third Annual Report – High-Temperature Materials and Reactor Component Development Programs, Volume I – Materials," GE-NMPO, GEMP-270A, February 28, 1964, p. 110.

TABLE 3.8

SUMMARY OF RADIATION EFFECTS IN BeO[a]

TYPES OF EXPANSION	
1. Lattice Expansion	(Anisotropic) - In 100°C irradiations, c-axis expansion approximately 8 times that of the a-axis in the dosage region from about 1.7 to 5 x 10^{20} nvt (≥ 1 Mev). Rate of volume expansion (versus dosage) differs below and above dosage of approximately 1.7 x 10^{20} nvt.[b] Initial rate is 0.2 to 0.3 percent per 10^{20} nvt, then increases to about 0.36 percent per 10^{20} nvt. Amounts to approximately 3.3 percent at 10^{21} nvt (≥ 1 Mev). In irradiations at temperatures higher than about 600°C, expansion is predominantly in c-axis.
2. Microcracking	Expansion due to porosity introduced by cracking at the boundary between grains of unlike orientation. Caused by stresses developed from anisotropy of lattice expansion; ultimately leads to powdering of specimen at volume expansion of about 6 percent. Occurs at higher dosages in smaller grain sizes, and at higher irradiation temperatures.
3. Helium Bubbles	Bubbles form in the grain boundaries at temperatures as low as 600°C, possibly lower. Estimates of bubble volume range from 20 to 40 percent of a total expansion of about 1 percent in specimens irradiated at 900° to 1000°C to dosage of about 10^{21} nvt. Helium formed in (n, 2n) and (n, α) reactions in Be. Formation rate is about 0.36 cm^3 He per gram BeO per 10^{21} nvt (≥ 1 Mev). Apparent helium diffusion rate, based on gross specimen dimensions is of the order of 10^{-8} to 10^{-9} per second for specimens 0.6 cm in diameter. Helium escape is greatest in specimens in which grain-boundary separation occurs.
4. Defect Clusters	Interstitial clusters predominate at irradiation temperatures up to approximately 600°C; vacancy clusters predominate at higher temperatures. Size ranges up to 1200 Å at dosages of 1 to 2 x 10^{21} nvt (≥ 1 Mev). Density appears to be 10^{15} to $10^{17}/cm^3$.
MACROSCOPIC EXPANSION AT TEMPERATURES UP TO 500° TO 600°C	
Two Types	(1) Total expansion = lattice expansion (2) Total expansion = lattice expansion + microcracking

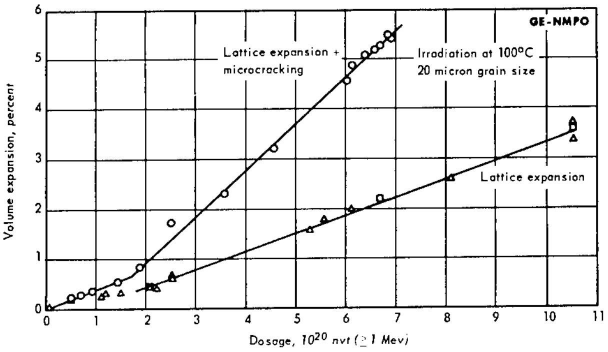

TABLE 3.8 (Cont.)

SUMMARY OF RADIATION EFFECTS IN BeO[a]

MACROSCOPIC EXPANSION AT ELEVATED TEMPERATURES

Two Types

(1) Total expansion = lattice expansion + defect clusters + helium bubbles

(2) Total expansion = lattice expansion + defect clusters + helium bubbles + microcracking

Clusters are major component in absence of microcracking. Lattice expansion decreases with increasing irradiation temperature and dosage; approximately 5 percent or less of total at about 1000°C.

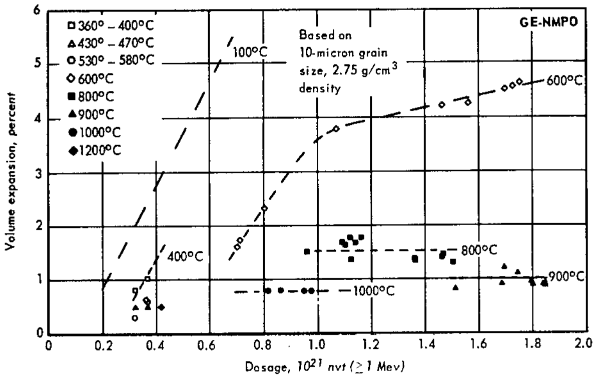

Estimated conditions for occurrence of types 1 and 2 in randomly oriented specimens of 5- to 20-micron grain size.

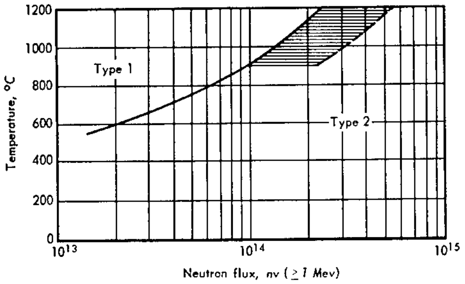

Estimated flux and temperature dependence of expansion.

$$\left(\frac{\Delta V}{V}\right)_m = \frac{K}{A}\,[1 - \exp(-At)]$$

or for repetitive irradiations,

$$\left(\frac{\Delta V}{V}\right)_m = \frac{K}{A}\,[1 - \exp(-At)] + \left(\frac{\Delta V}{V}\right)_o \exp(-At)$$

where:

$\left(\frac{\Delta V}{V}\right)_m$ = expansion exclusive of microcracking

$$\left(\frac{\Delta V}{V}\right)_m = \frac{1}{2}\left(\frac{\Delta V}{V}\right)_i + \frac{1}{2}\left(\frac{\Delta V}{V}\right)_v$$

$K = 3.3 \times 10^{-23}\,\phi$

$A_i = 0.113 \exp(-22{,}400/RT)$

$A_v = 2.54 \times 10^{-5} \exp(-9750/RT)$

and K is the defect production rate per second, ϕ is the neutron flux, nv (≥ 1 Mev), $(\Delta V/V)_o$ is the defect concentration at start of any repeat irradiation, A_i and A_v, respectively, are the annealing rate constants for interstitial and vacancy defects, R is the molar gas constant, cal/°K-mole, T is the absolute temperature, °K, and t is the irradiation time, seconds.

TABLE 3.8 (Cont.)

SUMMARY OF RADIATION EFFECTS IN BeO[a]

PROPERTY CHANGES (Observations to dosages of about 1.5 x 10^{21} nvt ($\geq$ 1 Mev)	
Strength	Increases by a few percent up to dosages at which grain-boundary separation occurs, then decreases markedly. Strength decrease begins at volume expansion ranging from 0.4 to 1.0 percent, the latter value occurring at the higher irradiation temperatures. Strength decrease in region involving grain-boundary separation is less the smaller the grain size.
Elastic Constants	Small decrease (1 to 2%) consistent with decrease in density in the absence of grain-boundary separation. Marked decrease in specimens involving grain-boundary separation.
Thermal Expansion	Not changed by irradiation.

[a] Summaries of the data obtained in this program appear in "Second Annual Report - High-Temperature Materials and Reactor Component Development Program, Volume I - Materials," GE-NMPO, GEMP-177A, February 28, 1963, pp. 152-174; and "Third Annual Report - High-Temperature Materials and Reactor Component Development Program, Volume I - Materials," GE-NMPO, GEMP-270A, February 28, 1964, pp. 110-134.

[b] B. S. Hickman, D. G. Walker, and R. Hemphill, International Conference on Beryllium Oxide, Sydney, Australia, October 21-25, 1963. (To be published in Journal of Nuclear Materials.)

expansion at 10^{21} nvt ($\geq$1 Mev) in 100°C irradiation. This value indicates a fractional volume change of 3.3 x 10^{-23} per neutron; hence, K becomes 3.3×10^{-23} ϕ where ϕ is the neutron flux, nv ($\geq$1 Mev). With these assumptions and values, the experimental data for expansion, flux, and irradiation were utilized in equation (3.2) to determine the annealing rate constants for interstitial and vacancy defects. The rate constants determined by equation (3.2) from the expansion, exclusive of microcracking, are plotted in the lower curve of Figure 3.4 as a function of reciprocal absolute temperature. These data repre-

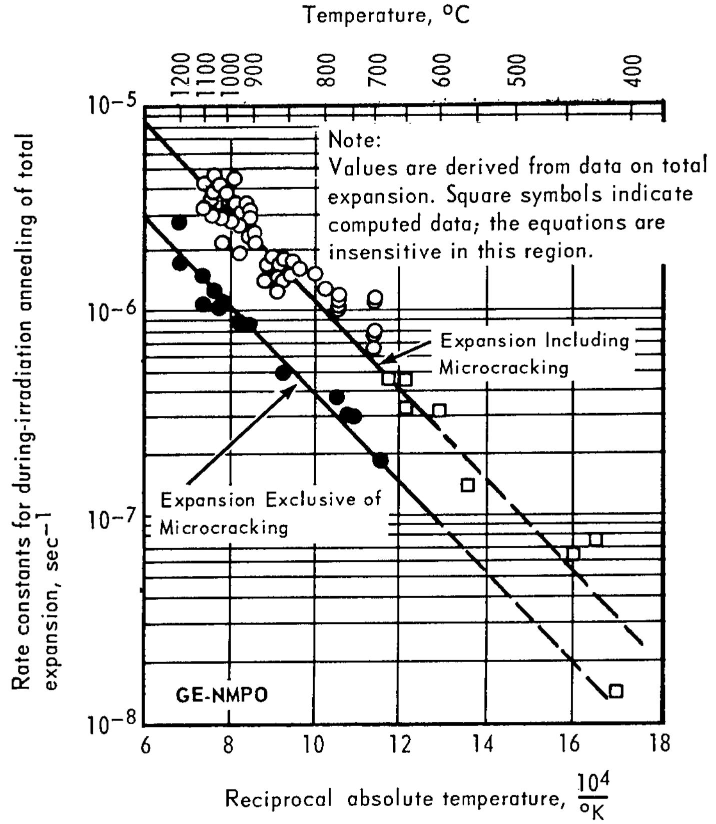

Note:
Values are derived from data on total expansion. Square symbols indicate computed data; the equations are insensitive in this region.

Fig. 3.4 – Annealing rate constants for UOX+MgO-grade BeO specimens of approximately 20-micron grain size and 2.9 g/cm^3 density

sent irradiation fluxes ranging from about 6 x 10^{13} nv to 3 x 10^{14} nv ($\geq$1 Mev) and irradiation times ranging up to approximately 5 x 10^{6} seconds, Table 3.9. The rate constants fall along a common line from about 1200°C down to about 650°C and can be represented by:

$$A_m = 6.1 \times 10^{-4} \exp(-10{,}300/RT) \qquad (3.3)$$

where R is the molar gas constant cal/mole-°K, and T is the absolute temperature, °K, and the subscript m refers to microscopic expansion, i.e., expansion exclusive of microcracking.

TABLE 3.9

RATE CONSTANTS FOR DURING-IRRADIATION ANNEALING OF BeO

Specimen Description		Irradiation Conditions				
Composition	Grain Size, microns	Dosage, 10^{20} nvt ($\geq$ 1 Mev)	Flux, 10^{14} nv ($\geq$ 1 Mev)	Temperature, °C	Total Volume Increase, %	Annealing Rate, 10^{-6} sec^{-1}
AOX	9	4.2	3.2	1200	0.5	1.9
	13	3.5	3.1	1200	0.3	3.7
UOX-MgO	11	4.2	3.2	1200	0.4	2.9
	12	4.1	3.1	1200	0.5	1.9
AOX	13	3.5	2.9	1070	0.6	1.3
	19	4.0	1.7	1070	0.5	1.1
UOX-MgO	20	4.0	1.7	1040	0.5	1.1
	20	5.0	2.1	1030	0.5	1.2
AOX	20	3.5	1.5	1030	0.4	1.1
UOX-MgO	11	9.7	2.7	1020	0.8	1.1
AOX	12	3.5	2.9	1000	0.6	1.1
	12	2.4	2.0	1000	0.4	1.3
	13	2.6	2.2	990	0.5	0.92
UOX-MgO	20	5.4	2.3	960	0.6	1.1
	12	9.6	2.1	920	0.9	0.79
AOX	17	8.6	1.9	800	1.2[a]	0.46
	10	3.0	0.65	700	0.5	0.39
UOX-MgO	5	2.8	0.61	660	0.5	0.27
	20	2.5	0.55	660	0.5	0.27
AOX	5	2.7	0.59	650	0.5	0.26
	17	8.3	1.8	600	1.9[a]	0.17
UOX-MgO	11	3.3	2.8	560	0.3	2.9
	11	3.3	2.8	530	0.3	2.9
	19	2.9	0.62	500	0.5	0.31
	11	3.7	3.2	470	0.5	2.0
	19	2.9	0.62	470	0.5	0.31
	11	3.3	2.8	430	0.5	1.7
	20	3.0	3.0	100	0.99[b]	(1.7 x 10^{-9})[b]
	20	10.0	3.0	100	3.3[b]	(1.7 x 10^{-9})[b]
	20	3.0	0.6	100	0.99[b]	(3.4 x 10^{-10})[b]
	20	10.0	0.6	100	3.3[b]	(3.4 x 10^{-10})[b]

[a] Determined from density measurement of crushed specimens.

[b] In the absence of experimental data at these particular fluxes, these are computed values based on combined lattice expansion and density measurements and the assumption that the expansion at this temperature is dependent on dosage and independent of flux. Experimental data justify this assumption.

Since limiting the rate-constant analysis to non-microcracked specimens is a severe restriction, utilization of all of the data was attempted by making the value of K large enough to encompass the volume increase in microcracked specimens. The value of K used (9 x 10^{-23}) was based on 9 percent volume expansion per 10^{21} nvt, which was obtained from 3 $\Delta c/c$; in general, the 100°C data indicate this rate of expansion in the microcracked region. Rate constants determined with the K value for all of the data on

UOX-MgO specimens of 20-micron grain size and density of 2.9 g/cm^3 are plotted in the upper curve of Figure 3.4. Since the expansion curves exhibit a "break" when microcracking occurs, these rate constants are not very accurate; however, the general pattern of the data is consistent with the more accurate data of the lower curve.

A rate constant curve for interstitial migration was defined from the volume expansion, $(\Delta V/V)_i$, indicated by the changes in the lattice parameters as recorded in Table 3.10. These rate constants were also computed from equation (3.2) with $K = 3.3 \times 10^{-23}\ \phi$. As indicated in Figure 3.5, these constants fall along a curve of somewhat steeper slope than that for microscopic expansion. The rate constant equation obtained is

$$A_i = 0.113 \exp(-22,100/RT). \tag{3.4}$$

Some of the scatter in the high-temperature points is attributed to a nonrepresentative defect state caused by interruptions in the irradiation with irregular reactor operation.

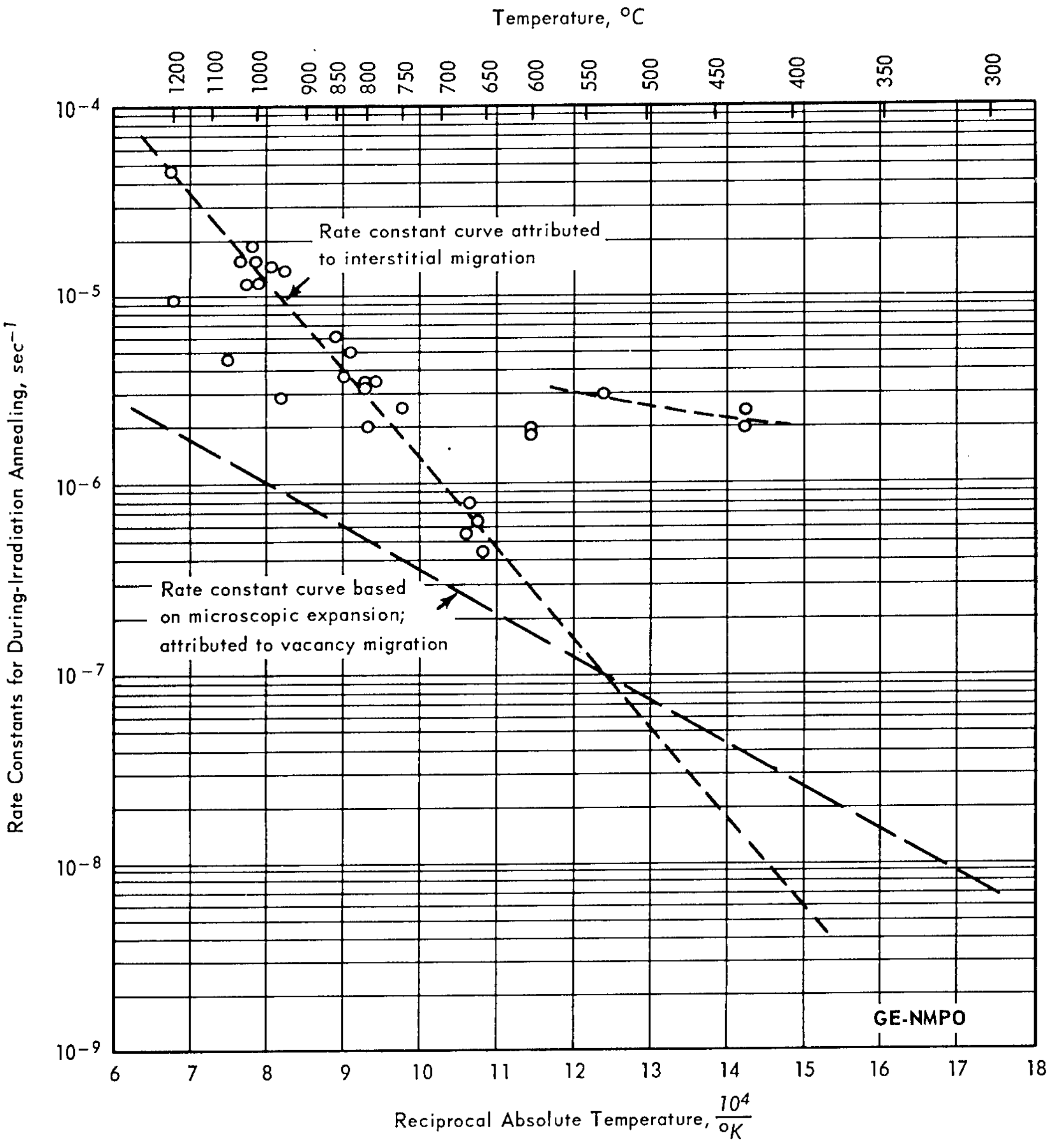

Fig. 3.5 – Rate constants for during-irradiation annealing of lattice expansion in BeO

TABLE 3.10

RATE CONSTANTS FOR DURING-IRRADIATION ANNEALING OF LATTICE EXPANSION IN BeO

Specimen Description		Irradiation Conditions				
Composition	Grain Size, microns	Dosage, 10^{20} nvt ($\geq$1 Mev)	Flux, 10^{14} nv ($\geq$1 Mev)	Temperature, ^{o}C	Lattice Volume Increase, %	Annealing Rate Constant, 10^{-6} sec^{-1}
AOX	13	3.5	3.1	1200	0.02	46
UOX-MgO	12	4.1	3.1	1200	0.11	9.3
AOX	20	3.6	1.5	1040	0.11	4.4
	20	3.5	1.5	1030	0.04	16
	18	5.2	2.2	1010	0.06	12
	12	2.4	2.0	1000	0.04	12
	20	5.4	2.3	1000	0.05	15
UOX-MgO	20	4.7	2.0	950	0.04	14
	12	11.7	2.6	940	0.30	2.9
	20	3.0	2.5	840	0.21	3.7
	20	3.5	2.9	830	0.19	5.0
	12	11.6	2.5	800	0.25	3.3
	7	11.1	2.4	800	0.25	3.1
AOX	17	8.6	1.8	800	0.33	1.9
	7	10.6	2.3	780	0.23	3.3
	19	2.6	2.2	750	0.27	2.5
	7	9.2	2.0	600	0.39	1.6
	17	8.3	1.8	600	0.31	1.9
UOX-MgO	11	3.3	2.8	430	0.43	1.9
AOX	10	16.3	2.9	1120	0.16	5.9
	8	15.8	2.8	1090	0.05	20.0
	44	5.9	2.5	1010	0.04	18.0
	78	9.1	3.1	988	0.07	15.0
	101	9.7	2.2	860	0.11	6.2
	18	2.8	0.6	670	0.25	0.77
UOX-MgO	5	2.8	0.6	670	0.35	0.53
	19	2.5	0.5	660	0.37	0.41
AOX	7	2.8	0.6	660	0.30	0.64
UOX-MgO	11	3.2	2.8	530	0.30	2.9
	11	3.2	2.8	430	0.35	2.4

The low-temperature points indicated by a separate dashed line are high because they represent high flux, short-time irradiations and are in a region in which equation (3.2) is insensitive. Rate constants determined from experimental data, which obey the relationship indicated by the curve, will decrease in magnitude with increasing irradiation time and will approach the rate constant of the curve as a limiting value.

A more complete description of the microscopic expansion, i.e., one extending to low temperatures, can be obtained from equations which describe the interstitial and vacancy concentrations independently. The vacancy concentration, $(\Delta V/V)_v$, can be derived from equations (3.2), (3.3), and (3.4). Based on the equivalence of the lattice and microscopic expansion in 100^{o}C irradiations, it is reasonable to assume that the volume contribution of interstitial and vacancy defects is equal. Therefore, we may write

$$\left(\frac{\Delta V}{V}\right)_m = \frac{1}{2}\left(\frac{\Delta V}{V}\right)_i + \frac{1}{2}\left(\frac{\Delta V}{V}\right)_v \tag{3.5}$$

The 1/2 factors enter into the equation because the same definition of K is utilized for each of the $(\Delta V/V)$ terms. For infinite irradiation time, the expansion (in this model) saturates at a value equal to K/A; hence, equation (3.5) becomes

$$\frac{K}{A_m} = \frac{1}{2}\frac{K}{A_i} + \frac{1}{2}\frac{K}{A_v} \tag{3.6}$$

and A_V may be evaluated to obtain

$$A_V = 2.54 \times 10^{-5} \exp(-9750/RT) \tag{3.7}$$

Although equations (3.4) and (3.7) represent extrapolated values at temperatures less than about 650°C, they yield, in combination with equation (3.2), correct values for the microscopic expansion for temperatures in the range of 100° to 1200°C for the time periods that have been investigated experimentally.

A supplementary form of equation (3.2) is of interest in computations of the expansion in repeat irradiations or for irradiations involving operating periods at different temperatures. Evaluation of the differential equation for first-order kinetics for an initial condition in which the defect concentration, C_o, is some quantity other than zero; substituting $(\Delta V/V)_o$ for C_o, the equation applicable to each irradiation step after the first is

$$\frac{\Delta V}{V} = \frac{K}{A}[1 - \exp(-At)] + \left(\frac{\Delta V}{V}\right)_o \exp(-At) \tag{3.8}$$

Some of the features of the expansion behavior indicated by the equations are of interest. There are at least two instances in which the equations predict expansion that is linear with dosage. One instance involves irradiations for time periods short in comparison to the magnitude of the annealing rate constant, A. The linearity with dosage in this case is readily apparent if it is recalled that for small values of x, the term $[1 - \exp(-x)] = x$ to a very good approximation; hence, writing K as $K'\phi$ gives

$$\frac{\Delta V}{V} = \frac{K'\phi}{A}[1 - \exp(-At)] \approx \frac{K'\phi}{A} At = K'\phi t \tag{3.9}$$

Thus, at each temperature there is some time of irradiation for which the expansion is linearly related to the dosage ϕt. This situation exists for all time periods of practical importance at irradiation temperatures less than 500° to 600°C. Similarly, in irradiations in different fluxes at constant temperature and constant irradiation time, the expansion is linearly related to the dosage. This is evident if the ratio of the expansion in two fluxes is examined:

$$\frac{\left(\frac{\Delta V}{V}\right)_1}{\left(\frac{\Delta V}{V}\right)_2} = \frac{\frac{K'\phi_1}{A}[1 - \exp(-At)]}{\frac{K'\phi_2}{A}[1 - \exp\ -At\ ]} = \frac{\phi_1}{\phi_2} \tag{3.10}$$

For constant temperature and time, all terms cancel except the flux so that the expansion is a linear function of the dosage.

The equations also predict saturation of the expansion. The significant features are that the saturation at a given temperature is dependent on the time of irradiation while the amount of expansion is determined by the flux. Figures 3.6 and 3.7 illustrate the predicted expansion behavior. The exposures in this program have not yet extended to time periods in which saturation would be expected; hence this feature is yet to be demonstrated experimentally. Factors that may alter or interfere with the predicted expansion include the defect structure and the helium gas which are discussed in the following sections.

Defect Structure

Studies of the defect structure were pursued with the electron microscope in efforts to obtain further information pertinent to the expansion and kinetics. Although efforts to de-

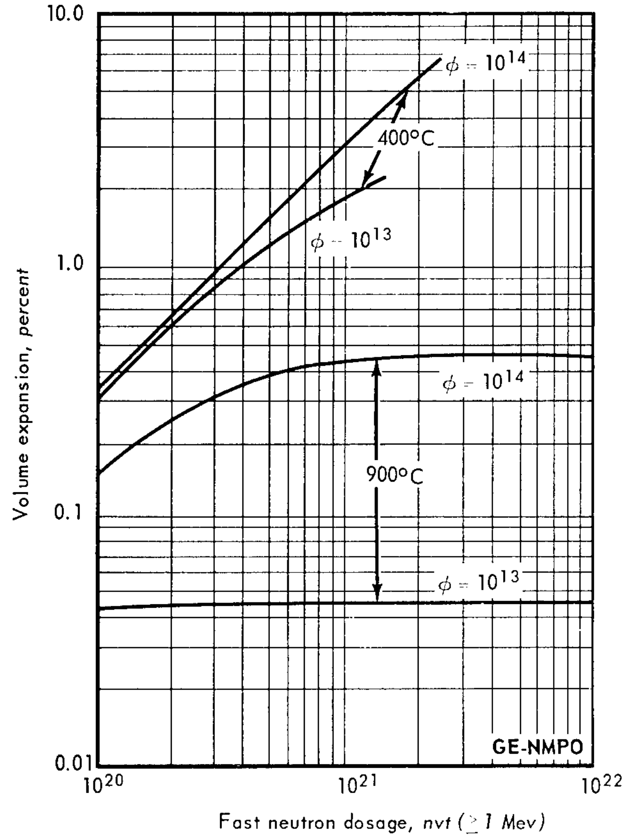

Fig. 3.6 – Computed volume expansion of BeO at 400°C and 900°C for neutron fluxes of 10^{13} and 10^{14} nv ($\geq$ 1 Mev). At saturation the volume expansion is proportional to the neutron flux.

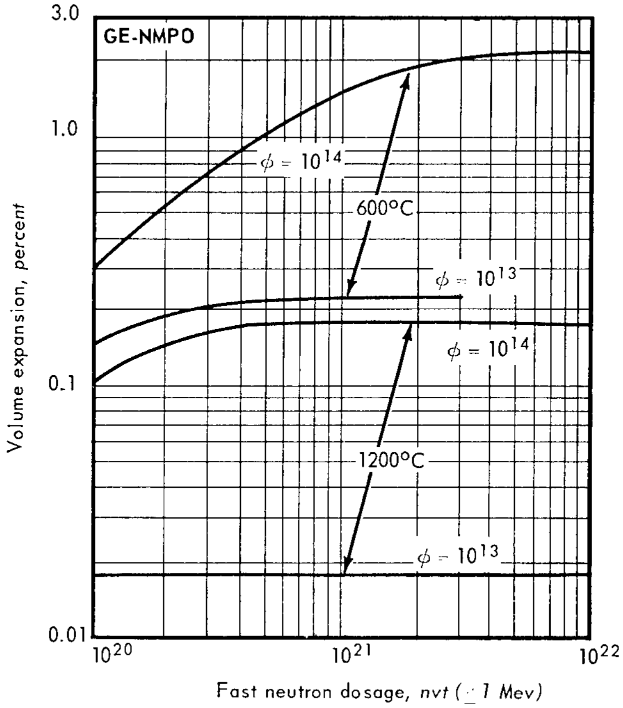

Fig. 3.7 – Computed volume expansion of BeO at 600°C and 1200°C for neutron fluxes of 10^{13} and 10^{14} nv ($\geq$ 1 Mev). At saturation the volume expansion is proportional to the neutron flux.

termine the number density of clusters formed at elevated temperatures were not particularly successful, identification of both interstitial and vacancy types of clusters was achieved.

Changes in the defect structure as a function of temperature at an approximately constant dosage of about 3.5 x 10^{20} nvt (≥1 Mev) are shown in Figure 3.8. At low temperatures, the defects consist of unresolvable dot clusters which increase in size with increasing irradiation temperature. Evolution of the dot clusters into planar clusters occurs in these tests at a temperature of about 650°C, while well-developed planar clusters are apparent at the higher irradiation temperatures.

Identification of the clusters in high-temperature irradiations as being of both interstitial and vacancy types was based on the techniques of Ashby and Brown.[*][†] The procedure consists of obtaining aberration-free,[‡] sharply focused dark-field micrographs under conditions in which the direction of the operating $\overline{g}$ vector[§] is known and can be compared with the asymmetric black and white strain contrast images of the defects. When complete account is made of the various rotations and inversions which occur in producing the images, the strain contrast can be used to deduce the nature of the defects, i.e., images whose white side is in the direction of positive $\overline{g}$ are due to vacancies, and images whose black side is in the direction of positive $\overline{g}$ are interstitials.

Although cluster identification has been made in several high-temperature specimens, the most complete analysis has been obtained on a BeO specimen which was irradiated to 2.5 x 10^{20} nvt (≥ 1 Mev) at 850°C. This sample contained a fairly sparse population of defects of approximately 150 Å average diameter, some of which could be resolved into loops having maximum diameters approaching 300 Å. By counting the defects in a unit area whose thickness was obtained from extinction fringes,[•] the average cluster density in this specimen was determined to be approximately 5 x 10^{15} per cm^3.

Figure 3.9 shows photographs obtained from a chip from this specimen. The chip was a wedge-shaped fragment which had cleaved approximately parallel to {11.0}. The photographs are oriented on the page so that the c-axis is vertical. Figure 3.9a shows a bright-field micrograph of the chip taken with the (00.2) reflection operating, and Figure 3.9b shows the corresponding electron diffraction pattern taken under these conditions. Arrows on the diffraction pattern indicate the $\overline{g}$ vectors pointing to the (00.2) and (00.$\overline{2}$) reflections used in obtaining the dark-field micrographs of Figures 3.9c and 3.9d.

The dark-field micrographs show a number of asymmetric images suitable for deducing the nature of the defects producing them, and indicate that both vacancy and interstitial clusters are present. Note that usable images which appear in both Figures 3.9c and 3.9d reverse contrast when the $\overline{g}$ vector is reversed from [00.2] to [00.$\overline{2}$], as expected. Some notable exceptions to this are found near the thin edges of the chip; these are circled on the micrographs. These latter images are not suitable for the analysis, since they do not

---

[*] M. F. Ashby and L. M. Brown, "Diffraction Contrast from Spherically Symmetrical Coherency Strains," *Phil. Mag.*, Vol. 8, No. 91, July 1963, pp. 1083–1103.

[†] M. F. Ashby and L. M. Brown, "On Diffraction Contrast from Inclusions," *Phil. Mag.* Vol. 8, No. 94, October 1963, pp. 1649–1676.

[‡] W. Bell, D. M. Maher, and G. Thomas, "Vacancy Aggregates in Quenched Copper Single Crystals," University of California, Report No. UCRL-11480, June 1964. Presented at the International Conference on Lattice Defects in Quenched Metals, Argonne, Illinois, June 15–17, 1964.

[§] The $\overline{g}$ vector is a reciprocal lattice vector pointing from the origin, or transmitted beam (000), to the diffraction spot (h k l) which is operating to produce the observed image contrast.

[•] G. Thomas, *Transmission Electron Microscopy of Metals*, John Wiley and Sons, Inc., New York, 1962, pp. 65–72.

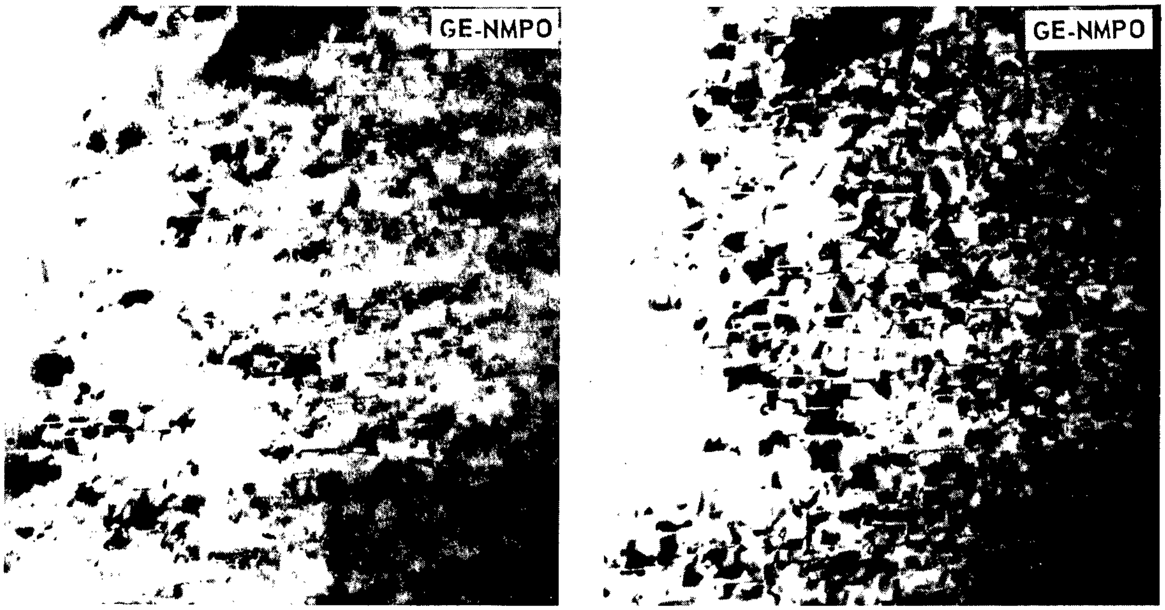

Neg. J-205 *Neg. J-206*

A. AOX-grade BeO irradiated at 1100°C to 1.6×10^{21} nvt

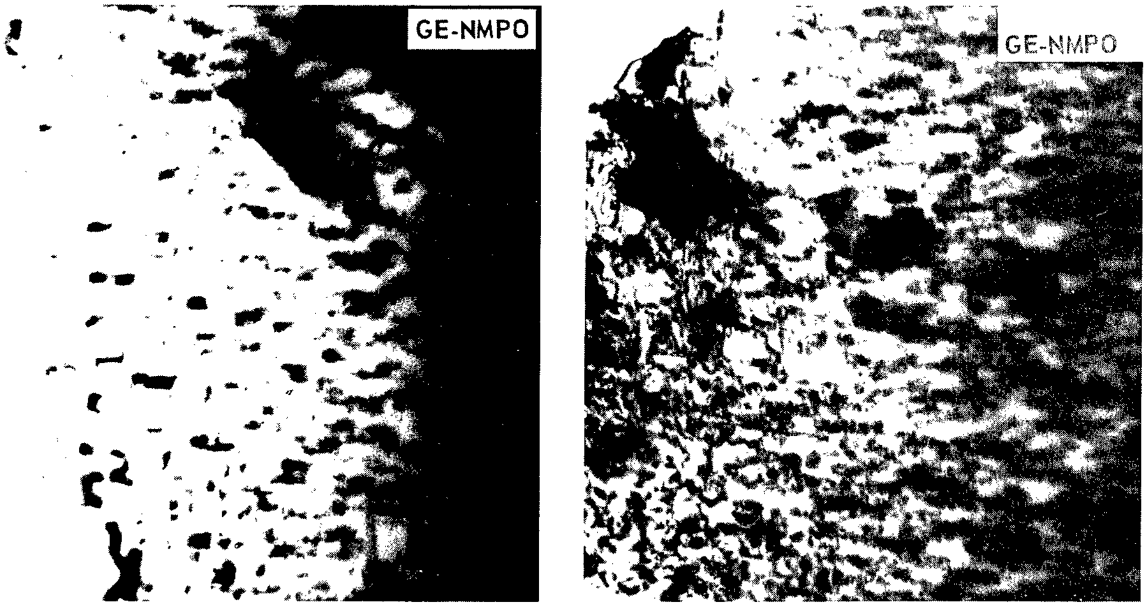

B. UOX + MgO-grade BeO irradiated at 900°C to 1.1×10^{21} nvt *(Neg. J-274)*

C. AOX-grade BeO irradiated at 650°C to 2.7×10^{20} nvt *(Neg. J-362)*

Fig. 3.8 – Electron transmission micrographs showing development of defect structure in irradiated BeO *(60,000X)*

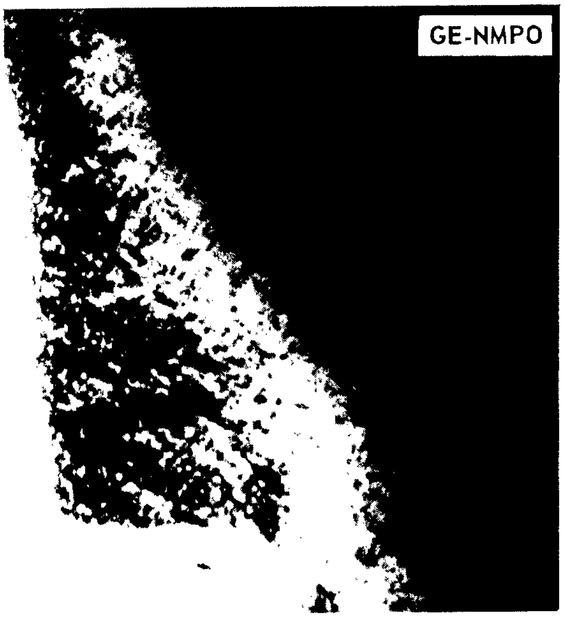

D. UOX + MgO-grade BeO irradiated at 530°C to 3.2×10^{20} nvt *(Neg. J-334)*

E. UOX + MgO-grade BeO irradiated at 430°C to 3.2×10^{20} nvt *(Neg. J-326)*

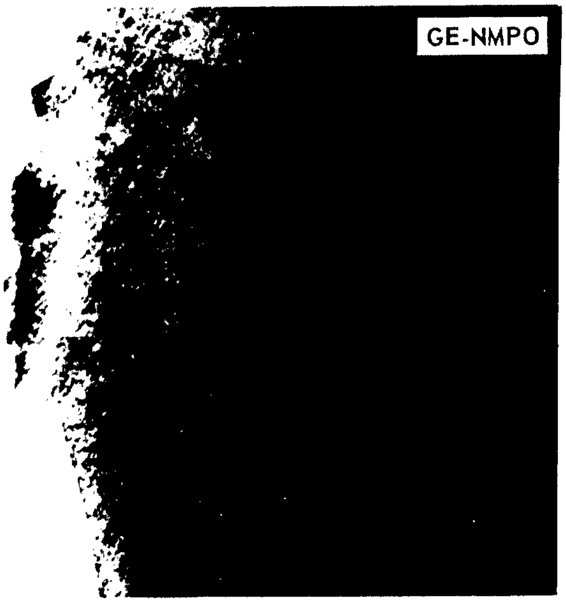

F. UOX + MgO-grade BeO irradiated at 360°C to 3.2×10^{20} nvt *(Neg. J-317)*

Fig. 3.8 (Cont.) – Electron transmission micrographs showing development of defect structure in irradiated BeO *(60,000X)*

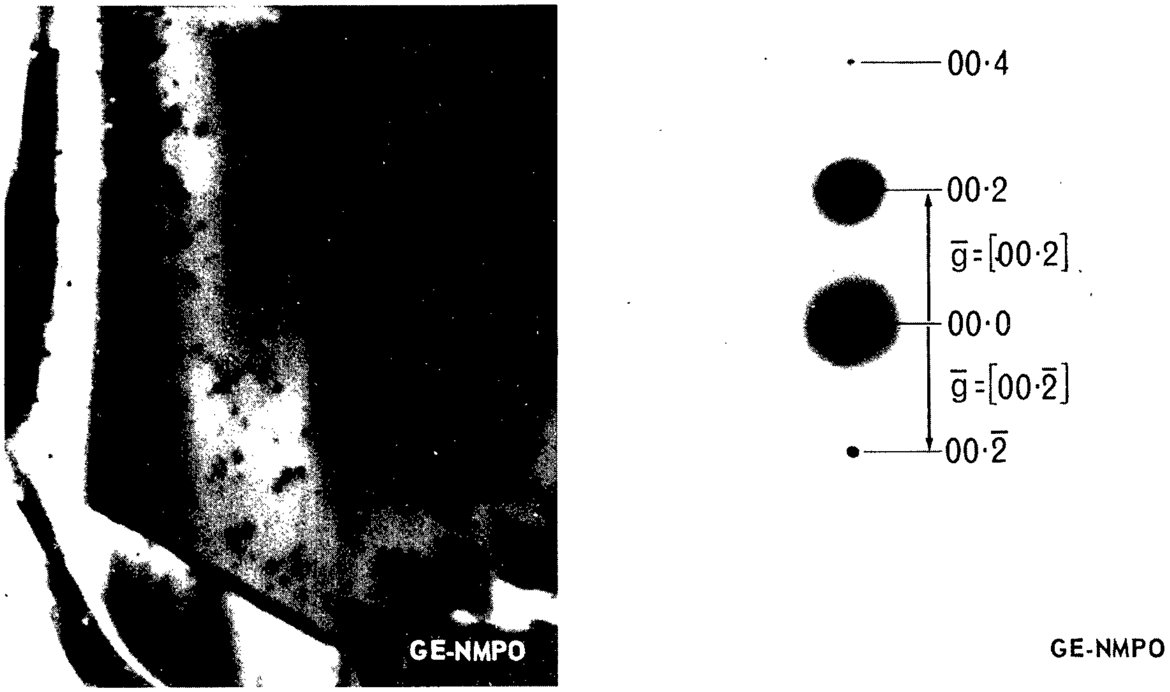

a. Bright field micrograph, (00.2) reflection operating. *(Neg. J480)*

b. Electron diffraction pattern of Fig. 3.9a. *(Neg. J481)*

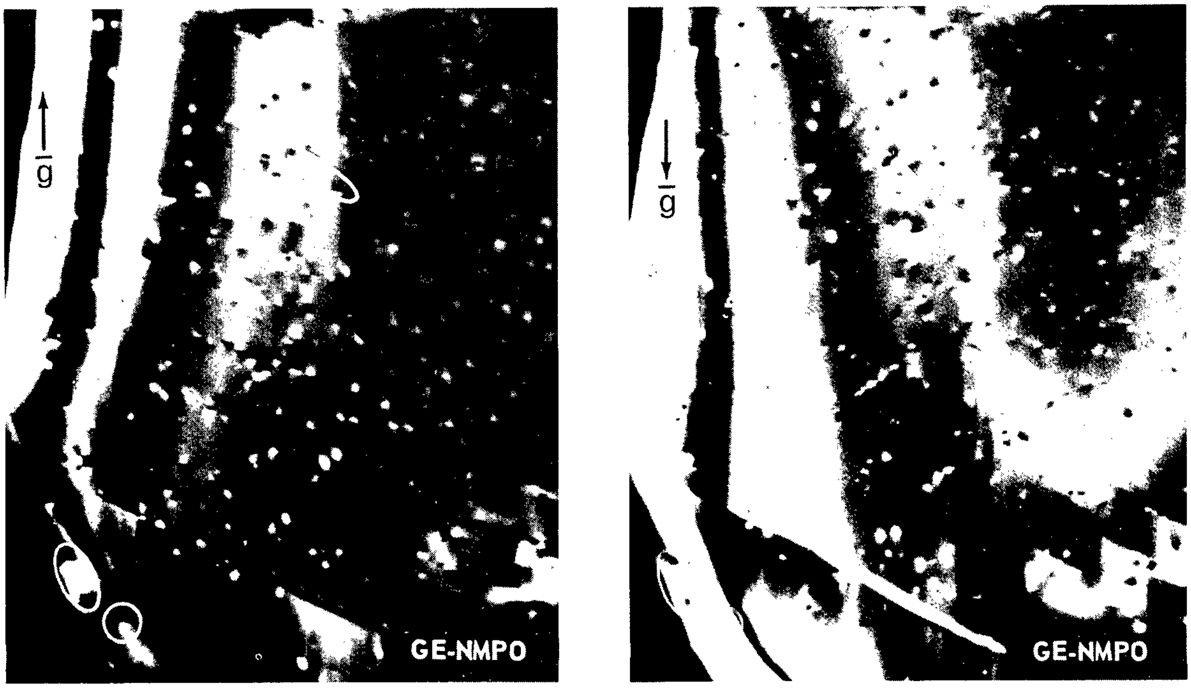

c. Dark field micrograph, $\bar{g}$ [00.2]. *(Neg. J483)*

d. Dark field micrograph, $\bar{g}$ [0.00$\bar{2}$]. *(Neg. J485)*

Fig. 3.9 – Transmission electron micrographs of BeO chip after 2.5×10^{20} nvt at 850°C. Variation of strain contrast with direction of $\bar{g}$ vector indicates presence of both vacancy and interstitial types of defect clusters. *(80,000X)*

reverse contrast when $\bar{g}$ is reversed. This is presumably due to the fact that they are located in regions of the chip where kinematical diffraction theory holds, whereas usable images must be located in regions governed by dynamical theory. Counts of images believed to be suitable for analysis indicate that vacancy clusters probably outnumber interstitial clusters by approximately two to one. Some examples of the two types of clusters are marked V and I, respectively, on the micrographs.

Identification of the cluster types and their relative abundance is qualitatively in agreement with the kinetic equations. The computed ratio of the concentrations of vacancies to interstitials for the irradiation condition is approximately 3.5 to 1; considering the range of cluster sizes and the possible variations of numbers of defects per cluster, the computed ratio appears reasonable in comparison to the observed ratio of approximately 2 to 1. The presence of vacancy clusters also indicates a difference between the low and elevated temperature expansion behavior; the clusters formed in 100°C irradiations have been identified as interstitial types.[*][†]

HELIUM BUBBLES AND DIFFUSION

Efforts were continued to define the role of helium in the expansion behavior. Measurements included determination of the helium concentration in irradiated specimens and further study of helium bubble formation; results of some significance were obtained in both areas.

Helium is formed in BeO in several reactions including Be(n, 2n) 2He, Be(n, α)Li, Li(n, α)H^3, and O(n, α)C. The principal reaction is the Be(n, 2n) which contributes roughly 80 percent of the total amount formed. All of the reactions are directly proportional to dosage except the Li(n, α) which builds up according to an exponential function and contributes to some nonlinearity of the amount formed as a function of dosage. Computations of the total amount of helium formed were revised late in CY-64 as a result of a recent determination of the Be(n, 2n) cross section by Felber, Farmelo, and Van Sickle.[‡] These authors obtained a cross section of 460 ± 60 millibarns for ≥ 2.7 Mev neutrons based on an Fe^{54}-Mn^{54} (and other dosimeters) cross section for fission neutrons of 61 millibarns.

Since the dosimetry in this program is based on an Fe^{54}-Mn^{54} cross section of 54 millibarns, the new helium yields have been converted into yields consistent with our dosimetry. On this basis, the total helium formed is approximately 0.33 cm^3 He per gram of BeO per 10^{21} nvt (≥ 1 Mev); however, the yield is slightly nonlinear with dosage as indicated subsequently in Figure 3.12. In previous reports, the amount of helium formed was taken as 0.366 cm^3 He per gram BeO per 10^{21} nvt (≥ 1 Mev).

Helium Bubbles

Previous study of helium bubbles showed that they formed in the grain boundaries at temperatures above approximately 600°C. At 1000°C and 10^{21} nvt (≥ 1 Mev), bubbles in specimens of nominal densities of 2.9 and 2.75 g/cm^3 were found to be nearly non-existent in materials of approximately 5-micron grain size and to increase in both size and number with increasing grain size. Based on the difference in expansion at this exposure in different grain sizes, approximately 20 percent of the 1-percent volume expansion of non-microcracked specimens of 20-micron grain size could be attributed to the bubbles. Rough confirmation of this value was obtained from bubble size - count estimates.[§]

---

[*] H. L. Yakel and B. S. Borie, *Acta Cryst*, Volume 16, 1963, p. 589.

[†] T. M. Sabine, Paper 15, International Conference on BeO, Sydney, Australia, October 1963. To be published in *Journal of Nuclear Materials*.

[‡] F. S. Felber, Jr., D. R. Farmelo, and V. C. Van Sickle, "The Integral Be^9(n, 2n) Cross Section," Pratt and Whitney Aircraft, PWAC-433, May 14, 1964.

[§] "Third Annual Report – High-Temperature Materials and Reactor Component Development Programs, Volume I – Materials," GE-NMPO, GEMP-270A, February 28, 1964, p. 129.

Further observations of bubbles in as-irradiated condition failed to add appreciably to these estimates of their contribution beyond the qualitative observation that bubbles are smaller and less numerous in microcracked specimens.

Some evidence of intragranular bubble formation was noted in fracture surfaces of the specimen used in the annealing experiments described in the preceding paragraphs. Bubbles in the fractured face of a grain are shown in Figure 3.10 for a specimen in the as-irradiated condition; this figure can be compared to the grain-boundary surface shown in Figure 3.11a. These bubbles appear to be lenticular rather than spherical in shape, and of the same orientation. Based on cleavage observations, the large dimension of the bubbles probably lies in either the prism (1010) or basal (0001) plane; the latter being the more likely in the irradiated material because of the clusters in this plane. Formations of this type have not been observed in other specimens; however, it is expected that the high-dosage samples now under investigation will provide further information.

Fig. 3.10 – Intragranular gas bubbles on cleavage surface
(Neg. 784C, 7500X)

Possibly significant results were obtained in annealing experiments. Electron micrographs of a non-microcracked specimen irradiated to 1.1×10^{21} nvt ($\geq$1 Mev) at 900°C were obtained before and after thermal annealing at various temperatures. Both annealing, or recovery, of the radiation-induced expansion and further expansion of the specimen were observed. During annealing, the temperature was raised in 50° to 100°C increments from the irradiation temperature and held at each temperature for approximately 30 minutes. One-third of the original volume expansion of 0.9 percent had annealed at the end of the 1300°C treatment. When annealed at 1355°C, the specimen began to expand, and after 12.2 hours exceeded the as-irradiated volume. The final volume expansion was 1.3 percent.

In contrast to this behavior, a specimen of the same composition (AOX-grade BeO, 20 microns in grain size with a density of 2.9 g/cm^3) irradiated to 1.04×10^{21} nvt at approximately 860°C did not expand during annealing. The radiation-induced volume expansion in this specimen was 1.6 percent, and the specimen exhibited an appreciable

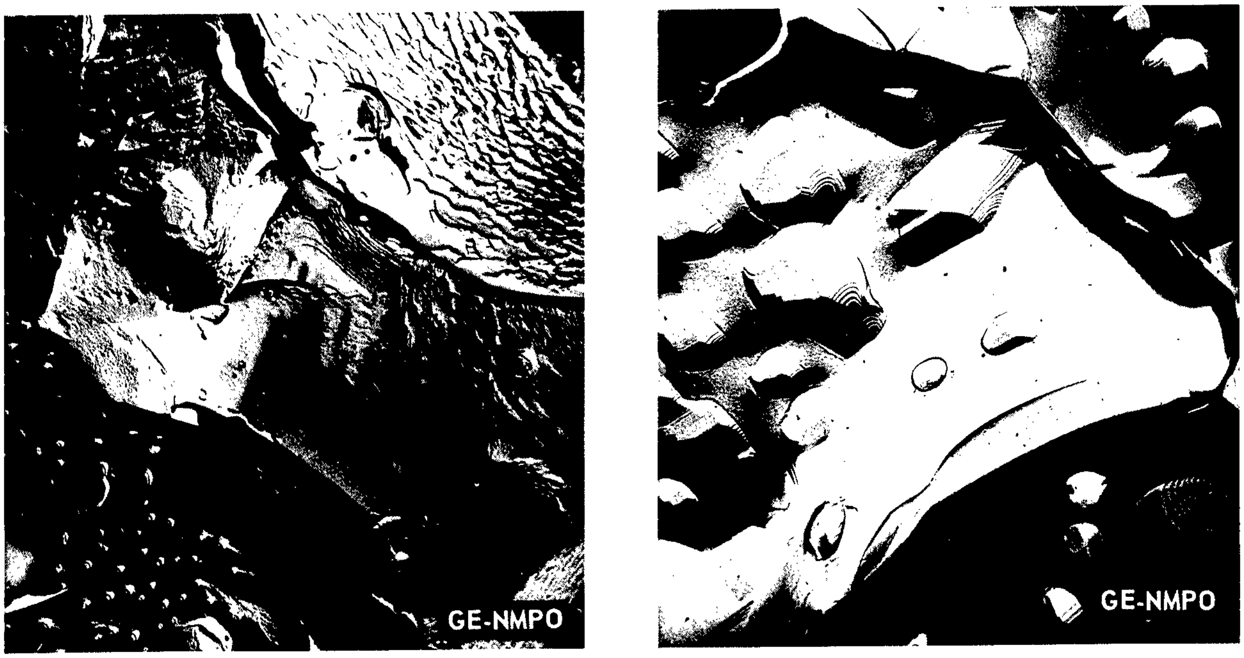

Neg. 784B, 3500 X

a. Fracture surface in as-irradiated specimen after 1.1×10^{21} nvt at 900°C

Neg. 787B, 3500 X

b. Fracture surface in specimen after annealing for 12.2 hours at 1355°C (the bubbles have grown to normal pore size of 1 to 2 microns)

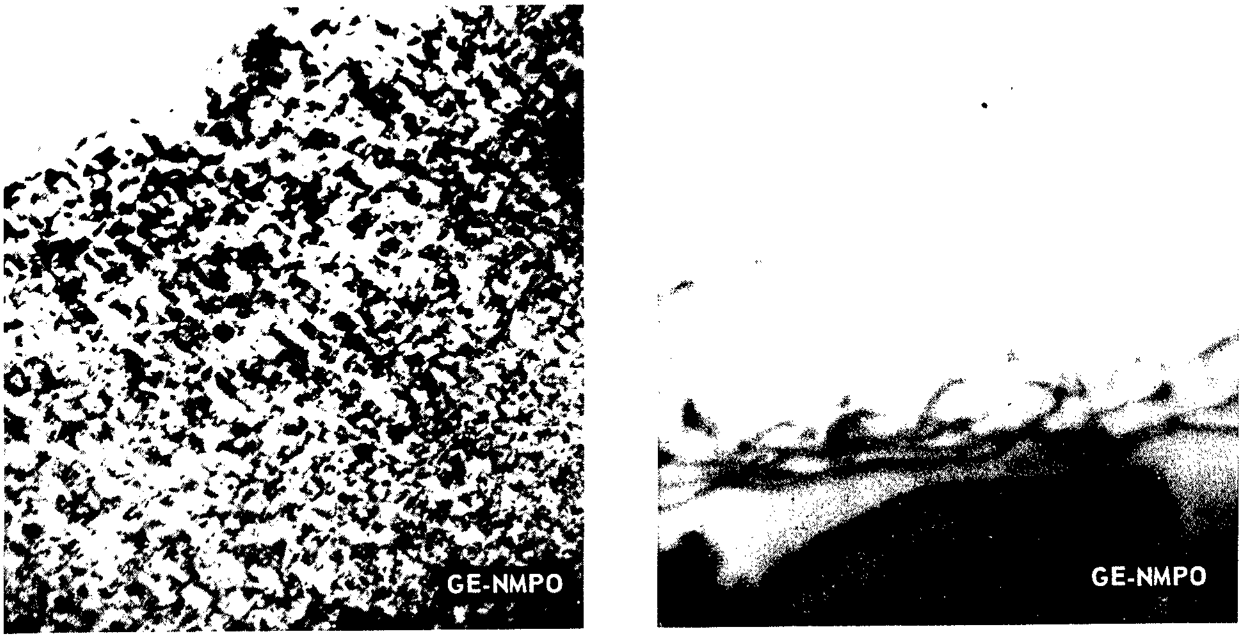

Neg. J-63, 60,000 X

c. Transmission micrograph showing defect clusters in the as-irradiated condition

Neg. J-81, 60,000 X

d. Transmission micrograph after annealing (the defect clusters have disappeared and dislocation tangles are apparent)

Fig. 3.11 – Helium bubbles and structural defects in irradiated BeO specimen

amount of grain-boundary separation. Seventy percent of this volume increase annealed as the temperature was raised to 1300°C. No expansion occurred during annealing for 4 hours at 1365°C.

Electron micrographs of the first of these specimens in the as-irradiated and irradiated and annealed condition showed that the volume expansion during annealing was caused by the collection of helium into bubbles which grew to the size of normal sintering pores (1 to 2 microns). Electron and transmission micrographs of representative areas of these specimens are shown in Figure 3.11. The volume expansion during annealing cannot be unambiguously assigned to helium, although such an assumption appears reasonable in view of the overall helium analysis data and of the lack of expansion in the irradiated specimen containing microcracks.

These results demonstrate the expansion potential of helium gas at dosages at which appreciable quantities of helium are formed. The data suggest the following conclusions on the expansion in irradiated specimens.

1. Expansion may be greater in the higher of two elevated irradiation temperatures due to growth of helium bubbles by expansion of the gas. This effect should be associated with the relaxation temperature which normally is considered to be aproximately 1000°C but may be lower under irradiation.
2. Some of the expansion that has not been accounted for may occur by growth of the pores normally present or by growth of helium bubbles to normal pore size. In either case, the effect on specimen expansion would be difficult to detect.
3. It appears unlikely that helium bubbles contribute significantly to expansion where microcracking occurs before appreciable quantities of helium are formed. At high dosages, the presence of helium bubbles in the grain boundaries possibly promotes microcracking by reducing the contact area between grains.

Helium Diffusion

Measurements of the helium concentration in specimens irradiated over a range of dosages and temperatures were made. A summary of these measurements is presented in Table 3.11, and the data are plotted in Figure 3.12 in terms of the helium concentration in the specimens as a function of dosage. One of the conclusions obtainable from either the tabular or graphical data is that microcracking significantly increases the helium escape or diffusion. The following points are pertinent.

1. About 25 percent of the helium formed escapes from extensively microcracked specimens irradiated at 100°C. The fraction of the helium retained is an approximately linear function of the dosage; however, since the dosages ranging from 3 to about 7×10^{20} nvt (≥ 1 Mev) were obtained in the same time period, the amount escaping is also proportional to the neutron flux. There was no difference in the escape in specimens of 4 to 20 microns grain size.
2. Many of the specimens irradiated at elevated temperatures retained a greater fraction of the helium than those irradiated at 100°C. For the dosages considered, microcracking in these specimens is limited or non-existent, especially in those of small grain size and those irradiated at the highest temperatures.
3. In measurements of specimens in bulk form and in powder form after crushing to a particle size equal to or smaller than the grain size, the helium concentration in the powder was about 75 percent of that in the bulk in non-microcracked specimens irradiated at about 1100°C. Further, the helium concentration in the bulk and the fraction retained in the powder was smaller in the lower of the two densities examined. In contrast, the helium concentration was identical in the bulk and crushed form in extensively microcracked specimens irradiated at 100°C.

TABLE 3.11

HELIUM CONCENTRATION AND DIFFUSION IN IRRADIATED BeO

				Irradiation Conditions			Helium			
Composition	Grain Size, microns	Bulk Density,[a] g/cm^3	Open Porosity, %	Temperature, ^oC	Time, 10^6 sec	Dosage, 10^{20} nvt ($\geq$ 1 Mev)	Observed Concentration, cm^3/g (NTP)	Fraction Of Total Formed[b]	Apparent Diffusion Rate,[c] 10^{-9}/sec	Apparent Diffusion Coefficient,[c] 10^{-9} cm^2/sec
AOX (crushed)[d]	6	-	-	100	1.76	0.8	0.020	0.77	15	1.3
	6	-	-	100	2.03	3.0	0.078	0.79	10	0.94
	6	-	-	100	2.03	5.6	0.132	0.70	23	2.1
	6	-	-	100	2.03	6.8	0.161	0.70	23	2.1
	6	-	-	100	2.03	6.8	0.162	0.70	23	2.1
AOX	5	2.725	6.5	600	4.64	9.2	0.21	0.67	12	1.1
	2	2.719	6.8	650	4.63	2.7	0.053	0.60	19	1.7
	7	2.763	0.1	660	4.63	2.8	0.064	0.70	10	0.91
	7	2.763	0.1	660	4.63	2.8	0.064	0.70	10	0.91
	5	2.739	3.5	800	4.64	10.6	0.28	0.77	5.6	0.51
	3	2.756	-	900	4.50	10.6	0.23	0.64	15	1.4
	8	2.588	3.9	1090	5.68	15.8	0.40	0.73	6.7	0.59
AOX (crushed)[d]	8	2.588	3.9	1090	5.68	15.8	0.31	0.57	19	1.8
AOX (crushed)[e]	8	2.588	3.9	1090	5.68	15.8	0.34	0.62	14	1.3
AOX	12	-	-	100	2.03	3.0	0.079	0.80	6.6	0.60
	12	-	-	100	2.03	4.1	0.093	0.68	26	2.4
	12	-	-	100	2.03	6.9	0.162	0.70	23	2.1
	10	2.641	8.3	460	4.64	2.4	0.069	0.87	1.5	0.14
	10	2.813	-	600	4.64	9.1	0.24	0.78	5.0	0.46
	10	2.861	-	630	4.63	2.1	0.059	0.86	1.8	0.16
	10	2.861	-	630	4.63	2.1	0.052	0.75	6.7	0.61
	12	2.824	-	800	4.64	11.0	0.26	0.69	11	0.97
	12	2.833	-	900	4.50	10.8	0.24	0.65	14	1.3
	10	2.796	2.1	1120	5.68	16.3	0.48	0.85	1.7	0.16
AOX (crushed)[e]	10	2.796	2.1	1120	5.68	16.3	0.44	0.78	4.0	0.37
AOX (crushed)[d]	10	2.796	2.1	1120	5.68	16.3	0.42	0.74	5.9	0.54
AOX	10	2.882	0.2	1200	1.13	3.5	0.086	0.74	30	2.7
	18	2.848	-	470	4.63	3.1	0.078	0.76	6.1	0.56
	17	2.822	3.6	600	4.64	8.3	0.19	0.69	11	0.97
	18	2.863	-	670	4.63	2.8	0.063	0.68	12	1.0
	17	2.842	2.7	800	4.64	8.6	0.27	0.92	0.29	0.027
	20	2.885	-	810	1.21	2.6	0.064	0.74	28	2.5
	20	2.742	-	890	4.50	9.2	0.22	0.70	10	0.93
	20	2.864	-	930	4.50	10.6	0.24	0.66	14	1.2
	20	2.772	-	1000	2.36	5.6	0.15	0.80	17	0.52
	35	2.867	-	450	4.63	2.2	0.064	0.89	0.96	0.088
	44	2.893	<0.1	1000	2.36	5.9	0.179	0.90	14	1.30
	44	2.893	<0.1	1000	2.36	5.9	0.178	0.90	14	1.30
	100	2.892	-	800	4.64	9.3	0.25	0.79	4.5	0.41
	100	2.931	1.3	900	4.50	9.7	0.24	0.73	8.1	0.74
UOX-MgO	4	-	-	460	4.63	3.0	0.056	0.56	24	2.2
	5	2.917	-	670	4.63	2.7	0.064	0.72	8.5	0.78
	5	2.742	~0.1	670	4.63	2.8	0.058	0.63	16	1.4
	7	-	-	170	4.56	2.3	0.051	0.68	12	1.07
UOX-MgO (crushed)[d]	11	2.883	-	360	1.17	3.3	0.060	0.55	95	8.7
	11	2.877	-	430	1.17	3.3	0.067	0.61	71	6.5
	11	2.880	-	530	1.17	3.3	0.062	0.57	95	8.7
UOX-MgO	11	2.877	-	430	1.17	3.3	0.067	0.61	71	6.5
	12	2.876	-	500	4.63	2.3	0.051	0.68	12	1.0
	11	2.880	-	530	1.17	3.3	0.067	0.61	71	6.5
	12	2.867	0.3	650	4.63	2.3	0.057	0.76	6.1	0.56
	10	2.872	-	750	4.50	8.7	0.223	0.76	6.2	0.57
	10	2.860	1.8	800	4.64	11.1	0.28	0.74	7.2	0.66
	10	2.867	0.6	900	4.50	10.8	0.29	0.78	5.1	0.47
	10	2.876	-	900	4.50	11.0	0.274	0.73	8.1	0.74
	11	2.751	<0.1	1200	1.01	4.2	0.106	0.76	28	2.5
	11	2.751	<0.1	1200	1.01	4.2	0.108	0.77	25	2.3
	20	-	-	100	2.03	6.9	0.163	0.70	23	2.1
	18	-	-	160	4.56	2.2	0.042	0.58	22	2.0
	18	-	-	320	4.56	1.9	0.049	0.79	4.6	0.42
	19	2.904	-	660	4.63	2.5	0.065	0.79	4.5	0.41
	41	2.929	-	440	4.63	2.3	0.037	0.49	34	3.1
EBOR	20	2.772	-	460	4.63	2.6	0.058	0.67	12	1.1
	20	-	-	560	4.63	2.6	0.042	0.49	34	3.1
	20	-	-	650	4.63	2.6	0.050	0.58	21	1.9

[a] Measured after irradiation. Open pore volume is expressed as percentage of bulk volume.

[b] Formation rate is taken as 0.33 cm^3 helium per gram of BeO per 10^{21} nvt ($\geq$1 Mev). See text.

[c] Computations are based on bulk volume of sample.

[d] Specimen was crushed to approximately 10-micron particle size.

[e] Specimen was crushed to approximately 40-micron particle size.

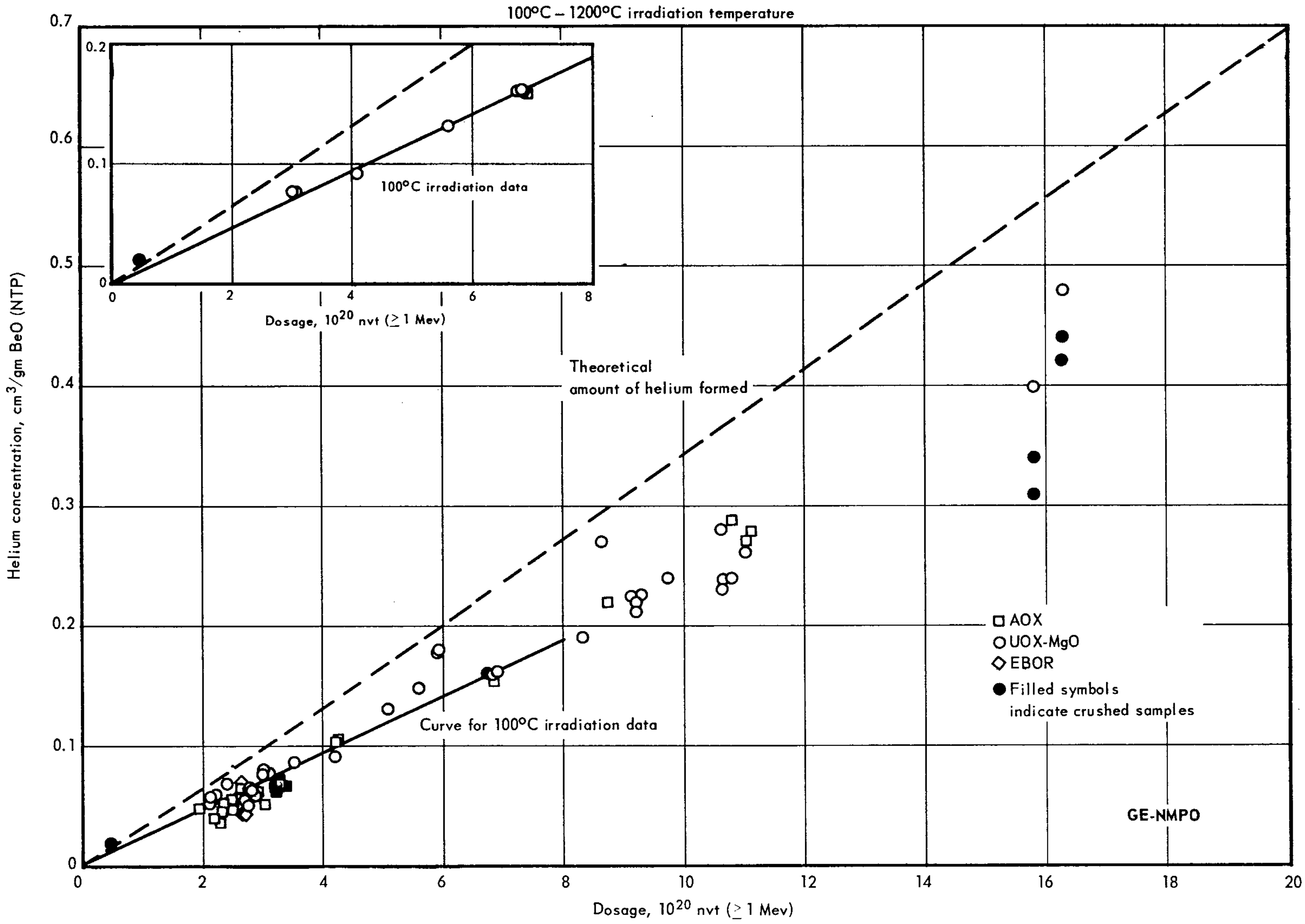

Fig. 3.12 – Helium concentration in irradiated BeO specimens of various grain sizes and densities as a function of fast-neutron dosage

These observations indicate that recoil as well as diffusion processes are the mechanism of helium escape. Alpha particles with energies sufficient for a recoil range of the order of 10 microns occur in the various reactions; hence, recoil from the large surface area exposed by microcracking probably accounts for the large helium loss in specimens irradiated at 100°C. The smaller helium loss in elevated temperature irradiations apparently results from the much slower diffusion processes since, in the absence of microcracking, recoil losses are limited to the surface area determined by the sample geometry and the open porosity.

The helium loss by diffusion has not yet been defined. Apparent diffusion coefficients based on a bulk diffusion model* are of the order of 10^{-9} to 10^{-11} cm^2/sec, as indicated in Table 3.11. Because of the recoil losses, comparison of these rates is valid only in the absence of microcracking and for specimens of the same surface area. Trial Arrhenius plots of the diffusion data for specimens considered to be of the same area indicate that the activation energy may be about 10 kcal; however, little confidence is placed in this value. Surface area measurements are being made.

Recent Macroscopic Expansion Results

Many of the dimensional measurements made during the year were on specimens irradiated at low fluxes and temperatures, and although useful in kinetic studies, the results were comparable to those obtained previously and will not be discussed separately. Data for two such tests are recorded subsequently in Tables 3.15 and 3.16; data for a third test (at 600° to 650°C) were presented in a previous progress report.†

Essentially new results were obtained in a high-temperature test of glass-phase compositions and a high-dosage test of specimens of the grain size - density series. Both tests were operated at approximately 1000°C, the first to approximately 10^{21} nvt (≥ 1 Mev) and the latter to 2 to 3 x 10^{21} nvt (≥ 1 Mev).

The results, recorded in Tables 3.12 and 3.13, indicate that the macroscopic expansion of the glass-phase compositions exceeds that of the AOX and UOX-MgO materials for comparable exposure. This indication is supported by the data for the EBOR composition in the high-dosage test in which the volume expansion of approximately 3 percent is about 0.5 percent larger than that of the AOX composition of slightly smaller grain size. Detailed examination of the lattice and microscopic expansion, microcracking, and helium content are in progress.

A rather unusual result was observed in further examination of three of the high-dosage specimens. These included AOX specimens of 5- and 20-micron grain size and an EBOR specimen with macroscopic volume expansions of 1.8, 2.4, and 3.3 percent, respectively. The lattice expansion in each case was approximately 0.04 percent and the microscopic expansion‡ was 0.8 to 1.0 percent, values essentially in agreement with computations from the kinetic equations. The unusual result was that the strength of each of the three samples was about 80 percent of that of unirradiated material; based on previous results, a much lower strength should have resulted if the large macroscopic expansion were due simply to microcracking. Density measurements also indicated limited microcracking; hence, the expansion does not appear to be an extension of the same types observed previously.

---

*Ibid., p. 131.

†"High-Temperature Materials Program Progress Report No. 34, Part A," GE-NMPO, GEMP-34A, June 19, 1964, Table 2.3, p. 15.

‡Determined from picnometer density of specimens crushed to particle sizes less than the original grain size.

TABLE 3.12

MACROSCOPIC EXPANSION OF BeO COMPOSITIONS CONTAINING GLASS-PHASE ADDITIVES IRRADIATED AT 950° TO 1050°C

Composition	Nominal		Flux, 10^{14}	Dosage, 10^{20} nvt ($\geq$1 Mev)	Expansion, %		
	Grain Size, microns	Density, g/cm^3			Length	Diameter	Volume
UOX + MgO	5	2.60	2.0	9.1	0.3	0.3	0.9
			2.0	9.1	0.3	0.4	1.1
	5	2.75	2.1	9.6	0.3	0.3	0.9
			2.2	10.0	0.5	0.4	1.3
			2.4	10.9	0.2	0.3	0.8
	5	2.90	1.7	7.8	0.4	0.4	1.2
			2.2	10.0	0.3	0.3	0.9
	10	2.90	2.0	9.1	0.4	0.3	1.0
AOX	5	2.90	1.5	6.8	0.6	0.5	1.6
			2.3	10.5	0.4	0.4	1.2
UOX + 1 wt % low silica glass	5	2.90	2.2	10.0	0.4	0.5	1.4
			2.4	10.9	0.6	0.8	2.2
			1.8	8.2	0.6	0.7	2.0
	5	2.90	1.9	8.7	0.4	0.5	1.4
			2.5	11.4	0.6	0.5	1.6
			1.5	6.8	0.6	0.3	1.2
			2.3	10.5	0.7	0.5	1.7
	20	2.90	2.2	10.0	0.4	0.4	1.2
			2.4	10.9	0.5	0.5	1.5
			2.3	10.5	0.5	0.5	1.5
			1.6	7.3	0.6	0.5	1.6
Medium silica	20	2.90	2.1	9.6	0.5	0.6	1.7
			2.6	11.9	0.6	0.7	2.0
			2.2	10.0	0.7	0.7	2.1
	5	2.90	2.6	11.9	0.5	0.5	1.5
High silica	20	2.90	2.0	9.1	0.5	0.5	1.5
			2.3	10.5	0.5	0.5	1.5
Bentonite glass, 1 wt %	5	2.90	2.6	11.9	0.6	0.6	1.8
	20	2.90	1.9	8.7	0.5	0.5	1.5
			2.2	10.0	0.4	0.3	1.0
Bentonite glass, 2 wt %	20	2.90	2.4	10.9	0.4	0.4	1.2
Al_2O_3, 1 wt %	5	2.90	2.2	10.0	0.7	0.3	1.3
EBOR (B-78)[a]	20	2.90	1.4	6.4	0.5	0.5	1.5
			2.3	10.5	0.4	0.4	1.2
			2.4	10.9	0.3	0.4	1.1
			2.4	10.9	0.3	0.3	0.9
EBOR (B-86)[a]	20	2.90	2.0	9.1	0.3	0.5	1.3
			2.3	10.5	0.2	0.3	0.8
			1.7	7.8	0.4	0.5	1.4

[a] B numbers refer to EBOR blocks from which samples were obtained.

TABLE 3.13

EXPANSION OF BeO IRRADIATED AT 950° TO 1050°C
TO A DOSAGE OF APPROXIMATELY 3 x 10^{21} NVT

Specimen Description			Irradiation Conditions		Expansion, %		
Composition	Nominal Grain Size, microns	Nominal Density, g/cm^3	Flux, 10^{14} nv ($\geq$1 Mev)	Dosage, 10^{21} nvt ($\geq$1 Mev)	Length	Diameter	Volume
UOX + MgO	5	2.60	1.91	3.0	0.8	0.6	2.0
	5	2.75	1.4	2.2	0.5	0.5	1.5
			1.6	2.4	0.6	0.5	1.6
			1.7	2.7	0.8	0.6	2.0
			1.8	2.8	0.8	0.5	1.8
			1.6	2.5	0.7	0.5	1.7
	5	2.90	1.9	3.0	0.8	0.5	1.8
			1.7	2.6	0.7	0.5	1.7
			1.5	2.3	0.5	0.3	1.1
			1.7	2.6	0.6	0.5	1.6
			1.8	2.8	0.7	0.6	1.9
	10	2.90	1.6	2.5	0.9	0.5	1.9
			1.4	2.2	0.8	0.4	1.6
			1.8	2.8	0.8	0.5	1.8
AOX	5	2.60	1.6	2.4	0.8	0.8	2.4
			1.8	2.8	0.7	0.8	2.5
			1.5	2.4	0.7	0.8	2.3
	5	2.75	1.8	2.7	0.6	0.6	1.8
			1.4	2.1	0.4	0.5	1.4
			1.6	2.4	0.5	0.5	1.5
			1.7	2.7	0.6	0.7	2.0
	20	2.90	1.5	2.3	0.6	0.6	1.8
			1.7	2.7	0.7	0.8	2.3
			1.6	2.5	0.7	0.8	2.3
			1.7	2.7	0.7	0.8	2.3
EBOR	20	2.90	1.5	2.3	0.8	1.0	2.8
			1.7	2.6	0.9	1.0	2.9
			1.9	2.9	1.0	1.1	3.2
			1.9	2.9	1.1	1.1	3.3
			1.6	2.5	0.9	1.0	2.9

DISCUSSION OF EXPANSION

In view of the importance of irradiation expansion in practical applications of BeO, a brief discussion and/or evaluation of the expansion equations and predictions is presented herein. Since most of the engineering properties, with the exception of thermal conductivity, do not appear to be changed appreciably prior to microcracking, the ideal situation would be to irradiate under flux and temperature conditions at which the volume expansion is less than that at which microcracking occurs. If the kinetic equations are accurate, these conditions exist, as indicated in Figure 3.13.

However, the accuracy of the kinetic equations and, hence the existence of such conditions, remains questionable. On the positive side, the equations seem reasonable within the concepts of the model and the foreseeable modifications to the constants probably will not alter the predictions appreciably. According to the model, the activation energies for the annealing rate constant are the migration energies of the defect species. The values

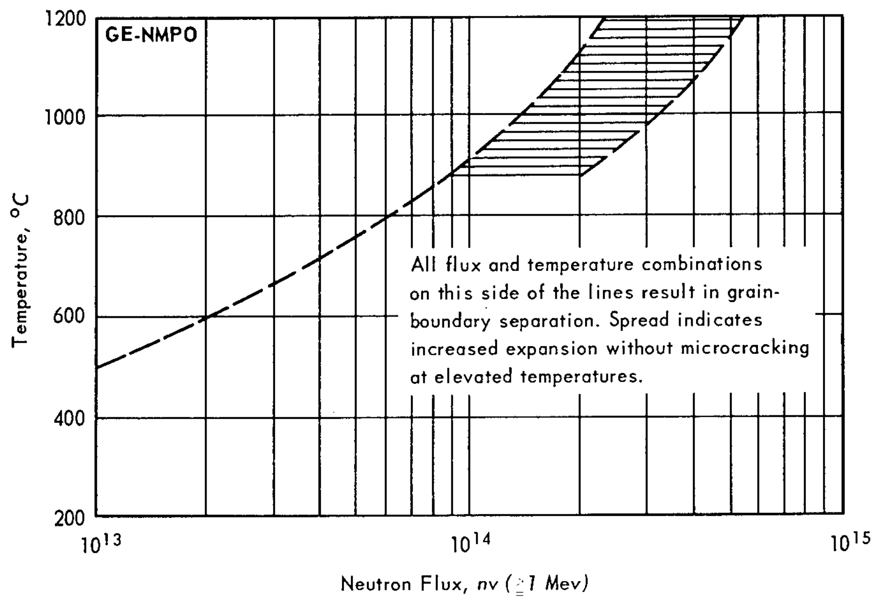

All flux and temperature combinations on this side of the lines result in grain-boundary separation. Spread indicates increased expansion without microcracking at elevated temperatures.

Fig. 3.13 – Estimated minimum irradiation temperature to avoid grain-boundary separation in BeO of 20-micron grain size and 2.9 g/cm^3 density

obtained, 22.4 kcal for interstitials and approximately 10 kcal for vacancies, are within the range expected for ionic - covalent materials, although the latter value seems rather low. Also, the small value of the pre-exponential term, particularly that for vacancies, is of the magnitude usually attributed to extrinsic diffusion, i.e., diffusion in which excess vacancies are caused by impurities.* This is the situation postulated in the model - that irradiation would create an excess of vacancies and interstitials over the number in thermal equilibrium. In these respects, the equation constants appear reasonable.

Some adjustment of these constants will undoubtedly be necessary but these are not expected to be very significant. One source of error involves the use of rate constants from short time data with the saturation, or infinite time, relationships in deriving the rate constant equation for vacancies. A trial calculation indicated that this error was small; hence, the laborious calculations necessary for a more accurate derivation did not appear warranted. A second and more significant error arises from the cycling of reactor power both during any given operational cycle as well as the shutdowns between cycles. In the ETR, reactor startup after shutdown involves, for a number of reasons, a few minutes at several intermediate power levels and there are relatively frequent intervals in which the intermediate power level is maintained for periods up to a few hours. In addition, the final test temperature is adjusted some minutes to hours after the reactor reaches full power. Since the specimen temperatures are maintained by nuclear heating, some dosage is accumulated in these periods at other than the nominal test temperature. Trial calculations based on the actual reactor power variations in one operational cycle indicated that the effect of the several shutdown cycles, in terms of expansion, amounted to a temperature approximately 100°C lower than the nominal test temperature for tests at 1000°

---

*The annealing rate constants are expected to be related to the diffusion coefficients by a proportionality constant which involves the average diffusion distance to the sinks at which the defects disappear. For BeO irradiated at elevated temperatures, assuming clusters of the order of 1000 Å diameter are present at a density of roughly $10^{16}/cm^3$, the proportionality constants for both vacancies and interstitials are of the order of 10^{-12}. Multiplication by such factors leads to very small pre-exponential terms for both types of defects.

to 1100°C. These variations can be taken into account only by iteration of the derivations; consequently, some error exists in the present constants. If the equations are reasonably correct, however, this error is negligible if, as is often the case, the final days of the operational cycle are at the desired test conditions. A third source of error arises from the assumption that macroscopic expansion in non-microcracked specimens is equal to microscopic expansion. Contributions of helium bubbles to the expansion thus enter into the constants. This error was minimized through the use of data from materials of small grain size and data from density measurements. Adjustments due to all three factors would amount to perhaps 2 to 4 kcal in the activation energies.

On the questionable side are the uncertainties regarding the annealing of defect clusters and the expansion due to helium. Although the presence of both vacancy and interstitial clusters assures that both types of sinks exist and hence that saturation is possible, there is at present no direct evidence that the clusters will not continue to grow as irradiation continues. The influence of the helium on the clusters may be the important factor. Although it appears possible for considerable helium to be retained in interstitial positions of the lattice, it seems likely that the helium occupies vacancies. If this is the case, the extremes to be expected include (1) helium escape in accord with vacancy annealing or (2) helium escape at a much slower rate than vacancy annealing because of the multiplicity of trapping sites in the form of clusters. In the first case, the helium concentration will saturate in accord with the equations while in the second case, the helium concentration, and the expansion, would continue to increase beyond the amounts predicted.

PROPERTY CHANGES IN IRRADIATED BeO

Property measurements on irradiated materials included enthalpy, elastic constants, strength, and thermal shock.

Enthalpy

Enthalpy measurements were made on unirradiated and irradiated specimens of AOX-grade and UOX + MgO-grade BeO compositions at temperatures of approximately 300°, 600°, and 900°C using a drop technique similar to that described by Victor and Douglas.* Results of the measurements, summarized in Table 3.14, indicate no change within about 2 percent after irradiation to approximately 10^{21} nvt at 1000°C.

ELASTIC CONSTANTS

In previous work, the dynamic elastic constants of irradiated specimens were found to be essentially unchanged in specimens in which microcracking did not occur. There was actually a small decrease of approximately 1 percent which appeared consistent with the decrease in density. In microcracked specimens, the elastic constants appeared to decrease more or less linearly with increasing volume expansion; however, this conclusion was not considered reliable because of the difficulties of measuring and identifying the resonant frequencies.†

The previous observations regarding microcracked specimens were confirmed using the modified high-frequency equipment described previously in this section of the report. With this equipment, the number of resonant frequencies was found to decrease with increasing expansion in the microcracked region. In general, it was possible to identify and measure resonant frequencies in specimens with volume expansion ranging up to about 2

*A. C. Victor and T. B. Douglas, "Thermodynamic Properties of Magnesium Oxide and Beryllium Oxide from 298° to 1200°K," *Journal of Research of the National Bureau of Standards*, Vol. 67A, No. 4, 1963, pp. 325–329.

†"Second Annual Report – High-Temperature Materials and Reactor Component Development Programs, Volume I – Materials," GE-NMPO, GEMP-177A, February 28, 1963, p. 130.

TABLE 3.14

COMPARISON OF ENTHALPY OF UNIRRADIATED AND IRRADIATED BeO

Composition	Sample Condition	Temperature, °C	Enthalpy ($H_T - H_{25°C}$), cal/g		Deviation From NBS Values, %
			NMPO	NBS[a]	
AOX	Unirradiated	315	96.4	98.5	-2.1
		314	96.6	98.3	-1.7
		314	96.4	98.3	-1.9
		917	371.3	372.0	-0.2
		919	369.1	373.0	-1.0
		922	374.5	374.0	0.1
	Irradiated	316	98.9	98.7	0.2
		312	96.1	97.2	-1.1
		316	99.3	98.7	0.6
		917	374.0	372.0	0.5
		920	373.1	373.0	0.0
		921	375.6	373.2	0.6
UOX+MgO	Unirradiated	312	98.7	97.2	1.5
		314	98.0	98.3	-0.3
		314	97.3	98.3	-1.0
		602	216.0	221.5	-2.5
		603	219.6	222.5	-1.3
		603	218.0	222.5	-2.0
		918	366.8	372.5	-1.5
		919	366.8	373.0	-1.7
		920	367.1	373.0	-1.6
	Irradiated	316	99.4	98.7	0.7
		316	100.8	98.7	2.1
		315	98.8	98.5	0.3
		603	218.1	222.5	-2.0
		603	220.8	222.5	-0.8
		604	219.2	223.0	-1.7
		915	367.4	370.7	-0.9
		917	367.6	372.0	-1.2
		925	367.2	375.7	-2.3

[a] These values were obtained by graphical interpolation of the tabular data presented in the referenced report. A. C. Victor and T. B. Douglas, "Thermodynamic Properties of Magnesium Oxide and Beryllium Oxide from 298 to 1200°K," Journal of Research of the National Bureau of Standards, Vol. 67A, No. 4, 1963, pp. 325-329.

percent following low-temperature irradiation. Data for samples irradiated at temperatures in the 150° to 360°C range and at approximately 500°C, respectively, are given in Tables 3.15 and 3.16, together with the volume expansion and strength change. The approximately linear decrease in the Young's modulus with increasing volume expansion of these specimens is shown in Figure 3.14.

Data will be obtained on specimens irradiated at elevated temperatures in the coming months.

Strength

Changes in the room-temperature strength of irradiated BeO have been found to follow a pattern that is simply related to microcracking. The strength increases up to 20 percent in 100°C irradiations and up to 40 percent in elevated-temperature irradiations where the volume increase is less than that at which microcracking occurs. Since the volume change at which microcracking occurs increases with increasing irradiation temperature, the

TABLE 3.15

DYNAMIC ELASTIC CONSTANTS OF BeO SPECIMENS IRRADIATED AT 150° TO 360°C

Specimen Description			Irradiation Conditions				Elastic Constants							
							Shear Modulus			Young's Modulus			Post-Irradiation Poisson's Ratio	Pre-Irradiation Room-Temperature Modulus Of Rupture %
Composition	Grain Size, microns	Density, g/cm^3	Temperature, °C	Flux, 10^{13} nv ($\geq$1 Mev)	Dosage, 10^{20} nvt ($\geq$1 Mev)	Volume Expansion, %	10^6 psi	10^{12} dynes/cm^2	Pre-Irradiation Value, %	10^6 psi	10^{12} dynes/cm^2	Pre-Irradiation Value, %		
UOX-MgO	5	2.740	345	5.0	2.3	0.7	18.7	1.29	99	46.0	3.17	98	0.23	106
	5	2.731	150	3.9	1.8	0.4	18.3	1.26	97	44.9	3.10	96	0.22	93
	5	2.740	135	3.4	1.6	0.8	18.7	1.29	99	46.0	3.17	97	0.23	98
	5	2.892	290	4.6	2.1	0.7	21.2	1.46	99	51.8	3.57	98	0.22	105
	5	2.836	335	5.6	2.6	1.0	8.8	0.61	43	23.4	1.61	45	0.33	37
	5	2.885	170	5.2	2.4	1.1	17.9	1.23	84	42.6	2.94	81	0.19	57
	7	2.842	190	6.0	2.7	1.7	9.4	0.65	46	22.0	1.52	42	0.17	28
	18	2.870	350	5.4	2.5	1.0	15.0	1.03	73	38.0	2.62	69	0.27	44
	17	2.871	150	4.2	1.9	1.1	13.1	0.90	64	32.6	2.25	60	0.25	9
	18	2.868	160	4.9	2.2	1.3	a	-	-	24.5	1.69	44	a	22
	71	2.772	355	5.8	2.6	1.4	6.6	0.46	35	15.8	1.09	29	0.19	23
AOX	4	2.732	190	6.2	2.8	2.4	a	-	-	a	-	-	a	18
	4	2.741	170	5.4	2.5	1.6	a	-	-	a	-	-	a	63
	17	2.836	170	4.8	2.2	1.9	a	-	-	a	-	-	a	14
	17	2.836	150	4.2	1.9	1.2	a	-	-	a	-	-	a	-
	62	2.753	350	5.6	2.6	2.1	a	-	-	a	-	-	a	7
EBOR	29	2.746	325	5.7	2.6	1.5	8.5	0.59	43	19.7	1.36	42	0.16	31
	29	2.754	360	5.9	2.7	1.7	7.6	0.52	38	17.6	1.21	37	0.16	-
	29	2.740	180	6.1	2.8	2.1	6.9	0.48	35	15.7	1.08	33	0.14	24
	29	2.757	165	5.3	2.4	1.3	10.3	0.71	52	23.8	1.64	50	0.16	38
	17	2.776	320	5.1	2.3	1.1	11.4	0.78	58	27.0	1.86	57	0.19	-
	17	2.782	185	4.6	2.1	0.8	10.6	0.73	54	25.2	1.74	53	0.19	42
	17	2.772	165	5.3	2.4	1.4	16.6	1.14	84	39.7	2.74	84	0.19	-
	24	2.766	330	5.3	2.4	0.9	8.8	0.61	44	20.0	1.38	42	0.14	32
	24	2.764	350	5.5	2.5	1.2	9.8	0.68	49	22.2	1.53	47	0.14	32
	24	2.749	190	5.7	2.6	1.4	8.1	0.56	41	18.4	1.27	39	0.14	-
	24	2.780	170	4.9	2.2	1.2	10.7	0.74	54	24.5	1.69	52	0.15	42

[a] Not measurable.

TABLE 3.16

DYNAMIC ELASTIC CONSTANTS OF BeO SPECIMENS IRRADIATED AT 440° TO 500°C

Specimen Description			Irradiation Conditions				Elastic Constants							
							Shear Modulus			Young's Modulus				
Composition	Grain Size, microns	Density, g/cm^3	Temperature, °C	Flux, 10^{13} nv (≥ 1 Mev)	Dosage, 10^{20} nvt (≥ 1 Mev)	Volume Expansion, %	10^6 psi	10^{12} dynes/cm^2	Pre-Irradiation Value, %	10^6 psi	10^{12} dynes/cm^2	Pre-Irradiation Value, %	Post-Irradiation Poisson's Ratio	Pre-Irradiation Room-Temperature Modulus Of Rupture, %
UOX-MgO	4	2.641	460	6.5	3.0	0.5	17.6	1.21	101	44.2	3.05	98	0.25	-
	4	2.623	480	6.5	3.0	0.5	17.3	1.19	100	43.7	3.01	104	0.26	75
	5	2.729	470	6.7	3.1	0.6	18.6	1.28	99	45.7	3.15	98	0.23	-
	5	2.755	470	6.7	3.1	0.5	19.0	1.31	99	46.8	3.23	99	0.23	-
	5	2.739	500	6.7	3.1	0.4	19.0	1.31	100	46.7	3.22	99	0.23	96
	5	2.903	500	6.4	3.0	0.6	21.6	1.49	100	52.7	3.63	99	0.22	-
	5	2.895	500	6.4	3.0	0.5	21.5	1.48	100	53.5	3.69	100	0.22	82
	5	2.908	500	6.4	3.0	0.6	21.6	1.49	100	53.0	3.65	99	0.22	-
	12	2.880	500	5.7	2.6	0.8	19.7	1.36	94	51.0	3.52	96	0.29	62
	12	2.879	470	5.7	2.6	0.7	20.4	1.41	98	51.4	3.54	96	0.26	-
	19	2.873	500	6.2	2.9	0.3	20.6	1.42	100	51.6	3.56	95	0.25	-
	19	2.894	470	6.2	2.9	0.7	19.7	1.36	94	51.3	3.54	93	0.30	76
	19	2.880	440	6.2	2.9	0.7	19.4	1.34	94	50.2	3.46	92	0.29	63
	39	2.877	470	5.7	2.6	0.5	19.6	1.35	98	50.7	3.50	102	0.29	-
	41	2.932	440	4.9	2.3	0.4	20.4	1.41	99	55.2	3.81	94	0.36	84
	41	2.936	440	4.9	2.3	0.4	20.4	1.41	98	55.5	3.83	94	0.36	-
AOX	2	2.713	460	6.1	2.8	0.6	17.6	1.21	98	42.6	2.94	97	0.20	132
	2	2.692	470	6.1	2.8	0.6	17.1	1.18	97	41.4	2.85	98	0.21	108
	7	2.756	490	6.7	3.1	0.6	19.2	1.32	102	46.7	3.22	98	0.21	-
	7	2.773	470	6.7	3.1	0.7	19.4	1.34	101	47.2	3.25	97	0.21	131
	10	2.853	480	5.2	2.4	0.1	20.1	1.38	97	48.8	3.36	95	0.21	42
	10	2.885	460	5.2	2.4	1.1	a	-	-	a	-	-	a	-
	18	2.90	500	6.6	3.1	0.9	a	-	-	a	-	-	a	16
	18	2.90	470	6.6	3.1	0.9	a	-	-	a	-	-	a	18
	18	2.90	470	6.6	3.1	1.2	a	-	-	a	-	-	a	-
	35	2.91	450	4.7	2.2	1.3	a	-	-	a	-	-	a	13
	35	2.91	450	4.7	2.2	1.0	a	-	-	a	-	-	a	-
EBOR	~20	2.790	450	5.6	2.6	0.5	19.5	1.34	99	46.6	3.21	99	0.19	-

[a] Not measurable.

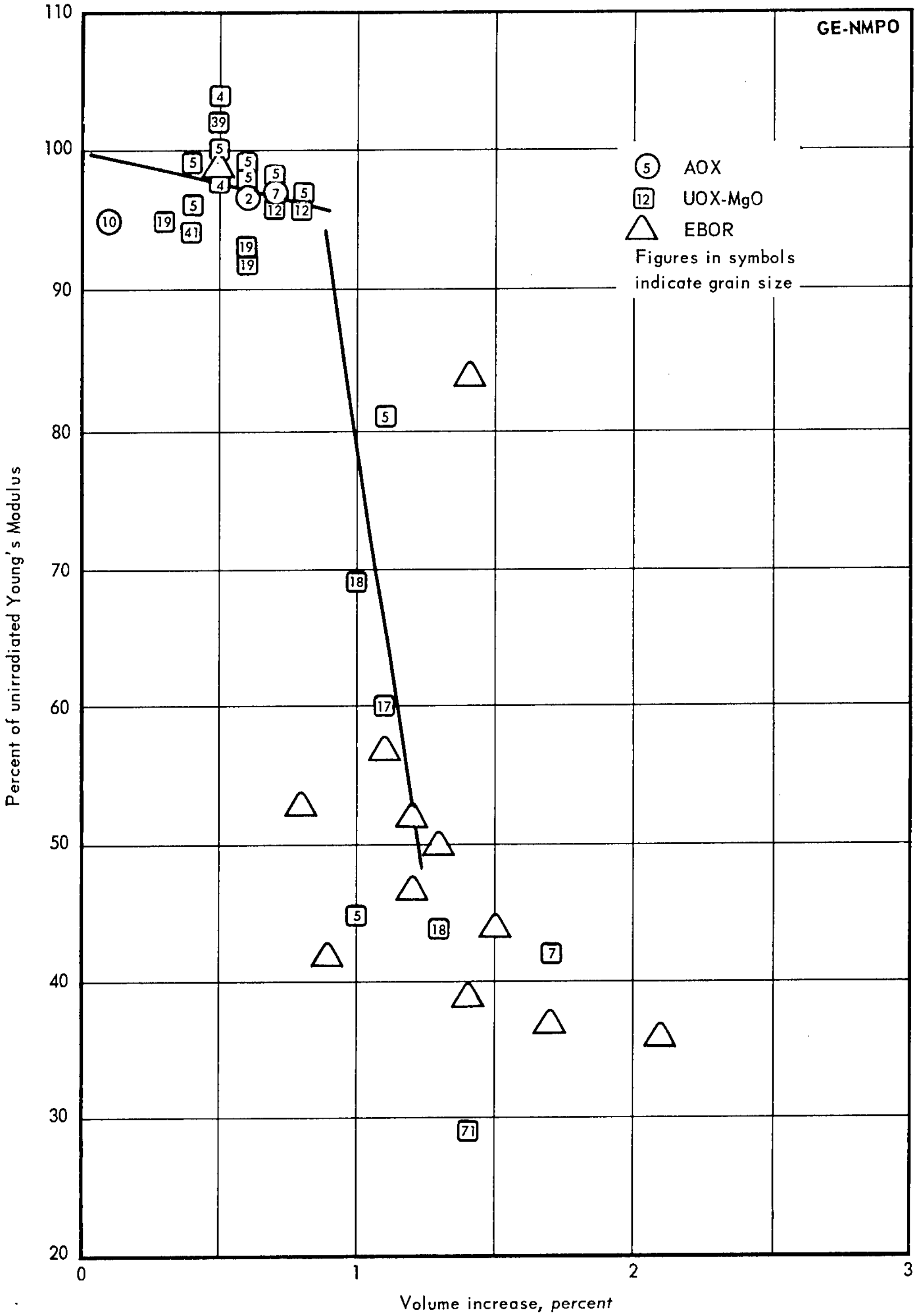

Fig. 3.14 – Young's Modulus of irradiated BeO specimens of various grain sizes and densities as a function of volume expansion

strength increase extends to larger volume change in elevated-temperature irradiations. Once microcracking occurs the strength decreases markedly with further volume expansion. The general pattern is illustrated in Figure 3.15.

Additional measurements completed during the year indicated that the elevated-temperature strength behavior is similar to that at room temperature. Specimens irradiated at 600° to 1000°C were tested at temperatures of 600°, 800°, or 1000°C; the test temperature in each case being equal to or less than the irradiation temperature. The results, recorded in Table 3.17 together with the results of room-temperature tests, show that the percentage change relative to the unirradiated material is approximately the same as that observed in the room-temperature measurements.

Thermal Shock

One of the features of the strength behavior noted previously in specimens irradiated at elevated temperatures was a greater strength decrease per unit volume increase than occurred in specimens irradiated at approximately 100°C. This greater decrease occurred over a relatively small range of volume increase, then the strength change versus volume curve appeared to coincide with that for 100°C irradiations. As a qualitative explanation, this behavior might have resulted from intergranular stresses due to thermal expansion anisotropy and the microcracking might have occurred on cooling from the irradiation temperature.

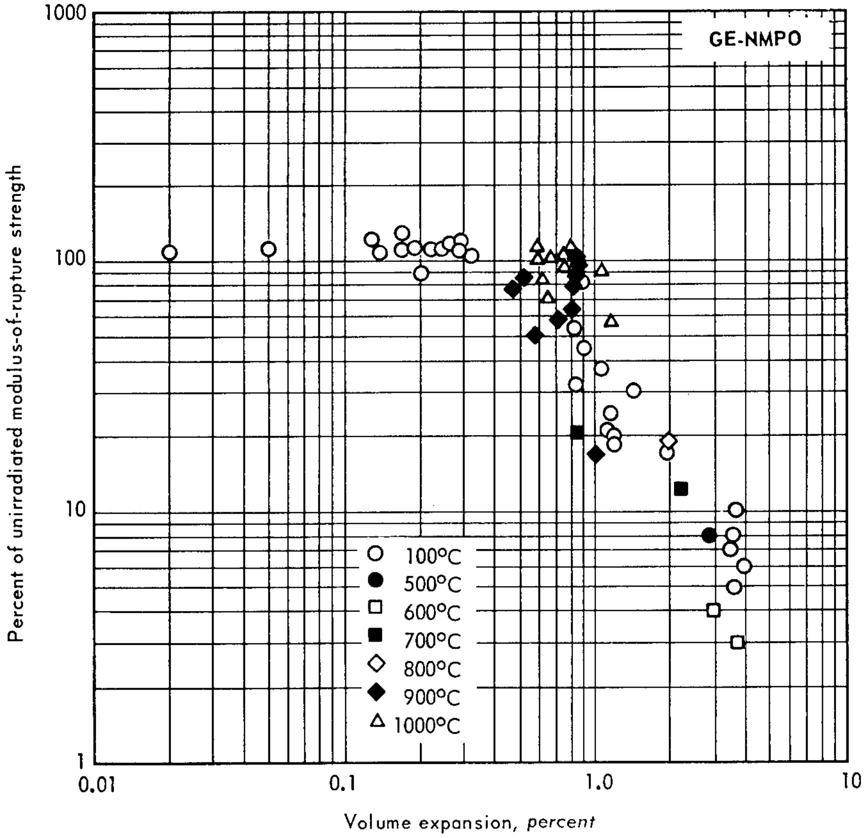

Fig. 3.15 – Strength changes in AOX-grade BeO of 20-micron grain size, 2.9 g/cm^3 density, after irradiation to dosages up to 1.5×10^{21} nvt (> 1 Mev) at temperatures from 100° to 1000°C

TABLE 3.17

MODULUS-OF-RUPTURE DATA ON BeO IRRADIATED AT ELEVATED TEMPERATURES

Specimen Description			Irradiation Conditions				Modulus Of Rupture					
							At Room Temperature			At 600°C		
							Irradiated			Irradiated		
Composition	Grain Size, microns	Density, g/cm3	Temperature, °C	Flux, 10^{14} nv (≥ 1 Mev)	Dosage, 10^{20} nvt (≥ 1 Mev)	Radiation Expansion, vol %	10^3 psi	10^3 kg/cm^2	Percent Of Unirradiated Value	10^3 psi	10^3 kg/cm^2	Percent Of Unirradiated Value
AOX	5	2.75	650	2.0	9.1	2.2	7.6	0.53	25	4.5	0.32	12
			600	1.9	8.7	2.3	7.8	0.55	26	4.9	0.34	14
			750	2.4	11.1	1.6	-	-	-	14.4	1.01	41
			775	2.2	10.2	1.5	13.3	0.94	44	9.4	0.66	27
			600	1.9	9.0	2.1	10.0	0.70	40	6.6	0.46	23
			600	1.8	8.5	2.0	11.4	0.80	46	9.4	0.66	33
	5	2.60	550	2.0	9.5	2.7	-	-	-	4.7	0.33	13
			650	1.9	8.9	1.9	10.0	0.70	32	8.6	0.60	23
			750	2.3	10.6	1.3	14.2	1.00	47	12.2	0.86	33
			775	2.2	10.4	1.1	12.7	0.89	42	11.6	0.82	31
	20	2.75	600	1.7	8.0	2.6	1.6	0.11	5	1.3	0.09	4
			550	1.8	8.5	3.1	1.0	0.07	3	2.1	0.15	6
			750	2.0	9.4	1.8	4.0	0.28	14	3.9	0.27	11
			775	2.0	9.3	2.0	3.5	0.25	12	3.6	0.25	10
			750	2.1	9.8	1.7	5.8	0.41	20	3.6	0.25	10
			775	2.0	9.5	1.8	4.7	0.33	16	3.6	0.25	11
	20	2.60	750	2.2	10.2	1.7	4.5	0.32	21	3.2	0.22	13
			800	2.2	10.0	1.7	3.8	0.27	17	3.2	0.22	13
			550	1.3	6.0	2.5	1.9	0.13	8	2.4	0.17	9
	80	2.90	750	2.1	9.8	2.4	-	-	-	1.1	0.08	6
			800	2.0	9.4	2.2	1.4	0.10	9	1.1	0.08	6
			550	1.5	7.1	-	-	-	-	0.2	0.01	1
			750	2.2	10.0	2.2	1.5	0.10	9	1.3	0.09	6
			800	2.1	9.7	2.2	1.7	0.12	10	1.7	0.12	9
	80	2.75	650	1.8	8.2	3.8	-	-	-	0.9	0.06	5
			750	2.0	9.2	2.8	1.8	0.13	13	1.3	0.09	8
			600	1.7	8.0	4.2	-	-	-	0.6	0.04	4

TABLE 3.17 (Cont.)

MODULUS-OF-RUPTURE DATA ON BeO IRRADIATED AT ELEVATED TEMPERATURES

Specimen Description			Irradiation Conditions				Modulus Of Rupture					
							At Room Temperature			At 800°C		
							Irradiated			Irradiated		
Composition	Grain Size, microns	Density, g/cm3	Temperature, °C	Flux, 10^{14} nv (≥ 1 Mev)	Dosage, 10^{20} nvt (≥ 1 Mev)	Radiation Expansion, vol %	10^3 psi	10^3 kg/cm^2	Percent Of Unirradiated Value	10^3 psi	10^3 kg/cm^2	Percent Of Unirradiated Value
AOX	5	2.75	850	2.0	9.0	1.0	-	-	-	11.3	0.80	38
			1000	3.2	11.5	1.0	31.0	2.18	103	24.2	1.70	69
			970	3.1	11.3	1.0	34.4	2.42	132	34.8	2.45	99
			940	2.8	10.0	1.2	36.8	2.59	141	37.2	2.62	106
	20	2.90	900	2.1	5.1	0.8	24.1	1.69	79	32.9	2.31	93
			900	2.1	5.1	0.8	34.5	2.43	108	39.6	2.78	107
	20	2.75	950	2.5	11.3	0.9	22.5	1.58	81	18.8	1.32	58
			970	2.1	5.0	0.6	26.2	1.84	101	31.2	2.19	103
	20	2.60	900	2.4	11.0	1.2	24.8	1.74	104	20.3	1.43	73
			900	2.4	10.8	1.1	31.4	2.21	131	28.5	2.00	102
			900	2.3	10.2	1.0	32.4	2.28	136	35.9	2.52	129
			850	2.0	9.2	1.1	21.4	1.50	89	27.7	1.95	100
			800	2.0	8.8	1.3	13.4	0.94	56	13.5	0.95	49
	80	2.90	900	2.4	11.0	1.4	2.2	0.15	14	3.4	0.24	19
			930	2.4	10.8	1.2	4.0	0.28	26	5.7	0.40	33
			900	2.3	10.1	1.3	-	-	-	3.2	0.22	19
			850	2.0	9.2	1.5	1.4	0.10	9	1.4	0.10	8
	80	2.75	950	2.8	10.0	1.0	5.7	0.40	39	7.5	0.53	46
			930	2.3	8.2	1.0	5.7	0.40	41	10.4	0.73	64
UOX-MgO	20	2.90	950	2.3	5.5	0.6	22.7	1.60	70	24.0	1.69	70

TABLE 3.17 (Cont.)

MODULUS-OF-RUPTURE DATA ON BeO IRRADIATED AT ELEVATED TEMPERATURES

Specimen Description			Irradiation Conditions				Modulus Of Rupture					
							At Room Temperature			At 1000°C		
							Irradiated			Irradiated		
Composition	Grain Size, microns	Density, g/cm^3	Temperature, °C	Flux, 10^{14} nv (≥ 1 Mev)	Dosage, 10^{20} nvt (≥ 1 Mev).	Radiation Expansion, vol %	10^3 psi	10^3 kg/cm^2	Percent Of Unirradiated Value	10^3 psi	10^3 kg/cm^2	Percent Of Unirradiated Value
AOX	5	2.75	1000	2.5	9.0	0.9	36.2	2.54	139	31.9	2.24	90
	20	2.90	1040	1.5	3.6	0.5	27.2	1.91	85	28.5	2.00	77
			1040	1.8	4.2	0.6	31.7	2.23	90	24.6	1.73	66
			1025	2.0	4.7	0.7	30.4	2.14	95	30.2	2.12	81
	20	2.75	1050	2.3	5.5	0.7	30.5	2.14	117	27.6	1.94	91
			1050	2.3	5.5	0.7	28.4	2.00	109	27.8	1.95	92
	50	2.90	1100	1.8	4.3	0.4	22.6	1.59	120	21.4	1.50	98
			1000	2.4	5.6	0.7	18.0	1.26	96	24.3	1.71	111
			1100	2.3	5.5	0.5	22.0	1.55	117	22.1	1.55	101
			1100	2.1	4.9	0.4	21.3	1.50	113	22.4	1.58	103
			1100	2.3	5.5	0.5	22.1	1.55	118	24.2	1.70	111
			1000	2.4	5.6	0.7	20.1	1.41	107	16.5	1.16	75
	80	2.75	1000	2.5	9.0	1.0	5.8	0.41	40	7.5	0.53	46
			1000	3.0	10.8	1.0	6.4	0.45	44	7.9	0.56	48
UOX-MgO	20	2.90	1050	1.8	4.3	0.4	25.7	1.81	85	29.6	2.08	84
			1030	2.1	5.1	0.5	27.9	1.96	92	29.8	2.10	84
			1030	2.1	5.1	0.5	25.3	1.78	83	32.5	2.28	92
			1030	1.7	4.0	0.4	23.2	1.63	76	34.7	2.44	98

Evidence in support of this explanation was obtained in a simple thermal shock test consisting of quenching specimens from elevated temperature into water at 20° to 25°C. Specimens irradiated at 1000°C and quenched from 800°C expanded due to microcracking 0.1 to 0.2 percent in volume in the first quenching and expanded less than 0.1 percent in three subsequent quenchings. In similar tests of specimens irradiated at approximately 600°C and quenched from 500°C, the expansion was again 0.1 to 0.2 percent in the first quenching and approximately the same in three additional quenches. In both tests, the volume changes appeared to be independent of the grain size over the range from 5 to 60 microns. In contrast, unirradiated specimens of the same range of grain sizes subjected to the same quenching treatment were not affected.

These results are considered significant. Although the quenching treatment is undoubtedly a severe test in comparison to the thermal cycles encountered in irradiation tests or reactor applications, it is indicative of the possible magnitude of the effects of repeated thermal cycling. Thermal cycling, therefore, can be expected to lead to variations in the macroscopic expansion and strength of the irradiated material.

3.4 SUMMARY AND CONCLUSIONS

An internally consistent picture of the defect structure and of the kinetics of the expansion of BeO was obtained during the year. For irradiation temperatures up to about 600°C, the expansion results from approximately equal concentrations of interstitial and vacancy defects, but at higher temperatures vacancies predominate. Cluster development was found to progress from small unresolvable dots at 100°C to planar clusters up to 1200 Å in length at 1200°C. The occurrence of both interstitial and vacancy clusters was established using dark-field electron transmission microscopy techniques.

Kinetic relationships were derived from the expansion data which show that the during-irradiation annealing of both interstitial and vacancy defects follow first-order kinetics. Equations which describe the microscopic expansion, $(\Delta V/V)_m$, i.e., the expansion exclusive of that due to microcracking, are: given

$$\left(\frac{\Delta V}{V}\right)_m = \frac{K}{A}\,[1 - \exp(-At)] \tag{3.11}$$

or for repetitive irradiations

$$\left(\frac{\Delta V}{V}\right)_m = \frac{K}{A}\,[1 - \exp(-At)] + \left(\frac{\Delta V}{V}\right)_o \exp(-At) \tag{3.12}$$

where:

$$\left(\frac{\Delta V}{V}\right)_m = \frac{1}{2}\left(\frac{\Delta V}{V}\right)_i + \frac{1}{2}\left(\frac{\Delta V}{V}\right)_v$$

$$K = 3.3 \times 10^{-23}\,\phi$$

$$A_i = 0.113 \exp(-22{,}400/RT)$$

$$A_v = 2.54 \times 10^{-5} \exp(-9750/RT)$$

and K is the defect production rate per second, ϕ is the neutron flux nv (≥ 1 Mev), $(\Delta V/V)_o$ is the defect concentration at start of any repeat irradiation, A_i and A_v, respectively, are the annealing rate constants for interstitial and vacancy defects, R is the molar gas constant cal/°K-mole, T is the absolute temperature, °K, and t is the irradiation time in seconds. These kinetic equations describe the expansion reasonably well over the temperature range from 100° to 1200°C; however, the predicted saturation of the expansion is yet to be observed experimentally and remains questionable due to uncertainty regarding the effects of helium.

Some progress was made in determining the helium behavior. Escape of the helium was found to be dependent on surface area, particularly on microcracking. In bulk specimens, about 25 percent of the helium formed escaped in 100°C irradiations in which the samples were extensively microcracked, while less gas escaped at elevated temperatures at which microcracking did not occur or was small. About 75 to 80 percent of the helium retained in specimens irradiated at elevated temperatures remained in the grains, the remainder appearing as helium bubbles at the grain boundaries. Preliminary evidence indicated that diffusion of the helium from bulk specimens in the absence of microcracking followed kinetics similar to those ascribed to vacancies. The bubbles were found to contribute about 20 percent of the 1 percent expansion in materials of 20-micron grain size irradiated at 1000°C and 10^{21} nvt (≥ 1 Mev); a potential for further expansion was demonstrated in post-irradiation annealing experiments at approximately 1300°C.

In property measurements, no change in the enthalpy of irradiated specimens was observed up to 900°C for specimens irradiated at 1000°C. The elevated-temperature strength of specimens irradiated at elevated temperatures was found to be essentially the same as that of unirradiated material in the absence of microcracking which occurs at approximately 0.5 to 1.0 percent volume expansion. Changes in the elastic constants follow the same pattern as the strength changes.

3.5 PLANS AND RECOMMENDATIONS

Efforts will continue to define the factors influencing the expansion, particularly the annealing of clusters during irradiation and the role of helium in cluster or bubble form. These efforts will include further irradiation of previously irradiated samples to check the existence of saturation of the expansion and, tentatively, an irradiation to determine during-irradiation annealing of clusters. Measurements of property changes will be continued, particularly on the thermal conductivity of irradiated material.

4. FISSION GAS DIFFUSION IN UNFUELED CERAMIC MATERIALS

(57069)

The objective of this program is to advance the basic knowledge of fission gas diffusion and radiation damage in unfueled ceramic materials.

This work is concerned with the diffusion of Kr, Xe, and I atoms in ceramic oxides (MgO, BeO, Al_2O_3, and ZrO_2) subsequent to their injection via ion bombardment. The diffusion characteristics of these heavy atoms are deduced by an analysis of the amount of diffusant remaining in a sample as a function of time at constant temperature.

No results on this study are yet available

[illegible]

4.1 ION BOMBARDMENT STUDIES

For reasons discussed in the previous annual report,* an ion gun (Figure 4.1 and 4.2), similar in design to the one described by Carlston and Magnuson,† was fabricated. The assembled apparatus and vacuum system is shown in Figure 4.3. The entire apparatus is housed in a walk-in hood.

Positive krypton ion currents of 1 to 28 microamperes were measured at the Faraday Cage with the ion source operating at accelerating potentials up to 35 kev. Ion-beam characterization studies‡ on a 20-kev beam using aluminum foil targets showed a krypton inventory reproducibility of 6.2 percent for seven successive bombardments. Energetic neutrals formed in the source or along the beam trajectory amounted to 7.5 percent. The effect, if any, of these neutrals would be to give an injected ion absorption distribution more skewed toward the incident surface than that predicted by machine calculation.

The non-uniform areal distribution of the ion beam has proven thus far to be the major obstacle preventing the obtainment of useful diffusion specimens. Figure 4.4, an autoradiograph of an aluminum target positioned near the focal point of a 20-kev Kr^{85} beam, vividly shows the degree of nonuniformity, the darker area having the greater krypton concentration. Some improvement in the areal distribution was obtained with an unfocused beam.

Although, krypton ions will be injected into the ceramic targets at energies in excess of 30 kev, characterization studies were conducted at potentials of 20 kev because the insulators between the extractor and bottom plate had deteriorated through use so that arcing occurred at the higher potentials. The use of Teflon insulators corrected this condition. Targets injected with krypton at the higher accelerating potentials showed no improvement

---

*"Third Annual Report – High-Temperature Materials and Reactor Component Development Programs, Volume I – Materials," GE-NMPO, GEMP-270A, February 28, 1964, p. 138.

†C. E. Carlston and G. D. Magnuson, "High Efficiency Low-Pressure Ion Source," *Review of Scientific Instruments*, Volume 33, 1962, p. 905.

‡"High-Temperature Materials Program Progress Report No. 42, Part A," GE-NMPO, GEMP-42A, December 18, 1964, p. 17.

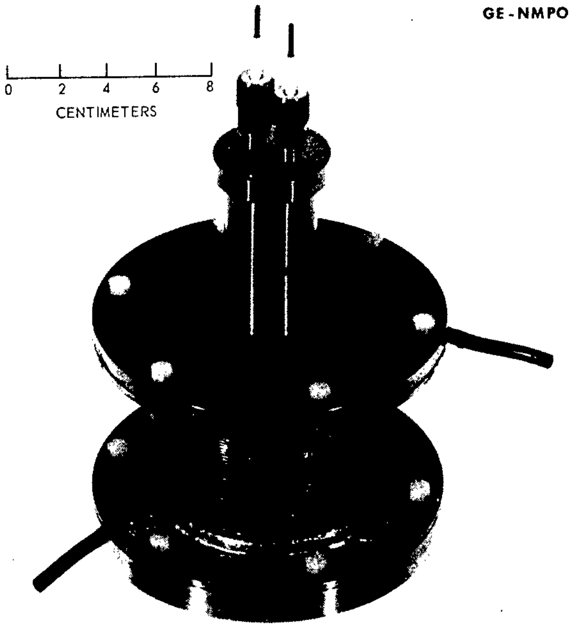

Fig. 4.1 – Magnetically confined oscillating electron ion gun *(Neg. P64-1-3)*

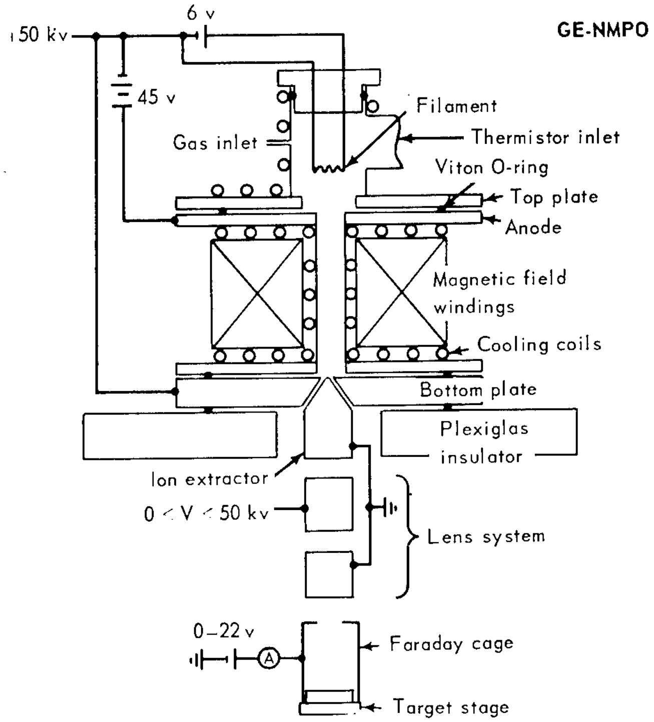

Fig. 4.2 – Magnetically confined, oscillating electron-bombardment ion source

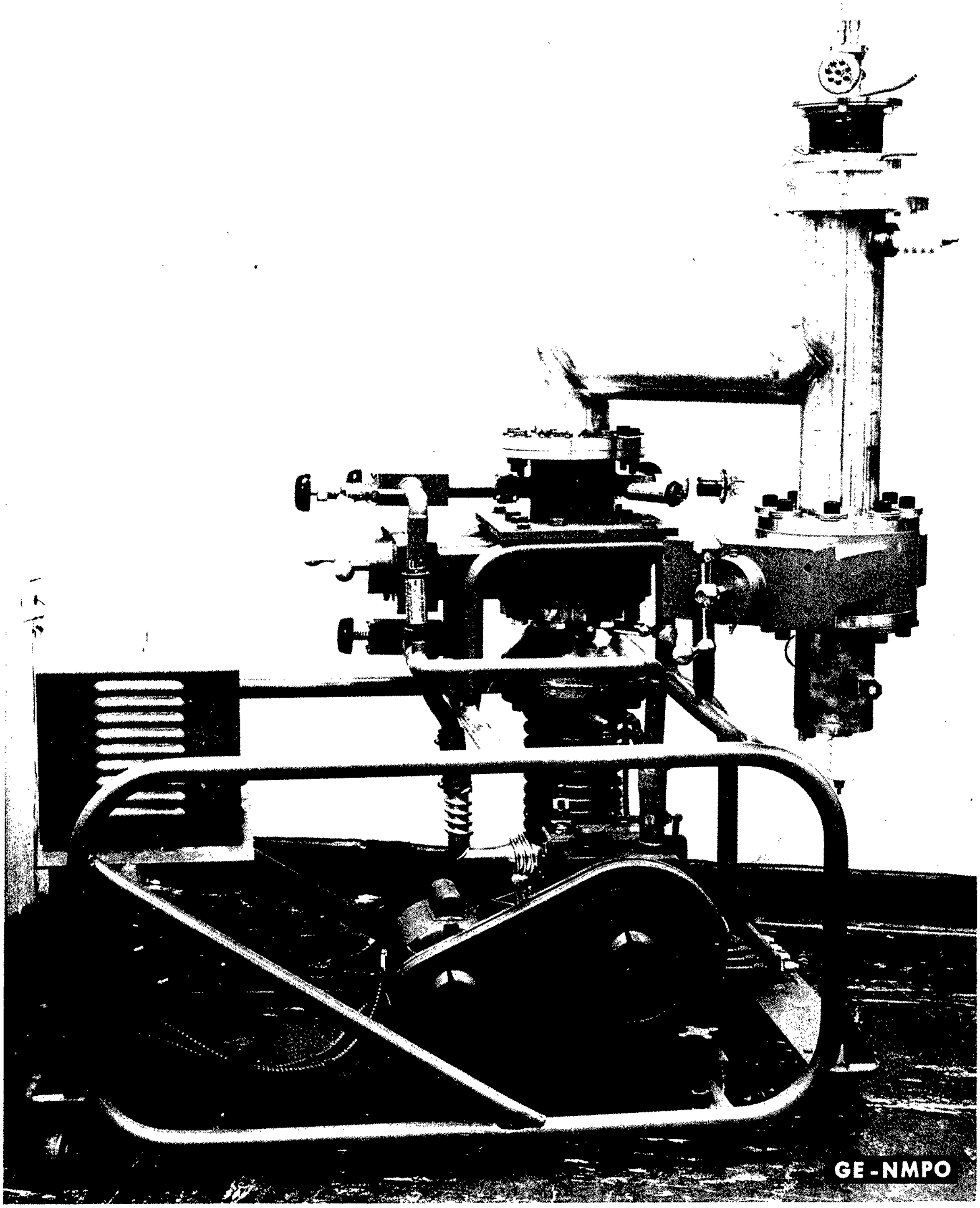

Fig. 4.3 – Ion gun assembly *(Neg. P64-3-24)*

Fig. 4.4 – Autoradiograph of a 20-kev krypton injected aluminum target (darker area has the greatest krypton concentration)

in their areal distribution. The neutral content of the beam was not measured at the higher potentials, but, based on time-of-flight considerations, it could be expected to decrease.

A study is now in progress to ascertain if an improvement in the areal distribution can be achieved by increasing the distance between the extractor and the bottom plate. The reason for this change is that dimensional effects on electrical field perturbations between the extractor and the bottom plate would have less influence on the ion trajectories at greater extractor-plate separations. Changes in the filament shape are also being studied to determine if it is affecting the areal distribution. Point source and spiral configurations are being used for comparison with targets injected while using a helical filament.

4.2 SUMMARY AND CONCLUSIONS

Ion gun characterization studies have shown that the present beam is unfavorable for uniform loading of ceramic targets because of poor areal distribution. This problem is inherent in the ion gun and necessary corrective action is being determined.

4.3 PLANS AND RECOMMENDATIONS

If the results of studies in progress show no improvement in the beam areal distribution, it will be necessary to use an unfocused beam and collimators to reduce the beam diameter. The mono-energetic character of the beam will be checked by measuring atom ranges in bombarded aluminum using the method of Davies* and by determining the retarding potentials required to annihilate the beam at the target. Characterized alumina targets†‡ as well as other ceramics will then be bombarded at room temperature with Kr^{85} and the back diffusion studied as a function of time at temperature. This is to be followed by a study of the effects of target surface characteristics and bombardment-produced damage within the target on the transport of injected krypton.

---

*J. A. Davies, et al., "A Radiochemical Technique for Studying Range Energy Relationships for Heavy Ions of Kev Energies in Aluminum," *Canadian Journal of Chemistry*, Vol. 38, 1960, pp. 1526–1534.

†"High-Temperature Materials Program Progress Report No. 34, Part A," GE-NMPO, GEMP-34A, April 15, 1964, p. 21.

‡"High-Temperature Materials Program Progress Report No. 36, Part A," GE-NMPO, GEMP-36A, June 19, 1964, p. 23.

5. FISSION PRODUCT TRANSPORT PROCESSES IN REFRACTORY-METAL FUEL SYSTEMS

(57070)

The purpose of this program is to study fission product transport processes in refractory-metal fuel systems at temperatures exceeding 1700°C in inert or reducing atmospheres.

As a part of the overall evaluation of refractory metals in reactor applications, fission product diffusion studies and studies on the effects of fission product impurities on the mechanical properties of Ta, W, Mo, Re, Nb, and alloys of these metals are being conducted. The fission product diffusion work is directed toward correlating the parameters of time, temperature, diffusion path length, grain size, and impurities with the transport of fission products through refractory metals.

The work to date was confined to three major areas: (1) diffusion of rare gases (Kr^{85}) in arc-cast tantalum, (2) permeation of rare gases (Kr^{85}) through arc-cast tantalum, and (3) effect of fission products as impurity atoms on the mechanical properties of refractory metals.

5.1 DIFFUSION STUDIES

The problems associated with studying the diffusion of rare gases in metals are: (1) dissolving the gas in the metal, (2) diffusing the gas into the metal without the complications of post-solution heating, and (3) measuring the diffusion rate. To avoid post-solution heating, the glow discharge process using heated metal cathodes was selected to dissolve and diffuse the gas simultaneously.* The experimental program concentrated on development of two techniques for preparing arc-cast tantalum samples containing diffused krypton and a technique for measuring diffusion rates.

Sample Preparation

Two methods were developed for injecting krypton into heated metal cathodes with the glow discharge process. The first method involved a hollow cathode which was heated by the discharge process itself. The second method used self-resistance heating of the cathodes.

The hollow cathode technique was used to demonstrate the feasibility of simultaneously dissolving and diffusing krypton in hot cathodes. A hollow cathode, prepared from an arc-cast tantalum rod, was injected with krypton (containing Kr^{85}) under glow discharge conditions which heated the sample to over 1600°C. Results from grinding studies on this cathode indicated that krypton was dissolved and diffused into tantalum at least 12.5 microns. Further studies were made to develop this technique with a simpler cathode geometry. Parallel plates, used to approximate the hollow cathode configuration, were in-

---

*"Third Annual Report – High-Temperature Materials and Reactor Component Development Programs, Volume I – Materials," GE-NMPO, GEMP-270A, February 28, 1964, p. 141.

jected with krypton at temperatures of 1100° to 1250°C. The X-ray diffractograms of these samples after discharge revealed significant lattice expansion for high levels of loading, again indicating krypton dissolution in tantalum at elevated temperatures under glow discharge conditions. Extensive sputtering and apparently channeling and tunneling effects were also noted. When these samples were post-discharge heated to temperatures in excess of 1300°C, significant bubble formation occurred.

Results from samples prepared with the hollow cathode technique indicated that the levels of loading were variable, the Kr^{85} areal distribution was non-uniform, and a uniform sample temperature was not achieved. In addition, sample surfaces after discharge were too rough to measure diffusion rates with the use of sectioning techniques.

Initial results on self-resistively heated wires indicated that negligible krypton was dissolved. However, if a tantalum foil of relatively large surface area (>400 mm^2) is resistively heated, it can be loaded with measurable levels of activity (5 to 10 disintegrations/min-mm^2) while maintaining a smooth surface and good temperature control. These samples could be readily sectioned by the procedures to be described. Details of the two loading techniques and results are summarized in Table 5.1.

TABLE 5.1

SUMMARY OF TWO HEATED-SAMPLE GLOW DISCHARGE LOADING TECHNIQUES AND RESULTS

Discharge Conditions	Hollow Cathode	Resistance-Heated Planar Cathode
Voltage	350 - 600 volts	350 - 600 volts
Current	0.1 - 2.5 amperes	>0.05 amperes
Pressure	2 - 10 Torr	2 - 10 Torr
Method of heating	Plasma	Self-resistance
Temperature control	Difficult	Readily controllable
Final Product		
Maximum surface area	~600 mm^2 in a 2-liter chamber	>600 mm^2 in a 20-liter chamber
Surface finish	Rough	Smooth
Areal distribution	Non-uniform	Fairly uniform
Levels of loading	Potentially high but variable	Moderate and fairly controllable

To prepare the larger surface area samples, a vacuum bell jar assembly was adapted for use as a glow discharge apparatus. A few short-term experiments at high temperature (15 to 30 minutes at 1700° to 1800°C) demonstrated the advantages of this approach. However, decomposition of the rubber vacuum seals and insulators inside the bell jar resulted in extensive surface contamination on the samples. One cathode, self-resistively heated to 1700°C and subjected to glow discharge for 15 minutes at a pressure of 4 to 8 Torr of krypton (containing 2 x 10^{-5} mole fraction Kr^{85}), was only slightly contaminated and was analyzed using the procedures to be described. A new vacuum and bell jar assembly (Figure 5.1) was completed; the optical system which will be used for measuring sample temperature is being calibrated with the new apparatus.

SAMPLE ANALYSIS TECHNIQUE

Diffusion analysis techniques employed to determine concentration gradient data generally included grinding, chemical and electrochemical etching, and anodization and stripping of the sample substrate. Because of the possibility of complex surface damage effects, a method for determining the entire concentration gradient across the sample was desired.

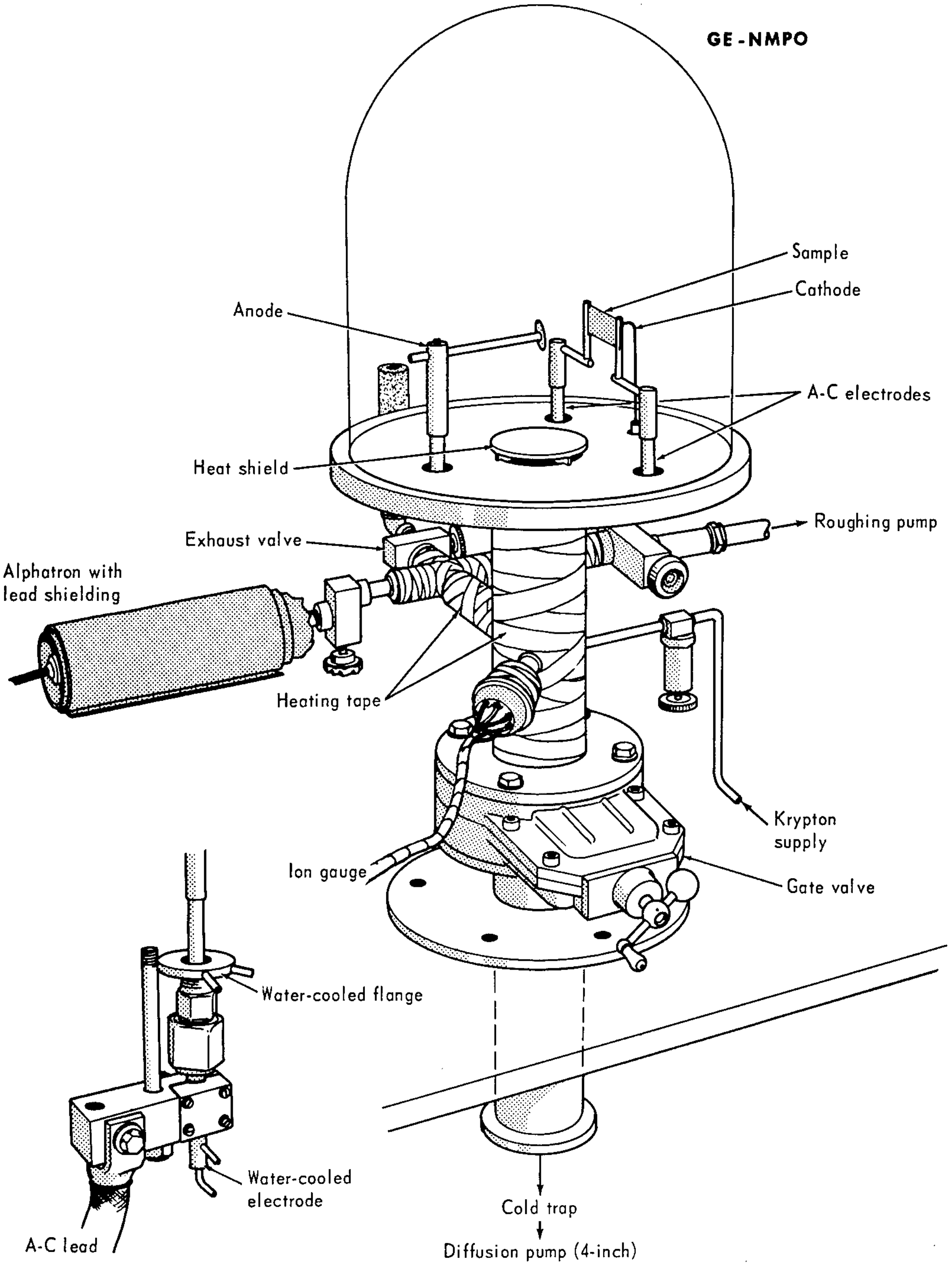

Fig. 5.1 – Glow discharge apparatus for injecting krypton into hot cathode

The relatively short time at temperature and the consequently short diffusion-path lengths anticipated in this work required a method which would remove very thin films (sections) and allow accurate determination of the thickness removed. Anodization* of tantalum to Ta_2O_5 and subsequent stripping of the dense, loosely adherent oxide film was successfully used in sectioning the samples. The thickness of the layer to be removed can be closely controlled by means of the applied potential. Accurate values for the oxide film thickness can be determined by means of its capacitance.

Samples were sectioned by electrolytically oxidizing the surface in a solution which contained 0.05 to 0.2 weight percent KF and 0.73 weight percent Na_2SO_4. The anodization-limiting thickness was found to be 17.55 ± 0.25Å/V for Ta_2O_5 (8.38 ± 0.13Å/V of tantalum) as determined from the film's measured capacitance and the relation* given in equation (5.1)

$$T = (2.42 \pm 0.04) \times 10^2 \text{ A/C} \qquad (5.1)$$

where

T = thickness of Ta_2O_5 film, Å
A = surface area of sample, cm^2
C = capacitance of the film, microfarad

The presence of fluoride ions permits the oxide film to be stripped smoothly off an anodized sample. The thinnest section that can be accurately removed is about 200Å.

CALCULATION OF DIFFUSION COEFFICIENT

The above described sectioning procedure was used to section the cathode which was prepared at 1700°C, and a similar cathode subjected to glow discharge at ambient temperature (< 700°C). These cathodes were 130-micron-thick arc-cast tantalum sheet with about 600 mm^2 total surface area. Each sample was sectioned by anodizing and stripping; the total remaining activity in the sample was counted after each section was removed.

In order to minimize errors in determining the amount of Kr^{85} activity in each section, the beta absorption curve for Kr^{85} in tantalum was determined. The attenuation of the 0.67 Mev Kr^{85} beta was found to be negligible over the range of interest.

The Kr^{85} concentration in the sample prepared at ambient temperature was normalized to the concentration in the sample prepared at 1700°C. With the exception of the activity in the first section, the concentration profile was then subtracted from the Kr^{85} concentration profile for the sample prepared at 1700°C. The corrected residual activity remaining in the heated sample at each point was subtracted from the immediately preceding data point to obtain the Kr^{85} concentration in each thickness of sample removed. The resulting curve for the diffusion-caused Kr^{85} concentration distribution is shown in Figure 5.2.

An approximate value for the diffusion coefficient based on these data and the "thin film" solution† to the diffusion equation was given previously.‡ The following considerations make an analysis at this time tenuous. The solubility of rare gases in metals is low, and the distribution curve has two apparent linear regions extending over a factor of 100 change in concentration. It is not known if the solubility limit of krypton in tantalum is exceeded in the surface or even deeper in the sample or if the surface concentration changes with time. A knowledge of the boundary conditions which fit the conditions in

---

*D. A. Vermilyea, G. E. Research Laboratories; Schenectady, New York; private communication.

†Paul G. Shewmon, *Diffusion in Solids*, McGraw-Hill Book Company, Inc., New York, 1963, pp. 7–8.

‡"High-Temperature Materials Program Progress Report No. 42, Part A," GE-NMPO, GEMP-42A, December 18, 1964, p. 19.

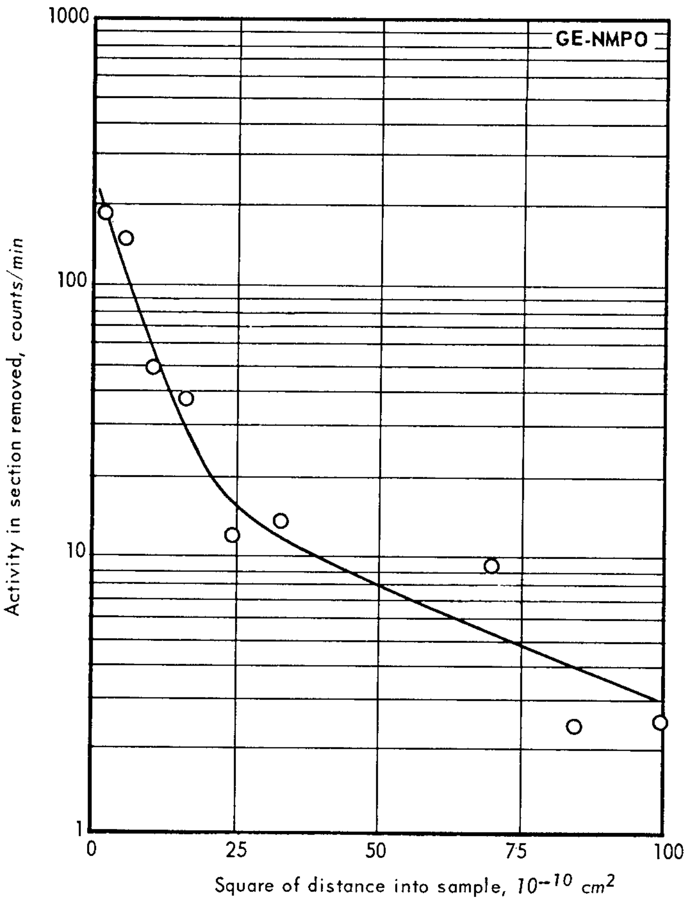

Fig. 5.2 – Distribution of Kr^{85} in arc-cast tantalum sheet after glow discharge at a sample temperature of 1700°C

the sample during the experiment is necessary for a solution to the diffusion equation. Experiments will be run using different times at constant temperature and/or thinner sections to determine what these boundary conditions are.

5.2 PERMEATION STUDIES

A permeation technique was employed to aid in the identification of rare gas transport processes and to supplement the diffusion studies. The permeation of krypton through arc-cast tantalum was studied by heating small evacuated cans in an environment of krypton containing Kr^{85} (1.285×10^{-7} to 1.285×10^{-3} mole fraction Kr^{85}) and beta- and gamma-counting the specimens periodically to detect the presence of Kr^{85}. The specimens, which were evacuated hollow right circular cylinders about 6 mm in diameter and 13 mm long with a 0.5-mm wall thickness, were fabricated by electron-beam-welding high-purity arc-cast tantalum end plates on tubing of similar material. Specimens were tested in a tungsten muffle, containing krypton gas, which was located within a tungsten resistance furnace. The test temperature of the specimen was measured directly with an optical pyrometer. After each test interval, the specimens were beta- and gamma-counted. Periodically, the specimens were checked for leaks using helium gas at 7 kg/cm^2 to insure that ready communication of gases to and from the interior of the specimen did not occur.

No beta or gamma activity was detected in the samples for any of the test conditions (Table 5.2). The source strength was increased in later experiments in order to increase

TABLE 5.2

SUMMARY OF RESULTS FROM PERMEATION EXPERIMENTS USING ARC-CAST TANTALUM AND KRYPTON GAS

Specimen	Time, hr	Temperature, °C	Pressure, Torr	Kr^{85}, mole fraction	Maximum Possible Permeation Coefficient[a]
Ta-1	1	1730	266	1.3×10^{-7}	Sample was run to determine at what temperature significant permeation might occur.
	1	1950	265	1.3×10^{-7}	
	1	2140	265	1.3×10^{-7}	
	1	2230	263	1.3×10^{-7}	
	1	2340	264	1.3×10^{-7}	
	1	2450	265	1.3×10^{-7}	
	1	2530	265	1.3×10^{-7}	
	2.5	2300	205	1.3×10^{-7}	
	36	2400	203	1.3×10^{-7}	
Ta-2	4	2100	204	1.3×10^{-7}	
Ta-4	36	2400[b]	245	1.3×10^{-5}	2.4×10^{-14}
	98	2400	615	1×10^{-5}	
	26	2400	618	1.3×10^{-5}	
Ta-5	2	2400	281	1.3×10^{-5}	
Ta-6	50	2400	235	1.3×10^{-5}	8.0×10^{-15}
	75	2400	615	1×10^{-5}	
	76	2400	615	1.3×10^{-3}	
Ta-7	50	2400	611	1.3×10^{-3}	1.2×10^{-14}
Ta-8	50	2400	618	1.3×10^{-3}	1.2×10^{-14}

[a] Maximum possible permeation coefficients at 2400°C calculated on basis of experimental conditions and no observed permeation. Units are ml of gas at STP-mm of wall thickness/cm^2 of surface area-cm of Hg pressure-sec.

[b] Maximum temperature for the equipment at the present time.

the gamma counting sensitivity. The absence of beta activity in all specimens indicated that no dissolution and diffusion of krypton occurred in the outer one-third of the specimen walls (range of β particles). The absence of gamma activity indicated that no detectable permeation of krypton occurred through the specimen wall. Calculations, based on test times, krypton pressure, and minimum detectable quantity of krypton, resulted in a permeation coefficient of krypton through arc-cast tantalum at 2400°C of less than 8×10^{-15} ml of gas at STP-mm of wall thickness/cm^2 of surface area-cm of Hg pressure-sec (or a leakage rate into the can of less than 8.2×10^{7} atoms/sec).

During the testing, significant changes occurred in the microstructure of the specimens. This is illustrated in Figure 5.3 in which an untested specimen and a specimen tested for 125 hours at 2400°C are compared. The average grain size increased from 20 to 30 microns to approximately 2000 microns. Grain boundaries became V-shaped as the grains enlarged and material was evaporated, as also shown by weight losses. Despite these changes, grain boundaries remained intact as evidenced by the lack of detectable permeation.

5.3 EFFECT OF FISSION PRODUCTS ON MECHANICAL PROPERTIES

Work was initiated late in this calendar year on the effect of fission products as impurity atoms on the mechanical properties of refractory metals. Specifically, the purpose is to isolate the effect on mechanical properties of fission product accumulation in a refractory metal, as distinct from the knock-on damage caused by recoiling fission fragments and other radiation effects. The approach selected is to add various amounts of the different fission product elements to refractory metals in the absence of radiation and to determine the effect on selected mechanical properties.

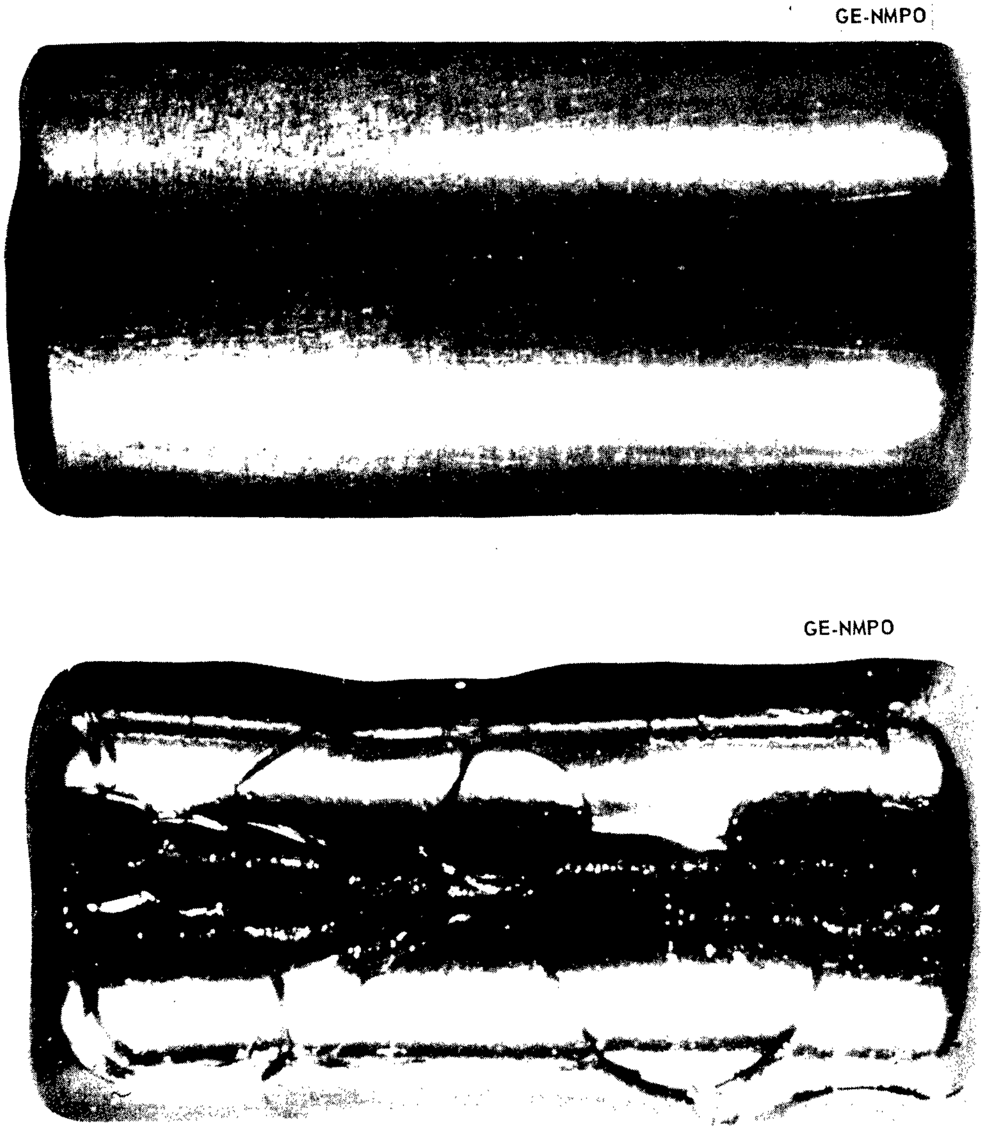

Fig. 5.3 – Untested arc-cast tantalum specimen and specimen tested 125 hours at 2400°C in krypton atmosphere *(Neg. P64-11-10, ~10X)*

In a fuel element a refractory metal may be used in conjunction with UO_2 in a cermet matrix or the refractory metal may be used as a cladding material. Fission products may enter the metal either by recoil or by migration across the metal - UO_2 interface. Recoil occurs independent of temperature, while fission product migration across the interface would be expected to make a significant contribution to the total fission product concentration only at very high temperatures.

To establish upper concentration limits for the experimental work, estimates of fission product content in a cladding arising from recoil and diffusion are being made for various conditions of burnup, volume fraction of fuel (UO_2) in the matrix, core geometry, and cladding thickness. The assumptions are that the UO_2 is dispersed homogeneously in the matrix, the distribution of fission products in the cladding is uniform, and the number of fission products varies directly with atom fraction of U^{235} burnup. The refractory metal chosen for initial studies is tantalum.

For the recoil calculation, it was assumed that one-fourth of the fission products born in a 5-micron-thick region adjacent to the cladding recoiled into the cladding. The change in fission product concentration with increasing cladding thickness was found to be relatively insensitive to geometry of the fueled core, varying essentially as 1/t, where the cladding thickness, t, was varied between 0.1 and 0.8 mm. For the specific conditions of 20 percent burnup in a pin-type fuel element which has a 1-cm-diameter core containing 50 volume percent of fully enriched UO_2 and is clad with 0.1-mm-thick tantalum, the concentration of all fission products born that recoil into the cladding is about 0.1 atom percent. In the case of the element with the largest fission yield, zirconium, the atom fraction would be about 160 ppm. Obviously, with the large number of parameters involved, the concentration can vary within a wide range, but the values given above can be used as practical upper limits for recoil into the cladding.

Calculations to determine the contribution of trans-interface migration are in progress. The results of a preliminary calculation, based on the previous assumptions and the additional assumption of complete homogenization of the fission products throughout the fuel element, indicate that the total fission product concentration in the cladding would be about 7.5 atom percent; for zirconium, this amounts to 1.3 atom percent.

The upper limit results for both recoil and diffusion are summarized for fission products of significant yield in Table 5.3. The concentrations shown in the table for the diffusion contribution must be considered further before the actual concentrations are chosen for the initial mechanical testing because of the diverse chemical and physical properties of the fission products. Examples of these considerations are enumerated below:

TABLE 5.3

CALCULATED UPPER LIMIT FISSION PRODUCT CONCENTRATIONS IN THE CLADDING OF A Ta-CLAD FUEL ELEMENT RESULTING FROM RECOIL AND DIFFUSION

Fission Products	Fission Yield,[a] %	Upper Limit Fission Product Concentration,[b] ppm Recoil[c]	Upper Limit Fission Product Concentration,[b] ppm Diffusion[d]
Alkali metals (Rb, Cs)	23	120	8,500
Alkaline earths (Sr, Ba)	20	100	7,400
Group[e] III B metals (Y, La)	12	60	4,400
Refractory metals (Zr, Nb, Mo, Tc)	59	300	21,800
Group VIII metals (Ru, Pd)	15	80	5,700
Rare earths (Ce, Pm, Sm, Nd)	50	260	18,500
Rare gases (Xe, Kr)	25	130	9,300
	204[f]	1050	75,600

[a] Fission product atoms created per fission event in percent (total = 200%), based on the tabulation by S. Katcoff, Nucleonics, Vol. 18, No. 11, 1960, pp. 201-208.

[b] Fission product atoms divided by total atoms in tantalum cladding.

[c] Atom fraction of fission product atoms introduced into the cladding by recoil.

[d] Atom fraction of fission product atoms introduced into the cladding by total homogenization of all fission products throughout fuel element (i.e., cladding and matrix).

[e] Periodic table groupings.

[f] Equilibrium yield values of stable or long-lived (T-1/2 > 30d) isotopes were used, but for some decay chains values were estimated and some overlapping occurred to give a total >200 percent.

1. The assumption of complete homogenization implies a fission product mobility that would probably not be available to elements such as zirconium which could form an oxide precipitate.
2. To isolate deleterious effects, fission products which are known to enhance the mechanical properties of tantalum will not be used in the initial testing.
3. The amount of individual fission products to be added to the test samples will be influenced by the impurity levels existing in commercially available tantalum. Analytical results from one sample each of commercially available tantalum powder and an arc-cast rod indicated metallic impurity levels between 1300 and 4700 ppm (atom fraction), with zirconium in the powder being 1100 ppm.

Selection of the specific fission product concentration to be used in initial testing, the technique of sample fabrication, and the particular mechanical properties to study is in progress.

5.4 SUMMARY AND CONCLUSIONS

The movement of krypton through high-purity arc-cast tantalum was studied by diffusion and permeation techniques. Krypton - tantalum diffusion couples were prepared at high temperatures using the glow-discharge technique in which planar cathodes were resistively heated and hollow cathodes were heated by the discharge process itself. The simultaneous dissolution and diffusion of krypton in tantalum was demonstrated using both cathodes. The planar cathodes had both sufficient Kr^{85} activity and smooth surfaces so that an anodization-stripping technique could be used successfully to measure Kr^{85} concentration distribution in the sample. A concentration distribution curve for an arc-cast tantalum foil loaded at about $1700^{\circ}C$ was determined.

A permeation technique was also developed for studying the movement of rare gases through refractory metals. Small evacuated cans fabricated from arc-cast tantalum were tested in an environment of krypton containing Kr^{85} and periodically monitored for radioactivity. The permeation coefficient of krypton in high-purity arc-cast tantalum at $2400^{\circ}C$ is less than 8×10^{-15} ml of gas at STP-mm of wall thickness/cm^2 of surface area-cm of Hg pressure-sec.

Work was initiated on the effect of fission products as impurity atoms on the mechanical properties of refractory metals. In order to determine a practical upper concentration limit of fission products for the experimental work, calculations of the concentrations of all significant fission products were made for both recoil and complete diffusion using reasonable assumptions of fuel element geometry and burnup. Because of the diverse chemical and physical properties of the fission products, the upper limit results for diffusion must be considered further before the actual concentrations are chosen for the initial mechanical testing.

5.5 PLANS AND RECOMMENDATIONS

Additional experiments will be conducted to measure the diffusion rate of krypton in high-purity arc-cast tantalum at elevated temperatures. Specific studies will be aimed at defining surface conditions during the experiments with respect to krypton concentration changes. Studies on the permeation of krypton through tantalum and various other refractory metals will be continued. Work on determining the effect of fission product impurities on the mechanical properties of refractory metals will be focused initially on identifying detrimental effects of fission products at predetermined concentration levels on the mechanical properties of tantalum.

6. INTERNAL CONVERSION CERAMIC FUEL ELEMENT RESEARCH

(57072)

The objectives of this program are to study the chemistry involved in the use of a fertile material (thoria) in stabilized fuel - BeO systems and to develop its capability as an internal conversion fuel element. In particular, the program includes research and development work on UO_2-ThO_2 and UO_2-ThO_2-Y_2O_3 systems that can be incorporated in BeO to result in an all-ceramic fuel element for gas-cooled reactors having extended life at temperatures up to 1400°C.

15 2.00

6.1 BASIC STUDIES OF THE UO_2-ThO_2-Y_2O_3 SYSTEM

At the beginning of this program, the influence of ThO_2 on reactor life* was studied to determine the amount of fertile material required and its effect on increasing the life of a BeO-moderated reactor. These studies showed that adding ThO_2 to a homogeneously fueled UO_2-Y_2O_3-BeO fuel element would result in a significant increase in the lifetime or removable energy potential of a nuclear reactor, and that ThO_2 contents in the range of 1 to 3 moles per mole of UO_2 would be the most useful. For example, the addition of 3 moles of ThO_2 per mole of UO_2 almost triples nuclear lifetime potential; however, the minimum burnup capability required to realize this lifetime is about 12×10^{20} fissions/cm^3. Based on these considerations, work was concentrated on fuels with UO_2-to-ThO_2 mole ratios ranging from 1:1 to 1:3 and Y_2O_3-to-UO_2 mole ratios of 0.55. Additional binary and ternary compositions were included in this study to provide supporting information on phase relationships, vapor pressures, and comparative fuel retention data.

Second generation cores utilizing U^{233} instead of U^{235} in a BeO-UO_2-ThO_2-Y_2O_3 fuel element were studied later by comparing these two fuel element systems in reactors having equal reactivities. The study showed that a greater quantity of ThO_2 can be included with the U^{233} fuel; with a ThO_2-to-UO_2 ratio of 7 to 1, the conversion ratio in a U^{233} fueled system would be about three times greater than in a U^{235} fueled system.

PHASE RELATIONSHIPS IN THE UO_2-ThO_2-Y_2O_3 SYSTEM

Previous work with BeO-base fuel systems showed that greater thermal stability could be attained if the fuel was added to the BeO as a well-crystallized homogeneous solid solution; also, a high degree of crystallinity was necessary to permit X-ray diffraction study of phase relationships in the area of interest. For these reasons, an extensive study was made of the reaction conditions necessary to promote single-phase solid solutions. Attempts to form well-crystallized UO_2-ThO_2-Y_2O_3 solid solutions were successful only after the three components were coprecipitated as hydrous oxides and reacted for 1 hour at 2200°C in argon. However, well crystallized UO_2-ThO_2 and UO_2-Y_2O_3 solid

---

*"Third Annual Report – High-Temperature Materials and Reactor Component Development Programs, Volume I – Materials," GE-NMPO, GEMP-270A, February 28, 1964, pp. 145–147.

solutions were formed by reacting the mixed oxides for 1 hour at 1850°C in air. The binary and ternary compositions are shown in Figure 6.1 after they were equilibrated in air; X-ray diffraction showed each composition to be face-centered cubic (FCC).

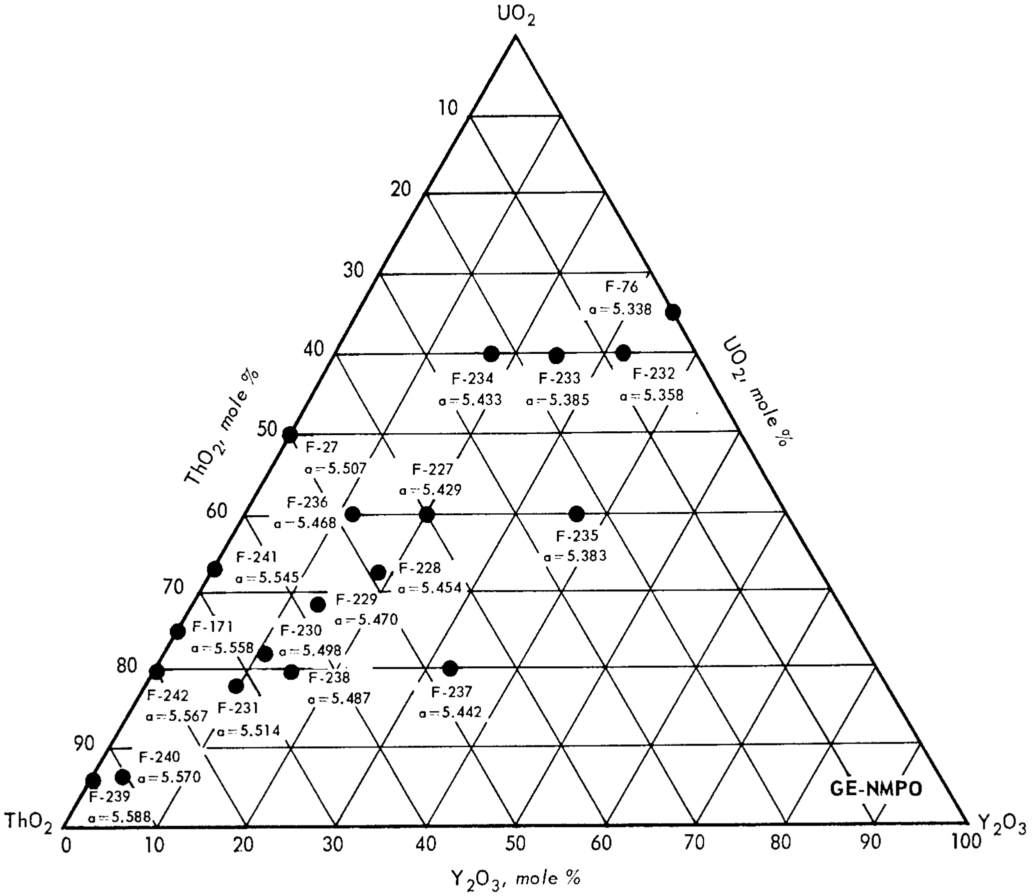

Fig. 6.1 – Lattice parameters of FCC solid solutions of UO_2-ThO_2-Y_2O_3 after equilibrating in air at 1200°C

UO_3 PARTIAL PRESSURES AS A FUNCTION OF COMPOSITION

Partial pressures of UO_3 over UO_2-ThO_2, UO_2-Y_2O_3, and UO_2-ThO_2-Y_2O_3 compositions were determined by a transpiration technique as part of a thermodynamic study* of UO_2 solid solutions. In addition, this study provided useful information on the relative thermal stability of UO_2-ThO_2 and UO_2-ThO_2-Y_2O_3 compositions and a comparison of UO_2-ThO_2 compositions with known UO_2-Y_2O_3 compositions. It also aided in screening and selecting fuel compositions for further study. With the transpiration method, UO_2 volatilizing as UO_3 is collected and analyzed chemically; the comparative rates of UO_2 volatility can be determined from these data as a function of temperature.

The UO_3 partial pressures were measured over the temperature range 1200° to 1500°C using -68°C dewpoint air at 1 atmosphere as the carrier gas. The results are shown in Figure 6.2 as an Arrhenius plot with previous data on U_3O_8 and UO_2 - 0.5Y_2O_3† for comparison. For a fixed UO_2-to-Y_2O_3 mole ratio of 1:0.55 (F-227, F-231, and UO_2-0.5Y_2O_3),

---

* "High-Temperature Materials Program Progress Report No. 34, Part A," GE-NMPO, GEMP-34A, April 15, 1964, pp. 32–39.

† "Second Annual Report – High-Temperature Materials and Reactor Component Development Programs, Volume II – Materials," GE-NMPO, GEMP-177B, (CRD), February 28, 1963, p. 31.

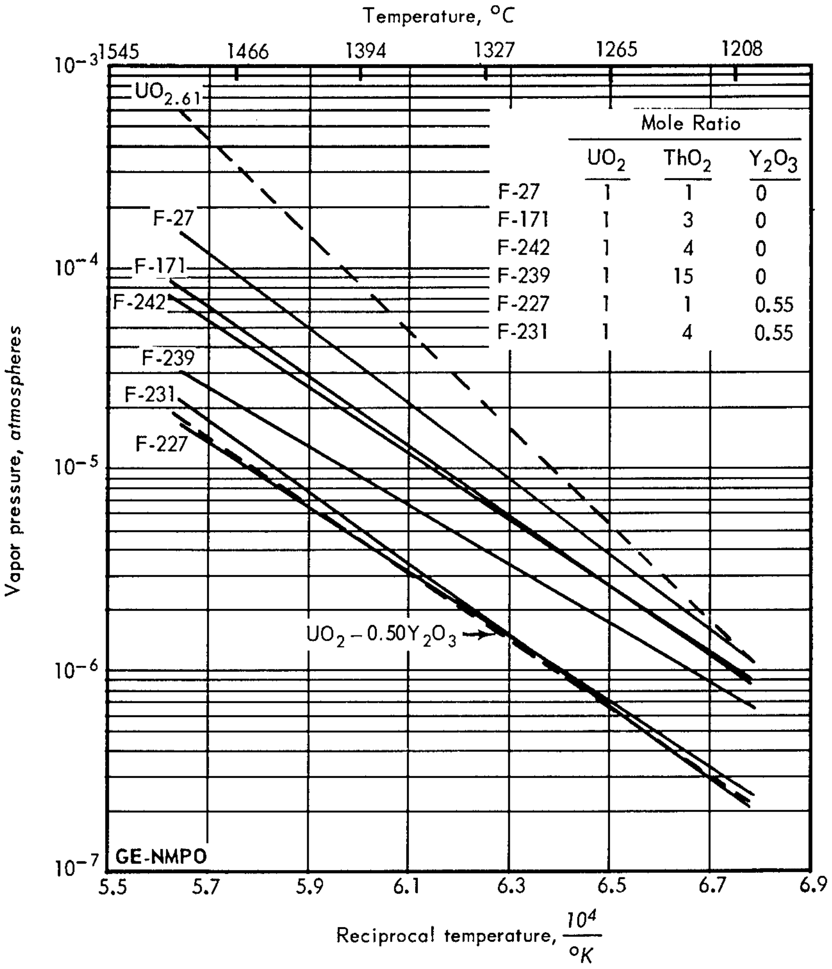

Fig. 6.2 – Partial pressure of UO_3 for various compositions in the UO_2-ThO_2, UO_2-Y_2O_3, and UO_2-ThO_2-Y_2O_3 systems in air

the UO_3 partial pressure does not change as increasing amounts of ThO_2 are added to the solution. The presence of 0.55 mole of Y_2O_3 in the UO_2-ThO_2-Y_2O_3 solid solutions results in a partial pressure of UO_3 which is lower by a factor of 3 to 6 than the same binary fuels without Y_2O_3. Partial pressure measurements on UO_2-ThO_2 fuel additives with mole ratios ranging from 1:1 (F-27) to 1:15 (F-239) show a decrease in the partial pressure of UO_3 with increasing ThO_2 content. If a correction for excess oxygen in the solid solution is made, the vapor pressures decrease in accordance with Raoult's Law. The partial pressures of these compositions are directly applicable in situations where the fuel is directly exposed to air. However, when the fuel is incorporated in a BeO matrix, other factors control the rate of UO_2 loss.

6.2 EVALUATION OF BeO-BASE FUEL MATERIALS

On the basis of the nuclear studies and preliminary fuel retention tests on composites of BeO fueled with various UO_2-ThO_2-Y_2O_3 solid solutions,* three ternary fuels and one binary UO_2-ThO_2 fuel were selected for further study. All fuel compositions were prepared by reacting the oxide mixtures for 1 hour at 1850°C in air and comminuting to -500 mesh (less than 25 microns) followed by blending with UOX-grade BeO.† The resulting

*"Third Annual Report – High-Temperature Materials and Reactor Component Development Programs, Volume I – Materials," GE-NMPO, GEMP-270A, February 28, 1964, pp. 150–152.

†UOX-grade BeO from Brush Beryllium Company, Cleveland, Ohio.

bodies were fabricated by the conventional extrusion process into tubes with a hexagonal external configuration having nominal sintered dimensions of 0. 76 cm across flats and circular bores 0. 5 cm in diameter. The fuel elements under study and their compositions are listed in Table 6. 1.

TABLE 6. 1

PHYSICAL AND MECHANICAL PROPERTIES OF BeO-BASE FUEL ELEMENTS CONTAINING UO_2-ThO_2 AND UO_2-ThO_2-Y_2O_3

Fuel Element Designation[a]	Fuel Composition				Effect Of Indicated Sintering Temperature[b] On Properties					
	Mole Ratio				2 Hours At 1675°C In H_2			1 Hour At 1800°C In H_2		
	UO_2	ThO_2	Y_2O_3	Fuel Content In BeO, vol %	Density, % of theoretical	BeO Grain Size, microns	Modulus Of Rupture,[c] kg/cm^2	Density, % of theoretical	BeO Grain Size, microns	Modulus Of Rupture,[c] kg/cm^2
11BF-27	1	1	0	7	94. 9	5	2430	98. 5	17	2470
11BF-227	1	1	0. 55	11. 5	98. 3	24	1990	99. 0	50	1430
7BF-229	1	2	0. 55	9. 5	98. 8	17	2850	99. 6	43	1530
5BF-230	1	3	0. 55	8. 5	98. 6	18	2720	99. 4	40	1550
11. 5BF-230	1	3	0. 55	25	99. 5	10	2870	99. 4	20	2380

[a] The first number of the fuel element designation is the UO_2 content of the specimen in weight percent.

[b] Sintering was done in hydrogen having a dewpoint of 0°C.

[c] Modulus-of-rupture measurements made at room temperature on hexagonal tubes 0. 76 cm across flats with a 0. 5 cm circular bore using four point loading on a 4. 46-cm span and 0. 152 cm/min crosshead travel. Each value is an average of four measurements.

PHYSICAL AND MECHANICAL PROPERTIES

A limited study of the physical and mechanical properties of UO_2-ThO_2 and UO_2-ThO_2-Y_2O_3-fueled BeO specimens was performed to confirm that their properties do not deviate significantly from properties determined from extensive measurements on other oxide fueled BeO systems.*† This program includes the effect of sintering temperature on density, grain size, and strength; elevated temperature strength; thermal expansion; and compressive creep.

Although the fuel elements under study were densified in 0°C dewpoint hydrogen at temperatures ranging from 1675° to 1850°C and times ranging from 1 to 7 hours, the results indicated that two particular sintering treatments, 2 hours at 1675°C and 1 hour at 1800°C, provided optimum effect on density, grain size, strength, and fuel retention. With the exception of the fuel elements containing UO_2-ThO_2 fuel (11BF-27), the fuel elements sintered to densities exceeding 98 percent of theoretical at both sintering temperatures.

Modulus-of-Rupture Strength

The effects of 1675°C and 1800°C sintering temperatures on density, grain size, and room temperature modulus-of-rupture strength are shown in Table 6. 1. Generally, high strengths were obtained by sintering at 1675°C. The grain size of fuel elements sintered at 1800°C was 2 to 3 times larger than those sintered at 1675°C. The Y_2O_3-containing fuel elements sintered at 1800°C decreased in strength, whereas strength of the fuel elements containing UO_2-ThO_2 (11BF-27) remained about the same.

The elevated-temperature modulus-of-rupture strength was determined on a representative fuel element composition (11BF-227 sintered for 2 hours at 1675°C). These results, Table 6. 2, indicate an increase in rupture strength with increasing temperature, reaching a maximum of 2900 kg/cm^2 in the temperature range 800° to 1000°C. At temperatures above 1000°C, the strength decreased (to 1810 kg/cm^2 at 1400°C).

---

* "Second Annual Report – High-Temperature Materials and Reactor Component Development Programs, Volume II – Materials," GE-NMPO, GEMP-177B, (CRD), February 28, 1963, pp. 75–80.

† G. T. Muehlenkamp, "Evaluation of BeO Fuel Element Containing a Stabilized Fuel Additive," GE-NMPO, GEMP-174, (CRD), May 29, 1963.

TABLE 6.2

MODULUS OF RUPTURE AS A FUNCTION OF TEMPERATURE FOR 11BF-227 FUEL ELEMENTS

Temperature, °C	Modulus Of Rupture,[a] kg/cm^2		
	Maximum	Minimum	Average
25	2330	1890	2060
800	3080	2660	2900
1000	3060	2630	2810
1200	2800	2490	2600
1400	2120	1370	1810

[a] Four-point loading with a 7.62-cm span and 0.152-cm/min crosshead travel. Five specimens were broken at each temperature.

Linear Thermal Expansion

Thermal expansion measurements of BeO containing 7 to 11.5 volume percent fuels were made from room temperature to 1200°C in air using a dilatometer; all of the compositions were fully oxidized prior to testing. Results of these measurements are given in Figure 6.3, along with as-received AOX-grade BeO* for comparison. The expansion of all fuel elements was essentially the same as that of non-oriented AOX-grade BeO.

Compressive Creep Studies

Previous studies showed that the compressive creep of high-density polycrystalline beryllium oxide can be predicted by the Nabarro-Herring model which is based on the stress-directed diffusion of vacancies.†‡ Deformation results from diffusional flow of vacancies within each grain away from those boundaries where there is a normal tensile force to boundaries having a normal compressive force. The creep rate is given by the relation expressed in equation (6.1):

$$\dot{\epsilon} = \frac{40\ D\Omega\sigma}{3\ kTd^2} \qquad (6.1)$$

where

$\dot{\epsilon}$ = creep rate
σ = applied stress
D = diffusion coefficient
Ω = vacancy volume
d = mean grain diameter
k = Boltzmann's constant
T = absolute temperature.

It has been suggested† that diffusion of the beryllium ion vacancy (D_{Be}) is the rate-controlling deformation mechanism.

---

*AOX-grade BeO from Brush Beryllium Company, Cleveland, Ohio.

†R. R. Vandervoort and W. L. Barmore, "Compressive Creep of Polycrystalline Beryllium Oxide," *Journal of American Ceramic Society*, Vol. 46, 1963, pp. 180–184.

‡R. E. Fryxell and B. A. Chandler, "Creep, Strength, Expansion, and Elastic Moduli of Sintered BeO as a Function of Grain Size, Porosity, and Orientation," *Journal of American Ceramic Society*, Vol. 47, 1964, pp. 283–291.

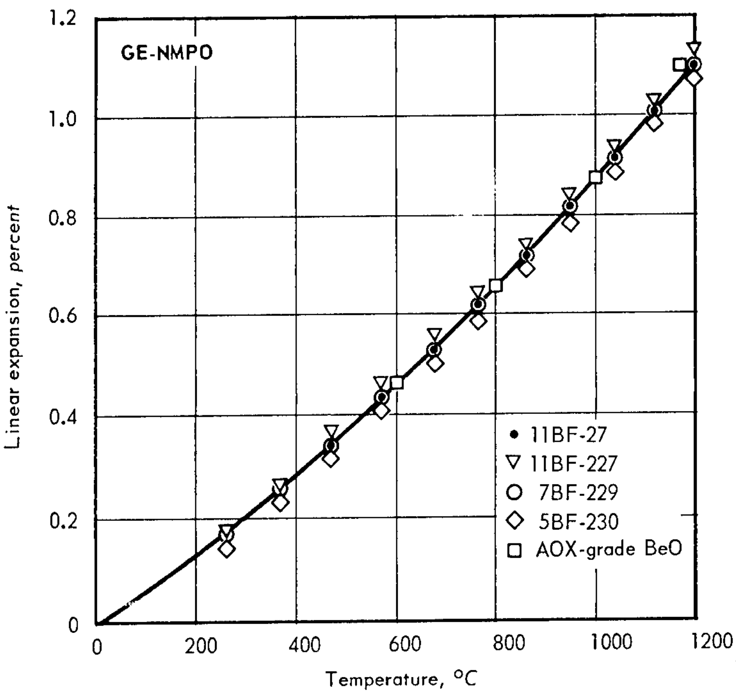

Fig. 6.3 – Linear thermal expansion of BeO and BeO fueled with UO_2-ThO_2 and UO_2-ThO_2-Y_2O_3 compositions

The objective of this investigation was to study the effect of the dispersed-fuel phase on the deformation mechanism of polycrystalline BeO. The compressive creep behavior of fueled BeO developed in this program was determined as a function of applied stress and temperature. The material parameters included volume fraction and composition of the fuel phase and grain size of the BeO matrix phase. These results were correlated with the basic relationship between creep rates and the variables, stress and grain size, for polycrystalline BeO.

The test materials included four fuel element compositions, 11BF-227, 7BF-229, 5BF-230, and 11.5BF-230 (see Table 6.1 for specimen compositions), sintered at 1675°C for 2 hours or at 1800°C for 1 hour to attain various grain sizes.* All specimens were in excess of 98 percent theoretical density. For comparative purposes, creep measurements were also made on two specimens of UOX-grade BeO, containing 3 weight percent ZrO_2, having grain sizes of 23 and 33 microns and a density of 97.5 percent of theoretical.

The 11BF-227, 7BF-229, and 5BF-230 test specimens were machined from hexagonal tubular fuel elements and were approximately 0.75 cm across flats with 0.5-cm circular bores and were 1.9 cm long. The 11.5BF-230 and BeO - $3ZrO_2$ specimens were solid cylinders 0.60 cm in diameter and 1.9 cm long. The ends of the specimens were square and parallel within 0.005 mm. The specimens were inspected before test by X-ray radiography and fluorescent penetrant techniques. Specimens with low density regions, cracks, or chips were rejected.

Compressive creep measurements were made at constant load obtained by column loading from outside the test furnace. To assure uniaxial stress, the test specimens were loaded in a high density aluminum oxide fixture consisting of load plungers 3.8 cm in

---

*Grain sizes listed in Figures 6.4 and 6.5 for the BeO phase were measured by the average intercept method using a conversion factor of 1.27 (i.e., $4/\pi$) to correct for the actual volume fraction of the BeO phase. The grain sizes in this section are the adjusted values.

diameter fitted into a sleeve having a wall thickness of 0.64 cm. Sapphire discs, separated from the specimen with platinum foil, were used to prevent reaction between the aluminum oxide plungers and the fueled BeO. Deformation was measured with a linear variable differential transformer utilizing sapphire extensometer rods which detected movement of the top of the specimen relative to the bottom.

The tests were made in dry air over a temperature range from 1200° to 1510°C. To determine the effect of stress and temperature, creep rates were measured at one or two stresses at a constant temperature. The temperature was increased to a second level and the creep rates were again measured at different stresses; in some cases, this procedure was repeated at a third temperature level.

With the exception of two tests, the initial measurements on the 11BF-227, 7BF-229, 5BF-230, and BeO - $3ZrO_2$ compositions were made at 1400°C at one or two stress levels over a time interval of 20 to 40 hours. The temperature was increased to 1510°C, and the creep rates were measured at several stress levels during the next 20- to 30-hour time intervals. Creep measurements on all 11.5BF-230 compositions and single tests on 15-micron 5BF-230 and 23-micron BeO - $3ZrO_2$ were made initially at 1300°C at one or two stress levels over a time interval of 50 to 100 hours, and then at 1400°C at two or three stress levels over 20- to 40-hour intervals. The creep rates of 17-micron grain size 11.5BF-230 were also measured at three stress levels at 1510°C.

The limited number of tests at 1200°C were run for 500 hours because of the very low creep rates and also to correlate results with an earlier study on BeO.* The creep rates for BeO - $3ZrO_2$ at 1200°C were obtained from this work. The results of measurements at 1510°C are given in Figure 6.4 as log-log plots of creep rate versus stress to illustrate the stress dependence of creep rate. All data are condensed in Figure 6.5 as log-log plots of creep rate versus the parameter stress/(grain size)^2.

With the exception of the fine-grained 11.5BF-230 composition, the creep rates of fueled and unfueled BeO were directly proportional to the applied stress. The high creep rates of the fine-grained 11.5BF-230 composition at 1400°C and the coarse-grained 11.5BF-230 composition at 1510°C were probably caused by grain boundary separation. Microstructural studies of these specimens after test showed extensive grain boundary separation. It is interesting, however, that the creep rates of the coarse-grained sample remained linear with stress under these conditions.

As shown in Figure 6.5, the creep rates of the fueled BeO with up to 11.5 volume percent of second phase are approximately linear with the parameter stress/(grain size)^2 at temperatures up to 1510°C. Furthermore, these creep rates are in good agreement with the rates for polycrystalline BeO as represented by the BeO-ZrO_2 data; the BeO-ZrO_2 data appear to be slightly lower at 1510°C. The creep rate of the 44-micron 11BF-227 material at 1400°C is high, indicating possible grain boundary separation. With the exception of several tests at high stresses, the creep rates of the 11.5BF-230 materials (25 vol % fuel phase) at 1200°C and 1300°C are in good agreement with the stress/(grain size)^2 parameter. At higher temperatures, the creep rates of both the 8- and 17-micron 11.5BF-230 materials are greater than the rates derived from the stress/(grain size)^2 relationship, the differences becoming greater with increasing temperature and decreasing grain sizes. As already noted, the high creep rates of these materials are probably caused by grain boundary separation.

A practical example of the above data can be made by assuming an all-ceramic reactor designed to provide a stress of 10 kg/cm^2 on the fuel elements for 30,000 hours at 1200°C.

---

*Fryxell and Chandler, loc. cit.

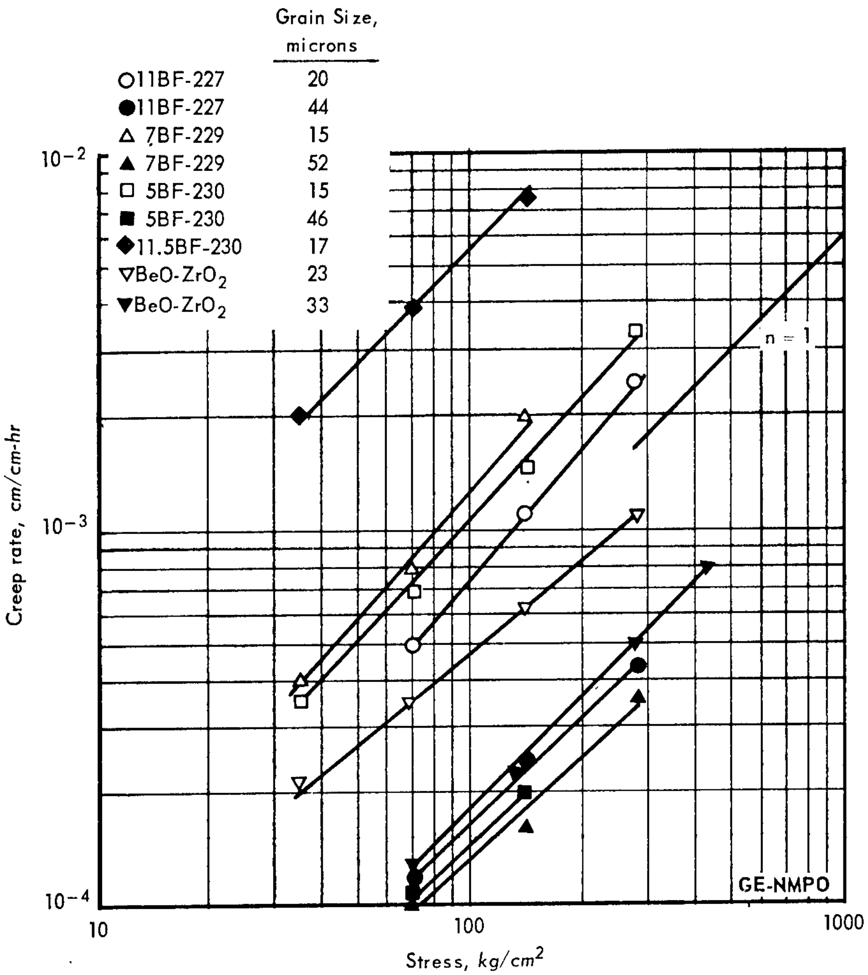

Fig. 6.4 – Creep rate of fueled and unfueled BeO as a function of stress at 1510°C

The value of the parameter stress/(grain size)^2 for the 11.5BF-230 fuel element having 25 volume percent fuel phase and 8-micron grain size would give a creep rate of 5 x 10^{-7} cm/cm-hr or a total deformation of about 1.5 percent in 30,000 hours. The 11.5BF-230 fuel element with a 17-micron grain size would deform 0.3 to 0.4 percent under the same conditions.

The agreement of the creep rates of fueled BeO materials with the parameter stress/(grain size)^2 suggests that deformation occurs by diffusional flow as predicted by the Nabarro-Herring relation. The diffusion coefficients derived from this relation should agree with those of measured self-diffusion. Diffusion coefficients were calculated from the average slope ($\dot{\epsilon}\ R^2/\sigma$) of the dashed lines in Figure 6.5. The calculated coefficients are plotted in Figure 6.6 together with coefficients obtained in self-diffusion measurements of oxygen in single-crystal BeO* and of beryllium in polycrystalline BeO of 99.3 percent density.† (The Be^7 curve represents an extrapolation of data obtained in the temperature range 1565° to 2010°C.) Diffusion coefficients calculated by Vandervoort and Barmore‡ from compressive creep studies on polycrystalline BeO are also included.

---

*J. B. Holt, "Self Diffusion of Oxygen in Single Crystal Beryllium Oxide," *Journal of Nuclear Materials*, Vol. 11, 1964, pp. 107–110.

†S. B. Austerman, "Diffusion of Beryllium in Beryllium Oxide," Atomics International, NAA-SR-5893, May 1961.

‡Vandervoort and Barmore, loc. cit.

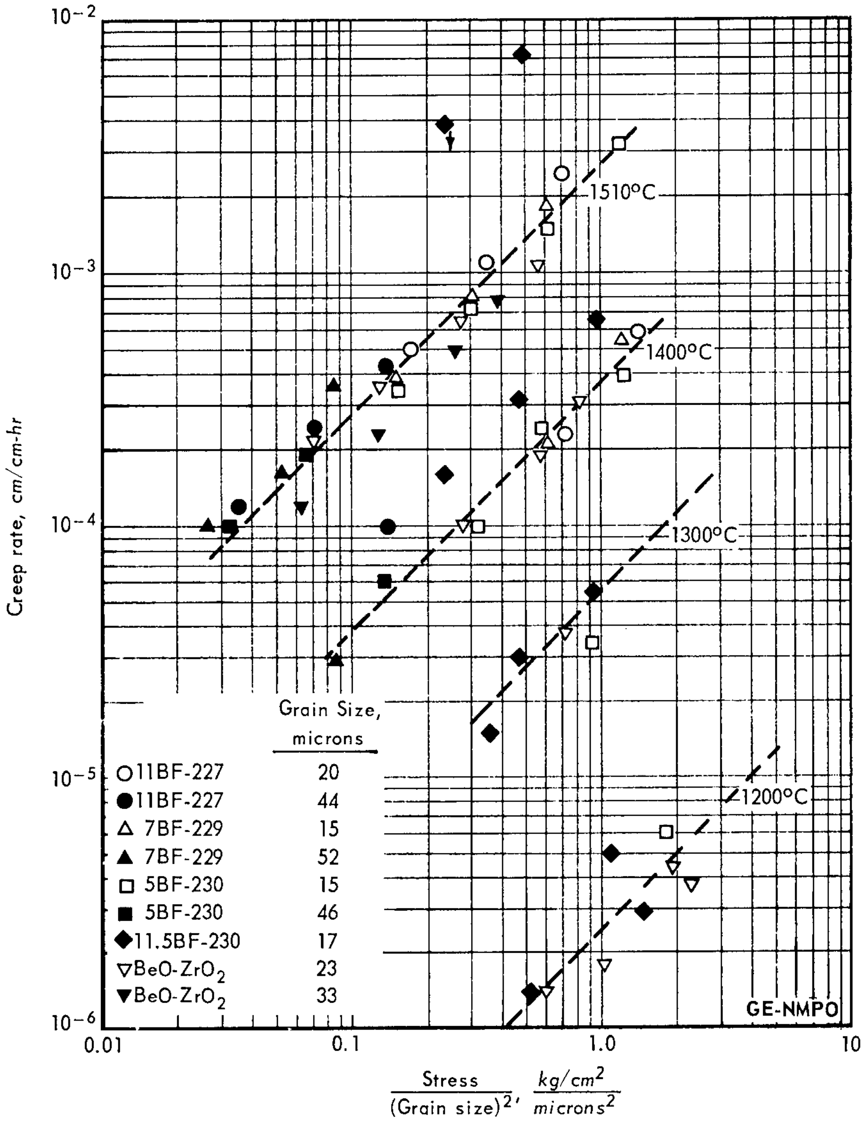

Fig. 6.5 – Creep rate of fueled and unfueled BeO as a function of stress and grain size

The diffusion coefficients and activation energy (~110 kcal/mole from Figure 6.6) calculated from the creep data on fueled BeO are in fair agreement with the data obtained from beryllium self-diffusion measurements and from the previous compressive creep study on polycrystalline BeO. Since oxygen diffusion (in a single crystal) occurs at a slower rate, this latter process should be rate-controlling. However, it is possible that oxygen diffusion may be enhanced in regions adjacent to the grain boundaries, as suggested by Paladino and Coble* for polycrystalline aluminum oxide. Therefore, diffusional flow of beryllium appears to be the rate controlling process in the creep of fueled BeO within the limits of temperature, stress, and composition of this study.

THERMAL STABILITY

In evaluating BeO-base fuel elements containing 7 to 25 volume percent UO_2-ThO_2 and UO_2-ThO_2-Y_2O_3, emphasis has been placed on fuel retention testing at elevated temperatures in atmospheres of air, helium, and helium containing small quantities of oxygen.

---

*A. E. Paladino and R. L. Coble, "Effect of Grain Boundaries on Diffusion Controlled Processes in Aluminum Oxide," *Journal of American Ceramic Society*, Vol. 46, 1963, pp. 133–136.

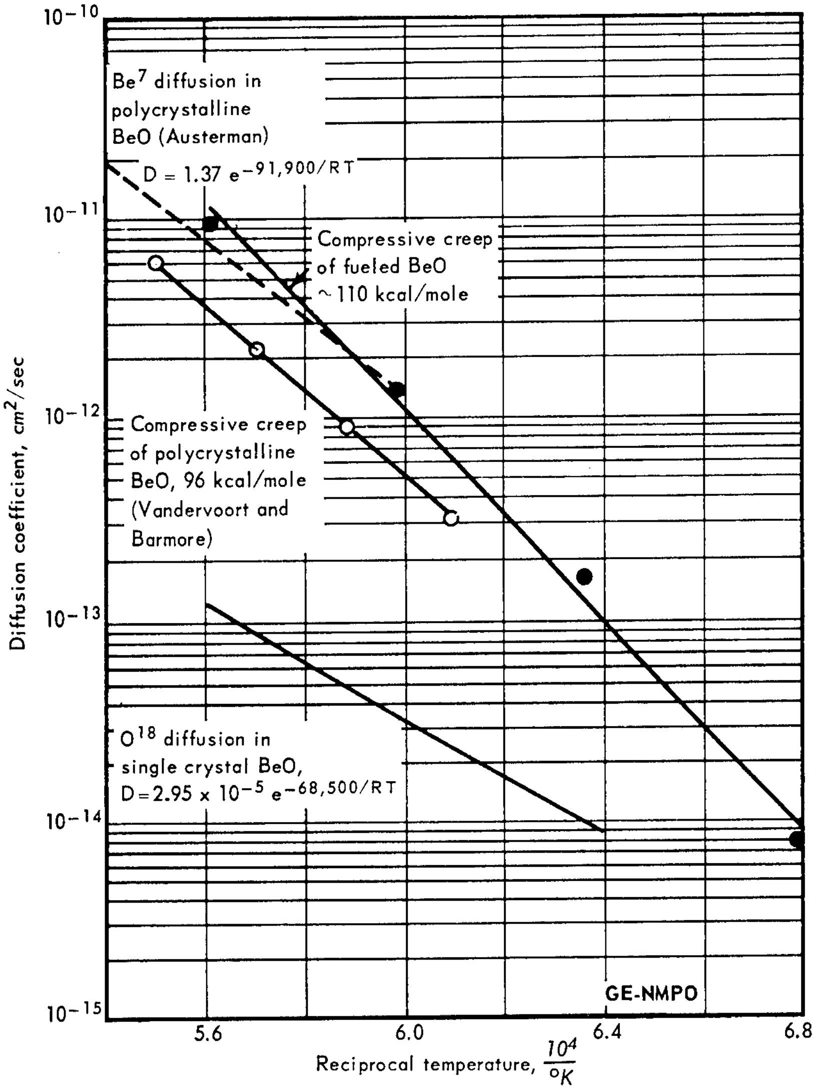

Fig. 6.6 – Comparison of calculated and measured diffusion coefficients

The tests in air were particularly severe and the results, calculated as UO_2 loss, provided a measurement of the capability of the fuel composition to resist oxidation of UO_2 followed by volatilization as UO_3. Fuel retention tests were carried out in a moving gas having a dewpoint of -68°C (to eliminate water vapor corrosion of the BeO matrix) and the rate of UO_2 loss was usually determined from weight change measurements made during the course of the test. At the test conclusion, UO_2 loss was determined by chemical analysis and the specimens were evaluated for any physical or mechanical changes.

Fuel retention tests of specimens sintered at 1675°C and 1800°C revealed a significant decrease in fuel loss from specimens sintered at 1800°C. Examination of the effect of sintering temperature using X-ray diffraction, ceramography, vapor pressure studies, and fuel retention tests disclosed a possible explanation for this behavior.

The tests in helium and helium containing small quantities of oxygen will provide a comparison of the capability of UO_2-ThO_2-Y_2O_3-fueled BeO elements in inert or slightly oxidizing atmospheres with the more extensive tests performed in air.

Fuel Retention Tests

Fuel retention tests (Table 6.3) were carried out on various BeO-base fuel element compositions at temperatures ranging from 1200° to 1650°C in moving air. Although the 1200°C tests are continuing, weight change data after 4000 hours indicate negligible UO_2 loss from most specimens with the maximum loss measuring 0.6 percent UO_2. The tests at 1400°C were completed after 2000 hours with weight change data indicating Y_2O_3-containing specimens sintered at 1800°C lost from 0.4 to 0.8 percent UO_2 while those specimens sintered at 1675°C lost 1.2 to 1.7 percent UO_2. The specimens fueled with UO_2-ThO_2 (11BF-27) lost 2.2 to 2.4 percent UO_2. During the test, all fuel elements increased slightly in density and the BeO grain size and modulus-of-rupture strength remained essentially unchanged.

Although the fuel elements under study were designed primarily for extended use at 1200°C, the results of initial testing at 1200°C and 1400°C indicated that a more severe test would be necessary to differentiate between the fuel stability of different compositions within a reasonable period of time. The test at 1650°C accelerated fuel loss and provided measurable UO_2 loss between specimens. The test also illustrated the excellent stability of some compositions at very high temperatures. For example, based on weight change data after 100 hours at 1650°C, Y_2O_3-containing fuel elements sintered at 1800°C lost from 0.3 to 3.3 percent UO_2 while the same compositions sintered at 1675°C and the UO_2-ThO_2 fueled specimens (11BF-27) sintered at 1675°C and 1800°C lost from 2.9 to 6.2 percent UO_2. All fuel elements increased in density during the test. The grain size or strength did not change in the specimens sintered at 1800°C; however, the specimens sintered at 1675°C increased in grain size and decreased in strength by 10 to 25 percent.

TABLE 6.3

FUEL RETENTION TESTS OF BeO-BASE FUEL ELEMENTS

Fuel Element Designation And UO_2 Content[a]	Fuel Composition				Sintering Temperature,[b] $^{\circ}$C	UO_2 Loss After Testing In Air At Indicated Time And Temperature, %		
	Mole Ratio			Fuel Content In BeO, vol %		4000 hr At 1200°C	2000 hr At 1400°C	100 hr At 1650°C
	UO_2	ThO_2	Y_2O_3					
11BF-27	1	1	0	7	1675	0.5[c]	2.4 (3.6)[d]	3.7 (4.1)
					1800	-	2.2 (3.9)	3.9 (4.0)
11BF-227	1	1	0.55	11.5	1675	0.0	1.7 (0.5)	4.6 (3.7)
					1800	-	0.8 (1.3)	3.3 (3.1)
7BF-229	1	2	0.55	9.5	1675	0.0	1.1 (0.9)	3.0 (2.3)
					1800	-	0.5 (0.3)	0.8 (1.4)
5BF-230	1	3	0.55	8.5	1675	0.0	1.7 (0.2)	2.9 (1.2)
					1800	-	0.4 (0.0)	0.3 (0.0)
11.5BF-230	1	3	0.55	25	1675	0.6	1.2 (0.0)	6.2 (4.6)
					1800	0.1	0.4 (0.2)	2.6 (1.4)
					1850	0.1	0.5 (0.0)	2.1 (2.0)

[a] The first number of the fuel element designation is the UO_2 content of the specimen in weight percent.

[b] Fueled BeO specimens were sintered for 2 hours at 1675°C, 1 hour at 1800°C, or 1 hour at 1850°C in hydrogen having a dewpoint of 0°C.

[c] UO_2 loss was calculated from weight change data, assuming all change was caused by UO_2 volatilizing as UO_3; each result is an average of two determinations.

[d] The UO_2 loss in parentheses was determined from chemical analyses of the specimen before and after testing.

Based on the relative volume content of fuel, specimens that did not contain Y_2O_3 lost more UO_2 than Y_2O_3-containing specimens, Table 6.3, and this loss appeared to be unaffected by different sintering temperatures. Comparisons of UO_2 loss at different test temperatures indicate the specimens currently being tested at 1200°C could remain on test for periods of time significantly longer than the presently accumulated 4000 hours without significant fuel loss. For Y_2O_3-containing specimens, sintering at 1800°C or 1850°C decreased UO_2 loss compared with the same compositions sintered at 1675°C.

The Effect of Sintering Temperature on Fuel Retention

During early work on fuel retention testing it was noticed that in every test containing compositions sintered at both 1675°C and 1800°C, the specimens sintered at 1800°C lost less UO_2 than those sintered at 1675°C. This effect became more apparent in testing the materials containing 25 volume percent fuel phase at 1650°C where UO_2 loss was much greater than at lower temperatures. The effect of sintering on the actual rate of fuel loss was obscured during the initial stage of testing because of weight increases caused by oxidation of the fuel phase.

To show the effect of sintering temperature on fuel loss explicitly, a transpiration method was used. With this method, the UO_3 volatilized from the fuel elements was collected and the amount determined by chemical analysis. The 11.5BF-230 specimens (containing fuel with $1UO_2$-$3ThO_2$-$0.55Y_2O_3$, mole ratio) were sintered at 1675°, 1800°, and 1850°C in hydrogen to densities of 99.5 percent of theoretical or higher. The test results during 100 hours at 1650°C in air, Figure 6.7, indicate that the fuel loss rate from the specimen sintered at 1675°C was higher than for the specimens sintered at 1800°C or 1850°C and was particularly high during the initial stages of testing. The transpiration data suggest that the UO_2 release was diffusion controlled over the total test time (as indicated by the fuel loss rate being nearly linear with the square root of time) with a rapid loss rate during the initial stages of the test followed by a relatively slow rate during the remainder of the test. The initial rapid loss is probably from surface fuel particles; as this fuel becomes depleted in uranium to a more stable fuel phase, a slower diffusion process of uranium from interior particles predominates.

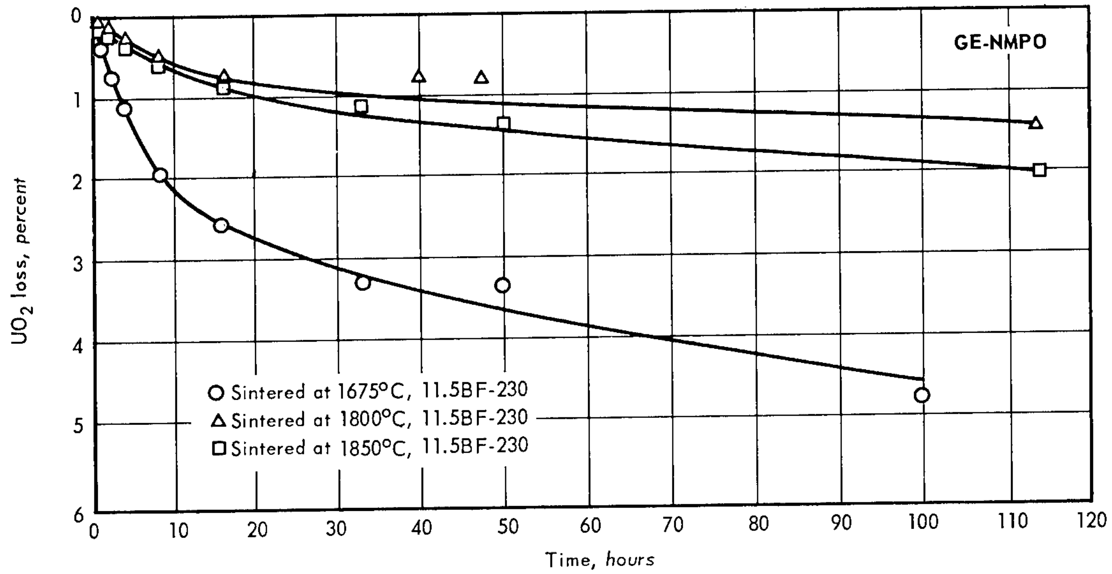

Fig. 6.7 – Fuel loss from BeO-base fuel elements in air at 1650°C as determined by a transpiration technique

The specimen sintered at 1675°C lost 3 percent UO_2 in the first 25 hours of testing with a total loss of 4.6 percent after 100 hours. The specimens sintered at 1800°C or 1850°C lost 1 percent or less UO_2 in the first 25 hours with a total loss of 1.5 to 2.0 percent UO_2 in 100 hours. Thus, it appears that sintering at 1800°C or 1850°C not only decreased the total UO_2 loss but particularly decreased UO_2 loss from the exposed fuel on the surface. In addition, the rate of loss after the first 25 hour period at 1650°C continued to be higher for the fuel element sintered at 1675°C.

A possible explanation of the effects caused by sintering at 1675°C or 1800°C has evolved from X-ray diffraction analysis of 11.5BF-230 fuel elements containing 25 volume percent $1UO_2$ - $3ThO_2$ - $0.55Y_2O_3$ fuel. Before blending with BeO, the fuel (reacted for 1 hour at 1850°C) contained two FCC phases with lattice parameters of 5.50 and 5.53 which converted to a single FCC phase upon sintering in hydrogen at either 1675°C or 1800°C. The lattice parameters of the bulk of the fuel phase were essentially the same at both sintering temperatures; however, very slight changes took place on the surface of the fuel element. Fuel elements sintered at 1675°C had fuel which remained single phase, but a trace amount of another phase identified by X-ray diffraction as $4BeO{\cdot}Y_2O_3$* was also found. Analysis of the surface of fuel elements sintered at 1800°C or higher showed no evidence of $4BeO{\cdot}Y_2O_3$, and the fuel contained two FCC phases with lattice parameters of 5.52 and 5.46 Å.

That the fuel structure formed by sintering at 1800°C is the most stable is indicated by (1) consistently lower fuel loss at all test temperatures and (2) the compound $4BeO{\cdot}Y_2O_3$ (formed on the surface of a fuel element during sintering at 1675°C and during fuel retention tests where UO_2 loss is incurred) cannot be found after a thermal treatment for 1 hour at 1800°C in hydrogen; however, a thermal treatment at 1675°C in hydrogen for 2 hours has no effect on the $4BeO{\cdot}Y_2O_3$. Presumably, the Y_2O_3 recombines with the solid solution at 1800°C but not at 1675°C.

Assuming that $4BeO{\cdot}Y_2O_3$ is formed (during sintering at 1675°C) from part of the Y_2O_3 originating from the UO_2-ThO_2-Y_2O_3 solid solution, then this removal of Y_2O_3 from the solid solution results in a less stable fuel phase. This in turn increases the partial pressure of UO_3 over the solid solution and results in an increased loss of UO_2 from the surface. In addition, a slight amount of liquid phase can form at temperatures above the BeO-Y_2O_3 eutectic (1580°C); this liquid phase increases the rate of uranium diffusion from the matrix to the surface and results in an increased loss of UO_2. Ceramographic observation of the fuel element surface after 100 hours at 1650°C in air showed fuel depletion, a slight amount of liquid phase, and peripheral grain growth,† only from the specimen sintered at 1675°C.

Other differences between fuel elements sintered at 1675°C and 1800°C (such as grain size, density differences, and the possible existence of stresses set up during sintering) were investigated and found to have no effect on fuel retention. Since there is no Y_2O_3 present in the 11BF-27 composition, the $4BeO{\cdot}Y_2O_3$ compound cannot form; consequently, sintering temperature has no effect on the fuel retention of this composition.

Fuel Retention in Helium

As can be concluded from the fuel retention data in air, the BeO-base fuel elements tested have excellent stability at high temperatures for extended times in oxidizing atmospheres. Gases such as He, N_2, or CO_2 have characteristics which should make them even better reactor coolants than air. Helium, in particular, is of interest because it has higher heat transfer capability and requires significantly less pumping power to circulate; i.e., for an equivalent size reactor having the same pumping power, a helium coolant would be capable of removing 2.5 times more heat than an air coolant. One potential advantage in using fueled BeO that is stable under oxidizing conditions is that gases (He, N_2, or CO_2) contaminated with significant quantities of oxygen could be used and engineering problems associated with air-tight reactor enclosures would be simplified.

To more thoroughly evaluate property changes which might occur in fueled BeO after long exposures in helium, fuel elements containing 7 to 25 volume percent UO_2-ThO_2 and

---

*S. F. Bartram, "Preliminary Report of X-Ray Studies on the BeO-Y_2O_3 System," GE-ANPD, DC 61-7-10, April 19, 1961.

†"High-Temperature Materials Program Progress Report No. 42, Part A," GE-NMPO, GEMP-42A, December 18, 1964, pp. 23–25.

UO_2-ThO_2-Y_2O_3 compositions were thermally aged in pure helium. In a later test a second set of specimens was aged in recirculating helium containing 5 volume percent oxygen. The first set of fuel elements was tested in a specially built apparatus at 1200°C in a purified recirculating flow of helium.* At the conclusion of this 2000-hour test, weight change measurements indicated little or no change in oxidation state or fuel loss during the test. In addition, no significant change in density, grain size, or strength occurred.

The second set of fuel elements was tested for 2000 hours at 1200°C in a recirculating atmosphere of helium + 5 volume percent oxygen. In contrast to the test in pure helium, all the specimens oxidized; the weight change data indicate most of the specimens had not reached the maximum oxidation level and no UO_2 loss was shown. A more complete evaluation of the test will be possible when chemical analyses and physical and mechanical property data are available.

6.3 IRRADIATION TESTING

Two BeO-base fuel elements fueled with 25 volume percent UO_2-ThO_2-Y_2O_3 (11.5BF-230) are being tested in the ETR (GEFP2-19 and GEFP2-23) to determine the effects of high burnup on physical integrity. One test (LTC-73) has been completed in the LITR to determine the kinetics of fission product release. All ETR tests were scheduled to operate at 1200° to 1250°C in an atmosphere of static helium + 5 volume percent oxygen, and the LITR test was scheduled for 2 weeks at 1250°C and 2 weeks at 1370°C in air coolant. The test specimens were unclad and were sintered 2 hours at 1675°C in hydrogen having a dewpoint of 0°C to 99.6 percent of theoretical density.

Fabrication of BeO-base fuel elements containing 25 volume percent fuel phase added as F-243 (UO_2-ThO_2-Y_2O_3 with a mole ratio of 1:7:0.55) was initiated. These fuel elements will be completely coated with BeO and irradiation tested to determine (1) the high burnup capability of fuels with a high ThO_2 content, and (2) the ability of BeO coatings to restrict fission product release from such fuel elements.

Status of the irradiation program is summarized in Table 6.4.

TABLE 6.4

IRRADIATION TEST PROGRAM FOR HIGH BURNUP OF BeO FUELED WITH UO_2-ThO_2-Y_2O_3 COMPOSITIONS

Test Number	Specimen Designation[a]	Fuel Composition, mole ratio UO_2	ThO_2	Y_2O_3	Operating Conditions Time, hr	Temperature, °C	Desired Burnup, 10^{20} fissions/cm^3	Status
GEFP2-19	11.5BF-230	1	3	0.55	1242	1000-1250	2 to 5	In progress
GEFP2-22[b]	6.2BF-243	1	7	0.55	-	-	1 to 2.5	Fuel elements being fabricated
GEFP2-23	11.5BF-230	1	3	0.55	1242	1000-1250	1 to 2.5	In progress
LTC-73	11.5BF-230	1	3	0.55	931	1200-1550	-[c]	Testing completed

[a] The first number of the fuel element designation is the UO_2 content of the specimen in weight percent. All fuel elements contain 25 volume percent fuel additive in BeO.

[b] GEFP2-22 fuel elements will be dip-coated with 0.004 to 0.007 cm of BeO over the entire external surface.

[c] Burnup not applicable; this is a dynamic test with the primary purpose of determining fission product release kinetics.

LITR IRRADIATION TEST LTC-73

Test assembly LTC-73 (Figure 6.8) consisted of six fueled BeO hexagonal fuel elements assembled around a BeO rod grooved for thermocouple placement. The 11.5BF-230 fuel elements were irradiated at constant flux in the LITR for a total of 931 hours at maximum temperatures between 1250° and 1550°C in air. The maximum indicated sample temperature was 1250° to 1265°C for 356 hours, 1340° to 1370°C for 367 hours, 1450° to 1500°C for 185 hours, and 1550°C for 23 hours as shown in Figure 6.9. Temperatures were maintained by regulating the air coolant flow.

---

* "High-Temperature Materials Program Progress Report No. 38, Part A," GE-NMPO, GEMP-38A, August 19, 1964, pp. 32–33.

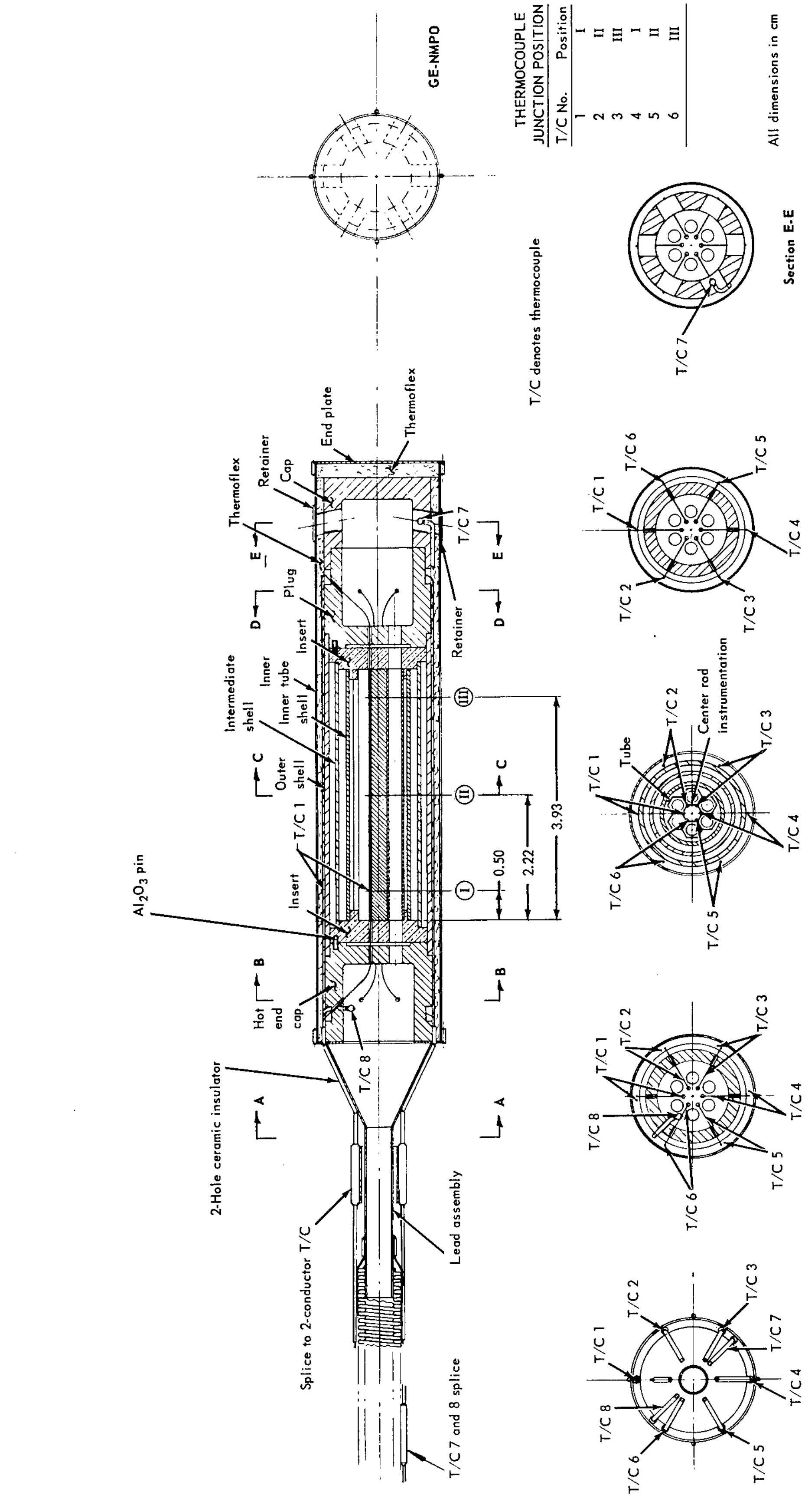

THERMOCOUPLE JUNCTION POSITION	
T/C No.	Position
1	I
2	II
3	III
4	I
5	II
6	III

Fig. 6.8—Inner tube assembly (*Dwg. 848D994*)

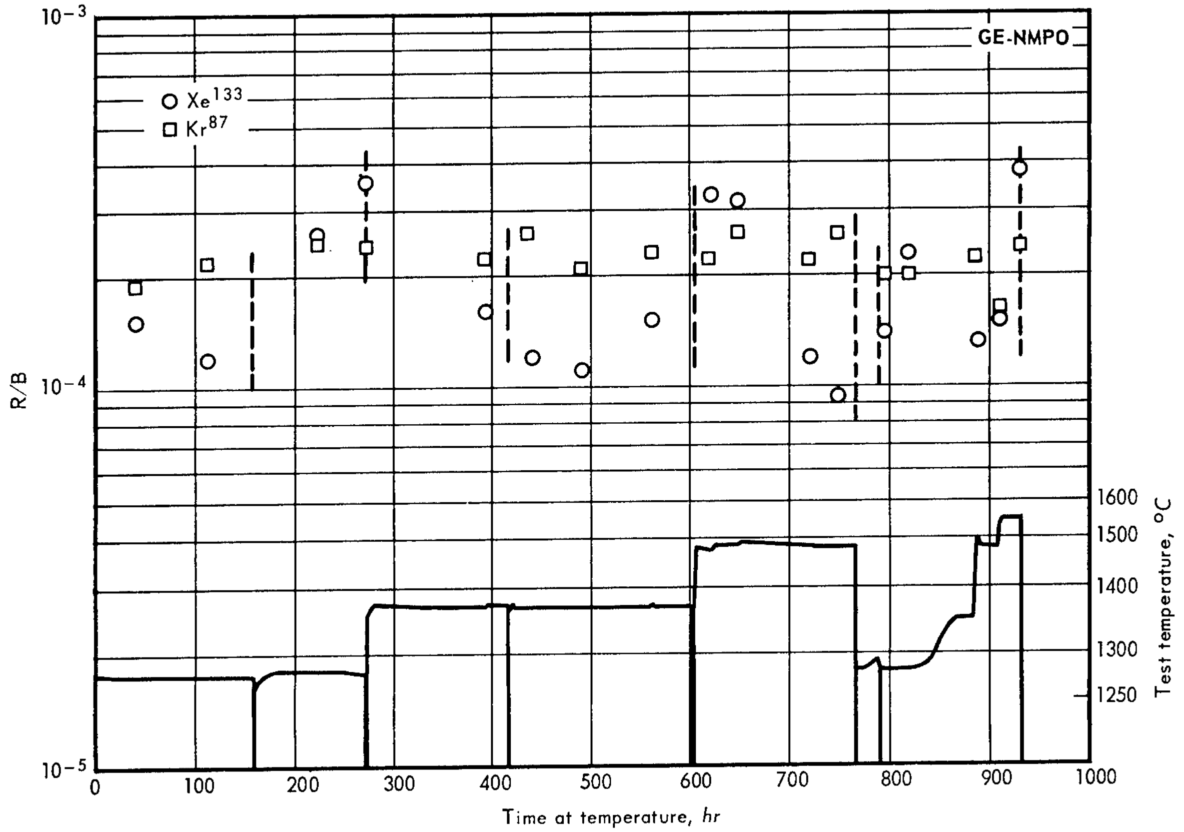

Fig. 6.9 – Xe^{133} and Kr^{87} release and thermal history of LITR test LTC-73

The off-gas from the test cartridge was sampled at regular intervals and analyzed for gaseous fission products. Fractional release (R/B)* data, Table 6.5, were obtained for Kr^{85m}, Kr^{87}, Kr^{88}, Xe^{133}, Xe^{135}, and Xe^{138} (measured as Cs^{138}).

Examination of the data, as presented in the table and Figure 6.9† shows (within data scatter) no time, temperature, or half-life dependence for the various isotopes which indicates that recoil is the dominant release process. This is supported by the release values of the short-lived (14-minute half-life) Xe^{138} which, because of its short half-life, is an excellent indicator for recoil release.

Previous tests‡ on stabilized UO_2-BeO systems containing less than 10 volume percent UO_2 have shown a significant diffusion contribution to fission gas release at temperatures exceeding 1350° to 1400°C. Contrary to these previous test results, the present data for 11.5BF-230 did not indicate that release was due to diffusion at temperatures as high as 1500°C, but a small diffusion contribution may be starting to appear at 1550°C. Since this lack of temperature dependence for fission gas release is a rather significant result, additional studies are planned to support the trap data.

The scatter of the Xe^{135} release data is not understood; it may be related to changes in flow characteristics (Reynolds number calculations indicated that flow was turbulent at all

---

*Fractional release is defined as the ratio of the rate of release of atoms from the specimen to the equilibrium production rate.

†The release levels shown in the figure which appear to coincide with temperature transients were in all cases determined before the temperature changes took place.

‡P. K. Conn, et al., "Studies of Fission Gas Release from In-Pile Tests: Recoil Loss from Ceramic Fuel Elements," *Proceedings of the Second Conference on Nuclear Reactor Chemistry*, TID-7622, July 1962, pp. 193–206.

TABLE 6.5

FISSION PRODUCT RELEASE FROM TEST LTC-73

Trap No.	Test Temperature, °C	Test Time, hr	Fractional Release (R/B),[a] 10^{-4}					
			Kr^{87}	Kr^{88}	Kr^{85m}	Xe^{135}	Xe^{133}	Xe^{138}[b]
C-1	1250	40.8	2	2	4	3	2	-
C-2	1250	111.4	2	2	4	4	1	3
Shutdown		157.8						
C-3	1260	223.9	3	2	5	5	3	-
C-4	1255	271.4	2	3	5	3	4	-
Shutdown		271.7						
C-5	1363	392.4	2	2	5	1	2	-
Shutdown		416.4						
C-6	1365	438.4	3	3	6	0.9	1	4
C-7	1365	487.6	2	3	5	0.9	1	-
C-8	1363	559.3	2	2	4	1	2	-
Shutdown		602.8						
C-9	1473	620.2	2	2	6	1	3	-
C-10	1485	645.4	3	3	6	0.7	3	-
C-11	1475	717.7	2	2	5	0.6	1	-
C-12	1475	745.4	3	2	6	0.7	0.9	3
Shutdown		765.9						
Shutdown		787.9						
C-13	1260	791.8	2	3	4	2	1	-
C-14	1260	815.7	2	2	4	3	2	-
C-15	1345	885.1	2	3	4	0.9	1	-
C-16	1475	907.7	2	2	3	0.6	2	-
C-17	1548	931.0	2	2	5	1	4	-
Shutdown		931.1	End of test					

[a] Fractional release is defined as the ratio of the rate of release of atoms from the specimen to the equilibrium production rate.

[b] The Xe^{138} was measured as Cs^{138}.

temperature steps) or to deposition of precursors in the exit line. Radiation level readings, taken where the off-gas line from the test capsule emerged from the top of the reactor pool, tended to increase with time and rising temperature above 1470°C; readings taken about 6 meters farther down stream were at background level and showed no time or temperature dependence.

The test specimens and off-gas ducting were removed from the reactor facility and are awaiting shipment to Evendale for post-irradiation examination and analysis.

ETR IRRADIATIONS

The two ETR test assemblies in progress (GEFP2-19 and GEFP2-23) are identical;* one is scheduled for eight cycles to give a burnup of approximately 5 x 10^{20} fissions/cm^3 and the other for four cycles to give a burnup of approximately 2.5 x 10^{20} fissions/cm^3. Depending on operating characteristics, the number of cycles may be increased. Both capsules have completed two cycles for 1242 hours test time at temperatures ranging from 1000° to 1250°C. The test temperatures have been particularly hard to control because of changes in reactor flux, coolant flow, and mechanical limitations. During the first cycle, capsule number GEFP2-19 operated at an average temperature of approximately 1000°C while GEFP2-23 averaged 1200°C. During the second cycle, the position of GEFP2-19 was shifted and the resultant temperature was increased to 1250°C while GEFP2-23 was partially shielded (to prevent an expected increase in flux) and the temperature decreased to between

---

* "High-Temperature Materials Program Progress Report No. 38, Part A," GE-NMPO, GEMP-38A, August 19, 1964, p. 36.

1000° and 1100°C. Other than problems of maintaining temperature, no significant difficulties were experienced in the two cycles completed to date.

6.4 SUMMARY AND CONCLUSIONS

A method was developed for reacting UO_2, ThO_2, and Y_2O_3 to form well-crystallized solid solutions. X-ray diffraction analysis of the area of interest in the UO_2-ThO_2-Y_2O_3-O_2 system shows a complete series of face-centered cubic solid solutions.

Partial pressure measurements of UO_3 from solid solutions of UO_2-ThO_2, UO_2-Y_2O_3, and UO_2-ThO_2-Y_2O_3 in air atmospheres show that the UO_3 pressure decreases as the ThO_2 content in the composition increases. The UO_3 pressures of fuel compositions containing 0.55 mole of Y_2O_3 per mole of UO_2 are lower by a factor of 3 to 6 than the binary UO_2-ThO_2 fuels.

The compressive creep behavior of fueled polycrystalline BeO with 8.5 to 11.5 volume percent UO_2-ThO_2-Y_2O_3 can be described by the Nabarro-Herring diffusion model at temperatures from 1200° to 1500°C. Compressive creep rates for BeO fueled with 25 volume percent fuel phase are also in agreement with the Nabarro-Herring model at temperatures up to 1400°C; however, at 1500°C the creep rates are higher than predicted.

Fuel retention tests of BeO-base fuel elements containing 7 to 25 volume percent UO_2-ThO_2-Y_2O_3 and UO_2-ThO_2 (for comparison) showed the following:

1. Fuel elements lost little (0.6% UO_2 maximum) or no UO_2 in 4000-hour tests at 1200°C in air. In tests for 2000 hours at 1400°C, Y_2O_3-containing specimens lost 0.4 to 1.7 percent UO_2 while the specimens containing no Y_2O_3 lost 2.2 to 2.4 percent.
2. Fuel elements tested for 2000 hours at 1200°C in pure helium and in helium + 5 volume percent oxygen showed no UO_2 loss and no significant change in physical or mechanical properties.
3. Fuel elements containing Y_2O_3 (sintered at 1800°C) consistently lost less UO_2 in tests at 1200°, 1400°, and 1650°C than the same composition sintered at 1675°C.

A probable explanation for the effect of sintering temperatures on fuel loss was evolved from the identification of the compound $4BeO \cdot Y_2O_3$ on the surface of fuel elements sintered at 1675°C.

Irradiation testing of fuel elements containing 25 volume percent UO_2-ThO_2-Y_2O_3 (11.5BF-230) in two ETR tests have completed 1242 hours at 1000° to 1250°C without difficulty. Irradiation testing in the LITR (LTC-73) for 931 hours at temperatures from 1250° to 1550°C have indicated that recoil is the dominant fission gas release process. No diffusion contribution was detected at temperatures up to 1500°C; this is contrary to previous experience with other fuel compositions and is not understood at this time.

6.5 PLANS AND RECOMMENDATIONS

Fuel retention studies in air will be continued and evaluations of the tests in helium will be completed. Non-nuclear testing of specimens to duplicate the irradiation test conditions will be continued.

Irradiation testing will be continued in the ETR on BeO-base fuel elements containing 25 volume percent UO_2-ThO_2-Y_2O_3 solid solutions (11.5BF-230). Work will continue on the fabrication of BeO-base fuel elements containing 25 volume percent fuel phase added as F-243 (UO_2-ThO_2-Y_2O_3 with a mole ratio of 1:7:0.55). These fuel elements will be coated with BeO and irradiated in the ETR.

7. OXIDATION-RESISTANT FUEL ELEMENT MATERIALS RESEARCH

(57001)

The objective of this program is to develop fuel element materials for use at high temperatures in air, steam, or other oxidizing coolants which are superior to presently available fuel materials in terms of high-temperature capabilities, long-time service life, and containment of fission products.

to p. 216

7.1 FUEL ELEMENT EVALUATIONS

The objective of the fuel element evaluation studies is to evaluate Fe-Cr-Al-Y cladding alloys in combination with UO_2 or UN for long-time stability in air or steam at temperatures to 1250°C. Fe-UO_2 and Cr-UO_2 core compositions were selected as the most promising for use in air-cooled or superheated steam reactors. Long-time laboratory tests are in progress covering a range of temperatures, and the first in-pile test of the Fe-Cr-Al-Y-clad Fe-UO_2 system was prepared. Both air-oxidation and steam-corrosion tests showed that 2541 (Fe - 25Cr - 4Al - 1Y) and 1541 (Fe - 15Cr - 4Al - 1Y)* alloys are excellent cladding materials. The problem of uranium diffusion was resolved, at least to 1100°C, by use of improved fuel forms in an iron matrix. The continuing test program is designed to demonstrate the time - temperature capabilities in air of selected fuel element systems. Specimens of 2541-clad Fe-UO_2 have proven reliable for at least 5000 hours at 1100°C and are continuing on test toward a goal of 10,000 hours.

URANIUM DIFFUSION STUDY

Early work on the 2541-clad Cr-UO_2 fuel element system revealed that uranium was diffusing through the cladding, particularly at high temperatures (~1250°C). To study the diffusion rate in terms of various core-to-cladding ratios, a heavy-walled disc-shaped die specimen with a thin window over the core was designed.† In this design a sintered core is loaded into the die specimen, hot-pressed in argon to densify the core and to insure a bond, and machined to 0.089 cm cladding thickness on one end.

Many of these 2541-clad specimens containing various core compositions were tested during the past year at 1100°C and 1250°C and periodically analyzed by X-ray fluorescence for uranium intensity on the surface of the thin section of cladding. Both Fe and Cr matrix materials were tested as well as various forms of UO_2 and UN fuels including ceramic grade powders (<40 microns), agglomerated fuel particles (75 to 150 microns), and ThO_2-stabilized UO_2. A visual indication of uranium diffusion was the darkening of the normal gray oxide film of the 2541 alloy cladding.

---

*The cladding compositions are in weight percent and the core compositions are in volume percent unless otherwise noted.

†"Third Annual Report – High-Temperature Materials and Reactor Component Development Programs, Volume II – Materials," GE-NMPO, GEMP-270B, February 28, 1964, p. 103.

In the die specimens tested at 1250°C, uranium began to diffuse through the cladding in 300 hours; the amount increased steadily with time until the tests were terminated at 1480 hours. These data are shown in Figure 7.1 in comparison with 1100°C test data for times up to 6400 hours. The relative uranium concentrations are shown for both the ceramic-grade UO_2 powder and the agglomerated fuel particles contained in Fe and Cr matrices. A significant reduction in uranium diffusion resulted when agglomerated fuel particles were used in the Cr matrix; however, this was less effective in the Fe matrix.

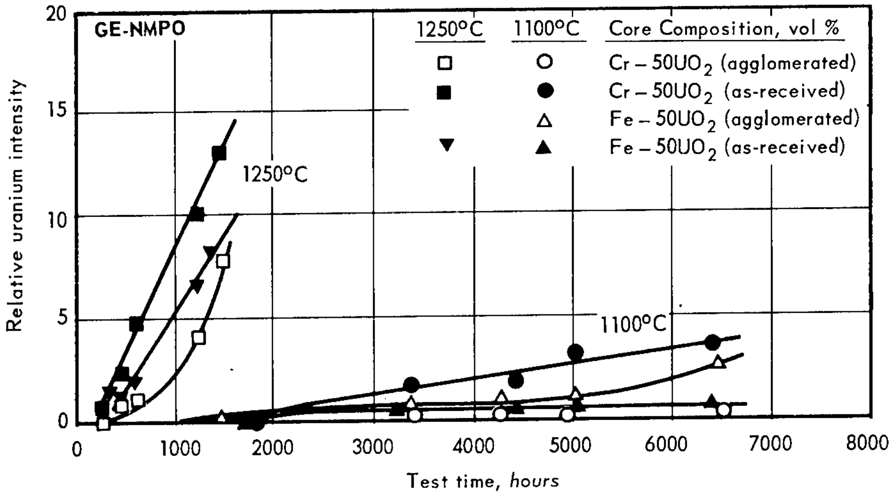

Fig. 7.1 – Relative uranium intensity on surface of Fe-Cr-Al-Y-clad die specimens containing various core compositions after testing at 1100°C and 1250°C in air

Within the limits of detection (~ 500 ppm), X-ray fluorescence analysis did not reveal uranium diffusion during the initial 1800 hours at 1100°C for any core composition. The specimens are continuing on test at 1100°C and currently have accumulated 7500 hours of test time.

FUELED CAPSULE TEST PROGRAM

Thermal stability test data are being obtained on various cladding - core combinations using cylindrical capsule specimens, 1.05 cm in diameter by 2.54 cm in length. The 0.76-mm-thick cladding is bonded to the sintered core by autoclaving at 1250°C.* After a preliminary proof-test to determine if cladding - core bonding was accomplished, the capsule specimens are subjected to long-time tests with goals of 10,000 hours at 950°C and 1100°C in flowing air. A few tests were conducted at 1250°C but, as discussed previously, the capsule life was less than 2500 hours at this temperature as a result of uranium diffusion. Specimens are analyzed periodically for uranium diffusion through the cladding, and other specimens are removed from test for metallographic study at the end of scheduled test periods of 1000, 3000, and 5000 hours.

One hundred and ten capsule specimens were put on test during the past year, and 45 of these are continuing on test at 950°C and 1100°C. Recently, specimens containing spheroidized UO_2 particles were placed on test, but test times are insufficient to show any advantage of this fuel form as yet. The X-ray fluorescence method of scanning the flat surfaces of die specimens for uranium diffusion through the cladding was adapted to the curved surface of capsule specimens.

* Ibid.

The capsule test program status for four general categories of fuel element systems is summarized in Figure 7.2. Typical specimens of two systems are shown in Figure 7.3 after long-time testing at 950°C and 1100°C in flowing air. Twenty-five specimens have completed up to 5200 hours of testing at 1100°C or 950°C; the appearance and oxidation penetration of the cladding surface of these specimens is such that a 10,000-hour life appears to be a realistic goal.

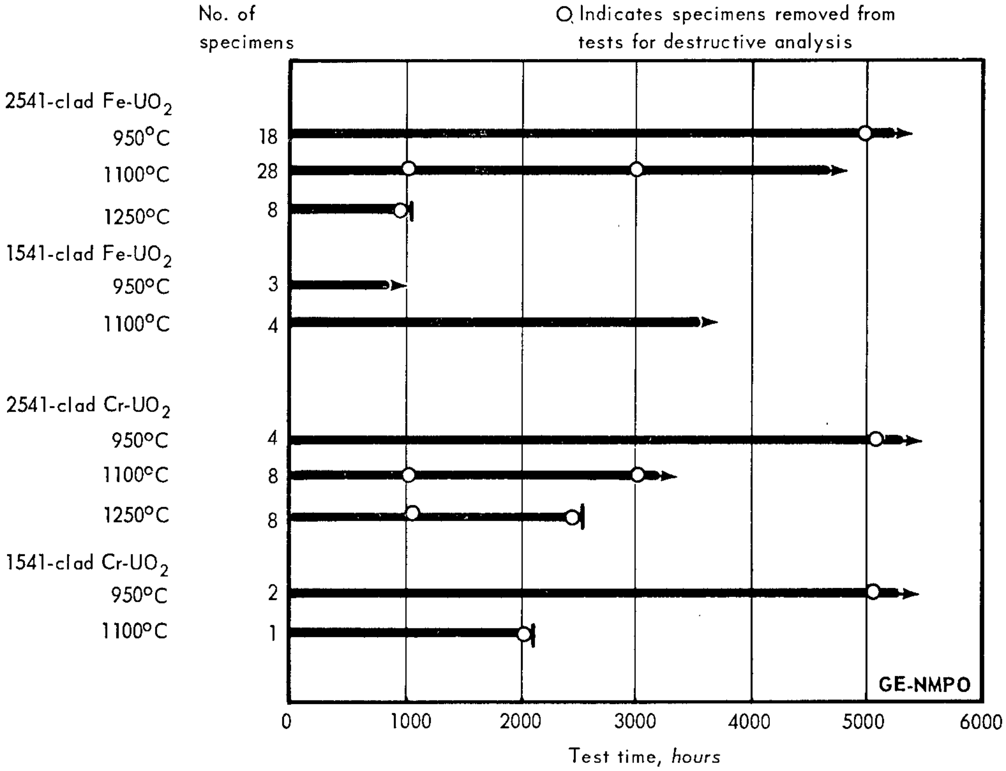

Fig. 7.2 – Status of 10,000-hour test program for Fe-Cr-Al-Y-clad Fe-UO_2 and Cr-UO_2 capsule specimens

X-ray fluorescence analyses have not detected uranium on the surfaces of most of the long-time test specimens containing UO_2 tested at either 1100°C or 950°C. Specimens containing UN in a chromium matrix showed relatively high uranium concentrations on the cladding surface after 3700 hours at 1100°C.

Metallographic examination and electron microprobe analyses for interdiffusion of the elements in the core and cladding of two specimens are shown in Figure 7.4; the microprobe data are superimposed on the microstructures of the scanned areas. The 2541-clad Cr - $50UO_2$ specimen was tested for 3025 hours at 1100°C and shows a concentration of yttrium near the cladding surface which is present as Y_2O_3 in the surface grain boundaries and as fine particles of YFe_9 scattered throughout the cladding. Within the sensitivity limits of the microprobe analysis (~ 500 ppm), no uranium was detected in the cladding. Interdiffusion of Fe and Cr was extensive causing an increase in the Cr content of the cladding to 32 percent and a concurrent diffusion of Fe into the Cr-UO_2 core to a depth of 250 microns.

The 2541-clad Fe - $50UO_2$ specimen was tested for 5035 hours at 950°C and shows no surface oxide layer and only mild penetration of grain boundaries. A slight diffusion of

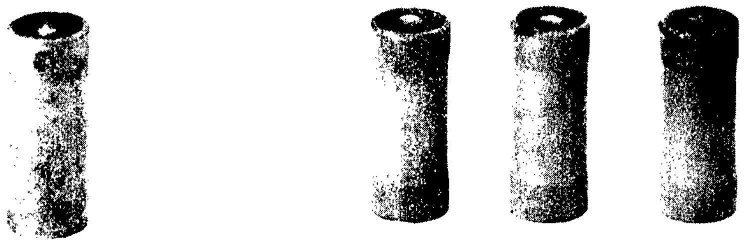

$Cr-UO_2$
5500 hours at 950°C

$Cr-UO_2$
3000 hours at 1100°C

GE-NMPO

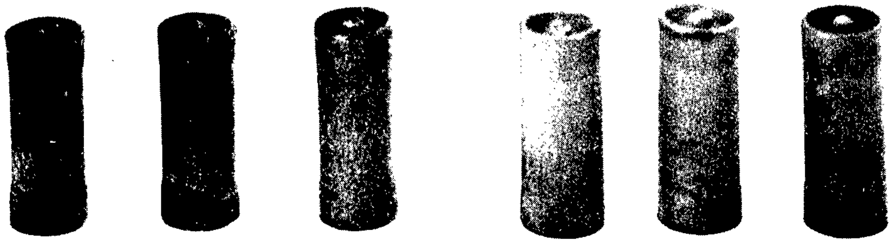

$Fe-UO_2$
4500 hours at 950°C

$Fe-UO_2$
3500 hours at 1100°C

Fig. 7.3 – Typical 2541-clad capsule specimens containing $Fe-UO_2$ or $Cr-UO_2$ cores after long-time testing at 950°C or 1100°C in air *(Neg. P65-1-20)*

Fe from the core into the cladding was indicated by the microprobe scans. Both Cr and Al diffused into the $Fe-UO_2$ core to a depth of 100 to 150 microns. The major Al concentration occurred at the interface where Al_2O_3 formed. Yttrium apparently did not diffuse into the core but existed as a coarse precipitate of YFe_9 in the cladding. The fact that no uranium was detected in the cladding or the Fe matrix of the core confirms the X-ray fluorescence analyses obtained during the test.

Although this capsule test program will continue, sufficient laboratory test data have been obtained to show that the 2541-clad Fe - $40UO_2$ fuel element has adequate stability for at least 5000 hours' service at 1100°C in air. These test data also show that the 1541 cladding alloy has oxidation resistance at 1100°C comparable to that of the 2541 alloy. Preparations are being made to test in-pile the 2541-clad Fe - $40UO_2$ system to evaluate the stability of this fuel element under conditions of high burnup.

7.2 Fe-Cr-Al-Y CLADDING ALLOY DEVELOPMENT AND FABRICATION

The objective of the Fe-Cr-Al-Y cladding alloy development and fabrication studies is to obtain alloys of improved strength and high-temperature stability for use as fuel element cladding in air or steam environments. The alloys being studied are the Fe-Cr-Al-Y type which exhibit excellent oxidation resistance through the formation of an adherent aluminum oxide film. These studies are concerned with establishing the inter-relationships of chemical composition, embrittlement caused by a phase instability, strength, air-oxidation resistance, and steam-corrosion resistance. Also, quantities of the more

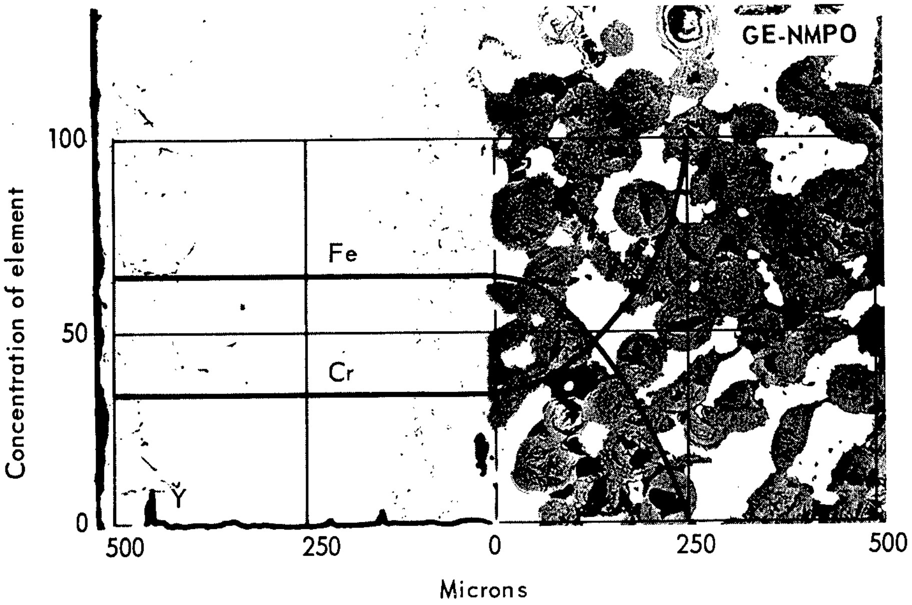

2541-clad Cr – 50UO$_2$
after 3025 hours at 1100°C *(Neg. 4987)*

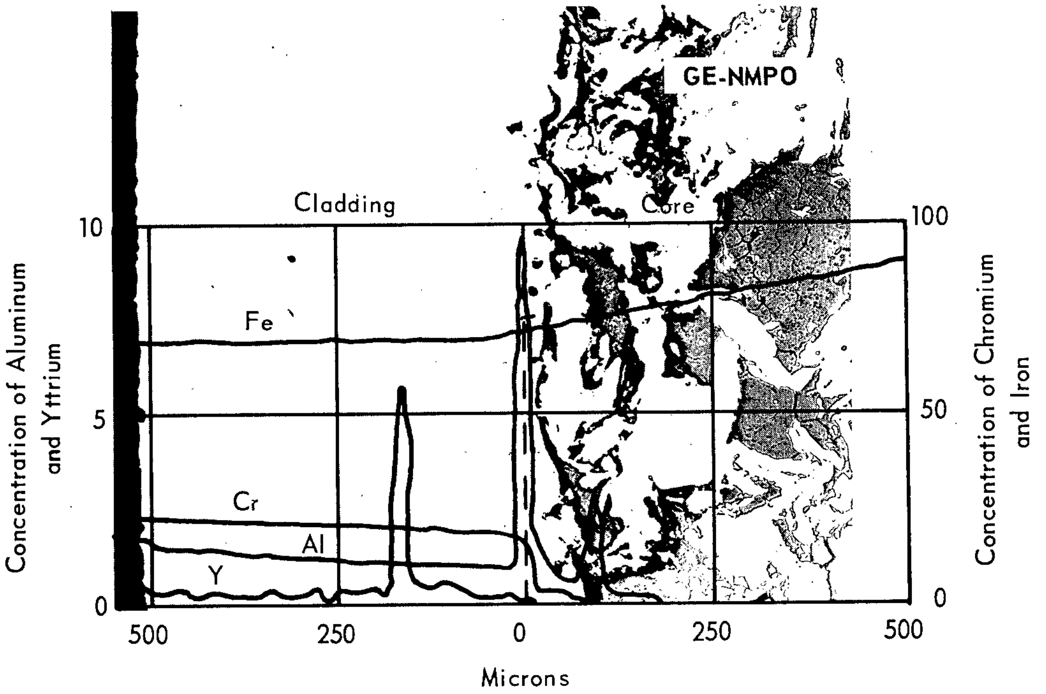

2541-clad Fe – 50UO$_2$
after 5035 hours at 950°C *(Neg. 5189)*

Fig. 7.4 – Electron microprobe analyses for various elements superimposed on photomicrographs of scanned areas of Fe-Cr-Al-Y-clad specimens showing interdiffusion that occurred during long-time testing at 950°C and 1100°C *(100X)*

promising alloys have been produced in the form of rod, sheet, and tubing for experimental fueled assemblies.

ALLOY PREPARATION

The alloys are prepared by vacuum induction melting in Al_2O_3 crucibles and casting into copper or graphite molds. Heats of up to 115 kilograms have been melted and cast into sound ingots. The cast structures are made workable by extrusion to rod at 1000°C with reduction ratios of 14-to-1. The extruded rods are either swaged to smaller diameters or press-forged and hot-rolled to sheet at 1000°C. Sheet stock is finish-rolled at room temperature from about 0.25 cm thickness.

In earlier studies, the raw materials used for melting were high-purity Fe, Cr, Al, and Y. During this past year, low-cost ferrochromium was substituted for high-purity chromium with no apparent reduction in quality of the alloys. Chemical analyses (Table 7.1) of six large heats of 2541 and 1541 alloys, melted in CY-64, indicate good control of composition and reproducibility of heats ranging in size from 45 to 90 kg.

TABLE 7.1

CHEMICAL ANALYSES OF 2541 AND 1541 ALLOYS PRODUCED BY VACUUM INDUCTION MELTING

		Analyzed Content											
		Weight Percent			Parts Per Million								
Heat No.	Composition	Cr	Al	Y	P	C	S	Si	Zr	Ca	H_2	O_2	N_2
MS-36	2541	25.51	4.3	0.41	58	48	11	28	43	13	1	120	4
MS-38	1541	14.49	4.48	0.57	59	30	16	20	25	14	<1	20	<1
MS-40	2541	24.25	4.60	0.52	75	31	18	36	28	17	<1	140	6
MS-41[a]	1541	15.36	4.44	0.43	91	31	14	85	45	15	<1	5	1
MS-42[a]	2541	24.10	4.50	0.50	115	72	23	340	<10	13	1	10	7
MS-43	1541	15.36	4.19	0.43	70	35	17	28	25	<10	1	10	<1

[a] Ferrochromium used as melting stock, all other heats made of high purity chromium.

TUBING PROCESSING

A quantity of tubing was produced by an outside vendor by warm drawing (300°C) tube blanks supplied by GE-NMPO. Tube blanks were produced by drilling rods or by hot extruding a billet over a mandrel. Initial tube quality was poor because of oxide stringers which were related to shrinkage cracks in the original ingots.[*] Ingot defects were eliminated through the use of tapered graphite molds to improve the ingot structure. Subsequent tubing quality was much improved.[†]

PHYSICAL METALLURGY

The Fe-Cr-Al-Y alloys consist of a two-phase structure, a ferritic (body-centered cubic) matrix and a dispersion of YFe_9 intermetallic compound. The solubility of yttrium in iron is less than 0.1 percent; therefore, most of the yttrium is present as YFe_9. The phase relationships are thus related primarily to the Fe-Cr phase diagram modified by the addition of aluminum. The basic Fe-Cr phase diagram is shown in Figure 7.5. Also shown is a tentative phase boundary modification caused by addition of 4 weight percent aluminum as determined in the present work. At temperatures below 520°C, precipitation of α', a Cr-rich ferrite phase, causes hardening and a loss in ductility of the alloys with high chromium content.

---

[*] "High-Temperature Materials Program Progress Report No. 35, Part B," GE-NMPO, GEMP-35B, May 28, 1964, p. 27.

[†] "High-Temperature Materials Program Progress Report No. 43, Part A," GE-NMPO, GEMP-43A, January 29, 1965, p. 14.

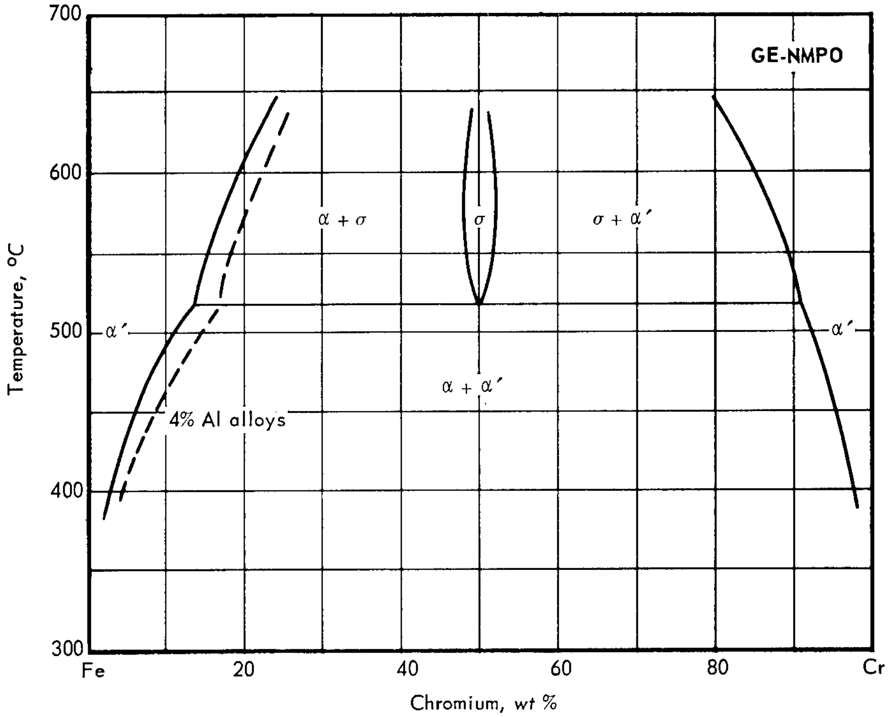

Fig. 7.5 – Low-temperature portion of the Fe-Cr binary and the Fe – 4Al – Cr pseudobinary phase diagrams

In aging experiments at 450°C, yttrium and aluminum additions increased the rate of aging but had little effect on the maximum hardness as shown in Figure 7.6. As the chromium content was reduced from 25 weight percent, the stability at 450°C was increased; however, the aluminum content had to be increased to maintain corrosion resistance. The improved stability of the resultant alloys is indicated in Figure 7.7. The as-annealed hardness of the alloys with high aluminum content is higher but they exhibit little or no aging at 450°C. The usefulness of the modified alloys will depend on the relationship between composition, corrosion resistance, and ductility.

OXIDATION RESISTANCE

The oxidation resistance of the 2541 alloy has been well documented. As the chromium content is reduced below about 15 weight percent, it is necessary to increase the aluminum content to maintain the excellent oxidation resistance at high temperatures. When chromium is eliminated from the alloy, the aluminum content must be increased to 7.5 to 10 weight percent (Figure 7.8). In tests at 900°, 1100°, and 1300°C, the oxidation behavior, based on weight change data and metallographic examinations, was similar over a wide range of compositions as indicated in Figure 7.9.

Selected alloys are being tested for times up to 10,000 hours in air at 450°, 550°, 730°, 900°, and 1100°C. Weight gain data for times up to 4000 hours at 900°C and 1100°C are shown in Figure 7.10. At lower temperatures, the weight gains are low enough to be within experimental error. Metallographic examination after 3000 hours indicated that surface oxide formation and internal structural changes were similar for all the alloys. At 900°C and 1100°C the formation of an adherent surface oxide of Al_2O_3 was accompanied by internal oxidation of yttrium. Y_2O_3 particles were formed to a depth of approximately 0.1 mm. At the lower temperatures, no internal oxidation occurred and only a thin film of surface oxide formed.

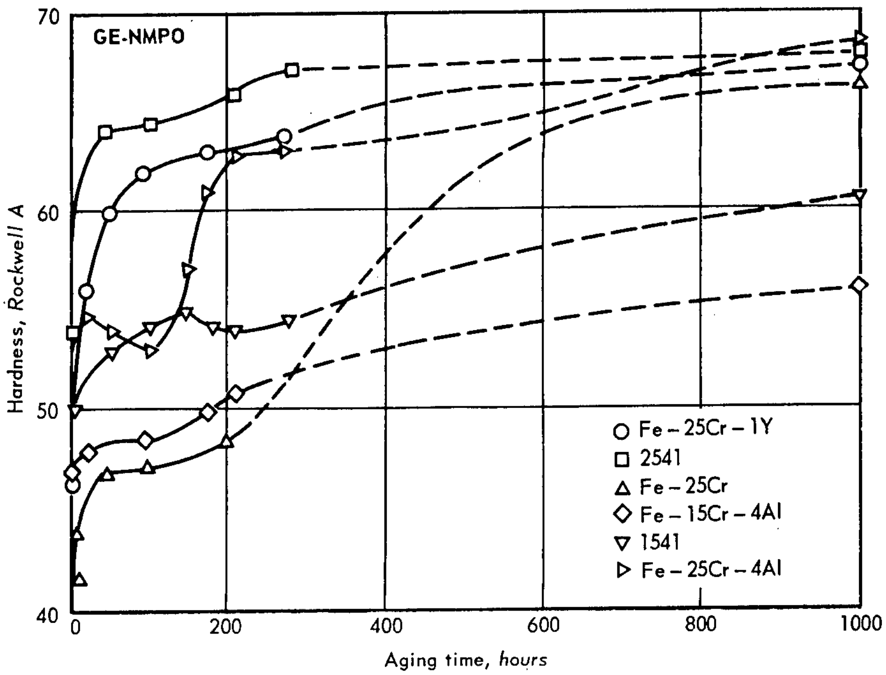

Fig. 7.6 – Room-temperature hardness versus aging time at 450°C for experimental Fe-base alloys with high Cr content

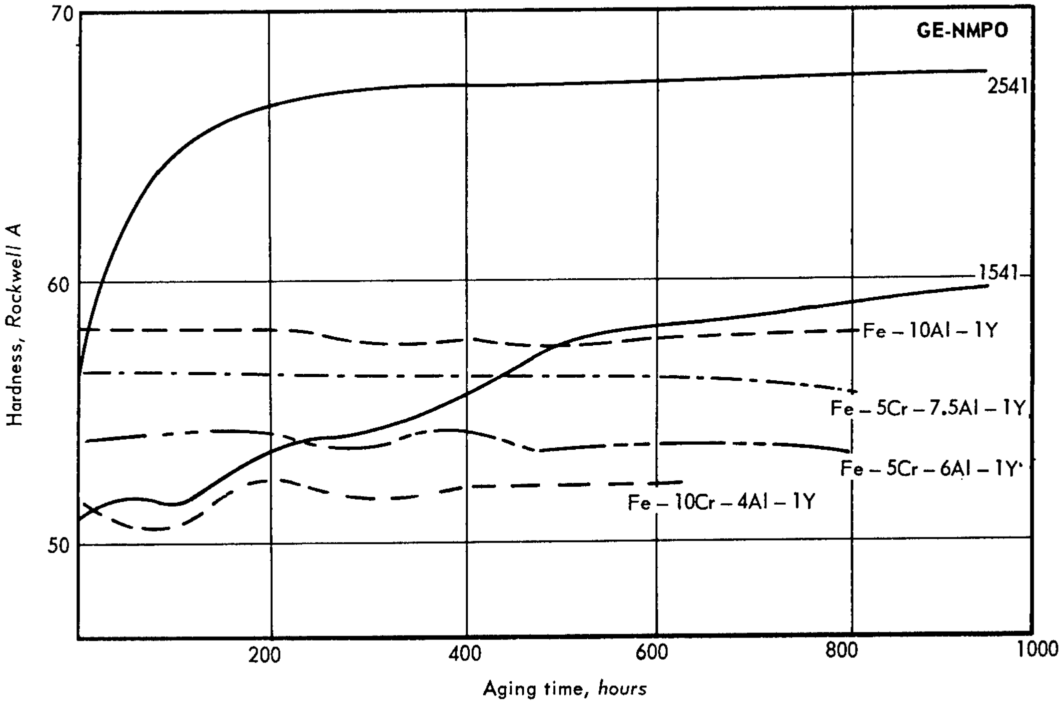

Fig. 7.7 – Room-temperature hardness as a function of aging time at 450°C for low-chromium-content Fe-Cr-Al-Y alloys compared to 2541 and 1541 alloys

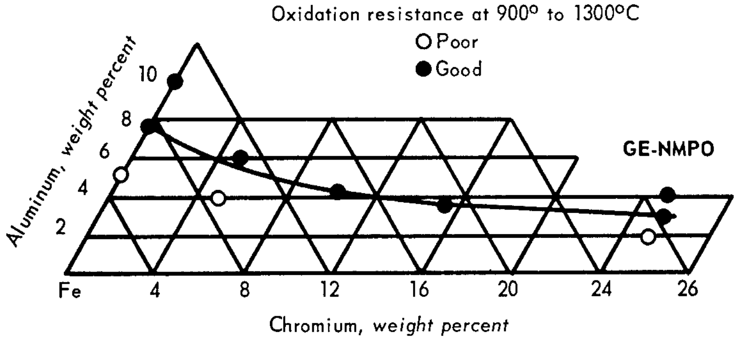

Fig. 7.8 – Portion of Fe-Cr-Al phase diagram showing chromium and aluminum contents needed for oxidation resistance at temperatures up to 1300°C. (All alloys contain 1 percent yttrium.)

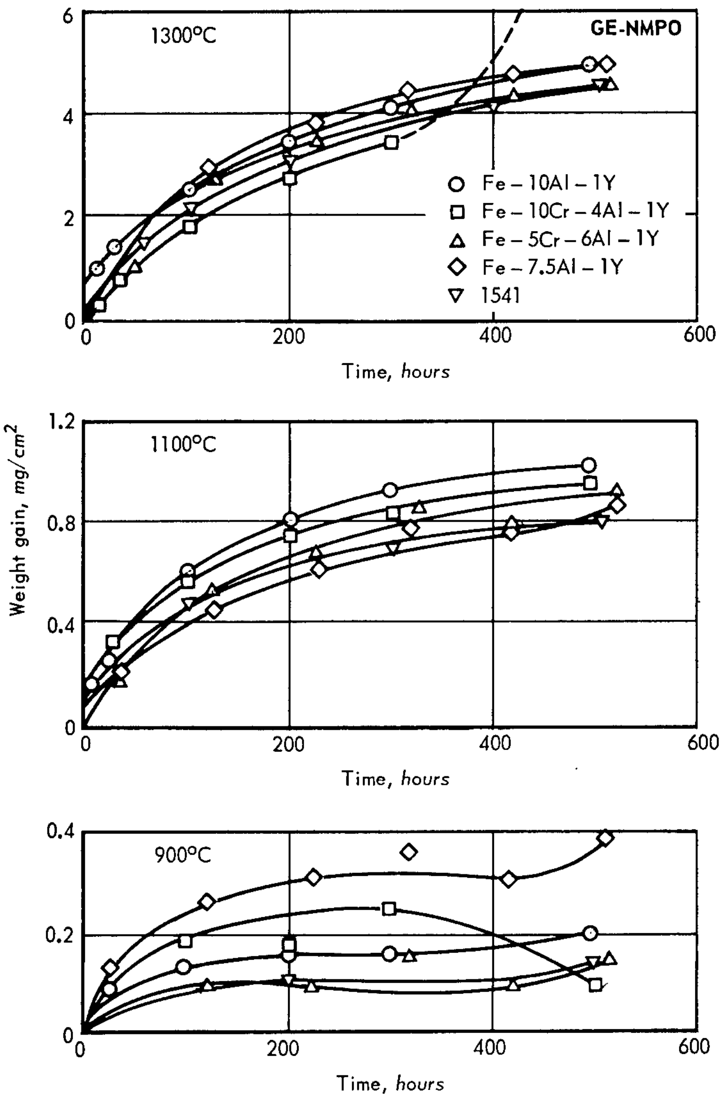

Fig. 7.9 – Oxidation rates of Fe-base alloys tested at 900°, 1100°, and 1300°C in static air

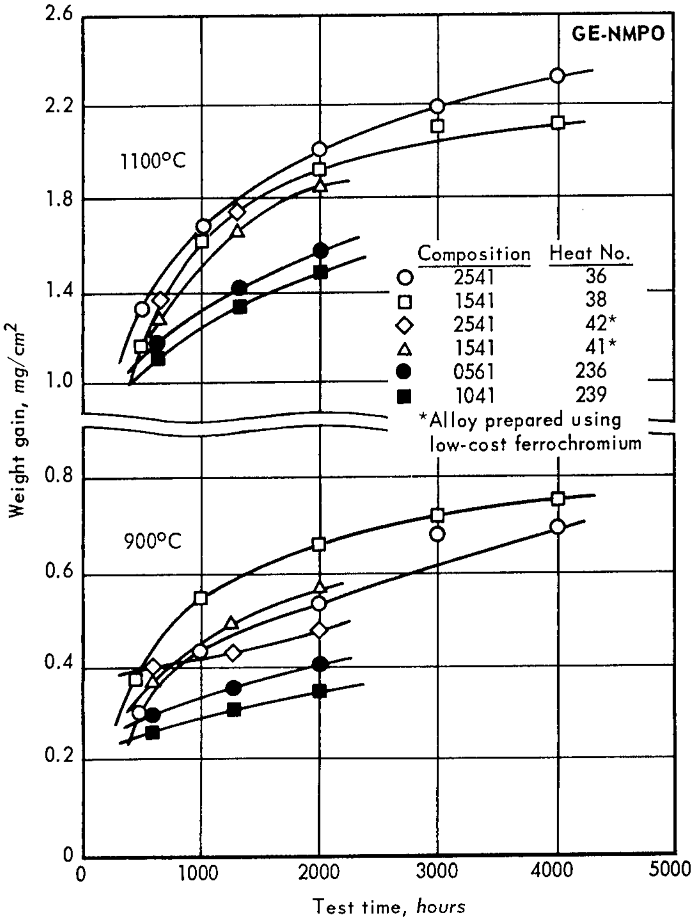

Fig. 7.10 – Weight gain as a function of test time at 900°C and 1100°C in static air for Fe-Cr-Al-Y alloys for times up to 4000 hours

STRENGTH

The Fe-Cr-Al-Y alloys possess low strengths at elevated temperatures; this is also a characteristic of ferritic stainless steels. To increase the high-temperature strength, niobium and molybdenum were added to several alloy compositions. These additions were effective strengtheners at temperatures up to about 900°C. The addition of 5 weight percent molybdenum to the 1541 composition doubled the tensile strength at 870°C. Tensile strength data for several alloys are shown in Figure 7.11 and stress-rupture data are shown in Figure 7.12. The rupture strength of Type 304 stainless steel is shown for comparison.

DUCTILITY

The room-temperature tensile ductility of the alloys ranges from 10 to 30 percent. At higher temperatures the ductility is increased. The effects of aging treatments at low temperature were evaluated by bend testing sheet specimens. Aging 2541 alloy at 450°C to maximum hardness resulted in an increase in the ductile-to-brittle transition temperature (DBTT) in bending from less than -80°C to approximately 110°C. For 1541 alloy, the increase was from less than -80°C to approximately 30°C. Based on limited data, the DBTT increases linearly with increase in hardness.

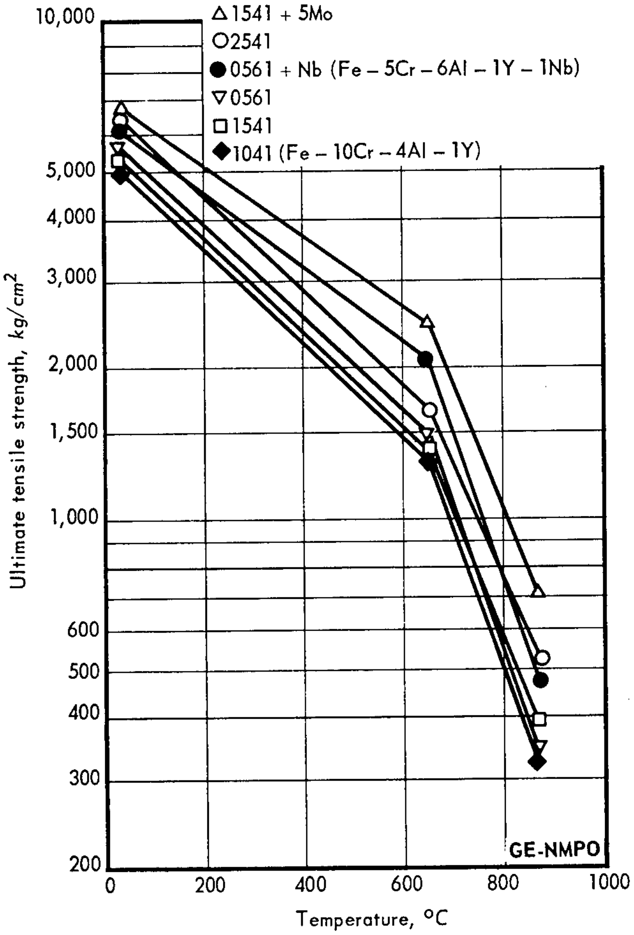

Fig. 7.11 – Tensile strength as a function of temperature for various compositions of Fe-Cr-Al-Y alloys

Impact tests were performed to compare the effects of variations in composition, heat treatment, and processing. For this preliminary screening, cylindrical notched specimens were broken by the Izod method. A quantity of 1541 alloy was supplied to the Naval Research Laboratory for further testing by the Standard Charpy test. Test specimens of the 1541 and 2541 alloys are being prepared for V-notch Charpy testing at GE-NMPO.

Preliminary impact data on the various alloys (Figure 7.13) indicate that yttrium increases the DBTT by about 150°C and is thus a controlling variable. Alloys with lower yttrium content (0.1 to 0.3%) are being evaluated for ductility, oxidation resistance, and weldability.

WELDING STUDIES

The weldability of Fe-Cr-Al-Y alloys is limited by the presence of the YFe_9 phase which melts at about 1350°C while the matrix melts at about 1450°C. As a result the fusion zone contains interdendritic films of the brittle YFe_9 phase. Fusion welds thus tend to be brittle at room temperature. However, post-weld annealing treatments at 1200° to 1300°C improved the weld ductility by spheroidizing the YFe_9 films. To further improve the weldability, lower yttrium contents are being evaluated. Initial results indicate improvement in the alloys containing 0.1 to 0.3 weight percent yttrium in place of the 0.7 to 0.8 weight percent normally used. Oxidation resistance of the weld was comparable to that of the base metal.

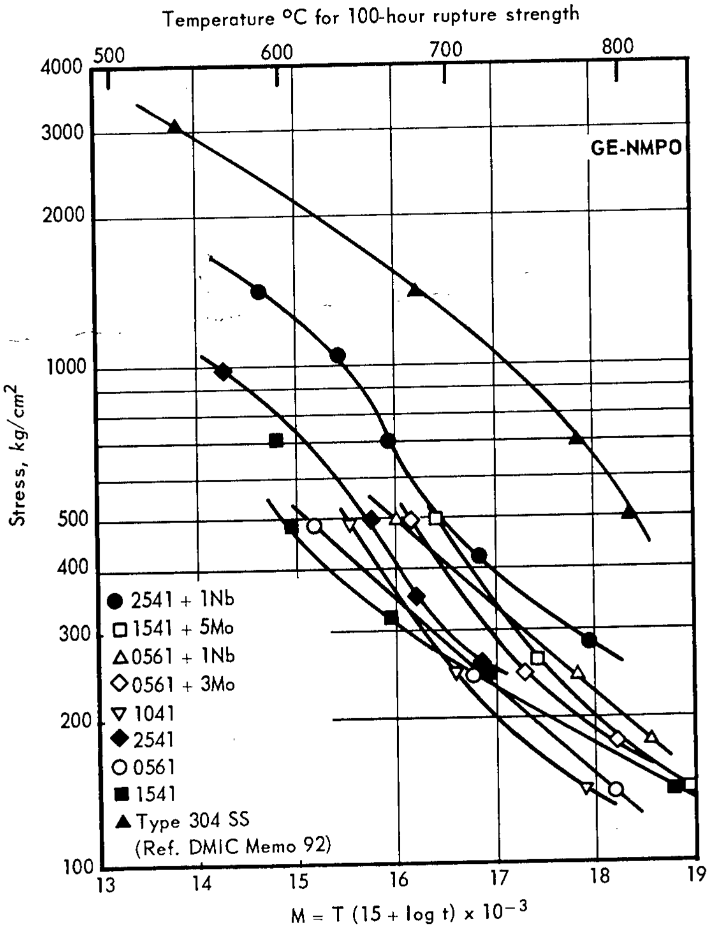

Fig. 7.12 – Rupture strength of various compositions of Fe-Cr-Al-Y alloys compared to Type 304 stainless steel

IRRADIATION EFFECTS

Irradiation effects on the properties of Fe-Cr-Al-Y alloys are being studied. Sheet specimens of 1541 alloy were irradiated at ambient temperature to a fast neutron dose of 3 x 10^{19} nvt in the ORR. After irradiation, specimens were annealed at 50°C temperature increments between 150° and 700°C for 1 hour at each increment, and room-temperature hardness measurements were made. The resulting data, shown in Figure 7.14, indicate that the effects of irradiation are removed by annealing for 1 hour at 300°C. The aged and irradiated material became softer than the aged control material when annealed at temperatures above 300°C. This indicates the possibility of irradiation-induced overaging or solutioning of the precipitate in the alloy. Heating above 500°C caused solutioning of the α' precipitate in the alloy.

In future tests the effects of irradiation on the ductility of these specimens will be evaluated.

Additional 2541, 1541, 1041 (Fe - 10Cr - 4Al - 1Y), and 0561 (Fe - 5Cr - 6Al - 1Y) alloys have been irradiated in the ETR to a fast neutron dose of 10^{20} nvt. The irradiation effects on their properties will be evaluated.

Irradiation of 1541 alloy tensile specimens at 450°C is scheduled to obtain data on the effect of irradiation on α' precipitation while at the optimum aging temperature.

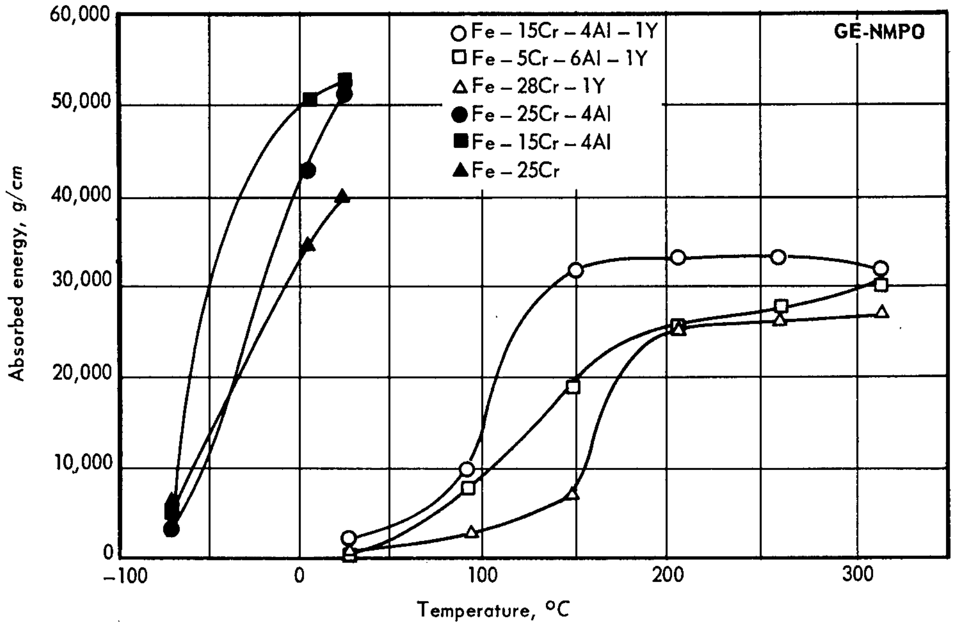

Fig. 7.13 – Absorbed energy as a function of temperature for a series of Fe-Cr-base alloys impact tested in the annealed condition. The ductile-to-brittle transition temperature point occurs at the midpoint between maximum and minimum energy.

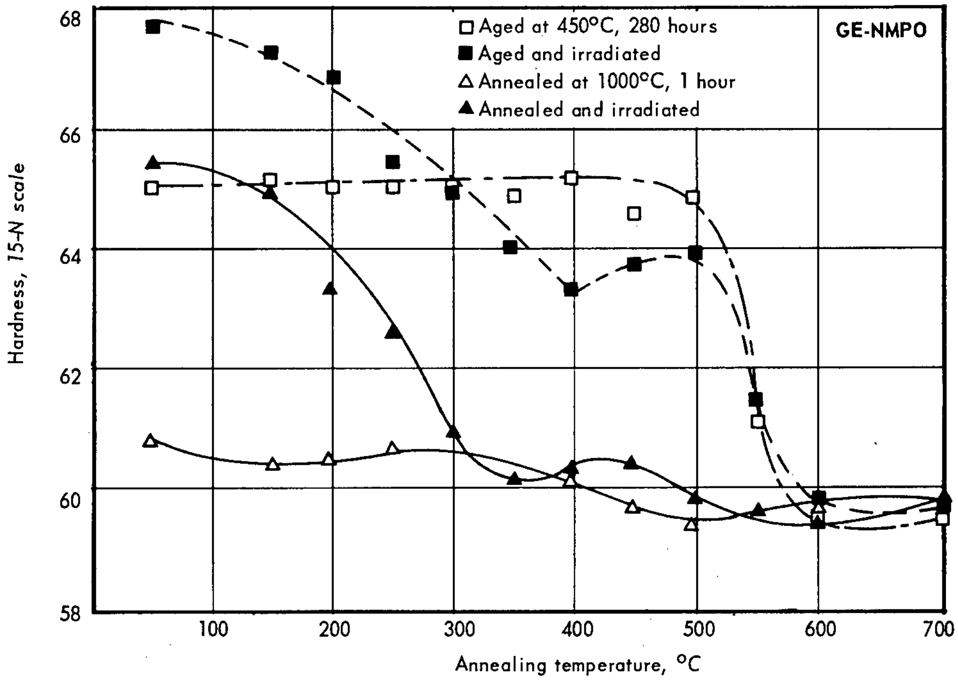

Fig. 7.14 – Hardness as a function of annealing temperature for 1541 alloy after irradiation to 3×10^{19} nvt in aged and annealed conditions. Specimens were annealed 1 hour in vacuum at indicated temperatures.

The 1541 alloy was included in a study of irradiation effects on alloy properties at GE-APED. Specimens were irradiated to a fast neutron dose of 2 x 10^{20} nvt at 700°C. Post-irradiation tensile tests will be conducted at room temperature and 700°C.

7.3 CHROMIUM-BASE ALLOY STUDIES

Chromium-base alloys merit consideration as possible future high-temperature cladding materials because of inherent oxidation resistance and high strength. Two primary problems are lack of room-temperature ductility and low resistance to nitrification during air oxidation. The objectives of this program are to improve both ductility and nitrification resistance.

DUCTILITY

As a result of previous work on chromium-base alloys containing Groups VII and VIII metal solutes, a theoretical explanation for the ductilizing effect of such additions was developed.* Additions of Re and Ru have been found to significantly improve the low-temperature ductility of chromium.

The essential feature of the postulation is the removal of interstitial impurities from solution in the matrix by formation of clusters in a more or less oriented array. Dislocation mobility is improved by the removal of interstitial impurities. In some cases a highly oriented array of clusters is considered likely, thereby providing easy dislocation movements along widely spaced $\{110\}$ and $\{112\}$ planes, normal slip planes in body-centered cubic systems. Data favorable to the postulation include the solubility - temperature relationships, elastic constants of the base metals, crystal structure of the solutes, hardness data, and shape and distribution of equilibrium precipitates in Cr-Ru alloys. Further work on Cr-Ru alloys will include aging studies to determine if Ru-rich clusters exist and to study the morphology of equilibrium precipitates.

A cooperative study with Battelle Memorial Institute on the deformation mode in Cr-Re alloys revealed that both $\{110\}$ and $\{112\}$ slip planes are active. This information supports the above postulation for the ductilizing effect of Re or Ru.

NITRIFICATION RESISTANCE

One of the limitations to the use of chromium-base alloys is the problem of nitrification during air oxidation. However, chromium-base alloys should be applicable for service in steam atmospheres if the nitrogen content of the steam is low enough. To determine if the equilibrium nitrogen level in the de-ionized feed water is high enough to embrittle chromium, a specimen of pure chromium was exposed to a steam atmosphere for 1000 hours at 1100°C. Chemical analysis of the specimen showed no nitrogen pickup although the feed water presumably contained an equilibrium amount of nitrogen (about 15 ppm). Slight hardening of the specimen correlated well with an equilibrium amount of oxygen pickup. Therefore, nitrification of chromium-base alloys should not be a problem in steam-cooled reactor applications.

7.4 CLADDING EVALUATIONS IN STEAM

The objectives of cladding evaluations in steam are to determine the effects of steam corrosion on Fe-Cr-Al-Y alloys and on other potentially useful commercially available alloys. This testing will also provide a comparison between air and steam corrosion resistance of the Fe-Cr-Al-Y alloys. Studies at GE-NMPO consist of testing in low-flow and low-pressure steam. Cooperative testing was also conducted at GE-APED in high-velocity and high-pressure steam.

---

*C. S. Wukusick, "On the Mechanism of the Rhenium-Alloying-Effect in Group VI-A Metals," GE-NMPO, GEMP-314, November 20, 1964.

LOW-PRESSURE TESTS AT 550° TO 1100°C

The test facilities used in this study were described previously.* Demineralized steam having a typical analysis of 0.8 to 1.2 megohm specific resistivity, 6.0 to 6.5 pH, and 3.0 to 5.0 ppm dissolved oxygen is used for all testing.

A number of alloys were tested for times up to 3000 hours at 730°C at 3 atmospheres pressure and a steam velocity of approximately 40 cm/sec. The weight change data for these tests are presented in Figure 7.15. As shown, the 2541 and 1541 alloys are equivalent to the better commercial alloys, such as 80Ni - 20Cr.

In tests performed at 1150°C, 1.1 atmospheres pressure, and 80 cm/sec steam velocity, the Fe-Cr-Al-Y alloys proved to be superior to the commercial alloys.

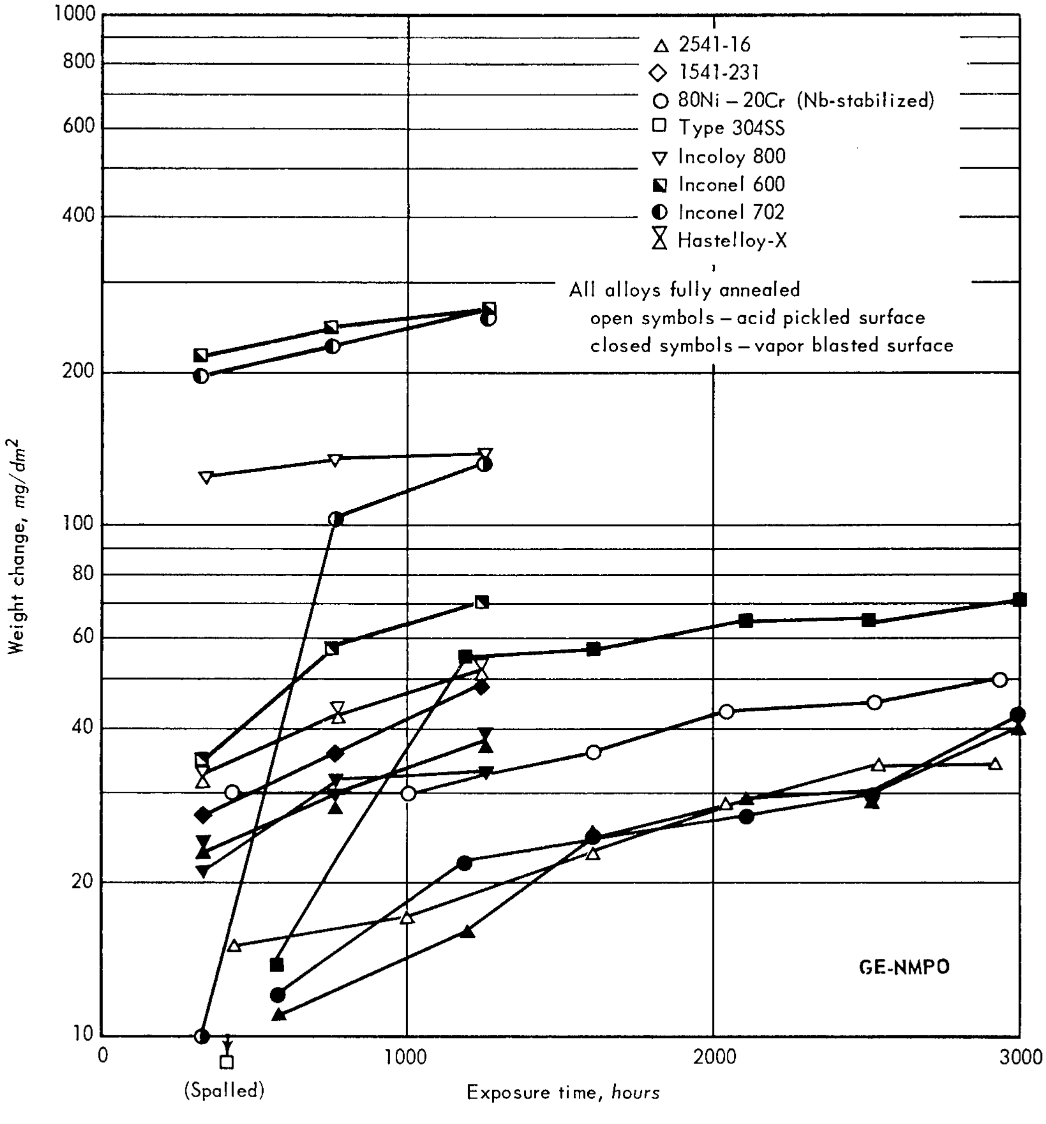

Fig. 7.15 – Weight change as a function of time up to 3000 hours in 730°C steam for 2541 and 1541 alloys compared to six commercial alloys

---

* "Third Annual Report – High-Temperature Materials and Reactor Component Development Programs, Volume II – Materials," GE-NMPO, GEMP-270B, February 28, 1964, p. 117.

Several Fe-Cr-Al-Y alloys (2541, 1541, 1041, and 0561) are being tested in steam at 550°, 730°, and 1100°C for comparison with air-oxidation tests. Based on results after 1000 hours, these alloys are equal in corrosion resistance at 1100°C. All exhibit a duplex oxide consisting of an inner layer of α-Al_2O_3 and an outer layer of Fe-aluminate. During oxidation in air only the α-Al_2O_3 surface oxide is formed. The weight gain in steam is greater than in air; the reasons for the difference have not been determined.

Steam corrosion tests at 550°C and 730°C indicate a dependence on chromium and aluminum contents. After 3000 hours at 550°C, the 1541 alloy exhibited formation of Fe_2O_3 oxide particles while the 2541 alloy exhibited negligible corrosion. The 1541 alloy, when pre-oxidized at 980°C, exhibited negligible corrosion in subsequent tests at 550°C. These results are demonstrated in Figure 7.16. Pre-oxidation in air at high temperature is effective in preventing low-temperature steam corrosion not only of the 1541 alloy but also the lower Cr-content alloys, 1041 and 0561.*

COOPERATIVE TESTING AT GE-APED

Specimens of 2541 alloy were tested at GE-APED for 4714 hours in 620°C superheated steam containing 20 ppm oxygen and 2.5 ppm hydrogen at a velocity of 20 fps and a pressure of 670 atmospheres. The data, based on a metal loss technique,† indicate that the alloys are more resistant to steam corrosion than Incoloy 800 alloy by a factor of about four.

Tensile properties measured at GE-APED showed that exposure to steam had little or no effect on either tensile strength or ductility.†

7.5 SUMMARY AND CONCLUSIONS

Fe B Cr

The 10,000-hour test program for Fe-Cr-Al-Y-clad Fe-UO_2 and Cr-UO_2 capsule specimens has progressed beyond 5000 hours at 950°C and 3000 hours at 1100°C for several fuel element systems. Sufficient out-of-pile data were obtained to show that the Fe B Cr Fe-Cr-Al-Y cladding not only is compatible with UO_2 but also has excellent oxidation resistance to high-temperature air. A series of in-pile tests of the 2541-clad Fe-UO_2 system will be conducted to determine the stability of this fuel element material under conditions of high burnup.

Cladding alloys containing 15 to 25 weight percent chromium are applicable for service temperatures above 520°C. At lower temperatures, embrittlement caused by α' precipitation will occur and alloys with lower chromium contents are desirable. For service in steam atmospheres at low temperatures, the alloys with low chromium content can be pre-oxidized at higher temperatures to improve corrosion resistance. The alloys with low chromium content are less resistant to steam corrosion than those with high chromium content. The presence of yttrium, while necessary for corrosion resistance, is detrimental to the impact properties of the alloys. Small additions of niobium and molybdenum are effective high-temperature strengtheners; however, they do not increase the high-temperature strength to the level of the austenitic stainless steels, such as Type 304 stainless steel.

to p 219

A theoretical explanation for the ductilizing effect of Re and Ru on Cr-base alloys was developed. The essential feature is removal of interstitial elements from the matrix by Re-induced clustering.

Initial experiments exposing pure chromium to steam at 1100°C indicate that nitrification should not be a problem in application of chromium-base alloys in steam-cooled components.

---

*"High-Temperature Materials Program Progress Report No. 43, Part A," GE-NMPO, GEMP-43A, January 29, 1965, pp. 21–23.

†"High-Temperature Materials Program Progress Report No. 41, Part A," GE-NMPO, GEMP-41A, November 30, 1964, pp. 23–25.

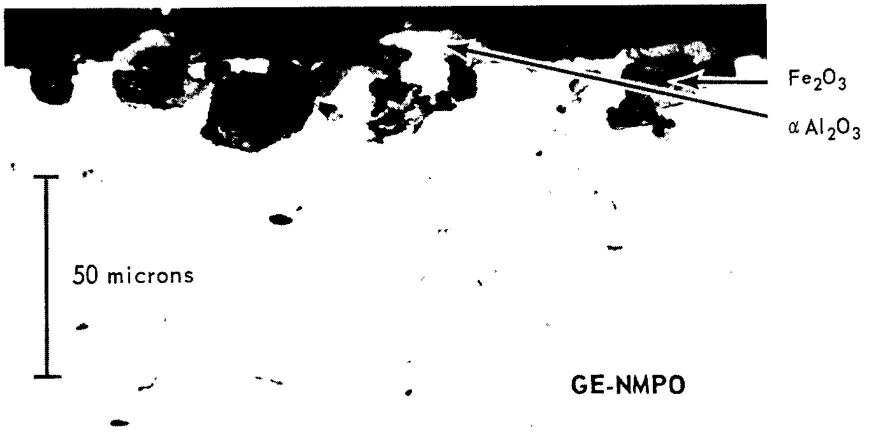

1541 Alloy, Untreated
(Neg. 4992)

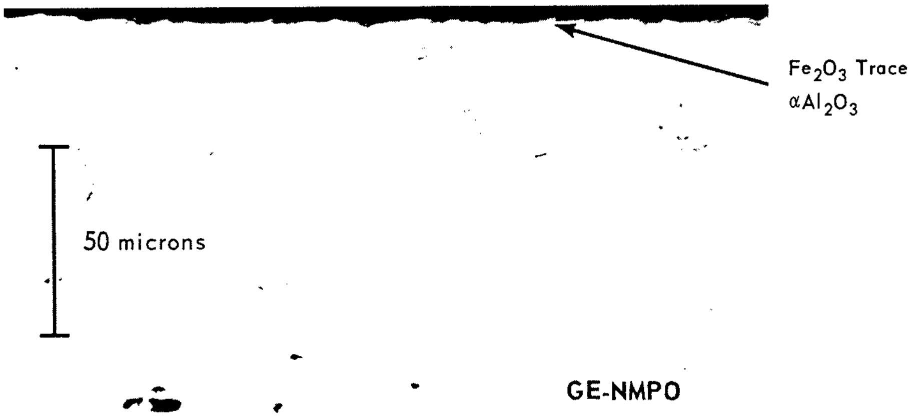

1541 Alloy, Pre-oxidized for
125 hours at 980°C
(Neg. 4993)

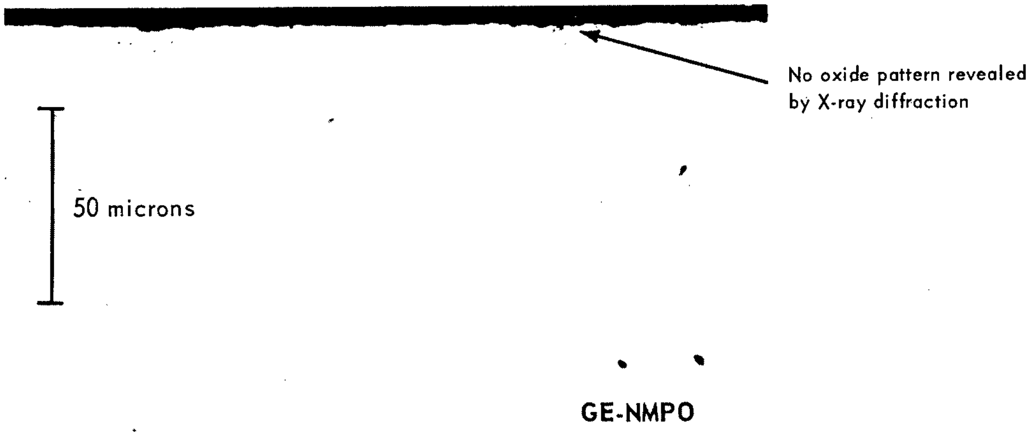

2541 Alloy, Untreated
(Neg. 4996)

Fig. 7.16 – Photomicrographs of superheat steam corrosion specimens of 1541 and 2541 alloys after 3000 hours in 550°C steam showing improved corrosion resistance of 1541 alloy by pre-oxidation. Oxides were identified by X-ray diffraction analyses.
(As-polished, 500X)

7.6 PLANS AND RECOMMENDATIONS

Laboratory testing of Fe-Cr-Al-Y-clad fueled specimens will be continued for times up to 10,000 hours at temperatures of 950°C and 1100°C in air with periodic analyses for uranium diffusion through the cladding. All specimens will be evaluated after their scheduled test period by metallographic and electron microprobe analyses. The program will be expanded to include testing of more promising fuel - cladding combinations in superheated steam.

A series of in-pile tests will be conducted to determine the effects of nuclear burnup and irradiation on the Fe-Cr-Al-Y-clad fuel elements at elevated temperatures in air.

The iron-base compositions developed to date will be fully evaluated for air- and steam-corrosion resistance for times up to 10,000 hours at temperatures from 450° to 1100°C. The effect of pre-oxidation treatments on steam-corrosion resistance will be evaluated, including possible effects of plastic strain on oxide adherence. Improvements in the strength of iron-base alloys will be attempted by dispersion-strengthening of the matrix. The effects of yttrium content on corrosion resistance, weldability, and notched impact properties will be determined. The properties of the 2541 and 1541 alloys will be investigated further.

Determining the mechanism by which Re and Ru improve the ductility of Cr is of primary importance because it will guide future Cr-base alloy development. Alloys in the Cr-Ru alloy system will be evaluated in an aging study to determine the credibility of the clustering theory.

Further experiments on the behavior of chromium-base alloys in steam atmospheres will be conducted.

8. HIGH-TEMPERATURE THERMOCOUPLE AND ELECTRICAL MATERIALS RESEARCH

(57014)

The objective of this program is to identify and establish the properties of reliable high-temperature thermocouples and electrical and electronic materials to provide instrumentation and electrical components for long-life, high-temperature reactors and reactor experiments.

PS 231

This task was initiated in Fiscal Year 1965, but a portion of the program was a continuation of a section of a previous task (Direct-Conversion High-Temperature Materials Research, 57011) which was terminated at the end of Fiscal Year 1964. To preserve technical continuity, that portion of the work continued is reported herein.

8.1 HIGH-TEMPERATURE THERMOCOUPLE DEVELOPMENT

The high-temperature thermocouple development effort is directed toward finding refractory-metal thermoelectric alloys that have higher thermoelectric outputs, greater sensitivity (microvolts/°C), better mechanical properties, and are more thermoelectrically stable in a high-temperature nuclear environment than present systems.

W - Tc ALLOYS

The thermoelectric output of technetium and W - 5Tc[*], previously reported,[†] showed W - 5Tc to have a higher thermoelectric output than tungsten or W - 5Re. Additional W-Tc alloys with additions of 3, 7, and 25 atomic percent Tc were studied. The fabrication procedure, previously described,[†] involved mixing -325 mesh powders, isostatically pressing into rods, and sintering.

Thermoelectric properties as a function of technetium content at temperatures ranging from room temperature to 2500°C are shown in Figure 8.1. Also included for comparative purposes are measured emf values for pure technetium and commercial tungsten wire. All alloys were referenced against commercial W - 26Re (wt %) wire.

Thermoelectric output of W - 3Tc appeared to be very close to the maximum positive thermoelectric output for W-Tc alloy systems. At 2000°C, thermoelectric output of W - 3Tc versus W - 26Re was approximately 5 millivolts higher than tungsten. Increasing the percentage of technetium in tungsten resulted in a steadily decreasing thermoelectric output relative to W - 26Re (wt %).

As can be seen in Figure 8.1, the 25 atomic percent technetium addition to tungsten did not suppress thermoelectric output as much as similar additions of rhenium to tungsten. As indicated in the figure, a thermocouple prepared from two W-Tc alloys would not produce as much thermoelectric output as that obtained from a W / W - 26Re

[*] Compositions in this section are in atomic percent unless otherwise noted.

[†] "High-Temperature Materials Program Progress Report No. 31, Part B," GE-NMPO, GEMP-31B, January 24, 1964, p. 61.

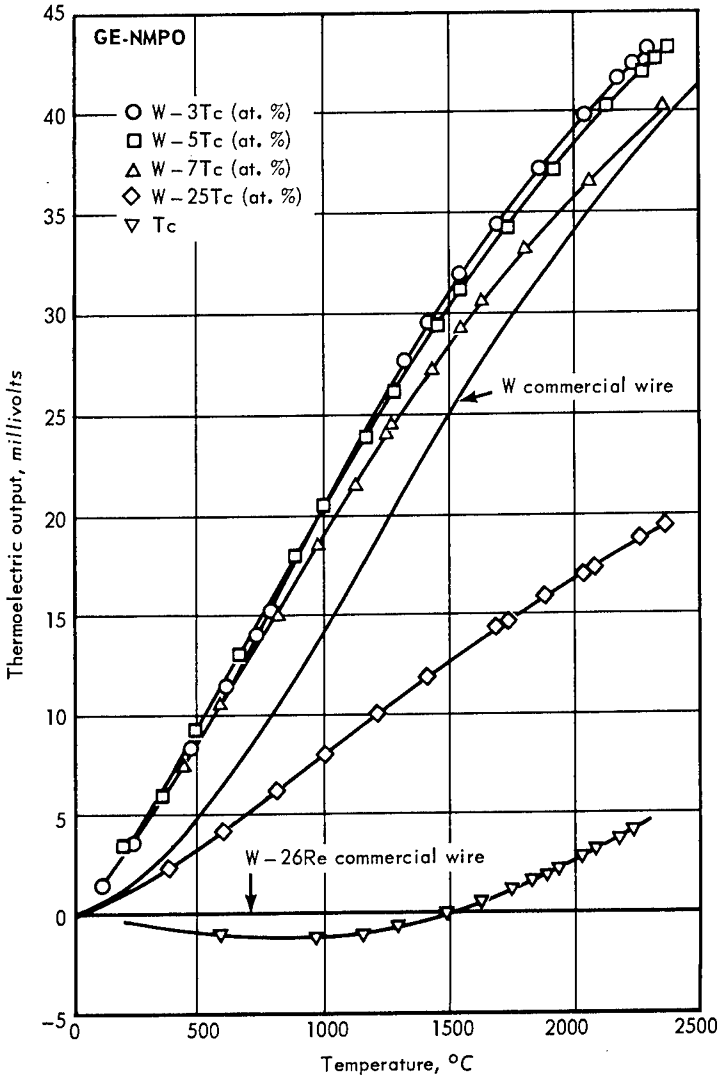

Fig. 8.1 – Comparison of thermoelectric output as a function of temperature for a series of W-Tc alloys versus W – 26Re commercial wire

(wt %) thermocouple. However, a W - 3Tc (at. %) / W - 26Re (wt %) thermocouple will produce a greater thermoelectric output. Phase diagrams presently available* indicate that not much more than 25 atomic percent technetium can be added to tungsten before producing a multiphase structure which would be thermoelectrically undesirable and of considerably lower melting point. Metallographic evaluation showed that W-Tc alloys (3, 5, 7, and 25Tc) were all single phase. In contrast to the good ductility of pure technetium, rods of these alloys did not exhibit any perceptible ductility in simple bend tests. Apparently, adding relatively ductile technetium does not increase the ductility of tungsten. Technetium as a substitute for rhenium in tungsten alloys could prove to be useful primarily because it has a lower thermal neutron cross section (85 barns for rhenium versus 22 for technetium). Transmutation of technetium into ruthenium does occur in a thermal neutron reactor but at a much lower rate than rhenium transmutes into osmium and, therefore, may exhibit less change in thermoelectric output as a function of neutron dosage.

*L. Brewer, "Prediction of High-Temperature Metallic Phase Diagrams," University of California, UCRL-10701, July 1963, p. 87.

W-Os ALLOYS

Tungsten alloys containing low osmium concentrations were investigated for several reasons. Under nuclear radiation, tungsten transmutes slowly into osmium, which affects thermocouple emf calibration as a function of temperature. To measure the effect of these transmutations, a study on various W-Os compositions was undertaken. For nuclear applications, osmium with its lower thermal neutron cross section might prove to be a better additive than rhenium in tungsten alloys.

Thermoelectric output of three W-Os alloys (0.5, 1, and 3Os) referenced to commercial W - 26Re (wt %) wire is shown in Figure 8.2 together with the previously determined output for pure osmium and commercial tungsten. Small additions of osmium to tungsten caused thermoelectric output to increase significantly, which suggests a possible

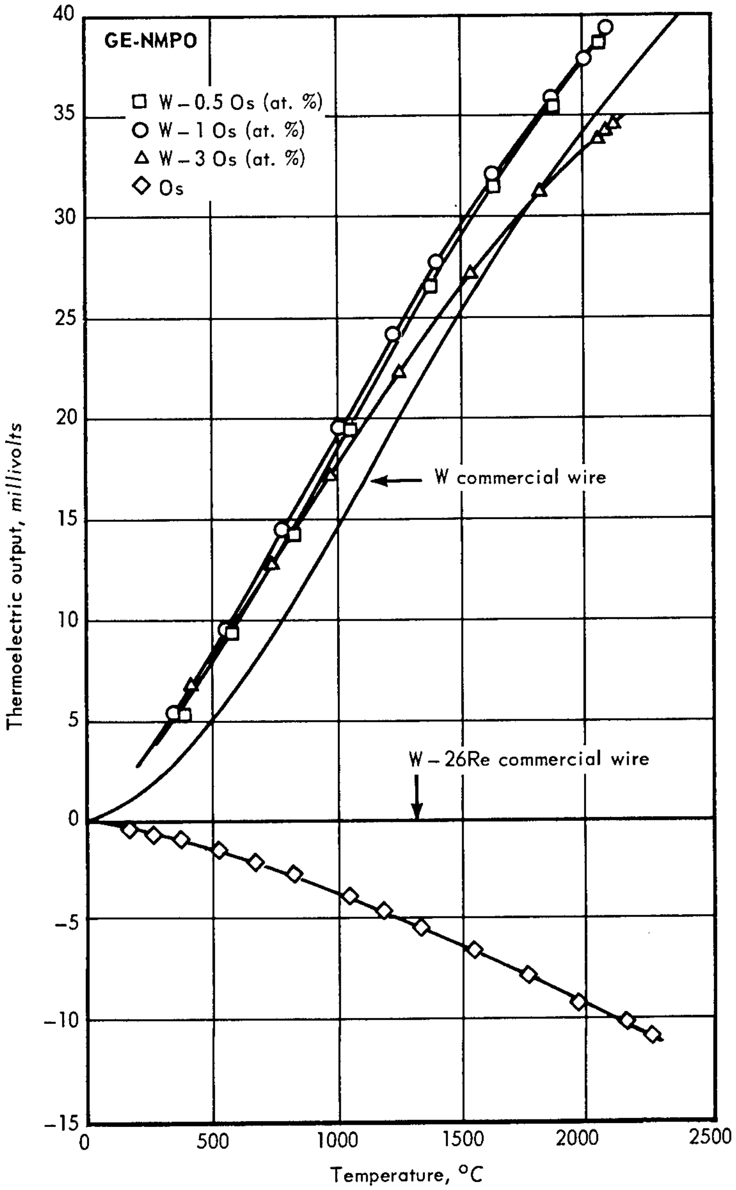

Fig. 8.2 – Comparison of thermoelectric output as a function of temperature for a series of W-Os alloys versus W – 26Re commercial wire

rapid change in W / W - 26Re (wt %) thermocouple calibration in a nuclear environment. A 0.5 atomic percent osmium addition to tungsten changed the thermoelectric output 3 to 4 millivolts, or approximately 200°C from that found for a W / W - 26Re (wt %) thermocouple. The curve of W - 0.5Os / W - 26Re (wt %), is very close to being linear over the temperature range of 25° to 2000°C.

Curves for W - 0.5Os and W - 1Os alloys are nearly identical. This suggests the addition of 0.5 Os to tungsten might aid in stabilizing a drift in the thermoelectric output of W / W - 26Re (wt %) when used for monitoring temperatures of long-time in-pile tests.

Re-Os ALLOYS

Rhenium alloys containing various concentrations of osmium were investigated to determine the effect that osmium has on thermoelectric output of rhenium as a function of temperature. Figure 8.3 shows the family of curves for this system. Thermoelectric outputs of Re-Os alloys up to 20 weight percent osmium are displaced slightly in a positive direction from the pure rhenium curve, whereas the output of 50 and 95 weight percent osmium alloys decreased toward the osmium curve. Since rhenium transmutes into osmium in a thermal neutron reactor, these characteristics may be useful in predicting thermoelectric changes.

W-Mo-Re ALLOYS

A number of W-Mo-Re alloy compositions made under a separate task remained ductile even after exposure to very high temperatures. Because ductility is important for thermocouple systems, these materials were tested for their thermoelectric output. The four alloys tested were W - 30Mo - 30Re, W - 20Mo - 30Re, W - 10Mo - 30Re, and W - 30Re.

Emf outputs of W-Mo-Re alloys relative to W - 25Re (wt %) commercial wire are shown in Figure 8.4. The substitution of molybdenum for tungsten did not significantly change any of the thermoelectric properties. These alloys have no thermoelectric advantage over W - 25Re (wt %).

8.2 THERMOELECTRIC OUTPUT CHANGES OF W / W - 25Re THERMOCOUPLES DUE TO NUCLEAR TRANSMUTATION

The need for accurate temperature measurements in nuclear reactors makes it necessary to determine any changes in emf response due to the transmutation in thermocouple systems.

The actual degree of change in emf output of a thermocouple caused by transmutation is difficult to assess because of the large number of variables involved. Important considerations are dosage, flux, and the relation of the flux gradient to temperature gradient along the thermocouple lead wires. The synthetic method of evaluating thermocouple errors, described below, was designed to give the maximum error possible under the assumed flux conditions.

Transmutation effects were investigated on W / W - 25Re (wt %) thermocouples because this is the most commonly used alloy for very high-temperature nuclear reactor experiments. Alloys representing the transmuted materials of tungsten and W - 25Re (wt %), after exposure to a 10^{14} thermal neutron flux environment for 0.5, 1, 3, and 6 months, were fabricated as 3-mm-diameter rods using techniques similar to those described previously.* The synthesized compositions were based on calculations established by Browning and Miller.† Thermoelectric properties were measured using a high-temperature

---

*"High-Temperature Materials Program Progress Report No. 27, Part B," GE-NMPO, GEMP-27B, September 30, 1963, pp. 69–70.

†W. E. Browning, Jr., and C. E. Miller, Jr., "Calculated Radiation Induced Changes in Thermocouple Operation," *Temperature: Its Measurement and Control in Science and Industry*, Vol. 3, Part 2, Reinhold, London, 1962, p. 271.

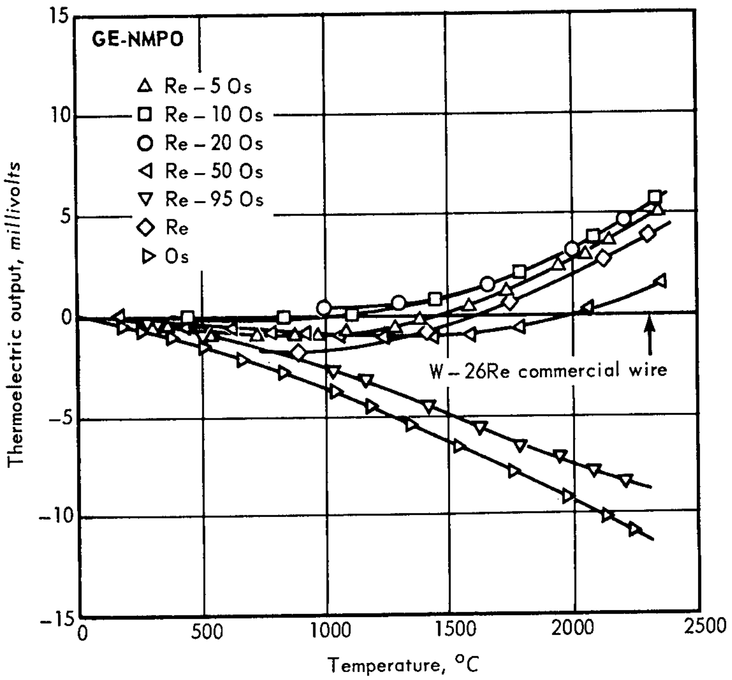

Fig. 8.3 – Comparison of thermoelectric output as a function of temperature for a series of Re-Os alloys versus W – 26Re commercial wire

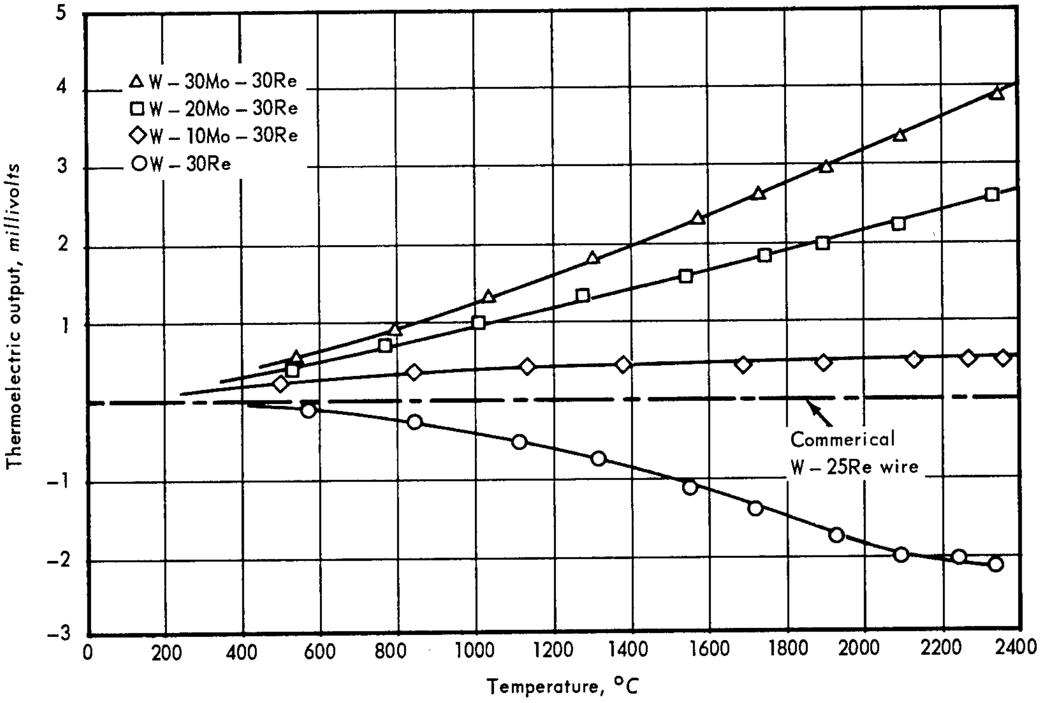

Fig. 8.4 – Comparison of thermoelectric output as a function of temperature for a series of W-Mo-Re alloys versus W – 25Re commercial wire

electrical resistance furnace as a heat source. All testing was done under a hydrogen or inert gas atmosphere. Since the rods were made to represent the transmuted compositions all along their length, the maximum thermoelectric errors were measured.

The thermoelectric output of the alloys representing transmuted tungsten and W - 25Re materials was compared with the output of untransmuted tungsten and W - 25Re materials, respectively.* The difference in outputs, which represented the error of the W / W - 25Re (wt %) thermocouple due to nuclear transmutation, is plotted in Figure 8.5 as a function of temperature.

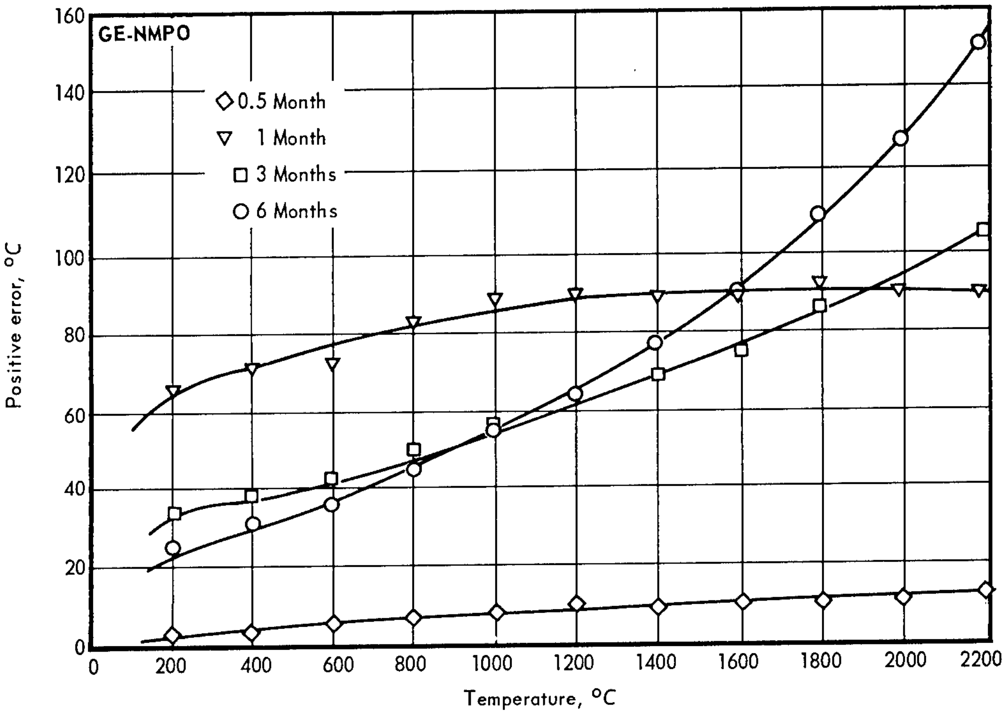

Fig. 8.5 – Deviation from initial calibration in degrees centigrade of a W / W – 25Re thermocouple alloyed to represent a transmuted composition after 0.5, 1, 3, and 6 months in a 10^{14} neutron thermal flux

An isothermal plot of the errors developed as a function of time at selected temperatures (Figure 8.6) presents a clearer picture of the effects of transmutation. The initial rapid increase in error was caused by the thermoelectric sensitivity of the tungsten leg to small amounts of rhenium additions. The data indicate that transmutation effects should be carefully considered when using W / W - 25Re (wt %) thermocouples in thermal neutron reactors.

8.3 HIGH-TEMPERATURE ELECTRICAL INSULATION MATERIALS

Thermocouple systems require materials that electrically insulate the two thermoelements from each other. Materials must be nonreactive with the thermoelements and also prevent electrical currents from passing between the two legs. Oxides of aluminum, magnesium, beryllium, and thorium are commonly used for this purpose. The melting point of Al_2O_3 is relatively low (2000°C), MgO decomposes at approximately 2200°C, and

---

* "High-Temperature Materials Program Progress Report No. 43, Part A," GE-NMPO, GEMP-43A, January 29, 1965, pp. 71–72.

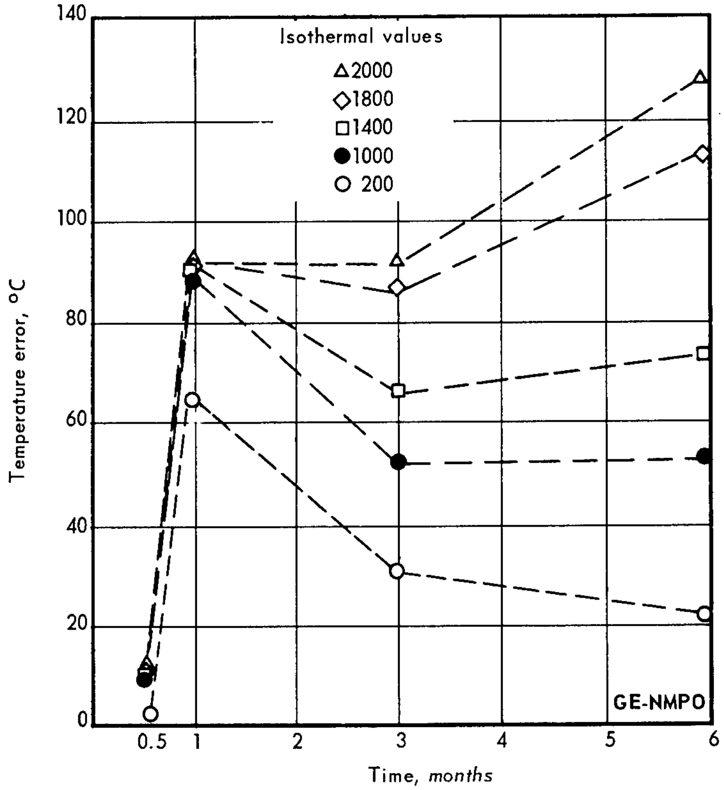

Fig. 8.6 – Expected temperature errors as a function of time resulting from transmutations of W / W – 26Re thermocouples

ThO_2 and BeO become electrically conductive above 2260°C and 2370°C, respectively, so that thermocouple errors become quite large. An insulator which can perform satisfactorily in a thermocouple system above 2500°C is essential for temperature measurements of advanced fuel elements now under development.

Most of the rare earth oxides melt below 2500°C but may be combined with higher melting oxides to produce materials possibly capable of higher temperature applications than those now available. The resistivity of oxides is dependent on a number of factors.* Some of these are: (1) temperature, (2) structure of material (single crystal or multigrained, grain size, and density), (3) chemical purity, (4) environment (vacuum, reducing, neutral or oxidizing, and furnace contamination, (5) method of measurement (four- or two-probe method, use of a-c or d-c, value of applied voltage, and time applied), and (6) change in composition with time (loss of oxygen to form suboxides). Careful control is therefore necessary to obtain meaningful results.

A schematic drawing of the resistivity-measuring circuit used is shown in Figure 8.7.. The four-probe method of measuring resistance was used to eliminate contact and lead resistance as much as possible. Fast simultaneous measurements of current and voltage were taken with a multichannel magnetic oscilloscope. Initial values of current and voltage were used to compute resistance and resistivity of the sample material, since these values would be unaffected by polarization and electrolysis effects, which are a function of the time of application of the applied d-c voltage. An a-c voltage, which would eliminate polarization effects, was not used since thermocouples generate a direct voltage.

*Julius Cohen, "Electrical Conductivity of Alumina," *Bulletin of American Ceramic Society*, Vol. 38, January – December 1959.

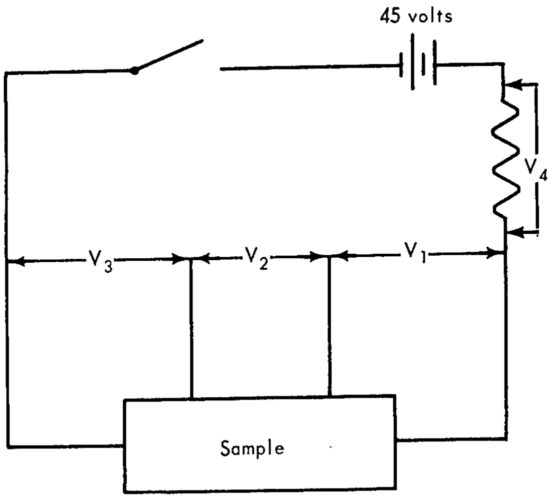

a. Schematic of apparatus

Fig. 8.7 – Schematic drawing of the electrical circuitry of the four-probe method used in making resistivity measurements on ceramic oxides

Resistance measurements were made by raising the temperature of the sample gradually in 100°C steps. After a reading was taken, the temperature was lowered to the previous value of temperature to determine if any change from the previous electrical measurement had occurred in the sample.

Electrical resistance between open-circuited electrodes in helium at high temperature was determined as a function of temperature and as a function of voltage between electrodes. For a value of sample resistance to be considered meaningful, it was arbitrarily decided that it should be less than 10 percent of open-circuited resistance.

A sample of Y_2O_3 was prepared from high-purity Y_2O_3 powders isostatically pressed into rods about 1.25 cm in diameter. These rods were presintered in air at 1000°C for 2 hours, followed by a 1700°C high-temperature treatment in hydrogen for 3 hours, and a final treatment in air for 1 hour at 1370°C. Final Y_2O_3 density was 97 percent of theoretical. The rods were then cut into 3-cm lengths and ground to 1 cm in diameter. Sample ends were tapered for increased electrical contact with the molybdenum electrodes. Two small holes were drilled 1 cm apart near the midsection of samples to facilitate attachment of 0.5-mm rhenium wires. This provided a means for measuring voltage across the three sample sections.

Figure 8.8 shows a plot of specific electrical resistivity of Y_2O_3 from 1600°K to approximately 2500°K in a helium atmosphere. Since the curve is a straight line on a log resistivity versus reciprocal absolute temperature scale, the resistivity can be expressed by equation (8.1):

$$\rho = A \exp \frac{E}{kT} \tag{8.1}$$

where

ρ is resistivity,
A is a constant,
E is an activation energy,
k is Boltzman's constant, and
T is absolute temperature.

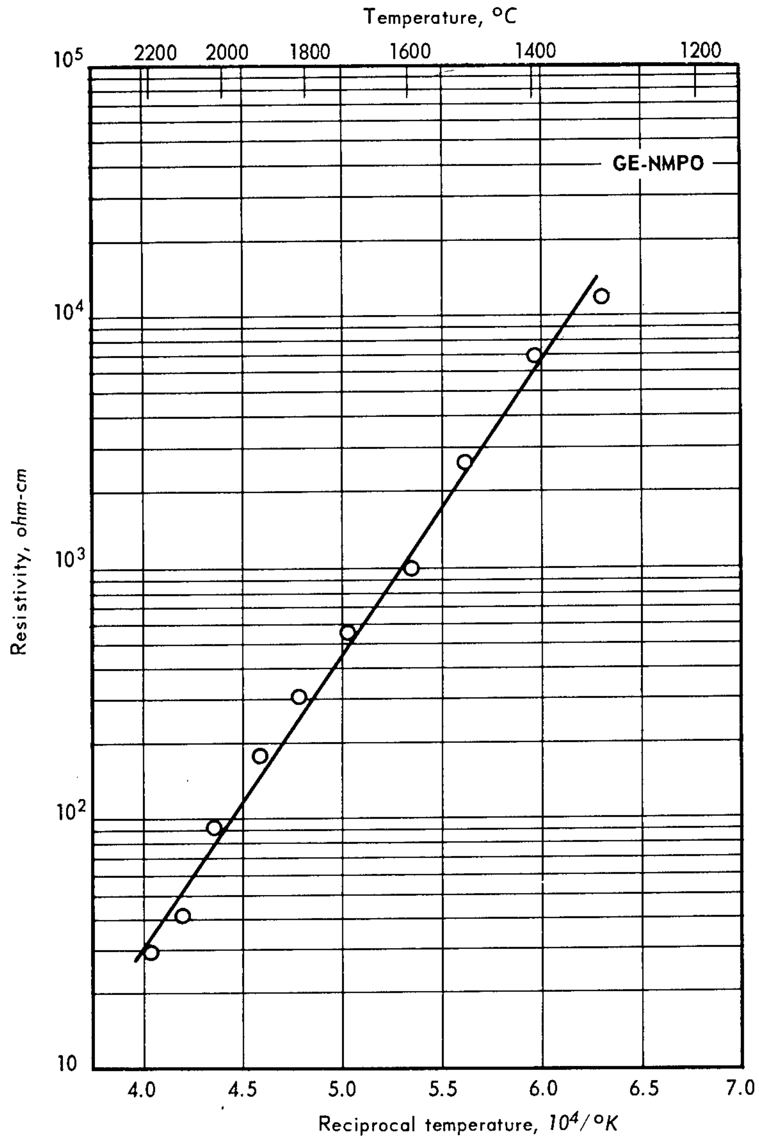

Fig. 8.8 – Resistivity of Y_2O_3 in helium as a function of reciprocal temperature

The straight line slope of the electrical resistivity curve over the temperature range measured suggests that the material acted as a simple intrinsic semiconductor. An interesting phenomenon occurred when hydrogen of unknown dewpoint was substituted for helium. The resistivity was reduced by approximately 50 percent of the value found in helium at 1600° to 1700°C. At 1200°C the resistance was somewhat higher in hydrogen.

The electrical resistivity of ThO_2 in helium and hydrogen was studied to ascertain if similar anomalies would be observed. Specimens were prepared from commercial powders cold-pressed into 1-cm OD by 4-cm-long rods at 2100 kg/cm^2, sintered in hydrogen at 2200°C for 2 hours, and then air-fired for 5 hours at 1400°C to remove carbon and fully oxidize any thorium that might have been produced during the hydrogen sintering cycle.

Tests were run so that hydrogen and helium were alternately changed at temperature. The resistivity of ThO_2 from 1400° to 2200°C in hydrogen and helium at atmospheric pressure is plotted in Figure 8.9 on a log resistivity versus reciprocal absolute temperature scale. Resistivity curves are almost parallel over the temperature range measured but differ by approximately a factor of ten. The literature resistivity curve, indicated in

Figure 8.9, was the same in both hydrogen and helium and correlates with the experimental data obtained in hydrogen.

Preliminary tests were run to check qualitatively if the resistivity of ThO_2 varied with oxygen partial pressure. A ThO_2 sample heated to 1800°C in flowing dry hydrogen of approximately -40°C dewpoint exhibited a resistivity value of 18 ohm-cm. When the dewpoint of inlet hydrogen was increased by passing the gas over water at 24°C at atmospheric pressure before entering the high-temperature furnace, the resistivity value increased in a few minutes to 70 ohm-cm. When dry hydrogen was again switched into the system, resistivity gradually decreased to the original 18 ohm-cm value. Since the only essential difference in the atmosphere as far as ThO_2 was concerned was the partial pressure of oxygen, it was concluded that electrical resistivity is sensitive to oxygen partial pressure.

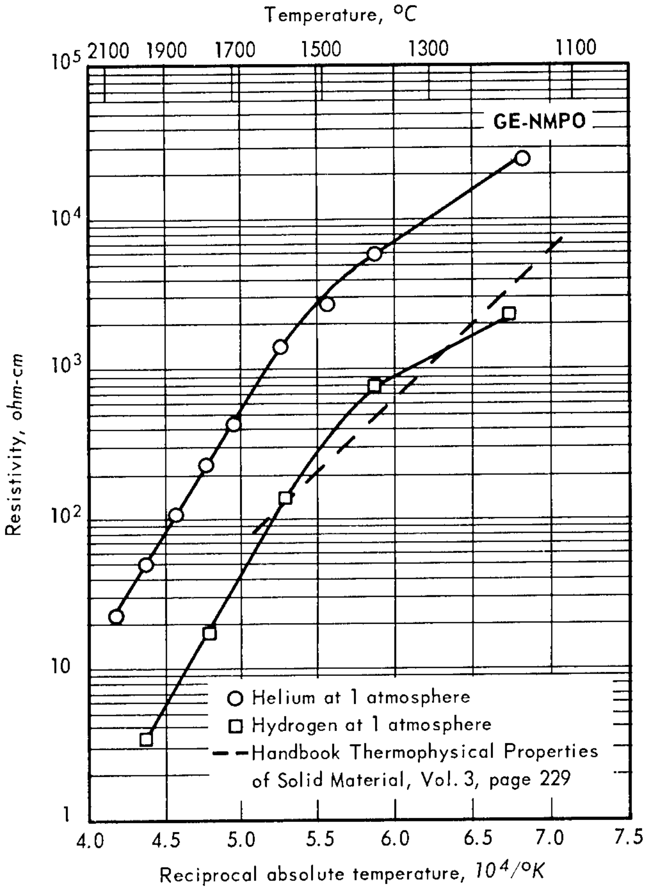

Fig. 8.9 – Electrical resistivity of ThO_2

8.4 HIGH-TEMPERATURE METAL-TO-CERAMIC SEAL

Gas-tight, high-temperature (1600°C), metal-to-ceramic seals have many potential applications in various nuclear energy activities as well as in other fields requiring electrically insulated lead-ins to hot gaseous or vacuum environments. High-temperature pressure-bonding techniques were investigated as a method for the fabrication of metal-to-ceramic seals. Metal and ceramic components were forced into intimate contact under high temperature and pressure so that they remain as an integral body.

As previously reported,* good metal-to-ceramic seals were formed between niobium and either Y_2O_3 or Lucalox† Al_2O_3 using a gas pressure of 700 kg/cm^2 at 1650°C for 1 hour. Additional work on Nb - Lucalox bonds involved bond strength testing, diffusion studies, and the use of transitional interfaces.

STRENGTH OF Nb - LUCALOX BONDS

A Nb - Lucalox bond was tensile-tested at room temperature. The bond was of flat geometry with 0.25-mm-thick niobium plates bonded to the 1.25-cm-diameter flat faces of a 3-mm-thick Lucalox disc. Aluminum pull rods were bonded with an organic bonding agent to each niobium plate. The organic bond failed under a stress of 8.1 kg/cm^2, indicating that the tensile strength of the seal exceeded this value.

A peel test was made by stripping 0.25-mm-thick niobium from the Lucalox surface of a Nb - Lucalox bond. Distinct cracking sounds were heard during peeling. Microscopic examination of the peeled metal strip showed that approximately 20 percent of the fracture surface area occurred through the Lucalox grains.

DIFFUSION STUDIES OF METAL-TO-CERAMIC BONDS

An electron microprobe analysis was made of the bonded interface area of a Nb - Lucalox seal to determine the nature of the metal-to-ceramic bond obtained by the high-temperature gas-pressure-bonding process. The seal was prepared in a cylindrical configuration with a 0.25-mm wall of niobium bonded to the inside and outside surfaces of a Lucalox tube (1.58 cm OD with a 1.57-mm wall). Following the bonding operation, the specimen was thermally treated at 1700°C for 6 hours in argon at ambient pressure to compare the interdiffusion area developed at the metal-to-ceramic interface as a function of time.

An electron microprobe trace and interface photomicrograph are shown in Figure 8.10. A diffusion zone approximately 10 microns wide was indicated. The electron microprobe trace of an as-bonded sample‡ showed a cross-diffusion zone of approximately 5 microns into each base material. The presence of a diffusion zone and increase in this zone upon heating for 6 hours at 1700°C showed that a diffusion bond and not merely a mechanical bond was achieved.

BONDING WITH TRANSITIONAL INTERFACE

The stability of metal-to-ceramic seals can be improved by the use of a transitional interface which would lower interface stresses due to thermal expansion differences and thermal gradients.

A high-temperature gas-pressure-bonding process was particularly successful in the formation of graded regions between niobium and Lucalox alumina. Addition of thin layers of mixed powders of niobium and sapphire (Al_2O_3) containing a small amount of MgO to develop a graded zone at the interface of niobium and Lucalox resulted in metal-to-ceramic seals of good strength and stability. An addition of MgO was used to promote sintering and control sapphire grain size.

Figure 8.11 is a photomicrograph showing the interface of a bond between niobium and Lucalox having a 0.25-mm zone of Nb - 50 volume percent mixture of Linde A sapphire plus 0.5 weight percent MgO adjacent to the niobium and a 0.05-mm zone of Linde A sapphire plus 0.5 weight percent MgO between the conglomerate region and the Lucalox. The seal, formed by bonding under a 700 kg/cm^2 pressure at 1650°C for 1 hour, was tested for thermal stability by exposing

---

*"Third Annual Report – High-Temperature Materials and Reactor Component Development Programs, Volume II – Materials," GE-NMPO, GEMP-270B, February 28, 1964, pp. 208–211.

†Trademark of the General Electric Company for commercial polycrystalline alumina.

‡"High-Temperature Materials Program Progress Report No. 35, Part B," GE-NMPO, GEMP-35B, May 28, 1964, p. 93.

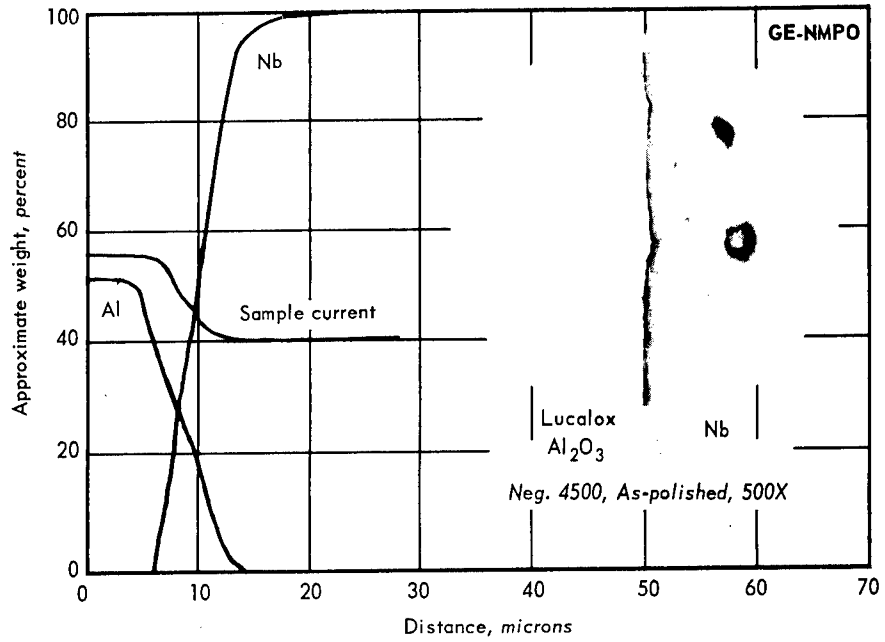

Fig. 8.10 – Electron microprobe trace and photomicrograph of the interface formed between Lucalox and Nb after bonding at 700 kg/cm^2 and 1650°C for 1 hour followed by heating for 6 hours at 1700°C at ambient pressure

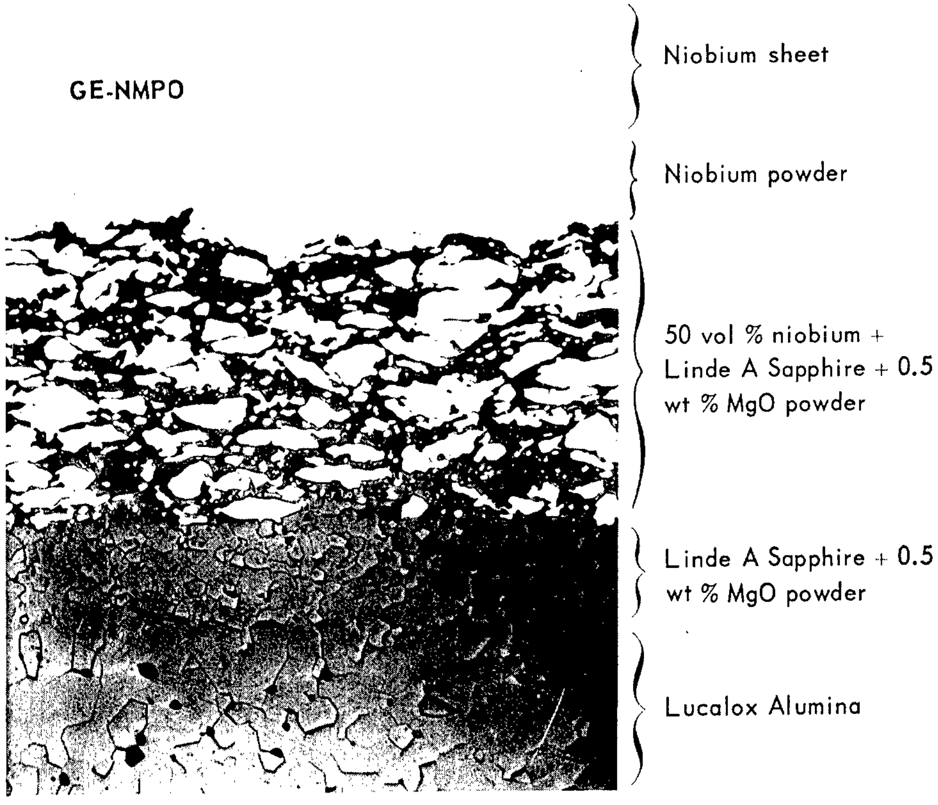

Fig. 8.11 – Photomicrograph of the ceramic-to-metal interface of a seal bonded with 700 kg/cm^2 at 1650°C for 1 hour followed by 466 hours at 1600°C *(Neg. 5155, as-polished, 150X)*

it for 466 hours at 1600°C in argon at ambient pressure with two returns to room temperature. Metallographic examination of the graded zone interface region after thermally testing showed no apparent defects with virtually perfect bonding observed throughout the region.

Figure 8.12 shows photographs of graded Nb - Lucalox seals formed by high-temperature gas-pressure-bonding under 700 kg/cm^2 pressure at 1650°C for 1 hour. The intact seal was found to be vacuum tight using the helium mass spectrometer (sensitivity 10^{-10} cm^3 air STP/sec)

8.5 SUMMARY AND CONCLUSIONS

Thermoelectric output as a function of composition and temperature for W-Tc, W-Os, Re-Os, and W-Mo-Re alloys was determined, and the W-Os showed some advantages for special applications.

Studies were performed on a W / W - 25Re thermocouple system to determine the effect of nuclear transmutation on thermoelectric outputs as a function of temperature. With the

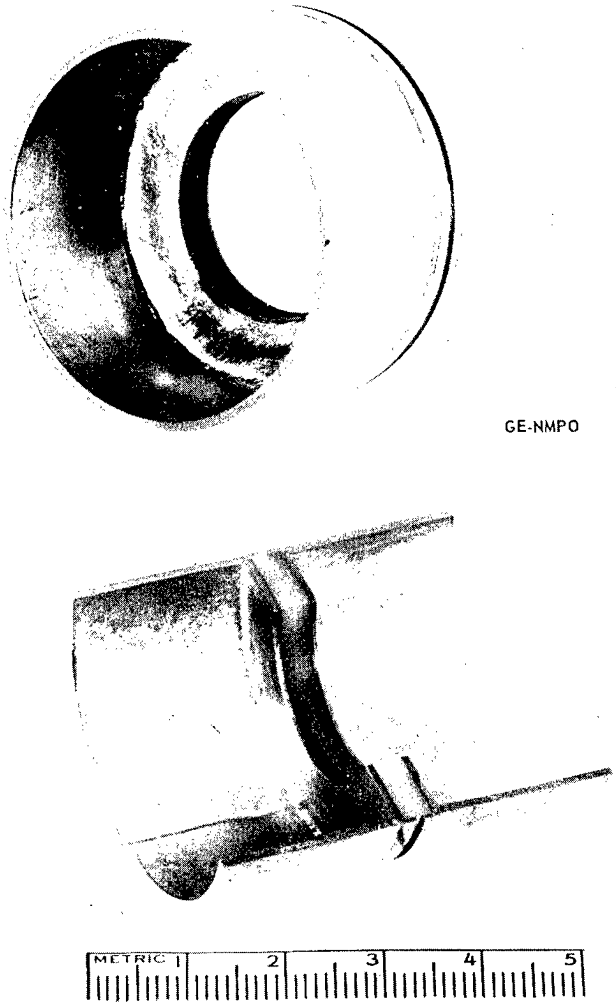

Fig. 8.12 – Photographs of a niobium-to-Lucalox graded metal-to-ceramic seal after autoclaving under 700 kg/cm^2 pressure at 1650°C. Note the sectioned specimen showing the position of the Lucalox. *(Negs. P64-11-26B, P64-11-26A)*

use of synthesized alloy composition, a positive error of approximately 100°C may be expected in a relatively short exposure time (1 month at 10^{14} thermal neutron flux) due to transmutation.

Electrical resistivity measurements on ThO_2 and ceramic oxides showed that high-temperature electrical resistance was strongly affected by oxygen partial pressure of the protective atmosphere surrounding the specimen.

Gas-tight, high-temperature (1600°C), metal-to-ceramic seals, prepared using high-temperature gas-pressure-bonding techniques, had good bond strength in tension (> 8.1 kg/cm^2) and exhibited excellent stability for 466 hours at 1600°C with two returns to room temperature.

End

8.6 PLANS AND RECOMMENDATIONS

Further alloy development studies will be conducted on various refractory-metal systems in an effort to develop thermocouple elements with greater sensitivity and resistance to changes of calibration resulting from nuclear transmutation.

In-pile experiments will be conducted in the ETR on W / W - 25Re (wt %) thermocouples with emphasis on calibration changes as a function of time and thermal neutron flux.

Continued experimentation will be carried out for measuring electrical resistance of ceramic oxides as a function of temperature and applied voltage in various atmospheres.

Pertinent mechanical and metallurgical operating characteristics will be determined on metal-to-ceramic seals. Testing procedures will be devised to correspond with anticipated operation conditions.

APPENDIX

REPORTS ISSUED DURING CALENDAR YEAR 1964

PROGRESS REPORTS

GEMP-270A
Third Annual Report - High-Temperature Materials and Reactor Component Development Programs, Volume I - Materials, February 28, 1964.

GEMP-270B
Third Annual Report - High-Temperature Materials and Reactor Component Development Programs, Volume II - Materials, February 28, 1964.

GEMP-270C
Third Annual Report - High-Temperature Materials and Reactor Component Development Programs, Volume III - Reactor Components Development, February 28, 1964.

METALLURGY

GEMP-31A and B
High-Temperature Materials Program Progress Report No. 31, January 24, 1964.

GEMP-35, A and B
High-Temperature Materials Program Progress Report No. 35, May 28, 1964.

GEMP-37, A and B
High-Temperature Materials Program Progress Report No. 37, July 31, 1964.

GEMP-39, A and B
High-Temperature Materials Program Progress Report No. 39, September 30, 1964.

GEMP-41, A and B
High-Temperature Materials Program Progress Report No. 41, November 30, 1964.

CERAMICS

GEMP-34, A and B
High-Temperature Materials Program Progress Report No. 34, April 15, 1964.

GEMP-36, A and B
High-Temperature Materials Program Progress Report No. 36, June 19, 1964.

GEMP-38, A and B
High-Temperature Materials Program Progress Report No. 38, August 19, 1964.

GEMP-40, A and B
High-Temperature Materials Program Progress Report No. 40, October 15, 1964.

GEMP-42, A and B
High-Temperature Materials Program Progress Report No. 42, December 18, 1964.

INSTRUMENTATION AND CONTROLS

GEMP-81
Reactor Instrumentation and Control Progress Report No. 81, March 31, 1964.

GEMP-82
Reactor Instrumentation and Control Progress Report No. 82, May 27, 1964.

GEMP-83
Reactor Instrumentation and Control Progress Report No. 83, July 31, 1964.

GEMP-84
Reactor Instrumentation and Control Progress Report No. 84, September 30, 1964.

GEMP-85
Reactor Instrumentation and Control Progress Report No. 85, November 30, 1964.

TOPICAL REPORTS

J. F. White, E. F. Juenke, and D. E. Burgbacher, "The UO_2-UO_3-Y_2O_3 System and Evaluation of the $UO_{2.9} \cdot 3Y_2O_3$ Composition," GE-NMPO, GEMP-263, March 31, 1964.

E. F. Juenke, "A Review of Recent Research on Refractory-Metal Carbides and Borides," GE-NMPO, GEMP-267, August 11, 1964.

A. D. Feith, "A Radial Heat Flow Apparatus for High-Temperature Thermal Conductivity Measurements," GE-NMPO, GEMP-296, August 31, 1964.

R. L. Treinen, "Final Report, High-Temperature Extension of Conventional Nuclear Sensors," GE-NMPO, GEMP-298, August 10, 1964.

"Final Report, Circulating Ball Reactivity Control," GE-NMPO, GEMP-299, December 7, 1964.

C. S. Wukusick, "On the Mechanism of the Rhenium-Alloying-Effect in Group VI-A Metals," GE-NMPO, GEMP-314, November 20, 1964

INVENTION DISCLOSURES

There were 41 invention disclosures resulting from the High-Temperature Materials and Reactor Component Development Programs at GE-NMPO.

PAPERS PRESENTED DURING CALENDAR YEAR 1964

J. P. Clark and A. W. Bauer, "Electromagnetic Testing of Thin Wall Refractory Metal Tubing," for Presentation at National Convention of Society for Nondestructive Testing, Los Angeles, California, February 1965, GE-NMPO, TM 64-10-26.

J. B. Conway and R. A. Hein, "Enthalpy Measurements of Solid Materials to 2400°C by Means of a Drop Method," Presented at Fourth Annual Conference on Thermal Conductivity held at USNRDL, San Francisco, California, October 1964, GE-NMPO, TM 64-8-27.

W. D. Feith, "Thermal Conductivity of Several Ceramic Materials to 2500°C," Presented at Fourth Annual Conference on Thermal Conductivity held at USNRDL, San Francisco, California, October, 1964, GE-NMPO, TM 64-10-4.

R. Van Houten and W. G. Baxter, "Titanium, Zirconium and Yttrium Hydrides as Space Shielding Materials," AIAA Paper No. 64-362, 1st AIAA Annual Meeting, Washington, D.C., July 1, 1964.

J. C. Marshall, R. Van Houten, and W. G. Baxter, "10,000 Hour Demonstration of Clad Yttrium Hydride as a Neutron Moderator," Transactions, American Nuclear Society, Vol. 7, No. 1, June 1964, p. 123. (Presented at the 1964 ANS Annual Meeting, Philadelphia, June 17, 1964.)

S. F. Bartram, E. F. Juenke, and E. A. Aitken, "Phase Relationships in the UO_2-UO_3-Y_2O_3 System," Journal of American Ceramic Society, Vol. 47, No. 4, April 1964.

E. A. Aitken, S. F. Bartram, and E. F. Juenke, "Crystal Chemistry of the Rhombohedral $MO_3 \cdot 3R_2O_3$ Compounds," Inorganic Chemistry, Vol. 3, 1964, p. 949.

E. F. Juenke and S. F. Bartram, "Crystallographic Data on UO_2WO_4 and UO_2MoO_4," Acta Crystallographica, Vol. 17, Part 5, May 1964, p. 618.

E. A. Aitken, "Recent Experiments on the Non-stoichiometric Behavior of UO_2," Presented at NASA-AEC sponsored meeting on High Temperature Refractory Fuel Elements, ANL, March 1964, GE-NMPO, TM 64-4-5.

E. A. Aitken, "Thermodynamic Properties of Substoichiometric UO_2," Presented at United States - Japan Meeting on Ceramic Nuclear Fuels, Hanford, October 27-30, 1964, GE-NMPO, TM 64-10-11.

R. E. Fryxell and B. A. Chandler, "Creep, Strength, Expansion, and Elastic Moduli of Sintered BeO as a Function of Grain Size, Porosity, and Grain Orientation," Journal of American Ceramic Society, Vol. 47, 1964, pp. 283-291.

J. O. Hibbits and S. Kallmann, "Some Rather Unusual Chemical Analyses," TALANTA, Vol. 11, 1964, p. 1443, Presented at the Eleventh Ottawa Symposium on Applied Spectroscopy and Analytical Chemistry, Ottawa, Canada, September 9, 1964.

J. O. Hibbits, S. Kallmann, W. Giustetti, and H. K. Oberthin, "A Specific Method for the Determination of Trace Amounts of Titanium," TALANTA, Vol. 11, 1964, p. 1464.

J. O. Hibbits, A. F. Rosenberg, R. T. Williams, and S. Kallmann, "Simultaneous Determination of Trace Amounts of Zirconium and Titanium," TALANTA, Vol. 11, 1964, p. 1509, Presented at the Twelfth Anachem Conference, Detroit, Michigan, October 23, 1964.

R. C. Rau, "Calcination of BeO from Basic Acetate Derived $Be(OH)_2$, "Journal of American Ceramic Society, Vol. 47, No. 4, April 1964, pp. 179-184.

R. C. Rau, "Electron Microscopy of Irradiated BeO," Journal of Nuclear Materials, Vol. 11, 1964, pp. 320-332.

R. C. Rau and W. J. Glover, Jr., "Thermal Decomposition of Europium Hydroxide," Journal of American Ceramic Society, Vol. 47, No. 8, August 1964, pp. 382-387, Presented at the 66th Annual ACS Meeting, Chicago, Illinois.

R. C. Rau, S. F. Bartram, and K. Lacefield, "Neutron Damage in BeO Single Crystals," Submitted to Journal of American Ceramic Society, Presented at the 66th Annual ACS Meeting, Chicago, Illinois.

R. C. Rau, "Electron Microscope Studies of Irradiated A-286 Alloys," Technical Papers of the Sixteenth Metallographic Group Meeting held March 28-29, at Hanford Atomic Products Operation, Richland, Washington, Nuclear Metals Report NMI-4998, pp. 95-107.

S. F. Bartram, "On Rare Earth Borates of Composition $3R_2O_3 \cdot B_2O_3$," Published in Rare Earth Research II (Proceedings of the Third Conference on Rare Earth Research, April 21-24, 1963), pp. 165-180, Gordon and Breach Science Publishers, New York.

R. C. Rau, "X-ray Crystallographic Studies of Europium Oxides and Hydroxides," Published in "*Rare Earth Research II* (Proceedings of the Third Conference on Rare Earth Research, April 21-24, 1963), pp. 117-134, Gordon and Breach Science Publishers, New York.

R. C. Rau, "Note on the Crystallography of Eu_2SiO_4," *Acta Crystallographica*, Vol. 17, 1964, pp. 1483-84.

E. W. Filer, C. A. Asaud, K. Lacefield, and R. B. Kull, "Metallographic and Ceramographic Preparation of Nuclear Materials," Presented at 18th AEC Metallography Group Meeting, Los Angeles, California, GE-NMPO, TM 64-6-23.

R. C. Rau, "Electron Microscope Studies of Radiation Damage in BeO," Presented at 17th Pacific Coast Regional Meeting of the American Ceramic Society, San Francisco, California, GE-NMPO, TM 64-10-20.

E. S. Funston, W. J. Kirkpatrick, and P. P. Turner, "Preparation of High Purity BeO Powder," *Journal of Nuclear Materials*, Vol. 11, 1964, pp. 310-319.

A. L. Clavel, J. C. Blake, and J. F. White, "Measurement of the Flow Characteristics of a Plastic Dispersion Mass," GE-NMPO, TM-63-4-9, Submitted to the American Ceramic Society for publication.

E. C. Duderstadt and J. F. White, "The Sintering of BeO to Variable Densities and Grain Sizes," GE-NMPO, Submitted to the American Ceramics Society for publication.

L. H. Sjodahl, "Orientation in Extruded BeO," *Journal of Nuclear Materials*, Vol. II, 1964, pp. 302-309.

L. H. Sjodahl and J. H. Westbrook, "Sintering of BeO and Solute Induced Grain Boundary Hardening," Submitted to the American Ceramic Society for publication.

C. G. Collins, "Radiation Effects in BeO," Submitted to the Journal of Nuclear Materials for publication.

B. A. Chandler and J. B. McConnelee, "Thermal Stress Evaluation of Ceramic Fuel Elements," *Journal of Nuclear Materials*, Vol. 11, 1964, pp. 273-301.

J. R. Beeler, Jr., "Monte Carlo Calculations of Order-Disorder," Presented at 93rd AIME Annual Meeting, February 16-20, 1964, New York.

J. R. Beeler, Jr., "Computer Experiments in Solid State Physics," Presented at Physical Metallurgy Gordon Conference, July 20-24, 1964, Meriden, New Hampshire.

J. R. Beeler, Jr., "Atomic Collision Cascades in Alpha-Iron," Presented at Symposium on Atomic Collision Cascades in Radiation Damage, A.E.R.E., Harwell, England, July 13-17, 1964.

J. R. Beeler, Jr., and D. G. Besco, "Displacement Efficiency in Iron," *Bulletin of the American Physical Society*, Vol. 9, 1964, p. 283.

D. G. Besco and J. R. Beeler, Jr., "Primary Damage State in Iron," *Bulletin of the American Physical Society*, Vol. 9, 1964, p. 284.

N. R. Baumgardt and J. R. Beeler, Jr., "Monte Carlo Annealing Calculations," *Bulletin of the American Physical Society*, Vol. 9, 1964, p. 294.

J. R. Beeler, Jr., "Pressure-Shell Neutron-Damage Saturation and Embrittlement in Depth: Monte Carlo Calculations," *Transactions of the American Nuclear Society*, Vol. 7, No. 1, 1964, p. 124.

J. R. Beeler, Jr., "Neutron Irradiation Damage and Annealing in Finite b.c.c. Iron Samples," Presented at 67th ASTM Symposium, Chicago, June 21-26, 1964, GE-NMPO, TM 64-11-33.

J. R. Beeler, Jr., and D. G. Besco, "Effects of Channeling on Damage Production in Iron," *Physical Review,* Vol. 134, 1964, p. A530.

J. R. Beeler, Jr., "Distribution Functions for the Number of Distinct Sites Visited in a Random Walk on Cubic Lattices: Relation to Defect Annealing," *Physical Review,* Vol. 134, 1964, p. A1396.

J. R. Beeler, Jr., "Primary Damage State in Neutron-Irradiated Iron," *Journal of Applied Physics,* Vol. 35, 1964, p. 2226.

R. K. Betts, "Superheat Steam Corrosion of Fe-Cr-Al Alloys Containing Yttrium," Published by AEC in Proceedings of Ninth Nuclear Superheat Meeting, SAN 8003.

C. S. Wukusick and J. F. Collins, "An Iron-Chromium-Aluminum Alloy Containing Yttrium," *Materials Research and Standards* (ASTM), December 1964.

E. A. Aitken, J. A. Edwards, and R. A. Joseph, "A Study of Uranium Oxide Activities in Solid Solutions of Urania-Thoria and Urania-Yttria," GE-NMPO, TM 64-7-31, June 1964.

J. E. Fox, "Excerpts From The Proceedings of the Rocket Reactor Materials Information Meeting," GE-NMPO, GEMP-293, July 1964.

P. K. Conn, H. C. Brassfield, J. D. Elkins, and R. E. Blevins, "The Behavior of a Refractory Metal with Regard to Fission Product Containment at High Temperatures," Presented at the American Nuclear Society Meeting, San Francisco, November, 1964. Abstract in: *Transactions of American Nuclear Society,* Vol. 7, 1964, p. 453, GE-NMPO, GE-TM 64-11-28.

C. C. Browne, R. E. Latta, and P. P. Turner, "Coated Fuel Particle Development and Evaluation," Presented at Meeting held at General Atomic Division of General Dynamics, San Diego, California, November 17-18, 1964, GE-NMPO, GE-TM 64-10-24.

E. S. Fitzsimmons, "Compressive Creep Behavior of Two Phase Oxide Systems," Presented at Meeting of Basic Science Division of American Ceramic Society, San Francisco, California, October 30, 1964.